# SOMATOSTATIN RECEPTOR TYPE 2 (SSTR2) FOR ADOPTIVE T CELL IMAGING, STIMULATION, AND ELIMINATION

A Dissertation

Presented to the Faculty of the Graduate School

of Cornell University

In Partial Fulfillment of the Requirements for the Degree of

Doctor of Philosophy

by

Yogindra Vedvyas

August 2018

# SOMATOSTATIN RECEPTOR TYPE 2 (SSTR2) FOR ADOPTIVE T CELL IMAGING, STIMULATION, AND ELIMINATION

Yogindra Vedvyas, Ph. D.

Cornell University 2018

Harnessing the immune system to recognize and destroy tumor cells has been the central goal of anti-cancer immunotherapy. Adoptive cell therapy (ACT) is a treatment that uses a cancer patient's own T lymphocytes with anti-tumor activity, expanded *in-vitro* and re-infused into the patient. The ability to genetically engineer human lymphocytes and use them to mediate cancer regression in patients, which has recently been demonstrated, has opened possibilities for the extension of ACT immunotherapy to patients with a wide variety of cancer types and is a promising new approach to cancer treatment. Clinical monitoring of ACT utilizes serial blood analyses to discern T cell activity. While useful, these data are 1-dimensional and lack spatiotemporal information related to treatment efficacy or toxicity. In this dissertation, I have utilized a human genetic reporter, somatostatin receptor 2 (SSTR2), and PET, to quantitatively and longitudinally visualize whole-body T cell distribution and antitumor dynamics using a clinically approved radiotracer. Initial evaluations determined that SSTR2-expressing T cells were detectable at low densities with high sensitivity and specificity.

While keeping a close eye on the status of immunotherapy is shown in the early part of this thesis, later topics address the ideal antigens to target tumors, more specifically targeting solid tumors. We turned to targeting inflammation, specifically intercellular adhesion molecule-1 (ICAM-1), as an ideal marker for solid tumors. ICAM-1, which has been implicated to play a critical role in tumor progression in various

types of cancer, has also been linked to cancer metastases, where this molecule facilitates the spread of metastatic cancer cells to secondary sites. The unique expression profile of ICAM-1 throughout solid tumor microenvironment makes ICAM-1 an intriguing molecular target, as evidence suggests that approximately 25% of all human cancer worldwide is associated with chronic inflammation.

Utilizing ICAM1 as a target, I share the success of using an ICAM1 specific chimeric antigen receptor (CAR) T cells to eliminate anaplastic thyroid cancer tumors, in a solid tumor mouse model. The first attempt was using the single-chain fragment-variable of R6.5, an ICAM-1 specific antibody. Followed by the utilization of the active domain (I-domain) of the natural ligand to ICAM-1, lymphocyte function associated antigen-1 (LFA-1). For I-domain CAR, many engineered affinity variants were studies, to help determine the ideal antigen to affinity, to maintain CAR T cell persistence without any systemic toxicities sometimes observed with ACTs.

# BIOGRAPHICAL SKETCH

Yogindra Vedvyas is the second child born to an Indian family between Anil Vedvyas and Vandhana Vedvyas in New Delhi, India. He grew up with the nickname Yogi, constantly being hazed as a child, due to a popular TV show at the time, “Mr. Yogi”. He immigrated to the US in 1999, with his family. He attended middle school and high school in Queens, New York, where he grew up with a diverse group of friends. With the nickname Yogi, the hazing never stopped, “Mr. Yogi” turned to Yogi-Bear, turned to Yugioo. He learned to find the humor in it, as he knew there are many variation still to come.

While he always enjoyed building things, taking things apart and try to put them back together, he never considered choosing a career in science. Through out high school and undergraduate studies, he was more interested in business and finance. It was a molecular biology requirement as an Undergraduate at Baruch College, which encouraged him to enroll in more science classes. This led to more and more course work in biology as an elective that led him to enroll at Hunter College to pursue a BA/MA in Molecular biology. From there he started working in the lab of Dr. Lesek Kotula at New York Blood Center. Eventually deciding to pursue graduate studies at Cornell, initially enrolling in the Masters of Engineering program. While doing an M.Eng project in the lab of Dr. Moonsoo Jin and Dr. David Putnam, it was evident that he enjoyed various protein engineering projects and drug/gene delivery systems.

With the support of Dr. Jin, he was able to enroll into the PhD program in Biomedical Engineering. It was a non-traditional route into science. His goal for a PhD was never just the degree; the primary goal was to successfully translate work from the bench into clinic. With the Jin Lab moving from Ithaca campus to New York, he was able to work on more clinically translatable projects. His PhD years have been productive with

many collaborations and publications, and the goal to translate work into the clinic is likely to come true. His most recent projects in CAR T cell are being validated in the Good Lab Practice (GLP) run, and an Investigational New Drug (IND) application with the FDA is being submitted. After a successful defense, he plans to carry this over the threshold.

Dedicated to Mom, Dad and my big brother Gaurav.

For their love, support and sacrifices.

# ACKNOWLEDGMENTS

First and foremost, I would like to express my deepest and sincerest appreciation to my advisor, Dr. Moonsoo Jin, for everything he has done for me. Dr. Jin is a thorough, self-critical, and enthusiastic scientist who believes nothing is impossible, and I hope I have acquired these traits for my future career. Looking back over the years of my training, I can only find how much I have grown intellectually and personally since the first day of joining his lab. Every conversation was a new lesson to learn and every lecture was an eye-opening experience for me. I have been constantly amazed and inspired by his attentiveness, perseverance, and the ability to connect on a broad range of topics, spanning many disciplines. I thank him for all that I have learned from him, and most importantly of course, for I have learned how to learn, and learn very well, all of which will undoubtedly make the rest of my life much richer in so many different ways.

I would also like to thank my committee members, Dr. David Putnam and Dr. Alexander Nikitin, for all the help they have provided during my training. I am also indebted to Dr. Peter Doerschuk, the tallest man with the most delightful laughter in the hallway of Weill Hall, for all the encouragements and getting me out of many jams. I would like to extend a special thank you to Belinda for the superfast administrative support and the warmest welcomes, even when I falter on paperwork…lots of paperwork.

I have had the luxury to work with many talented lab members. The lab migrated from Ithaca to New York City, and members from both campuses deserve acknowledgment. Jin lab is the place where I have constantly tested my limits every day and night for months and years, and it is with them I have been able to endure the seemingly everlasting challenges. I have learned a great deal from the post docs, Xuebo, Ling, Taehyun and Enda. Without their technical help and fruitful discussions I would not have had the success I have today. I also thank my labmates, Goose, Zoe, Fai, Spencer,

Susan and Marjan, for all their help and support. A big thank you to our undergrads Nikolai (Nik) Turner (TAS), Kathleen (Ms. Phung), and Evelyn (Evil!) for being wonderful and encouraging. The move to the Department of Radiology/Molecular Imaging Innovations Institute (MI3), provided a fantastic opportunity to learn from clinicians and clinical researchers; I am grateful to Drs. Ching Tung, Benedict Law, Richard Ting, John Babish, Paresh Kothari, Anastasia Nikolopoulou, Dohyun Kim, Vanessa Bellat, Hari Krishna Kommidi, James Kelly, and Alejandro Amor-Coarasa; All of them had a hand in teaching me Radiochemistry. A sincere Thank You to Cliona Stacks, Sindy Ozoria, and Haedar Abuirqeba; MI3 wouldn't function without them. I am especially grateful and indebted to Dr. Irene Min, Dr. Yanping Yang, Dr. Katherine Gray, and Jaclyn E. McCloskey—for providing a wonderfully constructive environment. Without them, this work would not be translating into the clinic. It is more than probable that I could not have finished much of the work presented in this dissertation without their diligent help.

TABLE OF CONTENTS

LIST OF FIGURES AND TABLES

# CHAPTER 1

# INTRODUCTION

## Adoptive T Cell therapy: A variety of options to translate to the clinic.

The application of Adoptive T cell (ATC) therapy has re-energized the field of cancer immunotherapy. These therapies are sub-classified into two main technologies of tumor immunotherapy: Chimeric Antigen Receptor Engineered T Cell (CAR-T) and Gene Modified T cell receptors (TCR). (Figure 1.1)[1]. Both these strategies have the common goal of improving the ability of T cell receptors to recognize and attack specific target cell antigens by means of genetic modification. Both platforms were introduced with the initial intention of using adaptive immunity, rather than more traditional therapies such as radiotherapy, chemotherapy, and surgery to treat cancer. Adaptive immunity has numerous beneficial properties that provides amenable treatment for cancer: 1) T cell responses are specific and thus can potentially distinguish between healthy and cancerous tissue. 2) T cell responses are robust, undergoing up to 1,000-fold clonal expansion after activation. 3) T cell response can be directed to the site of the antigen, suggesting a mechanism for eradication of distant metastases. 4) T cell responses have memory, allowing for the therapeutic effect to be maintained for years after initial treatment.

### *The evolution of TCR therapy*

TCR therapy evolved from the understanding that T cells are able to recognize and target specific antigens, presented to the major histocompatibility complex (MHC) proteins, that are present on the tumor and are not present or are poorly expressed on healthy tissue. Tumor-associated antigens (TAAs), neo-antigens or over expressed antigens, were identified by seminal studies in the 1990s [2], which conclusively demonstrated that immune cells could distinguish cancerous cells from healthy cells

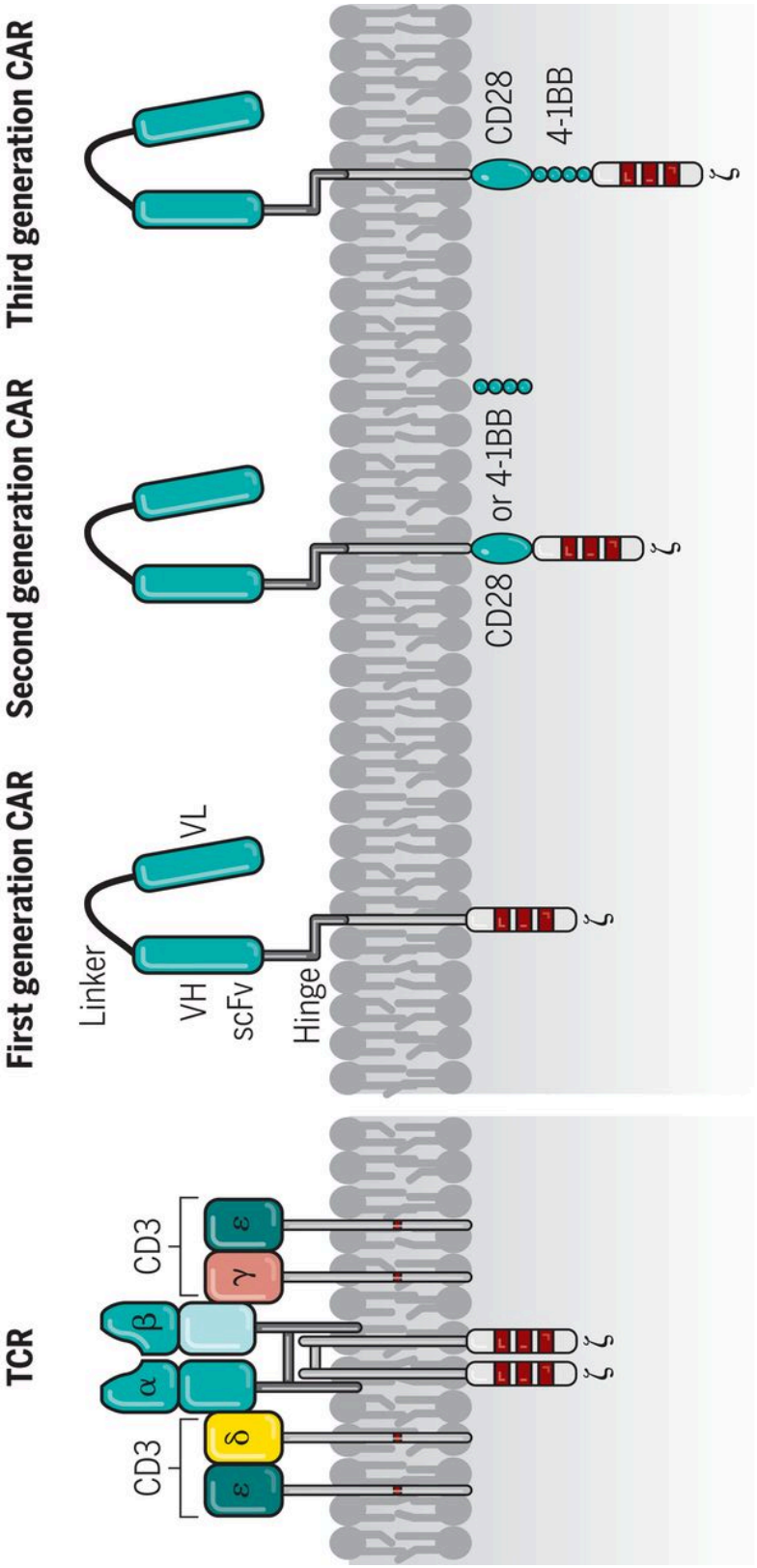
TCR
First generation CAR
Second generation CAR
Third generation CAR
CD3
CD3
ε
δ
α
β
γ
ε
ζ ζ
Linker
VH
scFv
VL
Hinge
ζ
CD28
or 4-1BB
ζ
CD28
4-1BB
ζ

**Figure 1.1 Molecular design of engineered TCR and CAR-T.**

T cells physiologically recognize their target by the T cell receptor (TCR) complex that is composed of the TCR α and β chain for recognition and the CD3 chains for signaling. The variable regions of each TCR chain (α and β) together bind to the MHC presented antigen. T cells can be genetically engineered with defined specificity by expression of recombinant TCR αβ chains of known specificity. In contrast to the TCR, the chimeric antigen receptor (CAR) is a polypeptide chain composed of a single chain fragment of variable region (scFv) antibody for antigen recognition, the extracellular spacer domain, a trans-membrane domain and the intracellular CD3ζ ("first generation" CAR), CD28-CD3ζ ("second generation" CAR) or the CD28-OX40-CD3ζ ("third generation" CAR) signaling chain. (Figure from Carl H. June (2018)) [3]

It was these tumor-infiltrating lymphocytes (TILs), which were able to recognized TAAs, that became the starting point for TCR therapy. In its earliest form it was demonstrated that TILs isolated from cancer samples and cultured with cytokines such as IL-2, exhibited cytotoxic activity against cancer cells *in vitro*[2]. Much more reliable therapeutic success was observed after advents of lymphodepletion (total body irradiation and chemotherapy), and selection of tumor-specific T cell clones generated from repeated antigen-specific stimulation of patient-derived (autologous) or donor-derived (allogeneic) T cells *in vitro*[4].

To further refine the therapy, tumor-reactive TCR must first be identified in T cells isolated from patients with naturally occurring anti-tumor activity, and can be engineered to increased affinity specificity by changing the complementarity-determining regions[5]. Alternatively, antigen-specific TCR can be derived from mice, that are engineered to express human antigens, expanding a subset of tumor reactive T cells. This enriched tumor reactive TCR repertoire cDNA is transferred, via viral transduction, back into the patient T cells[6]. A key theoretical concern with this approach is that engineered T cells contain both endogenous and engineered TCR (and thus possess dual specificity), which may lead to cross-reactivity after activation. The TCR chains from native and engineered TCR could also pair with each other to create novel TCR with new specificities. Despite this concern, side effects of genetically engineered T cell therapy have primarily been due to on-target off-tumor effects of TAAs expressed on healthy tissue. To put it in other words, the TAA was being expressed on healthy tissue, usually at a lower level of expression.

The success rate of these engineered TCR T cells has not been as successful as a mixture of TILs[7]. Despite the comparatively weak responses and safety concerns, there is a high interest in TILs ability to treat a wider variety of cancers and the potential to improve results by additional genetic modifications. Moreover, TCR engineered T cells are capable of penetrating the blood-brain barrier and inducing regression of brain metastases[8], with hope that patients with metastases at otherwise incurable sites may benefit from ATC. There was great success in melanoma targeting TCR, with specificity for gp100, cloned from melanoma reactive TILs, and transferred by retroviral means. This was then expanded to a few more melanoma specific targets such as MAGE-A3/4, MART-1, and NY-ESO-1/2.

There have been drawbacks noted for TCR therapies. Tumor cells may become invisible to TCR modified T cells due to repression of the MHC complex[9], mutations in β2 microglobulin [10], and compromising of antigen processing machinery[9, 11]. All of these changes may hinder antigen presentation and reduce TCR-mediated T cell activation. Engineering T cells with a recombinant TCR may produce additional safety hazards. Since the transgenic αβ TCR is being expressed with endogenous TCR, the transgenic and endogenous TCR may form miss-paired hetero-dimers. These misspairing of TCR chains can induce severe auto-reactivity due to gaining of an unpredictable specificity[12, 13]. The situation can theoretically be solved by switching the constant moieties of the transgenic TCR from human to non-human mammalian and by inserting additional cysteine bridges to facilitate

preferential pairing of the recombinant TCR αβ chains in the presence of the physiologic αβ TCR [14, 15].

While gene-modified T cells can be generated against many tumor antigens, TCR is still human leukocyte antigen (HLA)-restricted, meaning that new specificities must be described for each tumor antigen and HLA allele. The development of CARs provided a more universal approach to targeting tumor antigens that are expressed on the membrane of cancer cells.

*CAR-T therapy: An alternative to TCR therapy*

CAR-T therapy was introduced in the early 1990's, when Dr. Zelig Eshhar and his group showed how they could stably transduce, a new hybrid surface molecule on a T cells by using a lentivirus or retrovirus. This recombinant molecule, also named immunoreceptor, linked the antigen recognition with the downstream signaling machinery of the TCR. This 1$^{st}$ generation CARs were equipped with the extracellular domain with a tumor-binding moiety, typically a single-chain variable fragment (scFv), followed by a hinge/spacer of varying length and flexibility, a transmembrane (TM) region, and one or more signaling domains associated with the T-cell signaling (the stimulatory domain of the CD3ζ endodomain) to initiate T cell activation.[1] (Figure 1.1) These engineered T cells recognize their new target by CAR binding and become activated to secrete pro-inflammatory cytokines, amplify and lyse the cognate target cells. Since the binding is independent of MHC, independent of individual HLA subtype, CAR-T cells are not affected by MHC repression and loss of HLA molecules

on target cells. This also opened the door to non-typical T cell targets like carbohydrates and gangliosides.[16, 17]

However, full and lasting T cell activation requires two complementary signals: one provided by the TCR/CD3 and the other by co-stimulation domains, like CD28 or 41BB. Furthermore, prolonged T cell activation requires co-stimulation by autocrine factors, such as IL-2, which is only secreted upon TCR signaling activation and simultaneous CD28 signaling. This led to what is now classified as 2$^{nd}$ generation CAR. The most commonly used, 3$^{rd}$ generation CAR, an additional transducer domain (CD27, 41-BB or OX40) is added to the CD28 and ζ-chain to maximize strength, potency, and duration of the delivered signals[18-20]. (Figure 1.1)

In the past few years, there have been groups claiming a 4$^{th}$ generation CAR-T, where they fuse IL-12 to the base of the 2$^{nd}$ generation constructs. This is known as T cell redirected for universal cytokine-mediated killing (TRUCKs). TRUCKs augment T-cell activation and attract innate immune cells to eliminate antigen-negative cancer cells in the targeted lesion. This strategy allows to target additional non-susceptible cells in the tumor micro-environment by the inducible release of transgenic immune modifiers. Such TRUCK T cells can also treat viral infections, metabolic disorders, and auto-immune diseases[21]. Additional groups have taken this a step further and integrated the secretion of molecules such as IL-12, CD40L, 4-1BBL, or even additional scfv's to change the tumor microenvirnment or bypass immune checkpoint inhibition (PD1/PD-L1)[22].

**Inflammation as a target for Cancer: Up-regulation of ICAM-1 on tumors.**

Inflammation is the bodies' necessary response to harmful insult, in which a careful interplay between the immune system and damaged tissues mediate the healing process. The restoration is characterized by heat, pain, redness, and swelling, which is instigated by increased blood flow, accumulation of fluid, and release of chemicals, such as histamine and bradykinin [23]. This intricate process requires tight control over the various components of the immune system for achieving desired immune responses to eliminate the stimulus and heal in a timely manner[24]. Acute inflammation is a self-limiting transient response that usually results in controlled wound healing. Chronic inflammation, on the other hand, is a prolonged response prompted by dysregulated immunomodulation [25].

The link between inflammation and cancer was first postulated by Virchow in the 19th century, when he discovered the presence of leukocytes in tumors. Since then, many studies have strengthened this hypothesis, and recently, clear evidence that inflammation plays a role in tumor progression has been demonstrated [26]. Now, it is generally accepted that an inflamed milieu is a critical component of tumor initiation and progression, dubbing cancer as "wounds that do not heal."[27] In many cases, some form of chronic inflammation precedes tumor development. While initial inflammatory responses are a part of normal host defense, tumorigenic pathogens can sabotage host's immune response and establish chronic inflammation, facilitating cancer development. For example, persistent *Helicobacter pylori* infection is associated with gastric cancer and mucosa-associated lymphoid tissue lymphoma [28],

while infections with hepatitis B or C viruses can increase the risk of hepatocellular carcinoma [29].

Conversely, by mirroring wounds, tumors can also initiate inflammation. Once established, solid malignancies trigger an intrinsic inflammatory response that launches a pro-tumor microenvironment [30]. Tumors begin remodeling the neighboring stroma through secretion of chemokines/cytokines, recruitment of leukocytes, and initiation of angiogenesis [31, 32]. As a result of the transformation, tumor microenvironment is composed of innate and adaptive immune cells that co-exist with tumor cells as well as stromal cells, including mesenchymal cells, endothelial cells, and fibroblasts [33]. During this development, malignancies demand increasingly higher blood supply. When the tumor's metabolic needs are no longer met, the cells receiving insufficient levels of nutrients die, forming a necrotic core and releasing pro-inflammatory cytokines, such as IL-1 [34]. The augmented inflammation promotes further angiogenesis and the resultant wave of immune cells provides the tumor with necessary cytokines and growth factors [35]. Much attention has been given to the molecular and cellular pathways linking inflammation with cancer and the local tumor environment to identify new target molecules that could lead to improved diagnosis and treatment [30, 36]. Among the many molecular players involved in the complex response, key point in induction of inflammation is the transcription factor known as nuclear factor kappa-light-chain-enhancer of activated B cells (NFkB). Malignant epithelial cells manipulate NFkB, which controls various genes involved in inflammation, to be constitutively active. For example, in tumor-associated macrophages, activated NF-kB causes polarization of the cells into a phenotype that

suppresses cytotoxic T lymphocyte response, increases angiogenesis, and promotes tumor development [37]. One of the genes induced by the activation of NF-kB is intercellular adhesion molecule (ICAM)-1, known for its highly sensitive and localized expression in response to inflammatory signals.

ICAM-1 is a transmembrane glycoprotein belonging to the immunoglobulin superfamily of adhesion molecules and is composed of five extracellular Immunoglobulin G-like domains. ICAM-1 is continuously expressed at low levels on various cell types including fibroblasts, endothelial cells, and some leukocytes, but is profoundly inducible in inflammation [38, 39]. More specifically, inflammatory mediators, including lipopolysaccharide, IFN-**γ**, IL-1, and TNF**α** have been shown to cause strong induction of ICAM-1 in a wide variety of tissues and greatly increase binding of leukocytes, facilitating the infiltration of damaged tissues [40].

In line with the increasing reports on the importance of inflammation in tumor progression, ICAM-1 has also been implicated to play a critical role in tumor progression in various types of cancer [41-44], where its over-expression has been correlated to poor prognosis [44-46]. In addition, the expression level of ICAM-1 has also been linked to cancer metastases, where ICAM-1 facilitates the spread of metastatic cancer cells to secondary sites [44-46]. Not only is ICAM-1 over-expressed on many carcinomas, but it is also induced in the inflamed milieu in the vicinity of tumors[36, 47]. This unique expression profile of ICAM-1 throughout solid tumor microenvironment makes ICAM-1 an intriguing molecular target, which holds great potential as an important diagnostic tool for assessing the progression and prognosis of tumors. In therapy, using drug-delivery or immunotherapy methods targeted against

ICAM-1 would bypass the efforts often required in identifying proper tumor antigens for each type of cancer.

Integrin are members of a versatile family of noncovalently associated α/β heterodimeric cell surface receptors that stabilize cell-cell and cell-extracellular matrix adhesion during immune responses [47]. A type of leukocyte Integrin, αLβ2 or lymphocyte function associated antigen (LFA)-1, is constitutively expressed on all leukocytes and is the natural ligand for ICAM-1. Although originally identified using antibodies that inhibit T cell-mediated killing, LFA-1 is also critically important for other leukocyte functions, including adherence to endothelial cells, fibroblasts, and epithelial cells[38]. In resting lymphocytes, the integrin remains in a low affinity state but it is rapidly synchronized to undergo dynamic conformational changes during lymphocyte activation, which greatly increases its binding affinity to ICAM-1. In addition to the affinity modification, avidity alteration through clustering in the membrane plays an important role in regulating adhesiveness of LFA-1 to ICAM-1 [47]. Therefore, regulation of LFA-1 activation is pivotal for controlling leukocyte trafficking and immune responses in health and diseases.

**Difficulty with CAR-T cell against solid cancer, and strategies to overcome this hurdles**

Looking at recent clinical trials the most successful ones have been CARs, but those are only limited to leukemia/lymphoma and mostly non-solid tumors. TCR is mainly against melanoma due to the need for a TCR to have a homologous MHC on the Target cells. To date, CAR-T cells have demonstrated tremendous success in eradicating hematologic malignancies (e.g., CD19 CARs in leukemias). Two

autologous CAR-T cell therapies (Kymriah ™ and Yescarta ™) were recently approved by the FDA. Kymriah ™ is for the treatment of pediatric patients and young adults with refractory or relapse (R/R) B cell precursor acute lymphoblastic leukemia, while Yescarta ™ is for the treatment of adult patients with R/R large B cell lymphoma. In common, both are CD19-specific CAR-T cell therapies lysing CD19-positive targets. Many media reports have highlighted their dramatic efficacy in the short term [48].

However, this success has yet to be extrapolated to solid tumors. CAR-T cells have to surmount a lot of challenges in the solid tumor microenvironment. The two most favorable trials of ErbB2-CAR treating sarcoma, where 4 out of 17 patients showed stable disease, and GD2-CAR treating neuroblastoma, where 3 of 11 patients showed complete remissions [49]. The reason for CAR-T cells under-performing in solid tumor models is thought to be multifactorial. First, CAR-T cells must efficiently gather at the tumor site despite potential incompatibility between chemokine receptors present on T cell surface and chemokines secreted by tumors [50]. Second, CAR-T cells must infiltrate physical barriers posed by tumor stroma and interact with tumor cells in spite of possible antigen loss or heterogeneity. Third, CAR-T cells must overcome lack of nutrients, hypoxia, oxidative stress, acidosis, and immune-suppression [51, 52]. The exciting success of CAR-Therapy in hematologic malignancies is fueling the application of CARs in solid tumors. However, a more complete grasp over the major hurdles seen in solid tumors will be necessary to optimize CAR engineering.

As with most cancer therapies, there is an emerging set of toxicities associated with CAR-T cell therapies. In the case of CD19 CAR-T cells, these toxicities include B cell aplasia, tumor lysis syndrome (TLS), and cytokine release syndrome (CRS). Intravenous immunoglobulin can be used to replace quantitative antibody deficiency.

TLS has been managed successfully by standard supportive therapy, including hydration, alkalinization, allopurinol, and rasburicase [53]. In patients with B cell malignancies, CRS occurs at the time of peak levels of CAR-T cells in blood and bone marrow. Corticosteroids and cytokine blockade are currently being evaluated for patients with Chronic lymphocytic leukemia (CLL) and Acute lymphocytic leukemia (ALL). The tumor microenvironment contains multiple inhibitory factors to potentially suppress CAR-T cells. In order to prevent tumor cells from developing mechanisms to avoid the eradication by CAR-T cells, CAR-T biodistribution will help to analyze immune modulating cells (Tregs), Myeliod-derived suppressor cell (MDSCs), Immune checkpoints (e.g. PD-L1) and T cell suppressive cytokine.

For ACT, the T cell subset matters, adoptively transferred CD8+ T cell clones poorly persist[54] and need help of CD4+ T cell. Prolonged T cell anti-tumor response also requires resistance to repression in the tumor tissue. A number of efforts are currently undertaken to counteract tumor associated T cell repression, in particular mediated by Treg cells and checkpoint mediators. In animal models, CD28 co-stimulation without induction of IL-2 secretion protects a CAR redirected T cell response from Treg cell repression[55]. On the other hand, repetitive T cell stimulation upregulates CTLA-4, which acts as negative regulator to return the T cell to a resting stage. Administration of a CTLA-4 blocker, e.g., ipilimumab antibody, may prolong the anti-tumor activation of transferred T cells, although it is not locally restricted and will likewise affect all T cells[56, 57]. Expression profiling of TCR-engineered T cells demonstrates overexpression of multiple inhibitory receptors in persisting lymphocytes, including PD-1 and CD160. The latter is associated with decreased reactivity of TCR T cells in a ligand independent manner[58]. Essentially the same was observed for CAR-T cells[59].

**Disparities in imaging T Cell bio-distribution.**

The enthusiasm in CAR-T cell therapy, however, was dampened by reports on serious adverse events and fatalities after CAR-T cell administration[60-62]. In a clinical trial targeting ErbB2, healthy cells expressing low levels of the antigen in the lungs caused respiratory failure, leading to death. These rouge T cells were sufficient to trigger "on-target-off-organ" T cell activation[63]. In addition, CAR-T cell therapy can cause several alarming side effects, such as cytokine storms causing cytokine release syndrome (CRS), encephalopathy, and B cell hypoplasia. The trickiest of these be CRS, where the patients will have a fever, tachycardia, hypotension, capillary leak syndrome, and respiratory difficulty. Patients with encephalopathy will become confused and convulsive while patients with B cell dysplasia will have repeated infections due to poor immunity in vivo. These factors and other serious adverse events emphasize a careful evaluation of potential targets and the necessity for T cell dose escalation studies to balance anti-tumor efficacy and auto-immunity[64, 65]. Conventional methods used to monitor the immune system can be limited and biased. T cell responses are monitored most often through peripheral blood analysis and biopsy when appropriate. Blood measurements are the easiest and most robust method, providing information on cytokines, cell subsets, total cell quantity, and an easy method to track T cells in the periphery. However, blood sampling is limited by an inability to assess the T cell composition in alternative organs and tissues. These adverse events highlight the need to monitor ACT in patients. Furthermore, the inability to monitor these cells in-vivo makes it difficult to predict success or failure from the onset of therapy, and doesn't allow us to implement timely intervention in case there is toxicity. Specifically, a quantitative imaging modality such as Positron Emission Tomography (PET) is an essential tool that can be integrated into all ACTs.

PET is a powerful noninvasive imaging technique able to measure distinct biological processes in vivo by administration of a radiolabeled probe. Whole-body PET measurements track the probe accumulation providing a means to measure biological changes such as metabolism, cell location, or tumor burden. PET scanners detect the location of positron-emitting probes in vivo and produce a three-dimensional (3D) image. As the probe decays, positrons from the radionuclide annihilate with an electron in nearby tissue and emit two antiparallel 511 keV high-energy photons[66]. For immunotherapies (in particular understanding T cell responses), PET can be utilized for spatial and longitudinal tracking of T lymphocytes. Preclinical microPET scanners typically have spatial resolutions of 1–2 mm, whereas clinical scanners have a resolution of approximately 1 cm, which is sufficient to detect lymph nodes in both instances.[67]

Although PET has been utilized clinically for over 30 years, the recent development of additional PET radiotracers have dramatically expanded the use of PET to detect endogenous or adoptively transferred T cells in vivo. We have to be considerate to the criteria for selecting the ideal PET tracer for this work, particularly looking at aspects such as Specificity, Specific activity, and a favorable time window of PET. Specific activity is the ratio of the radiotracer molecule that is active, or in this case radiolabeled. It is ideal to have a very high specific activity, where a majority of the molecules injected in the patient is radiolabeled, as it would provide good counting statistics during the PET. However, it is also important to not violate the criterion of minimal mass effect due to the tracer, where the labeled ligands should not occupy more than 1 to 5% of the target receptor sites[68]. Time window of PET refers to turnover time of the tracer in tissue and must be within the time window of the PET technique and the radioactivity decay time of the labeling isotope. The commonly used positron emitters have rather short half-lives (ie. $^{68}$Ga, 68min; $^{18}$F, 108min, etc.).

Considering the radiation dose to the subject, the half-life should not be longer than is required for high-quality measurements.

When addressing the specificity, we are considering what target the PET is imaging. When it comes to successful imaging of T cells, there are 3 strategies that work: 1) pre-labeling T cells with radionuclides, 2) immuno-PET, and 3) genetically modified T cells to express a reporter gene. Each of these strategies has their advantages and disadvantages.

**The comparison of direct-labeling vs. immunoPET vs. genetically modified PET-reporter.**

Pre-Labeling T cells is a process in which cells of interest are harvested, incubated with the radiotracer of choice for intracellular uptake and retention, and then infused back into the patient for subsequent noninvasive detection. Generally, the radiotracers are taken up by cells via passive diffusion due to the use of lipophilic chelators and are retained by binding to intracellular proteins. There are many aspects of ex-vivo cell labeling that need to be optimized/determined to establish a reproducible radiolabeling procedure that does not cause toxicity for the cells of interest prior to imaging experiments, such as incubation time, radioactivity concentration per cell, retention of radioactivity over time, viability, radio toxicity, DNA damage, and altered phenotype or activation state. The significant drawbacks of this approach are the restricted longitudinal imaging due to radiotracer half-life, radiotracer dilution due to cell proliferation or cell death, and the small amount of radioactivity that can accumulate in each cell. In the context of radiolabeled T cells, strict attention needs to be made on cellular activation and cell death due to established radio-sensitivity of T lymphocytes. Although this is a relatively routine procedure in nuclear medicine, it is nonetheless a labor-intensive process. This

methodology has been used to detect sites of inflammation or infection using gamma-emitting radionuclides, such as $^{99m}$Tc-hexamethylpropyleneamine oxime ($^{99m}$Tc - HMPAO), to detect sites of inflammation or infection[69] Similarly, other radio-isotopes have been used like $^{18}$F, $^{64}$Cu, $^{89}$Zr or $^{111}$In, allowing to image T cell bio-distribution from 90 min to up to 7 days[68-70]. While the imaging strategy is specific to the re-infused T cells, this might not be the best option to image ACT's. Ex-vivo radiolabeling will not provide information about the presence of adoptively transferred cells, weeks post-reinfusion due to the limitation of radionuclide half-life. Consistent T cell handling, incubation times, radiolabeling efficiency, viability, and phenotype of T cells must be established for routine clinical use.

The immuno-PET strategies use radiolabeled proteins targeting extracellular epitopes of T cells, by utilizing high specificity of antibodies to T cell subset, such as CD8+ or CD4+ on T cells, or activation specific, such as the checkpoint inhibitors like CTLA-4 or PD-1 expressed on tumor-infiltrating cytotoxic T lymphocytes. The long circulation half-lives of intact antibodies that range from days to weeks requires the use of long-lived PET radionuclides, such as $^{124}$I (4.2 days), $^{89}$Zr (3.2 days), and $^{64}$Cu (12.7 hr.)[71-73]. Since intact antibodies have a circulation half-life of week's in-vivo, long-lived isotopes conjugated to full-antibodies result in increased radiation dose for the patient. To reduce radiation exposure, enhance the target-to-background at early times, and make use of short-lived radionuclides, antibody engineering has allowed for the construction of antibody fragments for immuno-PET, including diabodies/bivalent diabody (scFv dimer; ~55 kDa; half-life ~2–5 hr in mice) and minibodies (scFv-CH3 dimer; ~80 kDa; half-life ~5–10 hr)[74-76]. These engineered minibodies do not deplete CD8+ T cells in vivo, as they lack the full Fc domain used by effector cells such as Natural Killer (NK) cells.

While immuno-PET using intact antibodies and antibody fragments, is a useful tool, the targets developed so far target the entire T cell population in-vivo, not necessarily modified T cells such as TIL or CAR-T. In addition, antibodies also function indirectly by eliciting immune responses utilizing the antibody Fc domain engaging Fcγ receptors on immune cells (antibody-dependent cellular cytotoxicity) or complement (complement-dependent cytotoxicity).

The third strategy of genetically modified PET-reporter is perhaps the best option for tracking ACT bio-distribution. Cells are stably transduced to express a surface protein or enzyme, such as a PET reporter and are then monitored for location, quantity, and bio-distribution by the corresponding PET probe. The major limitations in reporter imaging are the need to genetically manipulate cells ex-vivo and the risk of immunogenicity from ectopic expression of a foreign protein. Pre-clinically a few PET-reporters have been adapted for ACTs: human Norepinephrine transporter (hNET), Sodium Iodine Symporter (NIS), human Somatostatin Receptor 2 (hSSTR2), and Herpes Simplex Virus Type 1 Thymidine Kinase (HSV-TK). So far, HSV-TK has been the only one attempted for T cell imaging in humans.

Human Norepinephrine transporter (hNET) as a PET reporter gene is detected by [$^{124}$I]-metaiodobenzylguanidine ([$^{124}$I]-MIBG) [77]. hNET was first shown with Adoptive T cells reactive to Epstein–Barr virus (EBV). Initially, T cells were injected intra-tumorally, where they were able to detect as little as $10^4$ cells per tumor in the microPET scan. Investigators then tracked the expansion/infiltration of these EBV reactive CD8+ T cells long-term, showing an increase in Tcell presence up to 28 days later.

Sodium Iodine Symporter (NIS) is another PET-reporter that is a transporter expressed endogenously in the thyroid and stomach. Ectopic expression of NIS can allow reporter gene imaging by administration of iodine radionuclides ($^{124}$I, $^{131}$I) for

PET [78] and even technetium-99m pertechnetate ($^{99m}$TcO-)[79]. One advantage to NIS is the high specificity demonstrated in-vivo without needing to synthesize or radiolabel a reporter-specific probe. A major hindrance to using this reporter is the endogenous expression of NIS in salivary and lacrimal glands, stomach, choroid plexus, ciliary body of the eye, skin, placenta, lactating mammary gland, thymus, and, to a lesser extent, the prostate, ovary, adrenal gland, lung, and heart[80, 81]. Liver is regarded as the major organ for metabolism of radio-iodinated thyroglobulin released from functioning thyroid tissues[82]. This obscures any real possibility of using NIS as a T cell PET-reporter.

Herpes Simplex Virus Type 1 Thymidine Kinase (HSV-TK) was initially used a suicide gene, showing cell elimination by compounds such as Ganciclovir (GCV)[83]. It was then adapted for PET using $^{124}$I and $^{18}$F [84, 85]. In each case, a radiolabeled acycloguanosine-like compound was able to visualize HSV-TK expression in mice. In 2002, Gambhir group explored a mutant form of HSV-TK with improved *V*max/*K*m for GCV (sr39TK)[86]. Initially, this mutant was used to monitor tumor burden in mice transplanted with sr39TK expressing leukemic cells [87]. This study was the first demonstration of the feasibility for PET reporter imaging of HSV-TK as a tool to monitor the location of systemic immune cells not located as a subcutaneous graft. Infused cells could be monitored by PET imaging for up to 15 days post-transplant. Most recent studies with HSV-TK have shifted away from the [$^{124}$I]-FIAU probe and instead utilize a penciclovir analog, 9-(4-[$^{18}$F]-fluoro-3-hydroxymethylbutyl) guanine ([$^{18}$F]-FHBG). These studies have successfully tracked the location and infiltration of tumor reactive T cells in mouse models of immunotherapy. The dual functionality and efficacy of sr39TK as a reporter and suicide gene were recently validated in a humanized mouse model [88, 89]. Human hematopoietic stem cells (HSCs) were transduced to express a TCR and sr39TK.

Engraftment and T cell development were tracked by [$^{18}$F]-FHBG signal. To ablate the engineered cells, therapeutic doses of GCV were given. Efficacy was determined by follow-up [$^{18}$F]-FHBG scans that displayed little to no signal in ablated animals [88]. However, when this as attempted in humans, expression of HSV-TK was immunogenic in patients with CD8+ T cells against the HSV-TK gene[90, 91]**.**

The type 2 human somatostatin receptor (hSSTR2) was originally targeted as a highly expressed target on neuroendocrine tumors, with SPECT and PET agents developed for diagnosis and staging [92]. Outside of these tumors, expression of hSSTR2 is low throughout the body making this a suitable PET reporter gene. Several studies have demonstrated longitudinal reporter imaging with [68Ga]-DOTATOC in mouse models[93, 94]. It is the low background signal from this clinically approved tracer and reporter that led us to pick hSSTR2 as our PET-reporter of choice, expanded on chapters 2-5.

**Dissertation outline**

Chapter 2 describes the development of intercellular adhesion molecule-1 (ICAM-1) targeting CAR-T for the treatment of aggressive thyroid cancer, a solid tumor model. This third-generation CAR-T leverages adoptive T cell therapy as a new treatment modality against advanced thyroid cancer. ICAM-1 CAR-T cells demonstrated robust and specific killing of anaplastic thyroid cell lines in-vitro and in-vivo. Even though these cells had heterogeneous levels of ICAM-1 expression, addition of cytotoxic CAR-T cells induced increased ICAM-1 expression such that all cell lines became targetable, mediating profound tumor killing that resulted in long term remission and significantly improved survival compared to that of untreated mice. Similar results were shown even with patient derived tumors.

Chapter 3 documents the utility of human somatostatin receptor 2 (SSTR2), as a PET reporter. Specifically to be used with ATC to quantitatively and longitudinally visualize whole-body T cell distribution and antitumor dynamics using a clinically approved radiotracer, showing T cells were detectable at low densities with high sensitivity and specificity. SSTR2-based PET was applied to ICAM1-targeting CAR-T cells to show the treatment dynamics in-vivo with anaplastic thyroid tumors. Particularly, this approach highlights how timely CAR-T cell infusions resulted in survival of tumor-bearing mice, while later infusions led to uniform death. Real-time PET imaging revealed biphasic T cell expansion and contraction at tumor sites among survivors, with peak tumor burden preceding peak T cell burden by several days.

Chapter 4 illustrates, utilizing the same PET reporter, to help establish safety criteria for CAR-T. Particularly evaluates the ideal affinity of the antigen recognition

moiety to use when developing a CAR-T therapy. A panel of affinity-variant CARs was constructed targeting ICAM-1, using its physiological ligand, LFA-1. Anti-tumor T cell potency in-vitro was directly proportional to CAR affinity and ICAM-1 density. Longitudinal T cell tracking by PET/CT and concurrent cytokine measurement revealed expansion and contraction kinetics of micromolar affinity CAR-T cells and inflammatory cytokines. Highlighting how utilizing a reduced affinity-targeting moiety, can significantly boost efficacy and safety.

Chapter 5 is a compilation of multiple studies underway, where the utility of SSTR2 is evaluated beyond a simple PET reporter. Here, we see the possibility of using this report to activate and control ACT. Furthermore, there are additional studies to show the utility of SSTR2 PET with CD19-CAR, which was recently approved by the FDA.

Chapter 6 includes concluding remarks and additional possibility that this work would translate to, and its potential for translation into clinic.

REFERENCES


1. Makalowski, J. and H. Abken, *Can Redirected T Cells Outsmart Aggressive Melanoma? The Promise and Challenge of Adoptive Cell Therapy*, in *Melanoma - Current Clinical Management and Future Therapeutics*. 2015.
2. Pardoll, D., *Does the immune system see tumors as foreign or self?* Annu Rev Immunol, 2003. **21**: p. 807-39.
3. Carl H. June, R.S.O.C., Omkar U. Kawalekar, Saba Ghassemi, Michael C. Milone., *CAR T cell immunotherapy for human cancer*. Science, 2018. **359**(6382): p. 1361-1365.
4. Ho, W.Y., et al., *In vitro methods for generating CD8+ T-cell clones for immunotherapy from the naive repertoire*. J Immunol Methods, 2006. **310**(1-2): p. 40-52.
5. Kershaw, M.H., J.A. Westwood, and P.K. Darcy, *Gene-engineered T cells for cancer therapy*. Nat Rev Cancer, 2013. **13**(8): p. 525-41.
6. Johnson, L.A., et al., *Gene therapy with human and mouse T-cell receptors mediates cancer regression and targets normal tissues expressing cognate antigen*. Blood, 2009. **114**(3): p. 535-46.
7. Morgan, R.A., Dudley, M. E., Wunderlich, J. R., Hughes, M. S., Yang, J. C., Sherry, R. M., et al. , *Cancer Regression in Patients After Transfer of Genetically Engineered Lymphocytes*. Science, 2006. **314**(5796): p. 126–129.
8. Morgan, R.A., Chinnasamy, N., Abate-Daga, D., Gros, A., Robbins, P. F., Zheng, Z., et al., *Cancer Regression and Neurological Toxicity Following Anti-MAGE-A3 TCR Gene Therapy*. Journal of Immunotherapy, 2013. **36**(2): p. 133–151.
9. Seliger, B., *Molecular mechanisms of MHC class I abnormalities and APM components in human tumors*. Cancer Immunol Immunother, 2008. **57**(11): p. 1719-26.
10. Sigalotti, L., Fratta, E., Coral, S., Tanzarella, S., Danielli, R., Colizzi, F., et al., *Intratumor heterogeneity of cancer/testis antigens expression in human cutaneous melanoma is methylation-regulated and functionally reverted by 5-aza-2 '-deoxycytidine*. Cancer Research, 2004. **64**(24): p. 9167–9171.
11. Marco Vitale, G.P., Beatrice Taroni, Giuliana Gobbi, Cristina Micheloni, and F.D. Rita Rezzani, Xinhui Wang, and Soldano Ferrone, *HLA class I antigen down-regulation in primary ovary carcinoma lesions: association with disease stage*. Clinical Cancer Research, 2005. **11**(1): p. 67–72.
12. Bendle, G.M., et al., *Lethal graft-versus-host disease in mouse models of T cell receptor gene therapy*. Nat Med, 2010. **16**(5): p. 565-70, 1p following 570.
13. Coccoris, M., et al., *T cell receptor (TCR) gene therapy to treat melanoma: lessons from clinical and preclinical studies*. Expert Opin Biol Ther, 2010. **10**(4): p. 547-62.
14. Kuball, J., Dossett, M. L., Wolfl, M., Ho, W. Y., Voss, R.-H., Fowler, C., & Greenberg, P. D., *Facilitating matched pairing and expression of TCR chains introduced into human T cells*. Blood, 2007. **109**(6): p. 2331–2338.

15. Cohen, C.J., et al., *Enhanced antitumor activity of murine-human hybrid T-cell receptor (TCR) in human lymphocytes is associated with improved pairing and TCR/CD3 stability*. Cancer Res, 2006. **66**(17): p. 8878-86.
16. Lo, A.S., et al., *Anti-GD3 chimeric sFv-CD28/T-cell receptor zeta designer T cells for treatment of metastatic melanoma and other neuroectodermal tumors*. Clin Cancer Res, 2010. **16**(10): p. 2769-80.
17. Yu, J., et al., *Anti-GD2/4-1BB chimeric antigen receptor T cell therapy for the treatment of Chinese melanoma patients*. J Hematol Oncol, 2018. **11**(1): p. 1.
18. Hombach, A. and H. Abken, *Costimulation tunes tumor-specific activation of redirected T cells in adoptive immunotherapy*. Cancer Immunol Immunother, 2007. **56**(5): p. 731-7.
19. Hombach, A.A. and H. Abken, *Costimulation by chimeric antigen receptors revisited the T cell antitumor response benefits from combined CD28-OX40 signalling*. Int J Cancer, 2011. **129**(12): p. 2935-44.
20. Hombach, A.A., et al., *Adoptive immunotherapy with redirected T cells produces CCR7- cells that are trapped in the periphery and benefit from combined CD28-OX40 costimulation*. Hum Gene Ther, 2013. **24**(3): p. 259-69.
21. Chmielewski, M. and H. Abken, *TRUCKs: the fourth generation of CARs*. Expert Opin Biol Ther, 2015. **15**(8): p. 1145-54.
22. Yeku, O.O. and R.J. Brentjens, *Armored CAR T-cells: utilizing cytokines and pro-inflammatory ligands to enhance CAR T-cell anti-tumour efficacy*. Biochem Soc Trans, 2016. **44**(2): p. 412-8.
23. Williams, T.J.a.M.J.P., *Role of prostaglandin-mediated vasodilatation in inflammation*. Nature, 1977. **270**(5637): p. 530-2.
24. Min, I.M., et al., *CAR T Therapy Targeting ICAM-1 Eliminates Advanced Human Thyroid Tumors*. Clin Cancer Res, 2017. **23**(24): p. 7569-7583.
25. Barton, G.M., *A calculated response: control of inflammation by the innate immune system*. J Clin Invest, 2008. **118**(2): p. 413-20.
26. Hanahan, D. and R.A. Weinberg, *Hallmarks of cancer: the next generation*. Cell, 2011. **144**(5): p. 646-74.
27. Dvorak, H.F., *Tumors: wounds that do not heal. Similarities between tumor stroma generation and wound healing*. New Englan Journal of Medicine, 1986. **315**: p. (1986).
28. de Martel, C. and S. Franceschi, *Infections and cancer: established associations and new hypotheses*. Crit Rev Oncol Hematol, 2009. **70**(3): p. 183-94.
29. Wu, S., et al., *A human colonic commensal promotes colon tumorigenesis via activation of T helper type 17 T cell responses*. Nat Med, 2009. **15**(9): p. 1016-22.
30. Mantovani, A., et al., *Cancer-related inflammation*. Nature, 2008. **454**(7203): p. 436-444.
31. Germano, G., P. Allavena, and A. Mantovani, *Cytokines as a key component of cancer-related inflammation*. Cytokine, 2008. **43**(3): p. 374-9.
32. Sica, A., P. Allavena, and A. Mantovani, *Cancer related inflammation: the macrophage connection*. Cancer Lett, 2008. **267**(2): p. 204-15.

33. de Visser, K.E., A. Eichten, and L.M. Coussens, *Paradoxical roles of the immune system during cancer development*. Nat Rev Cancer, 2006. **6**(1): p. 24-37.
34. Vakkila, J.a.M.T.L., *Inflammation and necrosis promote tumour growth*. Nature Reviews in Immunology, 2004. **4**(8): p. 641-8.
35. Karin, M., *Nuclear factor-kappaB in cancer development and progression*. Nature, 2006. **441**(7092): p. 431-436.
36. Coussens, L.M.a.Z.W., *Inflammation and cancer*. Nature, 2002. **420**(6917): p. 860-7.
37. Hagemann, T., et al., "*Re-educating" tumor-associated macrophages by targeting NF-kappaB*. J Exp Med, 2008. **205**(6): p. 1261-8.
38. Marlin, S.D.a.T.A.S., *Purified intercellular adhesion molecule-1 (ICAM-1) is a ligand for lymphocyte function-associated antigen 1 (LFA-1)*. Cell, 1987. **51**(5): p. 813-819.
39. Dustin, M.L., et al., *Induction by IL 1 and interferon-gamma: tissue distribution, biochemistry, and function of a natural adherence molecule (ICAM-1)*. Journal of Immunology, 1986. **137**(1): p. 245-54.
40. Rothlein, R., et al., *A human intercellular adhesion molecule (ICAM-1) distinct from LFA-1*. Journal of Immunology, 1986. **137**(4): p. 1270-4.
41. Kelly, C.P., et al., *Human colon cancer cells express ICAM-1 in vivo and support LFA-1-dependent lymphocyte adhesion in vitro*. American Journal of Physiology, 1992. **263**(6): p. 864-70.
42. Ogawa, Y., et al., *Expression of intercellular adhesion molecule-1 in invasive breast cancer reflects low growth potential, negative lymph node involvement, and good prognosis*. Clinical Cancer Research, 1998. **4**(1): p. 31-6.
43. Passlick, B., et al., *Expression of major histocompatibility class I and class II antigens and intercellular adhesion molecule-1 on operable non-small cell lung carcinomas: frequency and prognostic significance*. European Journal of Cancer, 1994. **30A**(3): p. 376-81.
44. Shimoyama, S., et al., *Overexpression of intercellular adhesion molecule-1 (ICAM-1) in pancreatic adenocarcinoma in comparison with normal pancreas*. Pancreas, 1997. **14**(2): p. 181-6.
45. Schroder, C., et al., *Prognostic value of intercellular adhesion molecule (ICAM)-1 expression in breast cancer*. J Cancer Res Clin Oncol, 2011. **137**(8): p. 1193-201.
46. Buitrago, D., et al., *Intercellular adhesion molecule-1 (ICAM-1) is upregulated in aggressive papillary thyroid carcinoma*. Ann Surg Oncol, 2012. **19**(3): p. 973-80.
47. Kurzinger, K., et al., *A novel lymphocyte function-associated antigen (LFA-1): cellular distribution, quantitative expression, and structure*. Journal of Immunology, 1981. **127**(2): p. 596-602.
48. Zheng, P.P., J.M. Kros, and J. Li, *Approved CAR T cell therapies: ice bucket challenges on glaring safety risks and long-term impacts*. Drug Discov Today, 2018.

49. Louis CU, e.a., *Antitumor activity and long-term fate of chimeric antigen receptor-positive T cells in patients with neuroblastoma*. Blood, 2011. **118**(23): p. 6050-6.
50. Slaney, C.Y., M.H. Kershaw, and P.K. Darcy, *Trafficking of T cells into tumors*. Cancer Res, 2014. **74**(24): p. 7168-74.
51. Howie, D., H. Waldmann, and S. Cobbold, *Nutrient Sensing via mTOR in T Cells Maintains a Tolerogenic Microenvironment*. Front Immunol, 2014. **5**: p. 409.
52. Zhou, Q., et al., *Program death-1 signaling and regulatory T cells collaborate to resist the function of adoptively transferred cytotoxic T lymphocytes in advanced acute myeloid leukemia*. Blood, 2010. **116**(14): p. 2484-93.
53. Cairo, M.S., et al., *Recommendations for the evaluation of risk and prophylaxis of tumour lysis syndrome (TLS) in adults and children with malignant diseases: an expert TLS panel consensus*. Br J Haematol, 2010. **149**(4): p. 578-86.
54. Antony, P.A., Piccirillo, C. A., Akpinarli, A., Finkelstein, S. E., Speiss, P. J., Surman, D. R., et al., *CD8+ T cell immunity against a tumor/self-antigen is augmented by CD4+ T helper cells and hindered by naturally occurring T regulatory cells*. Journal of Immunology, 2005. **174**(5): p. 2591–2601.
55. Kofler, D.M., et al., *CD28 costimulation Impairs the efficacy of a redirected t-cell antitumor attack in the presence of regulatory t cells which can be overcome by preventing Lck activation*. Mol Ther, 2011. **19**(4): p. 760-7.
56. Leach, D.R., Krummel, M. F., & Allison, J. P., *Enhancement of antitumor immunity by CTLA-4 blockade*. Science, 1996. **271**(5256): p. 1734–1736.
57. Pedicord, V.A., et al., *Single dose of anti-CTLA-4 enhances CD8+ T-cell memory formation, function, and maintenance*. Proc Natl Acad Sci U S A, 2011. **108**(1): p. 266-71.
58. Abate-Daga, D., et al., *Expression profiling of TCR-engineered T cells demonstrates overexpression of multiple inhibitory receptors in persisting lymphocytes*. Blood, 2013. **122**(8): p. 1399-410.
59. Moon, E.K., et al., *Multifactorial T-cell hypofunction that is reversible can limit the efficacy of chimeric antigen receptor-transduced human T cells in solid tumors*. Clin Cancer Res, 2014. **20**(16): p. 4262-73.
60. Brentjens, R., et al., *Treatment of chronic lymphocytic leukemia with genetically targeted autologous T cells: case report of an unforeseen adverse event in a phase I clinical trial*. Mol Ther, 2010. **18**(4): p. 666-8.
61. *<J. Clin. Oncol. 2006 Lamers.pdf>*.
62. Lamers, C.H.J., Sleijfer, S., Vulto, A. G., Kruit, W. H. J., Kliffen, M., Debets, R., et al., *Treatment of metastatic renal cell carcinoma with autologous T-lymphocytes genetically retargeted against carbonic anhydrase IX: first clinical experience*. Journal of Clinical Oncology, 2006. **24**(13): p. e20–2.
63. Morgan, R.A., et al., *Case report of a serious adverse event following the administration of T cells transduced with a chimeric antigen receptor recognizing ERBB2*. Mol Ther, 2010. **18**(4): p. 843-51.

64. Buning, H., et al., *Do CARs need a driver's license? Adoptive cell therapy with chimeric antigen receptor-redirected T cells has caused serious adverse events*. Hum Gene Ther, 2010. **21**(9): p. 1039-42.
65. Hawkins, R.E., et al., *Development of adoptive cell therapy for cancer: a clinical perspective*. Hum Gene Ther, 2010. **21**(6): p. 665-72.
66. Phelps, M.E., *Positron emission tomography provides molecular imaging of biological processes*. Proceedings of the National Academy of Sciences, 2000. **97**(16): p. 9226–9233.
67. Schmidt, K.C. and C.B. Smith, *Resolution, sensitivity and precision with autoradiography and small animal positron emission tomography: implications for functional brain imaging in animal research*. Nucl Med Biol, 2005. **32**(7): p. 719-25.
68. Madsen, K., et al., *Mass dose effects and in vivo affinity in brain PET receptor studies--a study of cerebral 5-HT4 receptor binding with [11C]SB207145*. Nucl Med Biol, 2011. **38**(8): p. 1085-91.
69. Hughes, D.K., *Nuclear medicine and infection detection: the relative effectiveness of imaging with 111In-oxine-, 99mTc-HMPAO-, and 99mTc-stannous fluoride colloid-labeled leukocytes and with 67Ga-citrate*. . Journal of Nuclear Medicine Technology, 2003. **31**(4): p. 196–201.
70. Lacroix, S., et al., *[18F]-FBEM, a tracer targeting cell-surface protein thiols for cell trafficking imaging*. Contrast Media Mol Imaging, 2013. **8**(5): p. 409-16.
71. Nayak, T.K., & Brechbiel, M. W., *Radioimmunoimaging with longer-lived positron-emitting radionuclides: potentials and challenges*. Bioconjugate Chemistry, 2009. **20**(5): p. 825–841.
72. Boswell, C.A. and M.W. Brechbiel, *Development of radioimmunotherapeutic and diagnostic antibodies: an inside-out view*. Nucl Med Biol, 2007. **34**(7): p. 757-78.
73. Tolmachev, V. and S. Stone-Elander, *Radiolabelled proteins for positron emission tomography: Pros and cons of labelling methods*. Biochim Biophys Acta, 2010. **1800**(5): p. 487-510.
74. Olafsen, T. and A.M. Wu, *Antibody vectors for imaging*. Semin Nucl Med, 2010. **40**(3): p. 167-81.
75. Tavare, R., et al., *Engineered antibody fragments for immuno-PET imaging of endogenous CD8+ T cells in vivo*. Proc Natl Acad Sci U S A, 2014. **111**(3): p. 1108-13.
76. Wu, A.M., *Engineered antibodies for molecular imaging of cancer*. Methods, 2014. **65**(1): p. 139-47.
77. Doubrovin, M.M., et al., *In vivo imaging and quantitation of adoptively transferred human antigen-specific T cells transduced to express a human norepinephrine transporter gene*. Cancer Res, 2007. **67**(24): p. 11959-69.
78. Penheiter, A.R., Russell, S. J., & Carlson, S. K., *The sodium iodide symporter (NIS) as an imaging reporter for gene, viral, and cell-based therapies*. Current Gene Therapy, 2012. **12**(1): p. 33–47.

79. Emami-Shahri, N., et al., *Clinically compliant spatial and temporal imaging of chimeric antigen receptor T-cells*. Nat Commun, 2018. **9**(1): p. 1081.
80. Riesco-Eizaguirre, G. and P. Santisteban, *A perspective view of sodium iodide symporter research and its clinical implications*. Eur J Endocrinol, 2006. **155**(4): p. 495-512.
81. Chung, J.-K., *Sodium iodide symporter: its role in nuclear medicine*. Journal of Nuclear Medicine : Official Publication, Society of Nuclear Medicine, 2002. **43**(9): p. 1188–1200.
82. Chung, J.K., Lee, Y. J., Jeong, J. M., Lee, D. S., Lee, M. C., Cho, B. Y., & Koh, C. S., *Clinical significance of hepatic visualization on iodine-131 whole-body scan in patients with thyroid carcinoma*. Journal of Nuclear Medicine : Official Publication, Society of Nuclear Medicine, 1997. **38**(8): p. 1191–1195.
83. Tiberghien, P., Reynolds, C. W., Keller, J., Spence, S., Deschaseaux, M., Certoux, J. M., et al., *Ganciclovir treatment of herpes simplex thymidine kinase-transduced primary T lymphocytes: an approach for specific in vivo donor T-cell depletion after bone marrow transplantation?* Blood, 1994. **84**(8): p. 1333–1341.
84. Gambhir, S.S., Barrio, J. R., Wu, L., Iyer, M., Namavari, M., Satyamurthy, N., et al., *Imaging of adenoviral-directed herpes simplex virus type 1 thymidine kinase reporter gene expression in mice with radiolabeled ganciclovir*. . Journal of Nuclear Medicine : Official Publication, Society of Nuclear Medicine, 1998. **39**(11): p. 2003–2011.
85. Tjuvajev, J.G., Avril, N., Oku, T., Sasajima, T., Miyagawa, T., Joshi, R., et al., *Imaging herpes virus thymidine kinase gene transfer and expression by positron emission tomography*. Cancer Research, 1998. **58**(19): p. 4333–4341.
86. S.S. Gambhir, E.B., M.E. Black, Q. Liang, M.S. Kokoris, J.R. Barrio, et. al., *A mutant herpes simplex virus type 1 thymidine kinase reporter gene shows improved sensitivity for imaging reporter gene expression with positron emission tomography*. Proceedings of the National Academy of Sciences of the United States of America, 2000. **97**: p. p. 2785.
87. L.Q. Le, J.H.K., S. Wong, K. Nguyen, S.S. Gambhir, O.N. Witte, *Positron emission tomography imaging analysis of G2A as a negative modifier of lymphoid leukemogenesis initiated by the BCR-ABL oncogene*. Cancer Cell, 2002. **1**: p. p. 381.
88. Griessinger, C.M., et al., *In vivo tracking of Th1 cells by PET reveals quantitative and temporal distribution and specific homing in lymphatic tissue*. J Nucl Med, 2014. **55**(2): p. 301-7.
89. Vatakis, D.N., et al., *Antitumor activity from antigen-specific CD8 T cells generated in vivo from genetically engineered human hematopoietic stem cells*. Proc Natl Acad Sci U S A, 2011. **108**(51): p. E1408-16.
90. C. Berger, M.E.F., E.H. Warren, S.R. Riddell, *Analysis of transgene-specific immune responses that limit the in vivo persistence of adoptively transferred HSV-TK-modified donor T cells after allogeneic hematopoietic cell transplantation*. Blood, 2006. **107**: p. p. 2294.

91. Traversari, C., et al., *The potential immunogenicity of the TK suicide gene does not prevent full clinical benefit associated with the use of TK-transduced donor lymphocytes in HSCT for hematologic malignancies*. Blood, 2007. **109**(11): p. 4708-15.
92. Gabriel, M., et al., *68Ga-DOTA-Tyr3-Octreotide PET in Neuroendocrine Tumors: Comparison with Somatostatin Receptor Scintigraphy and CT*. Journal of Nuclear Medicine, 2007. **48**(4): p. 508-518.
93. Zhang, H., et al., *Imaging expression of the human somatostatin receptor subtype-2 reporter gene with 68Ga-DOTATOC*. J Nucl Med, 2011. **52**(1): p. 123-31.
94. Zinn, K.R. and T.R. Chaudhuri, *The type 2 human somatostatin receptor as a platform for reporter gene imaging*. European Journal of Nuclear Medicine and Molecular Imaging, 2002. **29**(3): p. 388-399.

# CHAPTER 2

## CAR-T THERAPY TARGETING ICAM-1 ELIMINATES ADVANCED HUMAN THYROID TUMORS

**Summary**

Poorly differentiated thyroid cancer and anaplastic thyroid cancer (ATC) are rare yet lethal malignancies with limited treatment options. Many malignant tumors including papillary thyroid cancer (PTC) and ATC are associated with increased expression of intercellular adhesion molecule-1 (ICAM-1), providing a rationale for utilizing ICAM-1-targeting agents for the treatment of aggressive thyroid cancer. Therefore, we developed a third-generation chimeric antigen receptor (CAR) targeting ICAM-1 to leverage adoptive T cell therapy as a new treatment modality against advanced thyroid cancer. ICAM-1 CAR T cells demonstrated robust and specific killing of PTC and ATC cell lines in vitro. Interestingly, although certain ATC cell

---

This chapter was originally published in the Clinical Cancer Research (Min, I., Shevlin, E., Vedvyas, Y., Zaman, M., Wyrwas, B., Scognamiglio, T., Moore, M.D., Wang, W., Park, S., Park, S., Panjwani, S., Gray, K.D., Tassler, A.B., Zarnegar, R., Fahey, T.J., and Moonsoo M. Jin, M.M., *Clinical Cancer Research : an Official Journal of the American Association for Cancer Research* 23, no. 24 (December 15, 2017): 7569–83,) and is reprinted with permission. Vedvyas Y contributed CAR T vector construction, lentivirus production, T-cell transduction, Effector-to-target assay and cytokine analysis, animals & tumor growth analysis. This includes experiments and writing related to Figures 2.4, 2.6, 2.7, 2.8, 2.9, 2.10, 2.11, 2.12, 2.13, and 2.15.

,

,

lines showed heterogeneous levels of ICAM-1 expression, addition of cytotoxic CAR T cells induced increased ICAM-1 expression such that all cell lines became targetable. In mice with systemic ATC, a single administration of ICAM-1 CAR-T cells mediated profound tumor killing that resulted in long term remission and significantly improved survival compared to untreated controls. Patient-derived ATC cells overexpressed ICAM-1 and were largely eliminated by autologous ICAM-1 CAR T cells in vitro and in animal models. Our findings are the first demonstration of CAR T therapy for metastatic, advanced thyroid cancers that exhibit dramatic therapeutic efficacy and survival benefit in animal studies.

**Introduction**

Thyroid cancer is the most common malignancy of the endocrine system with an estimated 64,300 new cases being diagnosed in the US in 2016 [1]. This rate of diagnosis is increasing more rapidly than any other endocrine cancer in the US [2]. Most thyroid cancers are indolent and curable with standard treatments such as surgery, radioactive iodide (RAI) therapy, and thyroid stimulating hormone (TSH) suppression therapy for localized or regional disease. However, thyroid cancer patients can have widely different clinical outcomes depending on the pathological subtype. The follicular-derived thyroid cancers are divided into well-differentiated papillary thyroid cancer (PTC), follicular thyroid cancer (FTC), poorly differentiated thyroid carcinoma, and anaplastic thyroid carcinomas (ATC). The mortality rates of well-differentiated PTC (WDPTC), poorly-differentiated PTC (PDPTC), and ATC are reported to be 3–10%, 38–57%, and close to 100%, respectively [3]. Moreover, distant metastases occur at higher frequencies in PDPTC and ATC patients (representing

approximately 5% of all thyroid cancer patients), reducing their 5-year survival to 55.3% from 99.9% for localized, well-differentiated tumors [4]. The occurrence of ATC is fortunately rare estimated to be 2-5% of all thyroid cancers, but when it does occur it is rapidly lethal with a median survival of 5 months and 1-year survival rate estimated at 10-20% [5].

Research on targeted therapeutic interventions has focused on inhibiting aberrant pathways implicated in well-differentiated thyroid cancer, including RET-PTC translocations and BRAF point mutations (V600E) in PTC, and RAS point mutations in follicular and poorly-differentiated thyroid carcinoma (4). Vascular endothelial growth factor and its receptors have also been extensively studied and targeted with multikinase inhibitor drugs like sorafenib, sunitinib, and lenvatinib. While these strategies hold promise for extension of progression-free survival, there is little evidence for improved overall survival of thyroid cancer patients treated with these drugs (1). Moreover, there are no systemic therapies (cytotoxic and/or targeted) that aid survival or quality of life in patients with metastatic ATC. Multikinase inhibitor drugs have shown very limited response in ATC patients except for a few reported anecdotal cases [6, 7], highlighting an urgent need for new treatment modalities.

Recently, cancer immunotherapy and in particular, adoptive cell therapy (ACT) have made significant technological advancements leading to improvements in both efficacy and potential availability for the treatment of hematologic and solid tumors [8]. Successful application of ACT using unmodified cytotoxic T cells relies upon isolation and *ex vivo* expansion of patient T cells, typically tumor infiltrating T

cells (TILs), that recognize mutated or overexpressed tumor-associated antigens in an MHC-dependent manner. While successful in certain malignancies, most notably in melanoma [8], reliable extraction of TILs from a wider range of tumors is hampered by their low availability. Furthermore, tumors can down regulate MHC-I expression to render these T cell receptor (TCR)-based therapies less effective [9]. In order to enable effector T cells to target tumor antigens in a non-MHC-dependent manner, a CAR molecule that integrates antibody-derived antigen recognition via a single-chain fragment variable (scFv) and the zeta chain signaling domain from TCR complex was devised in the late 1980s [10]. Evolution of this design led to integration of additional signaling domains derived from co-stimulatory receptors such as CD28 and 4-1BB [11, 12] and these $2^{nd}$ and $3^{rd}$ generation CAR designs have shown remarkable success in hematologic cancers, particularly in B cell malignancies [13, 14]. Recently positive outcomes have also been observed in clinical trials treating solid tumors, including neuroblastoma, melanoma, and synovial cell carcinoma [8].

With the intention of developing a CAR T therapy applicable to recurrent, advanced thyroid cancer patients with no alternative treatment options, we first validated ICAM-1 as a suitable antigen for CAR-targeting by examining the correlation between ICAM-1 expression and malignant features in PTC and ATC. ICAM-1 is a member of the immunoglobulin superfamily, and is known to play a role in mediating cell-cell interactions such as leukocyte endothelial transmigration during inflammation [15]. Under non-inflammatory conditions, ICAM-1 expression is constitutively low and faintly detectable on endothelial cells. Increased ICAM-1 expression levels have been observed in multiple myeloma [16] and across many

disparate carcinomas including breast [17], pancreas [18], and gastric [19] tumors, and are correlated with tumor progression and metastatic capability [20]. Moreover, clinical trials support the safety and tolerability of targeting ICAM-1 using monoclonal antibodies [21-25]. Previous studies have shown that ICAM-1 expression is highly correlated with the both the malignancy and metastatic status of thyroid tumors, as well as the V600E of BRAF ($BRAF^{V600E}$) mutation [26, 27]. The stark correlation of ICAM-1 expression with adverse prognostic outcomes in thyroid cancer patients suggests that ICAM-1 may serve as a therapeutic target for advanced, recurrent thyroid tumors.

Extending our prior study on ICAM-1-specific CAR T cells [28], here, we describe the development and preclinical application of ICAM-1 targeting third-generation CAR T cells that showed marked eradication of ATC cell lines and patient-derived primary ATC cells in an ICAM-1-specific manner. The surface expression levels of ICAM-1 on ATC cell lines and patient-derived primary ATC cells were sufficiently high to discriminate them from healthy primary tissue cells. Our CAR T cell-based immunological approach has potentially wide-ranging applications for the treatment of other solid cancers where there is a strong association between ICAM-1 expression and adverse prognosis.

## Experimental Procedures

### *Study Approval*

Patient sample collection procedures were approved by the Weill Cornell Medicine Institutional Review Board, and patients' written consents were obtained prior to

inclusion in the study. All animal studies were approved by Weill Cornell Medicine's Institutional Animal Care and Use Committee.

***Cell lines and Primary cell culture***

8505C and BCPAP cell lines were purchased from DSMZ, Germany. FRO and KHM-5M cell lines were kindly provided by Dr. James A. Fagin (Memorial Sloan–Kettering Cancer Institute, New York, New York). HEK 293T, HMEC-1, and HeLa cells were purchased from ATCC. All cells except for HMEC-1 were maintained in RPMI medium supplemented with 10% FBS and 100 U/ml Pen/Strep. HMEC-1 cells were maintained in MCDB131 medium (ThermoFisher) supplemented with 10% FBS, 10 ng/ml Epidermal Growth Factor (ThermoFisher), 1 μg/ml hydrocortisone (Sigma-Aldrich), 10 mM glutamine, and antibiotics. Primary SAEC from healthy donors were purchased from Lonza and cultured in SABM media supplemented with SAGM bullet kit (Lonza). Primary kidney MVEC cells were purchased from Cell Systems and maintained in CSC complete media, which includes animal derived growth factors (CultureBoost) and 10 % serum (Cell Systems). Gene inactivation of ICAM-1 in 8505C was carried out using CRISPR plasmids available from Santa Cruz Biotechnology (sc-400098 and sc-400098-HDR). For some studies, cell lines were transduced with a fLuc-F2A-GFP lentivirus (Biosettia). $GFP^{+}$ and $ICAM\text{-}1^{Hi}$ cells were FACS sorted using the flow cytometry core facility at Weill Cornell Medicine. Peripheral blood mononuclear cells (PBMCs) were isolated over Ficoll-Paque PLUS (GE Healthcare) and cultured in Optimizer CTS T-cell Expansion SFM (Thermo Fisher) supplemented with 5% human AB serum (Sigma-Aldrich), 2 mM L-alanyl-L-

glutamine dipeptide, 100 U/ml Pen/Strep and 30 IU/ml human IL-2 (Cell Sciences). Nonadherent PBMCs were recovered after 24 hours and magnetically enriched for T cells using Dynabeads Human T Expander CD3/CD28 (Thermo Fisher) at a 2:1 bead/T cell ratio. Dynabead-bound T cells were subsequently cultured in IL-2–containing media at a density of 1-2 × $10^6$ cells/ml. Surgically resected fresh tumor tissues were cultured to establish patient-derived primary tumor cells with an endocrine pathologist (TS) reviewing each case to ensure correct diagnosis. Briefly, finely minced tumor tissues were digested with a mixture of collagenase and hyaluronidase (STEMCELL technologies) at 37°C on the shaker for 1 hour. After gently washing, tumor tissues were seeded on a 6-well plate in RPMI-1640 media supplemented with 10% FBS and 100 U/ml Pen/Strep.

***CAR T vector construction, Lentiviral production, and T cell transduction***

Engineering of R6.5 scFv into third generation pLenti plasmid has been described previously [28]. The sequence for rLuc was inserted into the vector using XbaI and SalI restriction sites. Production of lentivirus particles was described previously [28]. For transduction, human T cells were first activated for 24-48 hours by incubation with CD3/CD28 Dynabeads. At this point, cells were transduced by spinfection at 1,000 *g* for 1 hour at 32°C. T cells were also transduced a second time, 24 hours after initial transduction. The viral titer was adjusted to obtain a transduction level of approximately 50% by flow cytometry. During and following transduction, T cell media containing IL-2 was replaced with media containing human IL-7 (10 ng/ml) and IL-15 (5 ng/ml) (Peprotech).

***E:T assay and cytokine analysis***

Target cells ($5x10^3$) with fLuc expression were co-cultured with $1.25x10^4$ ICAM-1 CAR-transduced T cells in T cell media containing 150 μg/ml D-luciferin (Gold Biotechnology) with no addition of exogenous cytokines. Luminescence values were measured over time using a TECAN Infinite M1000 PRO plate reader and were normalized to control wells containing tumor and non-transduced parental T cell co-cultures. Supernatants from ICAM-1 CAR T and target cell co-cultures were quantitatively analyzed for the presence of Human IFN-γ and Human Granzyme B using the ELISA MAX™ Deluxe Kit and the LEGEND MAX™ Human Granzyme B ELISA Kit, respectively (both from BioLegend). Supernatant samples were spun for 3 minutes at 300 x *g* to remove debris and stored at -80° C, avoiding freeze/thaw cycles. Exogenous IFN-γ (Peprotech) was added to certain cells for analysis of ICAM-1 induction.

***Flow cytometry analysis for protein expression and cell cycle***

Staining of cell lines and primary cells were performed on ice for 20 minutes in 1x Hank's buffered saline solution (HBSS) staining solution containing 2% normal goat serum and 0.1% bovine serum albumin. ICAM-1 expression on cell lines and primary tumor cells was determined using mouse anti-human ICAM-1 R6.5 monoclonal antibody (5μg/ml) that was conjugated to Cy5.5 (Sulfo-Cyanine5.5 NHS ester, Lumiprobe) in laboratory or with secondary antibody against FITC-conjugated goat anti-mouse IgG (ThermoFisher) (R6.5 IgG was purified from hybridoma

(ATCC))[29]. Anti-human CD3-PECy5/CD4-PE/CD8-FITC cocktail, Alexa Fluor 647 anti-human CD3 (HIT3a), PE-conjugated EPCAM, APC-conjugated ICAM-1 (HA58) antibodies were from BioLegend. FITC-conjugated anti-mouse F(ab')2 antibody (ThermoFisher) was used to detect CAR expression in primary T cells. Live cell gating was determined by calcein blue (ThermoFisher) uptake. Organ tissues harvested from animals were macerated through a 70μm filter and after washing, tissue cell pellets were resuspended in red blood cell lysis buffer (BioLegend) on ice for 20 minutes. Mouse tissue cells were first blocked with mouse IgG (Sigma-Aldrich) at 2 μg/ml for 10 minutes, and then stained with primary antibodies. Dead cells and debris were excluded based on propidium iodide (PI, Sigma-Aldrich) staining at 1μg/ml. For cell cycle analysis, $5x10^5$ cells were seeded in 6-well plates overnight in RPMI media containing 10% FBS. Media was replaced with 2.5% FBS containing RPMI-1640 media in a subset of wells the following morning, and all cells were harvested and fixed 48 hours later using ice-cold PBS and 70% ice-cold ethanol, sequentially. After fixation at 4°C for 48 hours, cells were washed twice with PBS, treated with 100 ug/mL RNaseA for 30 minutes at 4°C, washed once with PBS, and stained with 50 ug/mL PI. For some experiments, cell cycle was determined by double staining of PI and FITC anti-BrdU antibody (BioLegend) after 30 min of incubation with 1 mM BrdU (Sigma-Aldrich) for 30 minutes. To determine Fas L- or TRAIL-induced cell death, His-tagged recombinant human Fas Ligand (TSFSF6, R&D systems) or TRAIL (TNFSF10, R&D systems) protein was added to the cells in media along with 2 μg/ml of anti-His crosslinking antibody (R&D systems). Flow cytometry

data were acquired using Gallios flow cytometer and was analyzed using Kaluza software (Beckman Coulter).

### *Cell Proliferation Assay*

The Vybrant MTT Cell Proliferation Assay Kit (ThermoFisher) was used to assess cell proliferation. $5x10^3$ viable cells were seeded per well in a 96-well plate in a final volume of 200 µL of RPMI-1640 media supplemented with 10% FBS. After overnight incubation, vemurafenib (Selleck Chemicals) was added to each well at a final concentration of 0.2% in phenol red-free RPMI-1640 media containing 2.5% FBS. After 72 hours, cells were fixed in MTT stock solution, as per manufacturer's instructions. Absorbance was read in an iMARK microplate reader (BioRad) at 490nm. For colony formation assays, $2x10^3$ cells per well were seeded in a 6-well plate. Treatment with vemurafenib was carried out as per the MTT assay. After 72 hours, cells were incubated in regular media for 10 days, followed by methanol fixation and staining with 0.1% crystal violet solution (Sigma-Aldrich).

### *Animals and Tumor growth analysis*

8-10-week-old female and male NOD-***scid***IL2Rg$^{null}$ (NSG) mice (Jackson laboratory) were used for xenograft experiments with ATC cells. GFP and fLuc-expressing 8505C ($0.75x10^6$ cells per mouse) and patient-derived ATC cells ($0.36x10^6$ cells per mouse) were i.v. injected to establish systemic metastasis establishment [30]. Longitudinal measurements of 8505C tumor burdens were taken using a whole-body optical imager (In-Vivo Xtreme 4MP, Bruker) 15 minutes after intraperitoneal injection of 100 µl of

150 μg/ml D-luciferin (GoldBio). During imaging, mice were anesthetized under 3% isoflurane at 2 L/min $O_2$. Image capture parameters were 4x4 binning collecting luminescence for 20 seconds. Total tumor burden was measured by generating full body region of interests (ROIs) and integrating total flux of luminescence using Bruker Analysis software. GFP-expressing livers, spleen, heart, and lungs were extracted from mice and imaged with a whole-body optical imager (In-vivo F-Pro, Bruker). Image capture parameters were no binning and 2 second exposure at 510 nm excitation and 530 nm emission. To track ICAM-1-CAR T cells expressing rLuc, mice were injected i.v. with 100 μl of RediJect Coelenterazine h (Perkin Elmer) and then immediately imaged using In-Vivo Xtreme 4MP (Bruker). Image capture parameters were 4x4 binning collecting luminescence for 60 seconds. For tumor burden analysis of patient-derived ATC-xenografts, mice were scanned with a 7T preclinical MRI scanner (Bruker Biospec 70/30 USR). Animals were placed prone headfirst into the system, with a respiratory sensor on their bodies to implement respiratory gating within coil (inner diameter, 3 cm). MR data was acquired with a RARE, or Rapid Imaging with Relaxation Enhancement, sequence using the following parameters: echo time = 8.710 milliseconds, repetition time = 1144.512 milliseconds, RARE factor = 2, number of averages = 18, total scan time = 32 minutes, FOV = 30 mm x 30 mm, spatial resolution = 0.117 mm/pixel, matrix size = 256 x 256, slice thickness = 0.5 mm, slices = 48. DICOM files were analyzed using open sourced software ITK-Snap. Tumor burden was calculated as a ratio of volume of tumor over volume of pulmonary cavity excluding heart.

***Immunohistochemistry***

Human tumor specimens were collected from patients undergoing surgery at Weill Cornell Medical College/New York Presbyterian Hospital. Formalin-fixed, paraffin-embedded human tissue blocks were cut at 5μm thick intervals and two consecutive slides were stained for ICAM-1 (G-5, Santa Cruz Biotechnology) and hematoxylin and eosin (H&E) at the Translational Research Lab at WCM Pathology and Laboratory Medicine [26]. Tumor xenografts were harvested, fixed in 4% paraformaldehyde in PBS, embedded in paraffin, and cut as 5μM sections. For lung tissues, 4% paraformaldehyde solution was perfused into the trachea to preserve the tissue morphology. All five lobes were separated and paraffin fixed. Consecutive slides were stained for H&E, human CD3, and GFP (Histowiz, Brooklyn). An endocrine pathologist (TS) reviewed each case to ensure correct diagnosis and to determine the tumor extent, CD3, GFP, and ICAM-1 staining in patient-derived and cell line xenografted tumor blocks.

***TCGA data reanalysis***

Clinical parameters, genomics and computational methods are described in detail in [31]. The results here are in whole or part based upon data generated by the TCGA Research Network: http://cancergenome.nih.gov/. The level of ICAM-1 RNA expression was given as a Z-score, which is the relative expression of an individual gene within tumor to the gene's expression distribution in a reference population. The ERK activity score is derived from 52 gene-signatures that were responsive to a MEK inhibitor in $BRAF^{V600E}$ melanoma cell lines [32]. $BRAF^{V600E}$-RAS score (BRS)

determines whether PTC exhibited a transcriptional program that related closer to tumors with $BRAF^{V600E}$ or RAS activating mutations by computing expression of 71 genes (details in [31]). Tumors with negative BRS were defined as $BRAF^{V600E}$-like, while those with a positive BRS were defined as RAS-like. The thyroid differentiation score (TDS) was determined by the relative transcription of 16 different thyroid function genes. Tumors with a positive TDS retain thyroid functions, whereas those with a negative TDS indicates a loss of normal thyroid cell function. Disease-free survival curves and overall survival curves were graphed using the Kaplan-Meier Method and were compared using the log-rank test. We analyzed the 80% power using a two-sided, 0.05 alpha level test to estimate whether the total number of events were sufficient.

***Statistics***

Comparisons between categorical vs. continuous variables were performed using the Mann-Whitney U/Krusker-Wallis test as appropriate. The Spearman correlation test was used to compare continuous vs. non-continuous variables. To account for multiple-testing bias, the *p*-value was adjusted using the Bonferroni correction. Statistical analysis was performed using Stata 14 (College Station, TX) or GraphPad Prism (La Jolla, CA). Graph representations were performed using GraphPad Prism.

## Results

### *Widespread overexpression of ICAM-1 in aggressive thyroid cancers*

Previous reports have demonstrated a positive correlation between ICAM-1 RNA and protein expression levels and the aggressive potential of PTC [26, 27], constituting ICAM-1 as a biomarker and a potential target for therapeutic interventions in thyroid cancer. PTCs are most commonly driven by two mutually exclusive somatic mutations, $BRAF^{V600E}$ or mutated RAS [31]. The $BRAF^{V600E}$ mutation is an established marker associated with activation of MAPK and downstream ERK signaling, reduced iodine uptake [31], and advanced clinical staging in PTCs [33]. Therefore, we investigated the characteristics of $BRAF^{V600E}$ versus RAS-driven PTCs with coexistent ICAM-1-overexpression (390 PTC patients in the Cancer Genome Atlas (TCGA) research database [31]) to understand the underlying signaling and differentiation properties. Expression of ICAM-1 mRNA in PTC positively correlated with an ERK activity metric (Spearman: 0.693, $p<0.0001$) (Figure 2.1A). ICAM-1 mRNA levels also associated better with tumors driven by $BRAF^{V600E}$ compared to RAS mutations ($BRAF^{V600E}$ and RAS-like tumors have negative and positive values in $BRAF^{V600E}$-RAS score (BRS), respectively; details in Methods section) (Figure 2.1B). Moreover, ICAM-1 mRNA expression in PTC patients was higher in those with the $BRAF^{V600E}$ mutation compared to WT BRAF (Figure 2.2A). These data suggest that ICAM-1 transcriptional control is linked to the activation of BRAF-

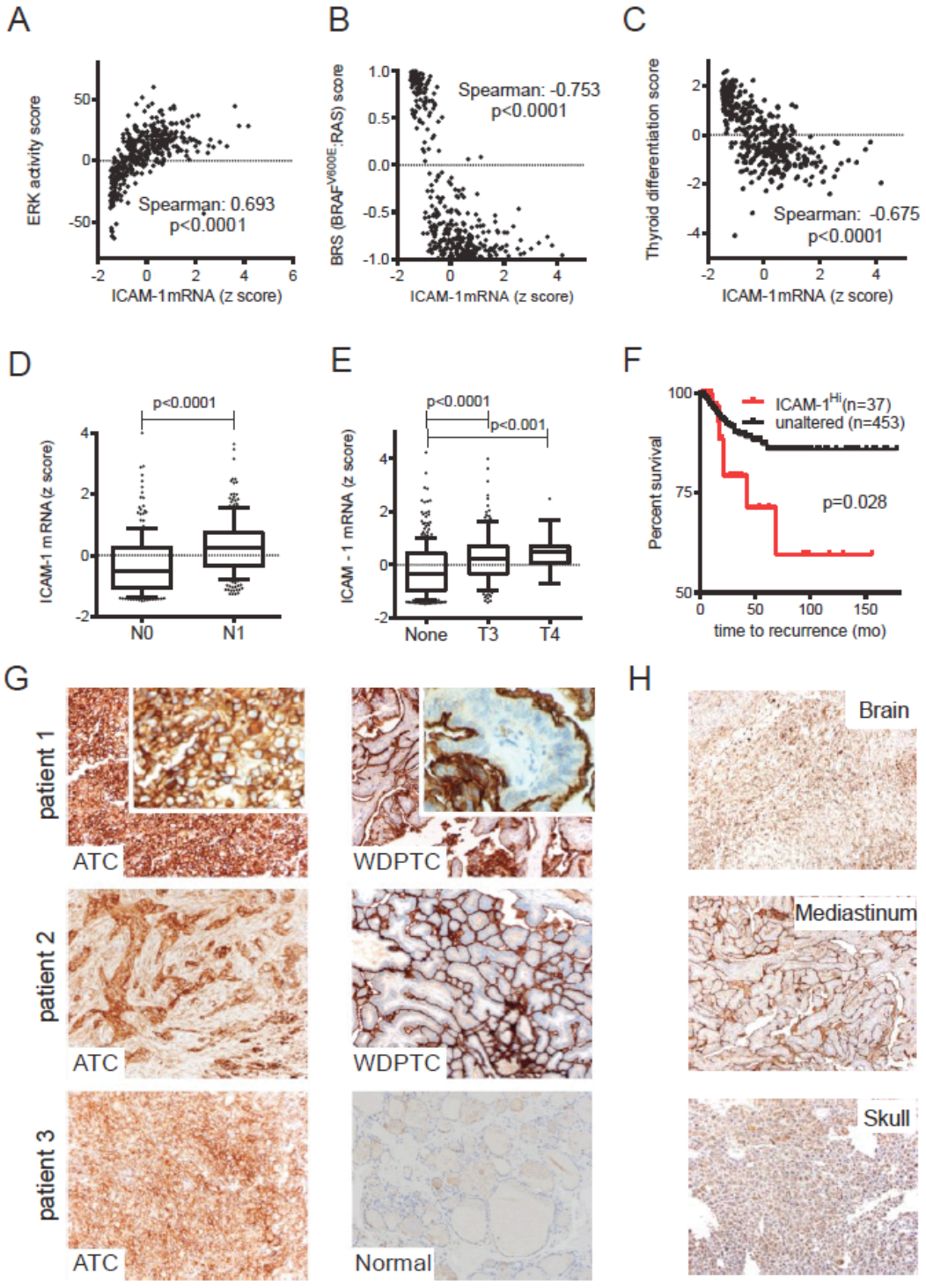
A
ERK activity score
Spearman: 0.693
p<0.0001
ICAM-1mRNA (z score)
B
BRS (BRAF^V600E;RAS) score
Spearman: -0.753
p<0.0001
ICAM-1mRNA (z score)
C
Thyroid differentiation score
Spearman: -0.675
p<0.0001
ICAM-1mRNA (z score)
D
ICAM-1 mRNA (z score)
p<0.0001
N0
N1
E
ICAM - 1 mRNA (z score)
p<0.0001
p<0.001
None
T3
T4
F
Percent survival
ICAM-1^Hi(n=37)
unaltered (n=453)
p=0.028
time to recurrence (mo)
G
patient 1
ATC
WDPTC
patient 2
ATC
WDPTC
patient 3
ATC
Normal
H
Brain
Mediastinum
Skull

**Figure 2.1 ICAM-1 overexpression is associated with recurrent, advanced thyroid cancer cells.** (A,B,C) Spearman's correlation analysis between ICAM-1 mRNA expression and ERK activity (A), $BRAF^{V600E}$-RAS score (BRS) (B), and thyroid differentiation score (C) were calculated using 390 PTC patient's genomics and clinical data available from TCGA analysis [31]. Algorithms for these scores have been described previously [31]. (D, E) Box plots compare tumor ICAM-1 mRNA levels via the absence (N0) or presence (N1) of tumors metastases to nearby lymph nodes (D) and cancer associated with extrathyroidal extension (E, None, no extension; T3, minimal extension; T4, moderate/advanced/highly advanced extension; n=226 and 232 for N0 and N1, respectively; n=338, 133, and 18 for None, T3, and T4 groups respectively). The solid, horizontal middle line in each boxplot indicates the median value; the upper and lower edges of each boxplot are the $75^{th}$ and $25^{th}$ percentiles respectively, and the top and bottom short horizontal bars denote the $90^{th}$ percentile and $10^{th}$ percentiles respectively. Filled circles indicate outliers. Mann-Whiney (D) and Krusker-Wallis (E) tests were used for determining statistical significance between groups. (F) Kaplan-Meier plot indicating a significant difference between recurrence-free survival rate of 490 PTC patients with unaltered or overexpressed (Z score > 1.5) ICAM-1 expression levels. (G) Representative ICAM-1-specific IHC images of ATC patient-derived tissue. Well-differentiated PTC (WDPTC) or normal thyroid tissue images on the same slide are shown for comparison on the right. H&E images of the corresponding tissues are provided in Figure 2.4. 20X magnification. Inset images are 40x magnification. (H) Representative ICAM-1 IHC results are shown for distant thyroid tumor metastases at 20X magnification.

MAPK-ERK signaling pathway in PTC. Overexpression of ICAM-1 in PTCs was associated with downregulation of thyroid-specific genes (Figure 2.1C), increases in lymph node metastases (Figure 2.1D), and extrathyroidal extensions (Figure 2.1E). PTC patients with high ICAM-1 expression are more likely to suffer from recurrence (Figure 2.1F) and to become refractory to treatments with conventional therapies such as RAI and TSH therapies (Figure 2.1C).

Next, we obtained tissue sections from patients with ATC, the most lethal form of thyroid cancer, and examined ICAM-1 protein expression by histology. All ten ATC tumor specimens displayed high grade ($3^{+}$) ICAM-1 staining with both cytoplasmic and membranous staining apparent in tumor cells (Figure 2.1G; hematoxylin and eosin (H & E) images of corresponding tumor blocks are provided in Figure 2.2). The fraction of tumor cells expressing ICAM-1 was also high, with seven out of ten samples staining diffusely positive, thus defining them as category 3 (>60% of total tumor cells stain ICAM-1 positive). The remaining three samples were grouped between categories 1 and 2 (1 = 1-29%, 2 = 30-59% positive cells among entire tumor). The ICAM-1 intensity score (defined as multiplying the immunoreactivity score and staining score) for our ATC patient samples was $7.8 \pm 2.1$ standard deviation (SD)), which is similar to that previously reported for RAI-refractory PTC and PDPTC [26]. The prevalence of ICAM-1 staining in ATC bears striking contrast to neighboring tissues in the same tissue slice, which display structurally limited ICAM-1 immunoreactivity at the apical membrane of WDPTC and

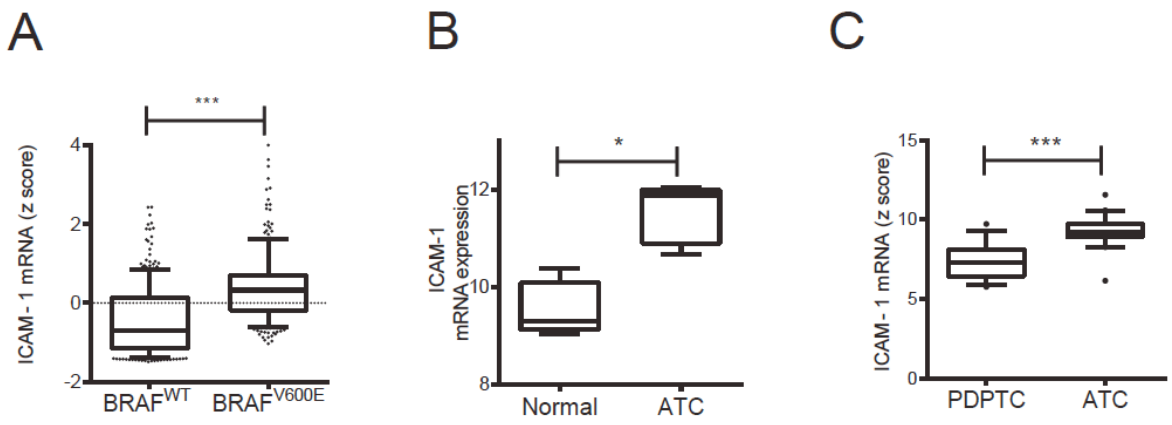


**Figure 2.2 PTCs with BRAF$^{V600E}$ mutations are associated with ICAM-1 overexpression.**

(A) ICAM-1 mRNA expression levels are compared between PTC patients with the BRAF$^{V600E}$ mutation or BRAF$^{WT}$ using the TCGA database [31]. (B) ICAM-1 mRNA expression level in patient ATCs is significantly higher than normal thyroid follicles [34]. (C) Comparison of ICAM-1 mRNA levels between PDPTC and ATC patients [35]. Statistical analysis was performed by Mann-Whitney test (***, $p<0.0001$; *, $p<0.05$).

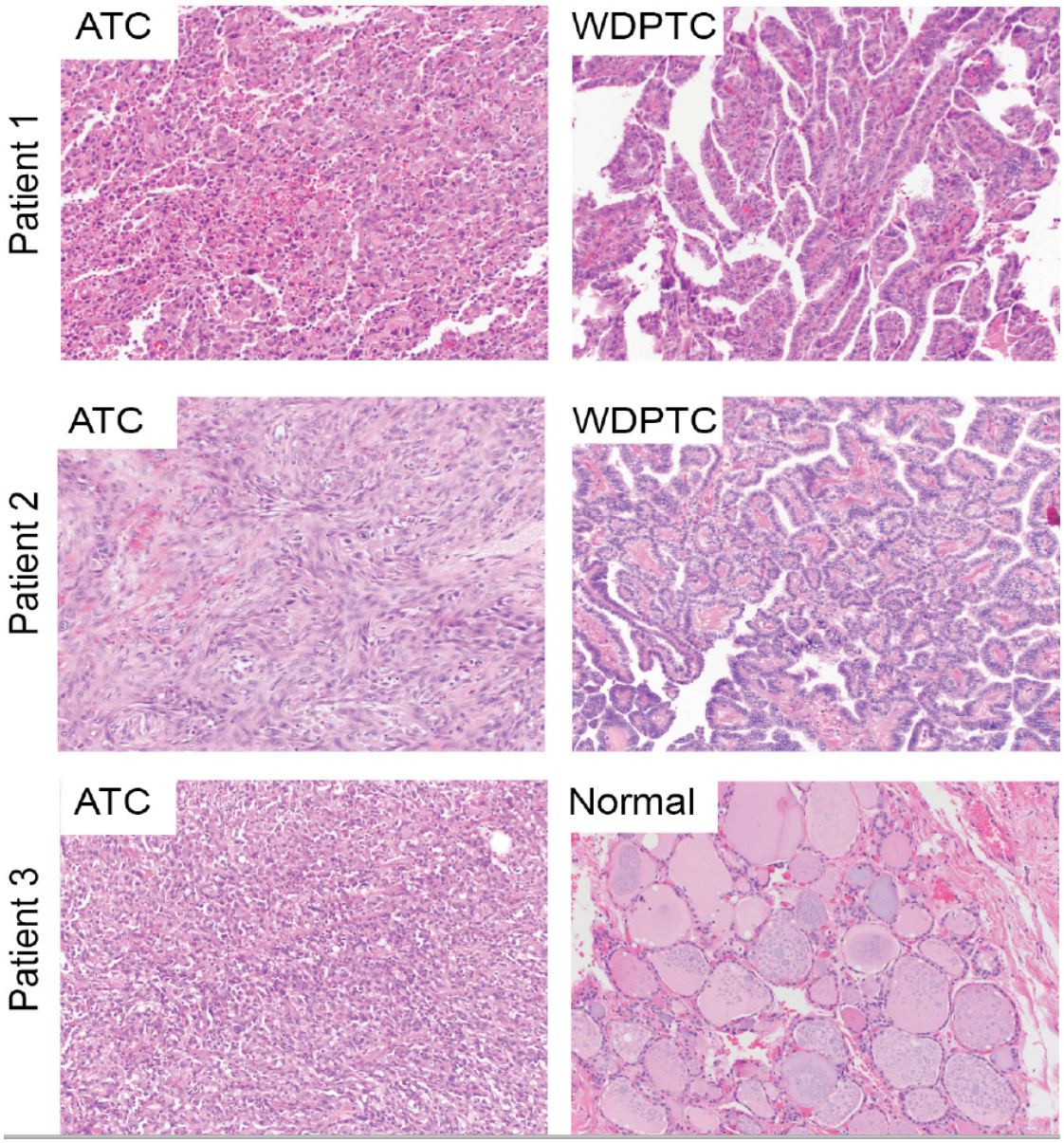


**Figure 2.3. Tumor tissue morphology in ATC patients.**

ATC tissue blocks used for ICAM-1 IHC as shown in Fig. 1G were also stained using hematoxylin and eosin. 20X magnification.

no ICAM-1 staining of normal thyroid follicles (Figure 2.3G, right). The demonstration of increased ICAM-1 protein expression in ATC agrees with previously reported ICAM-1 gene expression analyses that indicated significant differences in ICAM-1 expression between normal thyroid and PDPTCs (Figure 2.2 B & C) [34, 35]. We further analyzed ICAM-1 IHC within eight distant metastases originating from thyroid cancers (Figure 2.1H). Seven distant metastasis sites had category 3 ICAM-1 staining and four tissues displayed level $3^{+}$, demonstrating an overall ICAM-1 intensity score of $6.9 \pm 2.5$ (SD). Interestingly, metastatic thyroid cancers across each pathological subtype retained a similar ICAM-1 localization pattern. Distant metastases originating from WDPTC and follicular thyroid cancer displayed apical ICAM-1 staining, whereas poorly-differentiated follicular carcinoma and ATC exhibited broad ICAM-1 distribution with circumferential membranous staining (Figure 2.1H). Together, these findings demonstrate that ICAM-1 overexpression is a reliable molecular feature associated with PDPTC and ATC, and that circumferential membranous distribution of ICAM-1 is found in more advanced, metastatic thyroid cancers.

**ICAM-1 overexpression is associated with highly aggressive ATC cells**

We set out to investigate whether the level of ICAM-1 expression was linked to tumorigenic potency in established thyroid tumor cell lines. Several PTC and ATC lines were tested for the frequencies and levels of ICAM-1 expression by flow cytometry using the R6.5 monoclonal antibody [36]. The majority of thyroid cancer cell lines were ICAM-1 positive regardless of BRAF's mutational status (Figure

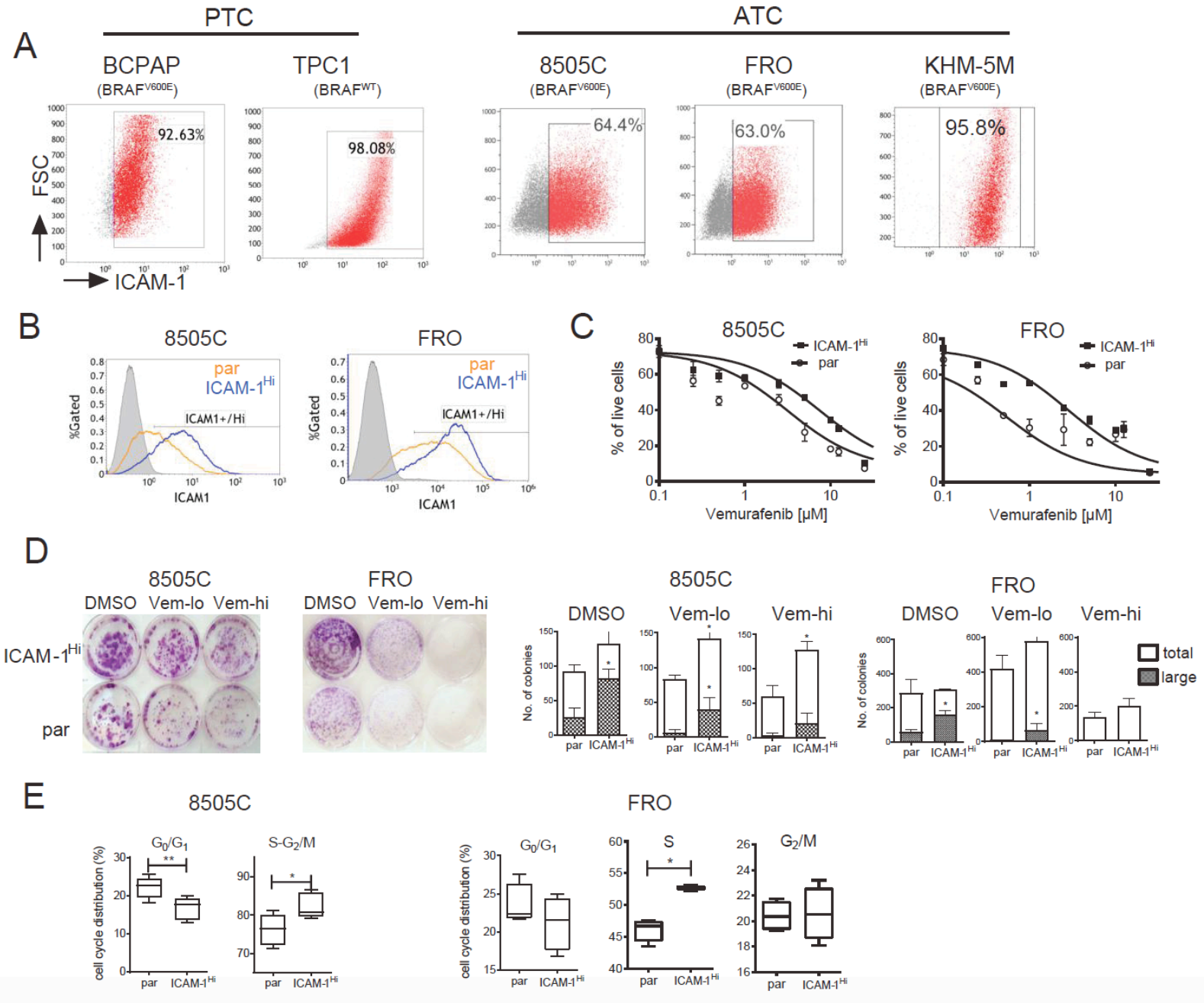
A
PTC
ATC
BCPAP
(BRAFV600E)
TPC1
(BRAFWT)
8505C
(BRAFV600E)
FRO
(BRAFV600E)
KHM-5M
(BRAFV600E)
92.63%
98.08%
64.4%
63.0%
95.8%
FSC
ICAM-1
B
8505C
FRO
par
ICAM-1Hi
ICAM1+/Hi
%Gated
ICAM1
C
8505C
FRO
ICAM-1Hi
par
% of live cells
Vemurafenib [μM]
D
8505C
FRO
DMSO
Vem-lo
Vem-hi
ICAM-1Hi
par
No. of colonies
total
large
E
8505C
FRO
G0/G1
S-G2/M
S
G2/M
cell cycle distribution (%)

**Figure 2.4. ICAM-1$^{+}$ is a biomarker for ATC.**

(A) Representative flow cytometry plots showing ICAM-1 expression in PTC (BCPAP, TPC1) and ATC (8505C, FRO, KHM-5M) cell lines. All cell lines except TPC1 harbor the BRAF$^{V600E}$ mutation. Boxes indicate cells that were determined to be ICAM-1 positive (shown as red dots) based on isotype controls. (B) ICAM-1 histogram plots of parental (par) (orange lines) and FACS sorted (ICAM-1$^{Hi}$) (blue lines) 8505C (left) and FRO cells (right). Gray histograms indicate isotype control stained par cells. (C) MTT analysis showing the percentage of live cells remaining after 72 hours of vemurafenib treatment in par and ICAM-1$^{Hi}$ cells isolated from 8505C (left) and FRO (right). IC50 values for ICAM-1$^{Hi}$ cells relative to par were increased 4.6-fold and 17.7-fold in 8505C and FRO cells, respectively (n=3, 6). (D) Representative images of cell colonies formed after treatment with vehicle DMSO, low (1.5 and 2.5μM for 8505C and FRO, respectively) and high (2.5 and 10μM for 8505C and FRO, respectively) doses of vemurafenib (left). Quantification of the total number of colonies and colonies of large size (> 2mm diameter) is shown on the right (*, $p<0.05$ by Mann-Whitney test, n=4). (E) Summary of cell cycle distribution between $G_0/G_1$ and proliferative phases of par and ICAM-1$^{Hi}$-enriched 8505C (left) and FRO (right) cells (*, $p<0.05$; **, $p<0.01$ by Mann-Whitney test) (n=6, 8 for 8505C and n=4 for FRO).

2.4A). Two ATC lines 8505C and FRO, displayed heterogeneous expression of ICAM-1 with ~60% of both populations staining positive for ICAM-1 (Figure 2.4A). Next, 8505C and FRO cells were stratified by sorting according to ICAM-1 expression to determine if ICAM-1 levels were associated with tumorigenic potential. 8505C and FRO cells that were >85% ICAM-1-positive (designated as ICAM-$1^{Hi}$) maintained their pattern of ICAM-1 expression across extended passaging to at least 10 passages (Figure 2.4B). 8505C-ICAM-$1^{Hi}$ and FRO-ICAM-$1^{Hi}$ cells were found to be more refractory to treatment with the BRAF inhibitor, vemurafenib, by 4.6 and 17.7-fold respectively, compared to their parental (par) counterparts (Figure 2.4C). Elevated vemurafenib resistance was also observed via colony formation assays, which demonstrated higher and larger colony-forming units in ICAM-$1^{Hi}$ populations (Figure 2.4D). Cell cycle analysis showed that both 8505C-ICAM-$1^{Hi}$ and FRO-ICAM-$1^{Hi}$ cells had a higher percentage of cells at the proliferating stage (S-$G_2$/M and S) relative to parental cells (Figure 2.4E & Figure 2.5). Taken together, ICAM-1-postive 8505C and FRO cells are distinguished by an increased resistance to vemurafenib and an elevated rate of proliferation, suggesting that ICAM-1 can serve as a biomarker for the aggressive nature of ATC cells.

**ICAM-1 targeting CAR T shows specific killing of malignant thyroid cells**

As the aggressive and vemurafenib-resistant features of ATC correlate with ICAM-1 overexpression, we developed an immunotherapeutic strategy specifically targeting ICAM-1 as a novel treatment for refractory ATC. To molecularly target ICAM-1, we inserted a scFv derived from the ICAM-1-specific R6.5 monoclonal antibody into a

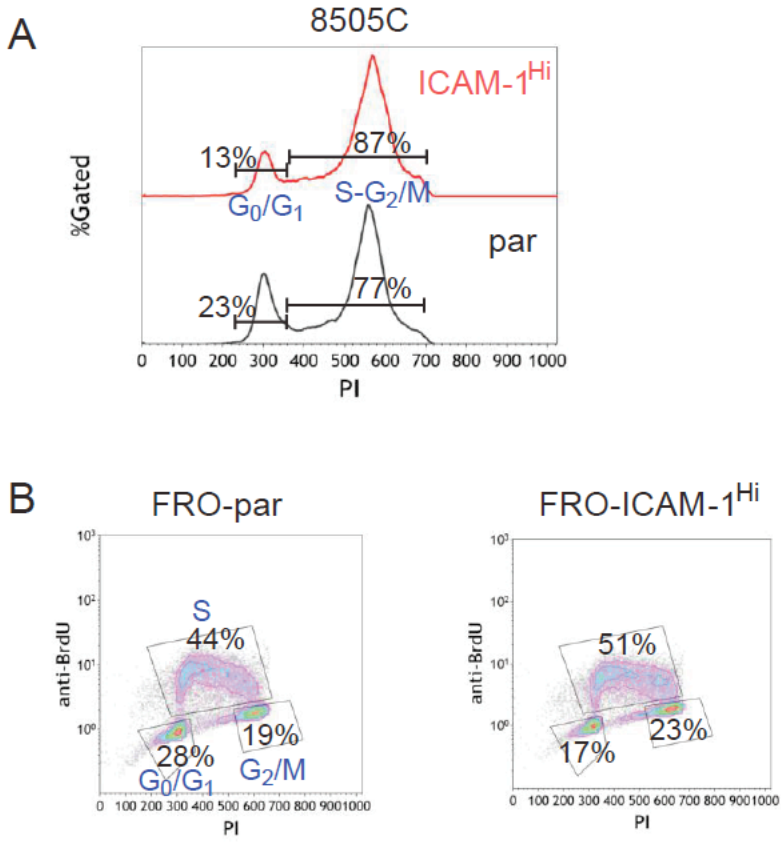


**Figure 2.5 ICAM-1-overexpressing ATC cell lines are more proliferative.**

(A) Representative flow cytometry histogram plots for cell cycle distribution as measured by propidium iodide (PI) staining of parental (par) 8505C and 8505C cells sorted for ICAM-1 expression (ICAM-$1^{Hi}$). (B) BrdU and PI staining shows an increased fraction of FRO-ICAM-$1^{Hi}$ cells at S and $G_2$/M phase relative to FRO-par cells.

third-generation CAR construct comprised of intracellular CD3ζ, CD28, and 4-1BB (CD137) signal transduction domains (Figure 2.6A) [12, 28]. An additional renilla luciferase (rLuc) reporter gene was also inserted downstream of the CAR via a P2A ribosomal skipping sequence for CAR T cell tracking *in vivo*. Lentiviral transduction of this ICAM-1 targeting CAR construct (hereafter referred to as ICAM-1 CAR) into $CD3^+$ T cells yielded between 20 and 60% CAR expression, which could be increased to approximately 100% after CAR-based sorting using an anti-mouse F(ab')2 antibody (Figure 2.6B). ICAM-1 CAR expression on primary T cells did not alter the CD4:CD8 ratio or T cell proliferation (Figure 2.7), suggesting a lack of self-directed cytotoxicity despite endogenous ICAM-1 expression on primary T cells.

We tested the ability of ICAM-1 CAR T cells to eliminate PTC, ATC, and control cells with and without ICAM-1 expression using varying ratios of T cells (effector) to target cells (E:T) (Figure 2.6C). For this assay, we first established target cell lines with stable expression of GFP and firefly luciferase (fLuc) via transduction with a fLuc-F2A-GFP lentivirus and flow cytometry-based sorting for $GFP^+$ cells. PTC BCPAP cells, which are mostly ICAM-$1^+$, were eliminated fastest by ICAM-1 CAR T cells relative to 8505C and FRO cells which have lower ICAM-1 expression (Figure 2.6C). HEK 293T cells, with diminutive ICAM-1 expression, were largely protected from ICAM-1 CAR T cells, displaying slow, gradual cell death from non-specific T cell activity. Compiled data from E:T assays at the 2.5:1 E:T ratio demonstrated that ICAM-1 CAR T lysed BCPAP, HeLa, and FRO cells with similar kinetics followed by 8505C cells at a reduced rate (Figure 2.6D). Mock-transduced T cells exhibited minimal effects on all tested cells except for BCPAP (Figure 2.6D). At

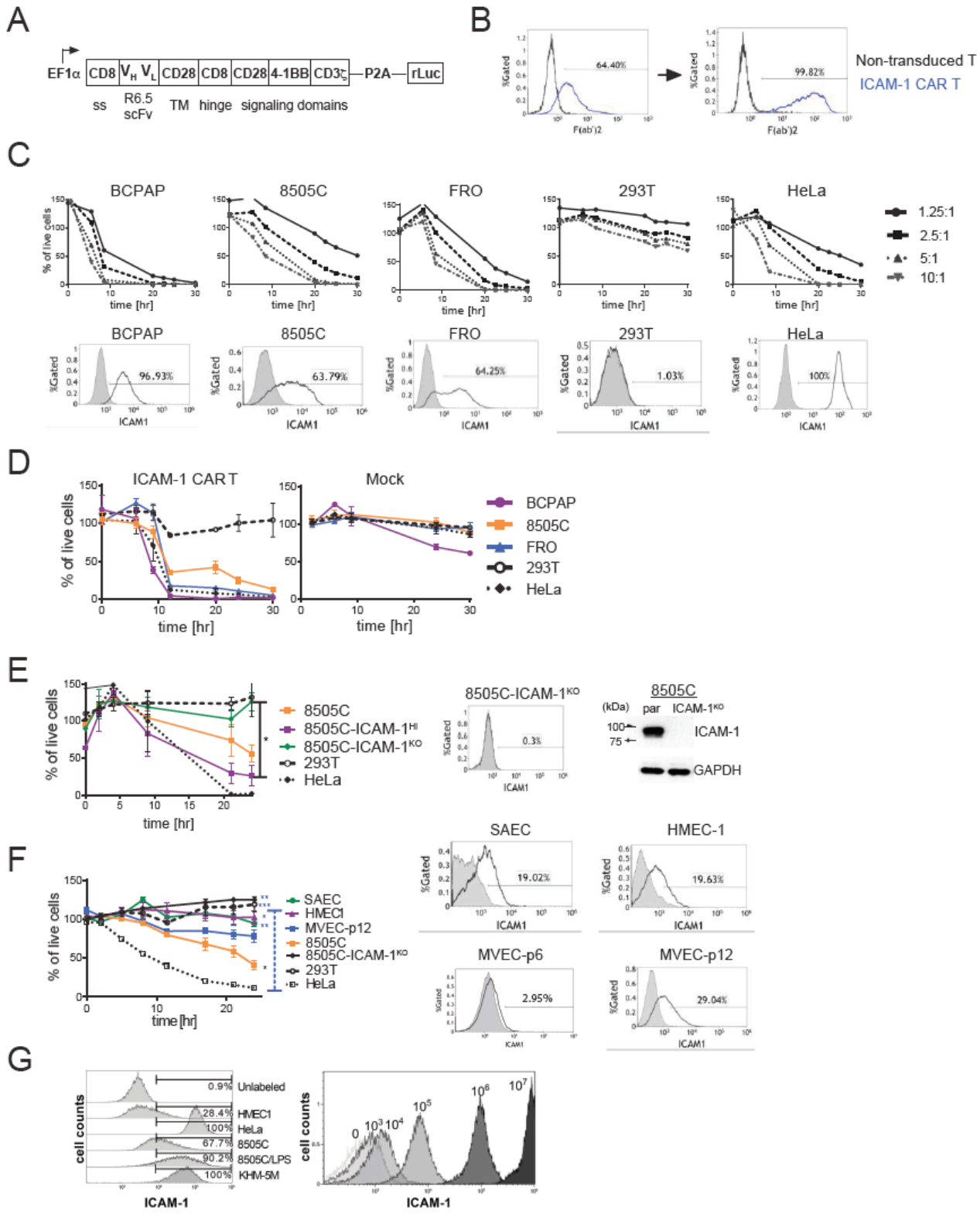
A
EF1α
CD8
$V_H$ $V_L$
CD28
CD8
CD28
4-1BB
CD3ζ
P2A
rLuc
ss
R6.5 scFv
TM
hinge
signaling domains
B
64.40%
99.82%
F(ab')2
Non-transduced T
ICAM-1 CAR T
C
BCPAP
8505C
FRO
293T
HeLa
% of live cells
time [hr]
1.25:1
2.5:1
5:1
10:1
%Gated
96.93%
63.79%
64.25%
1.03%
100%
ICAM1
D
ICAM-1 CAR T
Mock
BCPAP
8505C
FRO
293T
HeLa
E
8505C
8505C-ICAM-1HI
8505C-ICAM-1KO
293T
HeLa
0.3%
(kDa)
par
ICAM-1KO
100
75
ICAM-1
GAPDH
F
SAEC
HMECl
MVEC-p12
8505C
8505C-ICAM-1KO
293T
HeLa
19.02%
19.63%
2.95%
29.04%
G
0.9% Unlabeled
28.4% HMEC1
100% HeLa
67.7% 8505C
90.2% 8505C/LPS
100% KHM-5M
cell counts
ICAM-1
0
$10^3$
$10^4$
$10^5$
$10^6$
$10^7$

**Figure 2.6 ICAM-1-targeting CAR T activity is specific to the ICAM-1 expressing target cells.**

(A) Schematic demonstrating the ICAM-1 CAR T construct (B) Histogram plots demonstrate CAR expression in ICAM-1 CAR T cells was detected using a F(ab')2 antibody before (left) and after (right) sorting via F(ab')2. (C) (top) The percentages of live target cells remaining after exposure to ICAM-1 CAR T plotted over time. Values were normalized to target cells with no T cell addition. The E:T ratio was incremented by a factor of 2 from 1.25:1 to 10:1. (bottom) Flow cytometry plots indicating the level of ICAM-1 expression in target and control cells after staining with the R6.5 anti-ICAM-1 antibody. Gates for ICAM-$1^{+}$cells were determined based on staining with isotype control (grey filled histogram). (D) Compilation of the percentages of live target cells remaining after exposure to ICAM-1 CAR T and mock transduced T cells plotted over time (normalized against no T cell addition group, n=4-7 per target cell line). (E) ICAM-1 CAR T cytotoxicity against parental 8505C cells and 8505C cells with high (ICAM-$1^{Hi}$) or minimal (ICAM-$1^{KO}$) ICAM-1 expression. The plotted percentages of live cells were normalized against corresponding target cells incubated with non-transduced T cells to minimize the T cell alloreactivity. A statistical difference was observed between the number of live 8505C-ICAM-$1^{KO}$ and 8505C-ICAM-$1^{Hi}$ cells remaining at the 24 and 30 hr timepoint (*, $p<0.05$ by Dunn's multiple comparison test). 8505C-ICAM-$1^{KO}$ cells were generated using CRISPR/Cas9, and ICAM-1 expression levels were analyzed by flow cytometry and Western blot analysis (right). (F) ICAM-1 CAR T cytotoxicity against normal primary cells (SAEC, HMEC-1 and late passage (p12) MVEC) along with control target cells. Membrane-bound

ICAM-1 expression on normal primary cells was characterized by flow cytometry (right). For MVEC, passage 6 and 12 were compared for ICAM-1 expression. Dunn's multiple comparison tests at 24 hr were used to reveal statistical differences between the SAEC, HMEC-1, and 293T cells relative to HeLa cells when targeted by ICAM-1 CAR T. Statistical difference between 8505C and 293T cells were *, compared, $p<0.05$; **, $p<0.01$; ***, $p<0.001$ ($n=3$-6 per target cells). (G) Histograms of latex beads coated with a fixed number of R6.5 anti-ICAM-1 antibodies were analyzed by flow cytometry on the right. Histograms plots for various target cells with R6.5 antibody on the left were used to estimate the number of ICAM-1 molecules.

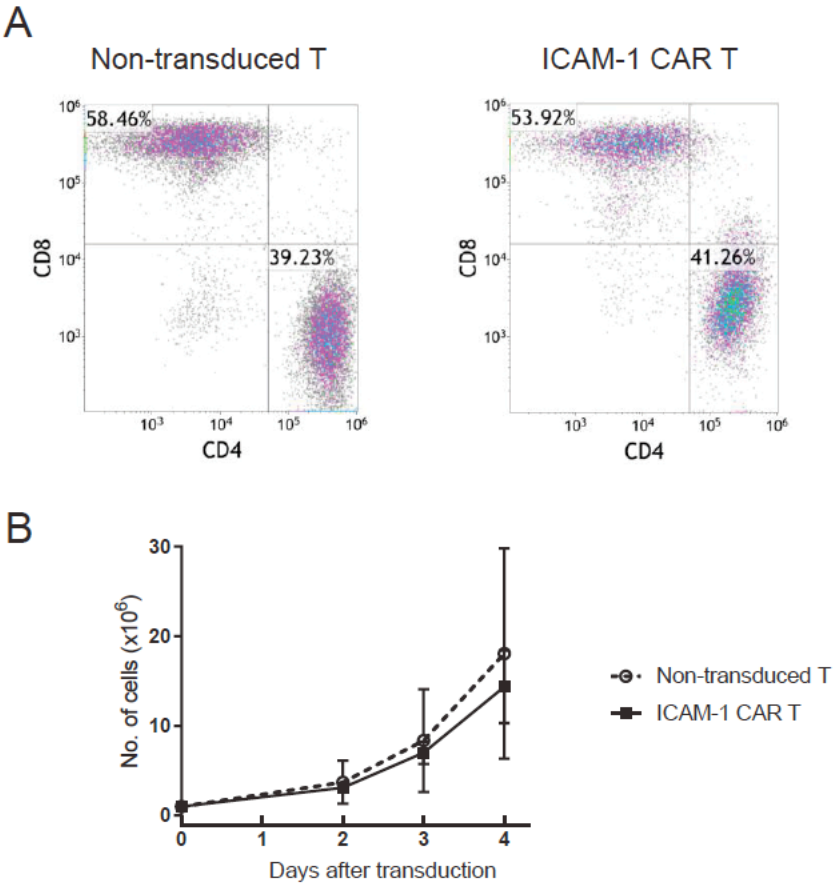


**Figure 2.7 ICAM-1 CAR T cell phenotype characterization.**

(A) Representative flow cytometry plots showing the composition of $CD4^+$ vs. $CD8^+$ T cells prior to and after ICAM-1 CAR expression in primary T cells. (B) The proliferative capacity of T cells after ICAM-1 CAR lentiviral transduction were not statistically different from non-transduced T cells (n=4-5).

the 20-hr time point, approximately 40% of 8505C cells remained viable after exposure to ICAM-1 CAR T cells, a percentage that equates with the level of ICAM-1 expression on 8505C cells (Figures 3C & 2.4A). The extent of ICAM-1 CAR T targeting of 8505C cells was dependent upon the level of ICAM-1 expression, as evidenced by the faster killing of 8505C-ICAM-$1^{Hi}$ cells compared to their lower ICAM-1-expressing parental counterparts (Figure 2.6E). Genetic disruption of ICAM-1 via CRISPR/Cas9 in 8505C cells (referred to as 8505C-ICAM-$1^{KO}$), abolished ICAM-1 CAR T mediated killing of 8505C cells thus demonstrating the targeting specificity of this treatment strategy *in vitro* (Figure 2.6E). Abolished ICAM-1 expression in 8505C-ICAM-$1^{KO}$ cells was confirmed by flow cytometry and western blot analysis (Figure 2.6E, right).

To address the potential for 'on-target, off-tumor' killing by ICAM-1 CAR T cells, we investigated whether ICAM-1 CAR T could target healthy human cells with normal ICAM-1 expression [37]. We chose glomerular microvascular endothelial cells (MVEC) and small airway epithelial cells (SAEC) that have the highest ICAM-1 expression among normal tissues according to the Human Protein Atlas database [37]. In contrast, these tissues have also been reported to stain poorly for ICAM-1 by immunohistochemistry (IHC) [17, 38]. By immunostaining with mAb R6.5, we found that SAEC, early passage (passage 6) MVEC, and late passage (passage 12) MVEC, were approximately 19%, 3%, and 29% ICAM-1 positive, respectively (Figure 2.6F right). As an additional comparison, we also added HMEC-1, immortalized dermal microvascular endothelial cells, which were 20% ICAM-1 positive. The levels of ICAM-1 expression in primary healthy cells were 2~10-fold lower than the 8505C and

FRO ATC lines (Figure 2.6C & 3F). The level of ICAM-1 CAR T cell-mediated killing of the lung, kidney tissue cells, and HMEC-1 was significantly lower than that observed for 8505C and HeLa cells. Indeed, the cytotoxicity directed against healthy tissue was not significantly different from that of the ICAM-1 negative cells, 293T and 8505C-ICAM-$1^{KO}$ (Figure 2.6F left). Therefore, the magnitude of ICAM-1 CAR T cytotoxicity was reflective of the frequency and the extent of ICAM-1 expression in target cells with non-malignant, ICAM-1 low cells exhibiting limited susceptibility.

In order to define the threshold level of ICAM-1 expression that is required for effectual cytotoxicity of ICAM-1 CAR T cells, we estimated the number of ICAM-1 molecules expressed on target cell surfaces by comparing R6.5 antibody binding to cells with 8 μm latex beads coated with known amounts of R6.5 antibodies (Figure 2.6G). From this comparison, we estimated that the primary healthy tissue cells and ATC lines display approximately $10^4$ and $10^5$ ICAM-1 molecules on their cell surfaces, respectively, suggesting a requirement for expression of $10^5$ ICAM-1 surface molecules per cell to enable efficient engagement and killing by ICAM-1 CAR T cells. Therefore, due to ICAM-1 CAR T's ability to discriminate between target thyroid cancer cells and primary tissue cells, ICAM-1 CAR T should exhibit a sufficiently high therapeutic index for clinical use.

**Surface ICAM-1 expression in thyroid cancer cells is modulated by IFN-γ, which affects the efficiency of ICAM-1 CAR T cytotoxicity**

8505C cells exhibited slower ICAM-1 CAR T-induced death compared to BCPAP and HeLa cells with approximately 40% of targets remaining alive at the 20-24 hr time

points when co-cultured at a 2.5:1 E:T ratio (Figures 3D & 4A). Interestingly, the viable 8505C cells that remained after incubation with ICAM-1 CAR T cells at 18 hr displayed an elevated level of ICAM-1 expression (7.5-fold increase in MFI) relative to non-exposed cells (Figure 2.8B). A similar elevation of ICAM-1 expression was measured in 8505C, BCPAP, and FRO cells after incubation in pre-conditioned media collected from 18 hr co-culture of 8505C cells with ICAM-1 CAR T cells suggesting that soluble factors released into the media by cytotoxic CAR T cells are responsible for ICAM-1 induction (Figure 2.8C). A hallmark of cytotoxic T cell activity is secretion of the $T_H1$ cytokine IFN-γ [12]. We therefore measured the concentration of secreted IFN-γ during ICAM-1 CAR T co-culture with target cells during the E:T assays. Release of IFN-γ by CAR T cells was highest when co-cultured with 8505C-ICAM-$1^{Hi}$ and HeLa cells, and remained at background levels with 8505C-ICAM-$1^{KO}$ and 293T cells (Figure 2.8D). Furthermore, addition of exogenous IFN-γ into thyroid cancer cell monocultures induced ICAM-1 expression in a dose-dependent fashion, thus identifying IFN-γ as a critical soluble factor responsible for ICAM-1 induction in target cells (Figure 2.8E).

Addition of IFN-γ at a concentration of $1x10^4$ pg/ml was sufficient to induce an approximate 10-fold increase in ICAM-1 expression (~$10^6$ molecules per cell) in all tested thyroid cancer cells (Figures 4E & 3G). The levels of IFN-γ secreted by ICAM-1 CAR T cells upon exposure to target antigen were also within a range capable of elevating ICAM-1 to those observed by exogenous IFN-γ addition. In contrast, ICAM-1 expression in 293T cells was absent either by addition of supernatant from HeLa

cells targeted by ICAM-1 CAR T (Figure 2.8C) or by administration of exogenous IFN-γ (Figure 2.8E). Addition of supraphysiological concentration of IFN-γ to early passage MVEC cells induced approximately 2-3-fold increase in MFI (Figure 2.8E). These data suggest that thyroid cancer cells are hyperresponsive to IFN-γ induced ICAM-1 elevation compared to nonmalignant, healthy cells. In addition, E:T assays with IFN-γ-stimulated target cells verified that ICAM-1 CAR T cells had an increased potency to target IFN-γ-stimulated 8505C cells (Figure 2.8F). By contrast, MVEC displayed no difference in cytolysis by non-transduced T or ICAM-1 CAR T cells after administration of IFN-γ except for increased cell death relative to cells without IFN-γ treatment. IFN-γ induction of ICAM-1 expression, therefore, may increase the therapeutic potency of ICAM-1 CAR T cells against thyroid cancer cells but minimally affect on non-malignant, normal tissues.

The direct cytotoxic effects mediated by CAR T cells derive from their release of soluble factors such as perforin and granzymes, in addition to tumor necrosis factor (TNF) death receptor signaling triggered by direct cell-to-cell contacts. The level of granzyme B secretion was found to mirror the rate of ICAM-1-dependent target cell killing, which was highest in 8505C-ICAM-$1^{Hi}$ followed by parental 8505C, and negligible in the 8505C-ICAM-$1^{KO}$ cells (Figure 2.8G). The dependence upon perforin/granzyme B-mediated target killing was also validated by the substantial inhibition of CAR-mediated cytotoxicity by addition of EGTA to E:T co-cultures (Figure 2.8H). In contrast, activation of the TNF death receptor pathway by exogenous addition of its ligand, TRAIL, had little effect on 8505C cell death, while gradual killing of FRO cells was observed with increasing concentrations of TRAIL (Figures

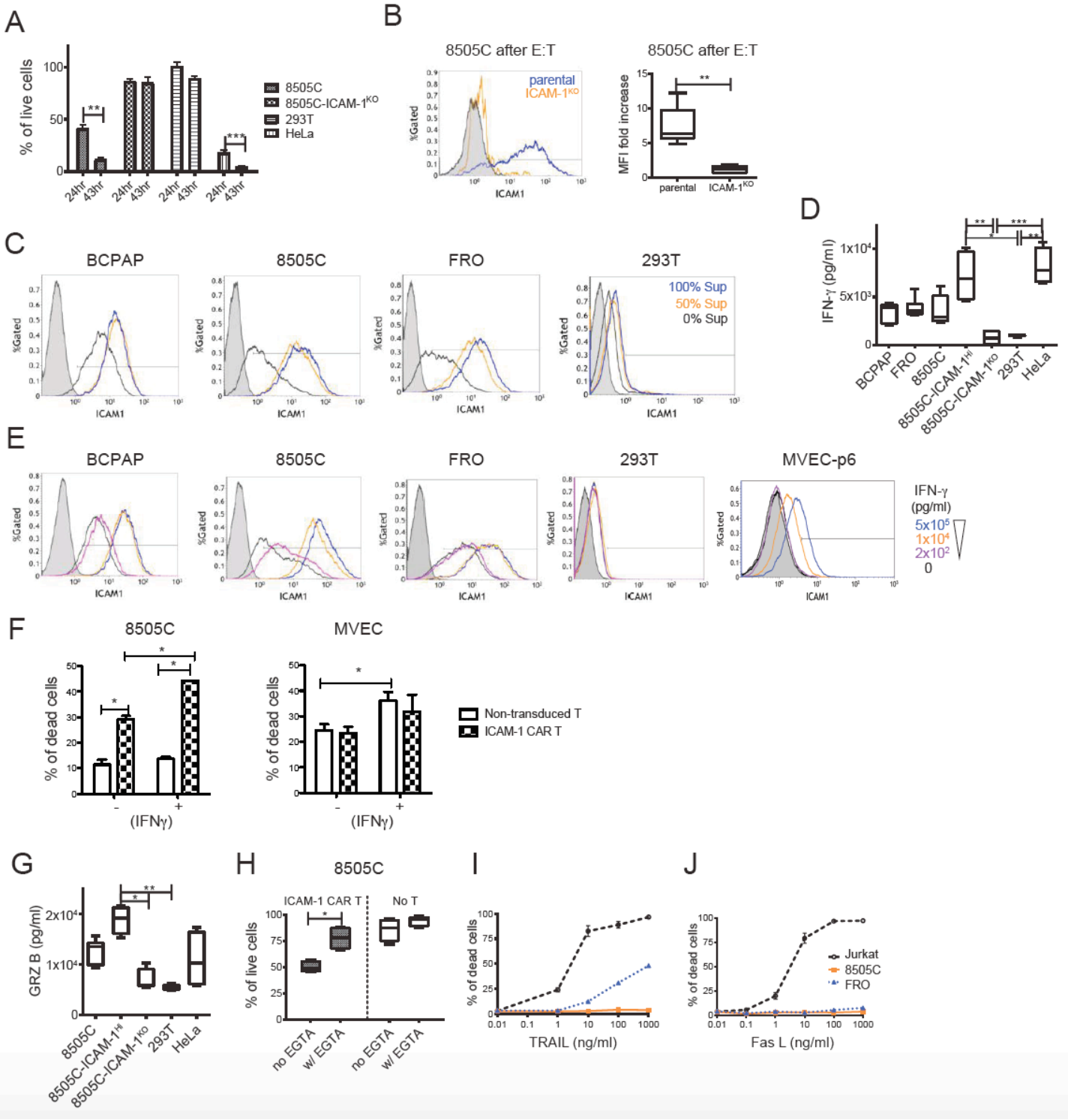
A
% of live cells
8505C
8505C-ICAM-1KO
293T
HeLa
24hr
43hr
B
8505C after E:T
parental
ICAM-1KO
%Gated
ICAM1
MFI fold increase
C
BCPAP
8505C
FRO
293T
100% Sup
50% Sup
0% Sup
D
IFN-γ (pg/ml)
BCPAP
FRO
8505C
8505C-ICAM-1HI
8505C-ICAM-1KO
293T
HeLa
E
MVEC-p6
IFN-γ (pg/ml)
5x10^5
1x10^4
2x10^2
0
F
8505C
MVEC
% of dead cells
Non-transduced T
ICAM-1 CAR T
(IFNγ)
G
GRZ B (pg/ml)
H
ICAM-1 CAR T
No T
% of live cells
no EGTA
w/ EGTA
I
TRAIL (ng/ml)
J
Jurkat
8505C
FRO
Fas L (ng/ml)

**Figure 2.8 ICAM-1 expression on thyroid cancer cells is IFN-γ inducible by enhancing target susceptibility to ICAM-1 CAR T.**

(A) The percentages of remaining viable target cells remaining after co-culturing with ICAM-1 CAR T cells were compared between 24 hr and 43 hr timepoints (n=6-9 per target cells). (B) After a 18 hr co-incubation with ICAM-1 CAR T cells, 8505C (blue line) and 8505C-ICAM-$1^{KO}$ (orange line) cells were collected and stained for ICAM-1 expression in live cells by flow cytometry (left). 8505C cells stained with isotype control are shown by gray filled histogram. Quantitation of the fold increase of ICAM-1 mean fluorescence intensity (MFI) is shown on the right relative to non-exposed cells (n=6 per target cells). (C) Representative flow cytometry plots show thyroid cancer cell ICAM-1 expression after 18 hr culture with in media spiked with supernatant derived from E:T experiments using ICAM-1 CAR T. Supernatants from the ICAM-1 CAR T: target cell assay were collected and added to the indicated target cells with no dilution (blue line), 50% dilution (orange line), or no addition (black line) to the culture media. (D) The IFN-γ levels in supernatants collected from E:T assays involving ICAM-1 CAR T against indicated target cells were measured using ELISA (n=4-8). Non-transduced T cells cultured with the same target cells produced levels of IFN-γ that were below the limit of detection. (E) Flow cytometry analysis demonstrating ICAM-1 expression changes in thyroid cancer and control cells upon direct administration of exogenous, serially diluted IFN-γ (pg/ml). (F) The percentages of cell death observed in untreated and IFN-γ ($1 \times 10^4$ pg/ml) added target cells were compared after addition of non-transduced T and ICAM-1 CAR T cells using flow cytometry analysis (n=3). (G) The concentration of secreted

granzyme B from an ICAM-1 CAR T: target cell assay (n=4-6) per condition. (H) 4 mM EGTA was added to E:T assay media to inhibit the perforin/granzyme cytotoxic pathway (n=4 per group). (I) Anaplastic thyroid cancer resistance to TRAIL-induced death (J) Anaplastic thyroid cancer resistance to FasL-induced death. The Jurkat T cell line served as a positive control for both treatments (n=3-4 per condition).

2.8I & 2.8J). We therefore confirmed that the degree of ICAM-1 CAR T cytotoxicity is commensurate with the levels of surface ICAM-1 expression in target cells. Furthermore, we identified IFN-γ as a crucial cytokine that can augment CAR T cytotoxicity that preferentially acts upon thyroid cancer cells.

**CAR T cells targeting ICAM-1 achieve rapid and enduring tumor eradication *in vivo***

In order to evaluate the anti-tumor efficacy of ICAM-1 CAR T *in vivo*, we utilized systemic xenografts of human ATC 8505C cells in immunodeficient NOD-***scid***IL2Rg$^{null}$ (NSG) mice [30]. To track and quantitate the growth of ATC in mice, we used parental 8505C cells transduced and FACS sorted to express GFP and firefly luciferase Lucwith approximately 100% purity. A total of 0.75 million 8505C cells were injected intravenously (i.v.) into each NSG mouse, with primary tumors localizing prominently in the lungs (Figure 2.9A). With unimpeded growth, tumors gradually metastasize to other organs including the bones and liver, resulting in death within one month (median survival is 28 days). Treatment occurred on day 14 post xenograft with mice receiving an i.v. infusion of either 3 x $10^6$ T cells transduced with an ICAM-1 CAR lentivirus (unsorted with 30-40% transduction levels) or an equal infusion of 3 x $10^6$ non-transduced T cells. A third group received no treatment. The specific cytotoxicity of administered ICAM-1 CAR T cells were validated *in vitro* and their CD4:CD8 ratios were additionally confirmed to be comparable with non-transduced T cells (Figure 2.10). At day 5 post-treatment with ICAM-1 CAR T, mice showed signs of tumor signal decrease and recovery of body weight, culminating in

complete tumor eradication and weight rebound within 12 days of treatment (Figures 5A-5C). The observed remission was durable such that ICAM-1 CAR treated mice exhibited a significant and substantial increase in survival (Figure 2.9D). Non-transduced T cells demonstrated minimal tumor-killing in mice, except for the occasional instances of donor T cell alloreactivity. *Ex vivo* fluorescence images of harvested organs taken 1 month after ICAM-1 CAR T treatment demonstrated that tumor lesions were strikingly diminished in the lungs and livers in contrast to the untreated group (Figure 2.9E). The reduction of tumor burden by ICAM-1 CAR T cells in the lungs was also evidenced by their lower (normal) weight compared to the 2.2-fold higher weight of the same organs from the untreated group (Figure 2.11).

The macroscopic descriptions of tumor eradication by ICAM-1 CAR T cells were validated at the cellular level by flow cytometry and IHC analyses. ICAM-1 CAR T treatment led to negligible levels of $GFP^+$ tumor cells in whole lungs and liver of ATC xenografted mice, in striking contrast to untreated groups in which approximately 18% and 4% of live cells were identified as $GFP^+$ in the lungs and liver, respectively (Figure 2.9F). IHC analysis revealed that ≤1% of the lung and liver tissues retained $GFP^+$ tumor cells at 70-80 days after a single administration of ICAM-1 CAR T cells (Figure 2.9G). Meanwhile, human $CD3^+$ T cells were still detectable in various organs at day 72 (Figure 2.9F & Figure 2.12A), which agreed with the assessment of CAR T cell persistence evidenced by whole body imaging (Figure 2.12B). These findings demonstrate the ability of ICAM-1 CAR T cells to mediate potent and enduring anti-tumor activities, leading to tumor eradication and significant improvements in long-term survival in ATC xenograft mouse models.

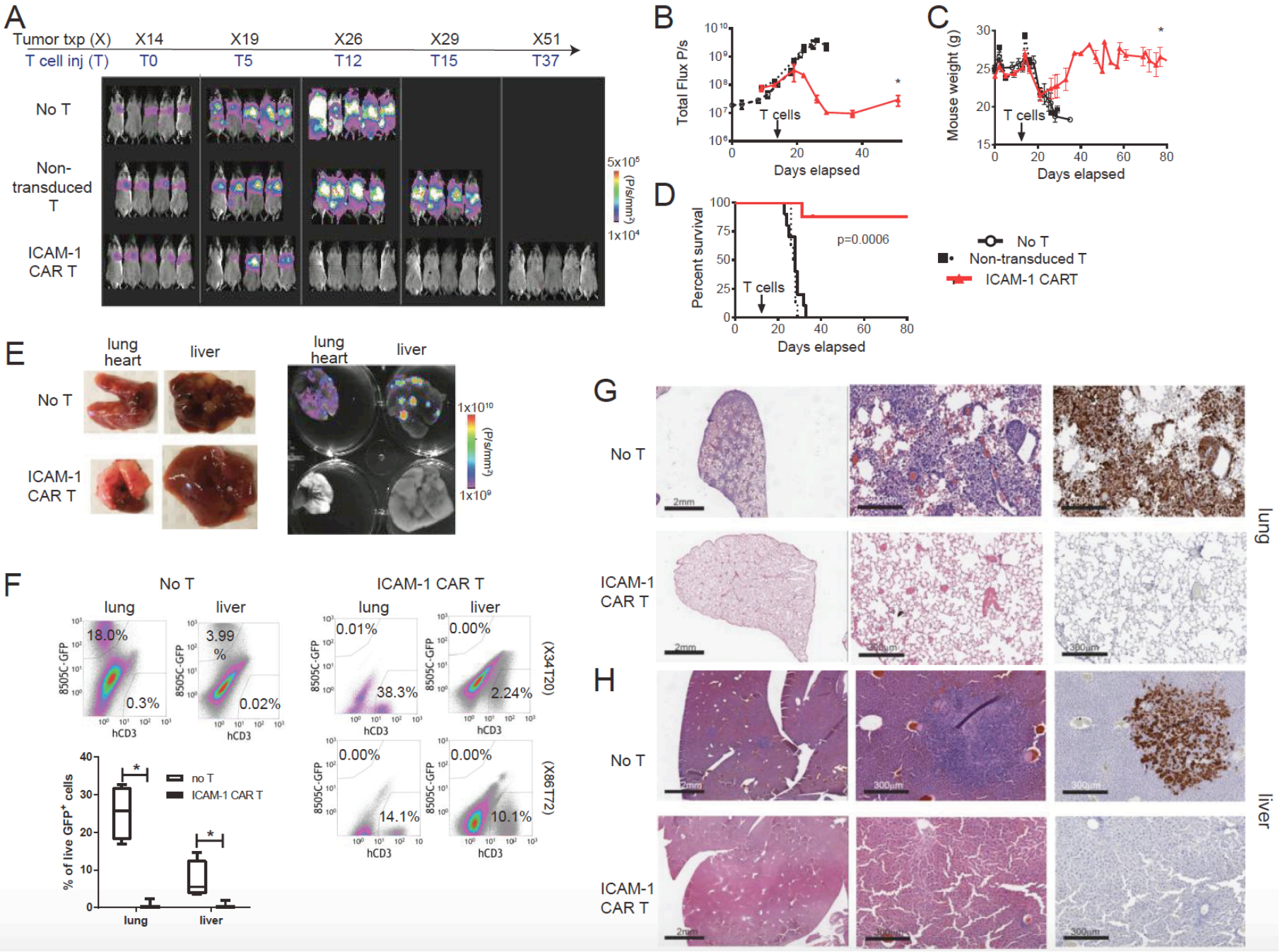
A
Tumor txp (X)
X14
X19
X26
X29
X51
T cell inj (T)
T0
T5
T12
T15
T37
No T
Non-transduced T
ICAM-1 CAR T
5x10^5
(P/s/mm²)
1x10^4
B
Total Flux P/s
T cells
Days elapsed
C
Mouse weight (g)
T cells
Days elapsed
D
Percent survival
p=0.0006
T cells
Days elapsed
No T
Non-transduced T
ICAM-1 CART
E
lung
heart
liver
No T
ICAM-1 CAR T
1x10^10
(P/s/mm²)
1x10^9
F
No T
ICAM-1 CAR T
lung
liver
8505C-GFP
hCD3
18.0%
0.3%
3.99 %
0.02%
0.01%
38.3%
0.00%
2.24%
(X34T20)
0.00%
14.1%
0.00%
10.1%
(X86T72)
% of live GFP+ cells
no T
ICAM-1 CAR T
G
No T
ICAM-1 CAR T
lung
H
No T
ICAM-1 CAR T
liver

**Figure 2.9 ICAM-1 CAR T cells show robust and enduring tumor eradication in ATC xenograft models.** (A) Representative total body bioluminescence images of $fLuc^+$ 8505C xenografted NSG mice following ICAM-1 CAR T cell administration. Control groups include untreated and non-transduced T cell-administered mice. (B) Quantitation of total body bioluminescence units in individual mice from (A) (no T cell group=open circle, non-transduced T cells=solid square, ICAM-1 CAR T=red triangle; p=0.05, n=8-10 per group). (C) Summary of body weight changes in mice left untreated or after treatment with non-transduced T cells or ICAM-1 CAR T cells. (D) Survival curves of 8505C xenografted mice comparing no treatment, treatment with non-transduced T cells, and treatment with ICAM-1 CAR T cells until 80 days post-xenograft. Statistical differences between different treatments were analyzed by Kaplan-Meier (n=8-10 per group). (E) (left) Gross inspection of 8505C xenograft primary (lung) and metastatic (liver) organs taken 20 days after ICAM-1 CAR T treatment compared with untreated mouse organs. (right) Ex vivo GFP fluorescence images of the organs merged with bright field images. Scale bar is shown on the right (Units are $P/s/mm^2$). (F) (left) Flow cytometry plots showing analysis of percentages of $GFP^+$ 8505C (y-axis) and human $CD3^+$ T cells in indicated organs extracted from untreated and ICAM-1 CAR T treated 8505C xenografted mice (20 and 72 days after T cell administration). (bottom) Compilation of the frequency of live, $GFP^+$ 8505C cells observed in the lung and liver with and without ICAM-1 CAR T treatment. (G, H) Representative IHC images showing H & E staining of low (left) and high (middle) magnifications of lung (G) and liver (H) tissues isolated from xenografted mice receiving no T cell (top) or ICAM-1 CAR T (bottom) treatment. The adjacent sections

were stained for GFP to identify tumor cells (right). Scale bar = 2 mm (left), 300 μm (middle, right)

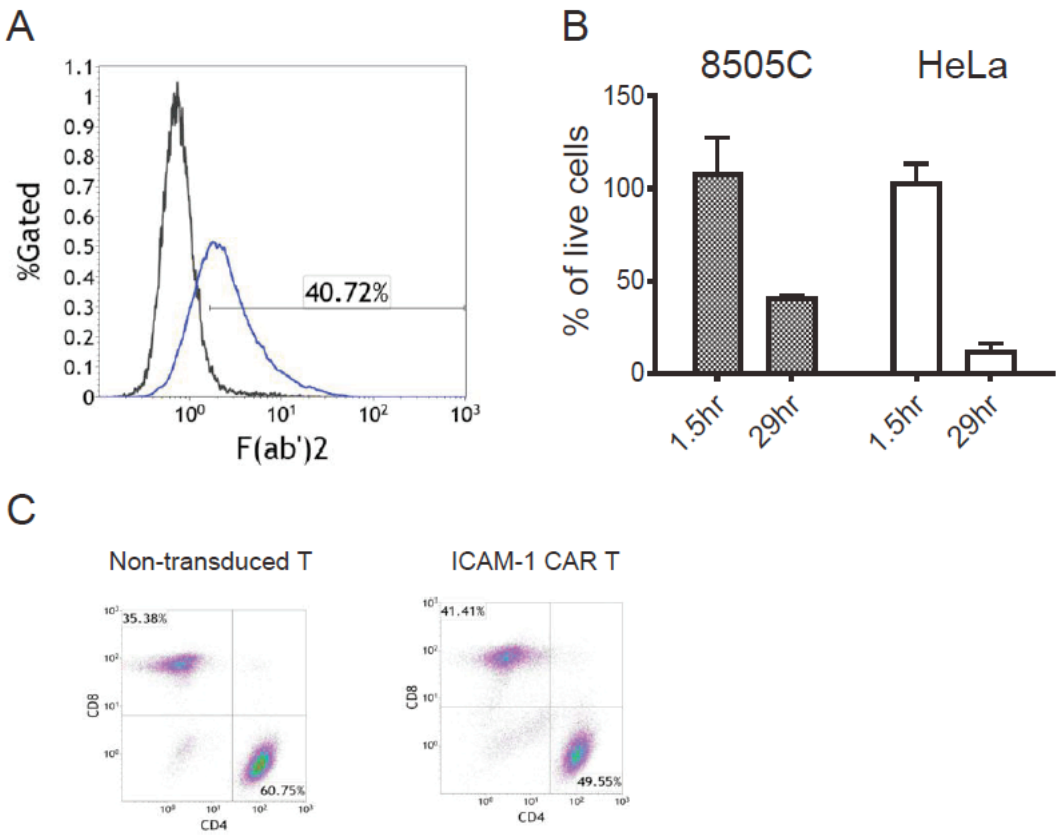


**Figure 2.10 Validation of ICAM-1 CAR T cells used *in vivo* experiments.**

(A) Transduction rate of ICAM-1 CAR construct in PBMC-derived T cells. (B) E:T assay of ICAM-1 CAR T cells against target cells. (C) Immunophenotype of non-transduced and ICAM-1 CAR T cells. The ratio of CD4:CD8 T cells were similar prior to and after ICAM-1 CAR expression in primary T cells.

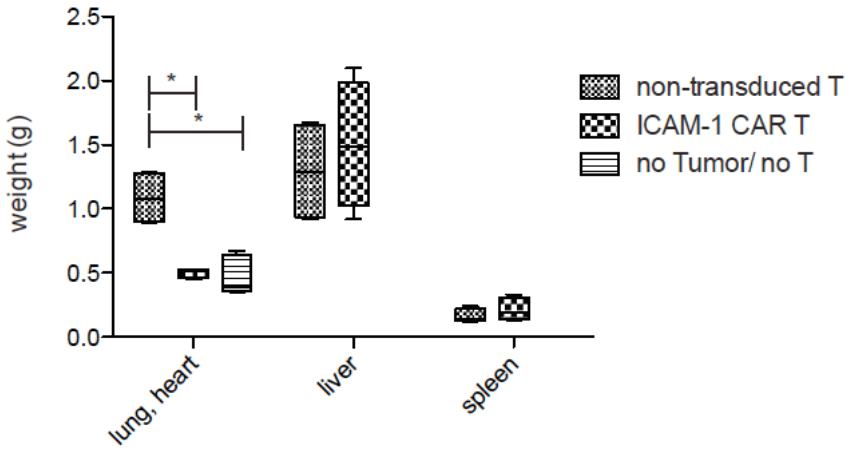


**Figure 2.11 Organ weight changes in ATC xenografted mice after ICAM-1 CAR T treatment.**

The weights (g) of lung and heart were significantly reduced in 8505C xenografts treated with ICAM-1 CAR T when compared with non-transduced T cell treatment group and were similar to the weights of healthy organs from NSG mice (no Tumor/No T group) (n=4-6 per group).

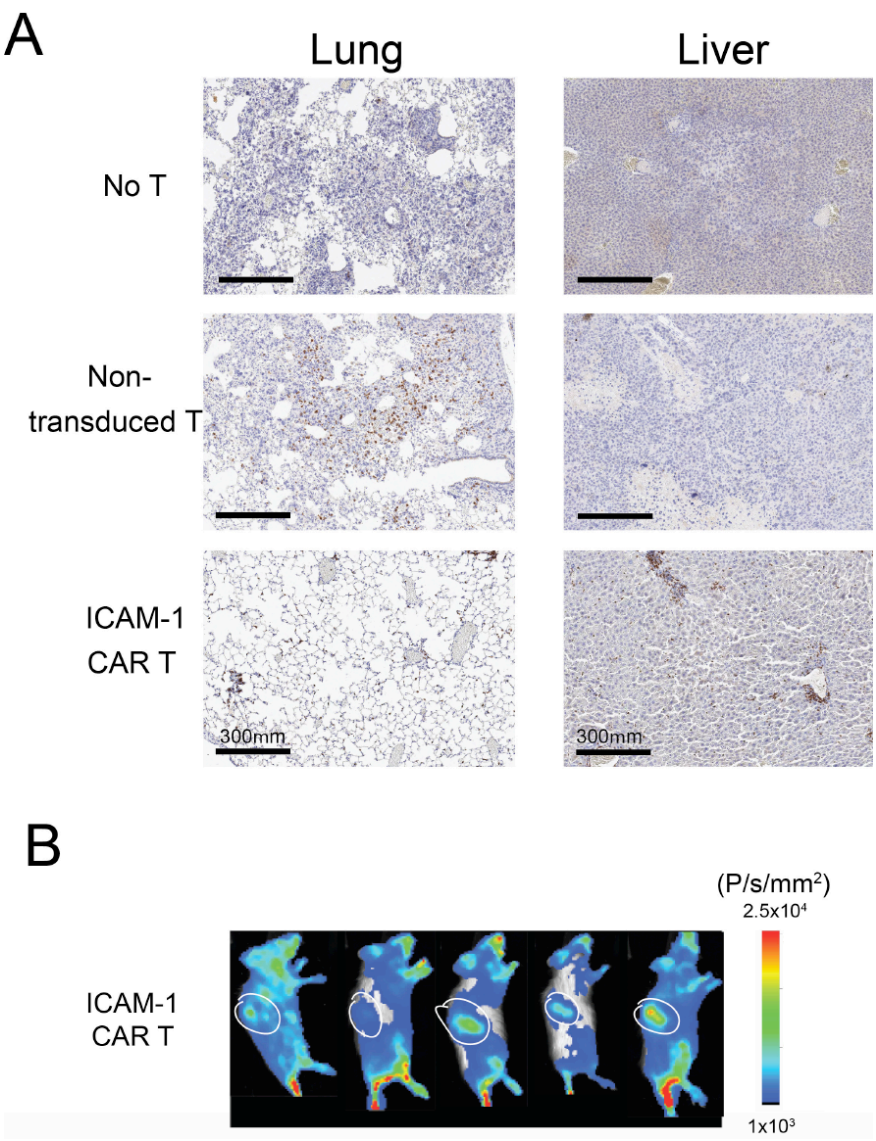


**Figure 2.12 CAR T cells in ICAM-1 CAR T treated and ATC xenografts.**

(A) Representative IHC images of $CD3^+$ T cells in 8505C xenograft tissues treated with ICAM-1 CAR T cells compared to untreated or non-transduced T cell treatment. (B) Bioluminescence of RLuc activity is detectable in spleens and other organs of ICAM-1 CAR T-treated mice at X86T72. No detectable RLuc activity is measured in NSG xenografts without treatment or treatment with non-transduced T cells. Spleen is demarcated with a white line.

**Autologous ICAM-1 CAR T eliminates thyroid cancer patients' tumor cells *in vitro* and *in vivo***

Acknowledging the modeling deficiencies of using donor-derived T cells to treat allogeneic, cell line-derived tumor cells, we wanted to test the therapeutic efficacy of ICAM-1 CAR T cells in a more realistic setting using patient-derived tumors and autologous T cells. We therefore initiated primary cultures of fresh tumor specimens derived from PDPTC and ATC thyroid cancer patients. Surgically removed tumor blocks were IHC stained for ICAM-1, which exhibited ICAM-1 expression at the $3^+$ level of intensity (Figure 2.13A & 6B). After 2-5 days of primary culture, the majority of PDPTC and ATC cells were dual positive by flow cytometry for surface expression of ICAM-1 and epithelial cell adhesion molecule (EPCAM), a marker for follicular epithelial cells (Figure 2.13A & B). While PDPTC tissues indicated sparse (~10%) ICAM-1 expression by IHC, expression after sub-culturing was over 90%. Several factors may account for such a discrepancy in ICAM-1 expression including unintended induction of ICAM-1 due to culturing conditions and selective growth of ICAM-$1^+$ cells in culture.

Next, we tested cytotoxic activity of autologous ICAM-1 CAR T cells against patient-derived tumor cells. ICAM-1 CAR T cells obtained from a PDPTC patient eliminated autologous thyroid tumor cells with similar kinetics to HeLa cells with no reactivity toward 293T cells (Figure 2.13A). Similarly, ICAM-1 CAR T cells derived from an ATC patient lysed autologous primary tumor cells, HeLa, and 8505C cells at comparable rates, achieving near 100% killing by 48 h. The rate of killing was somewhat slower in the autologous setting compared to the previously observed

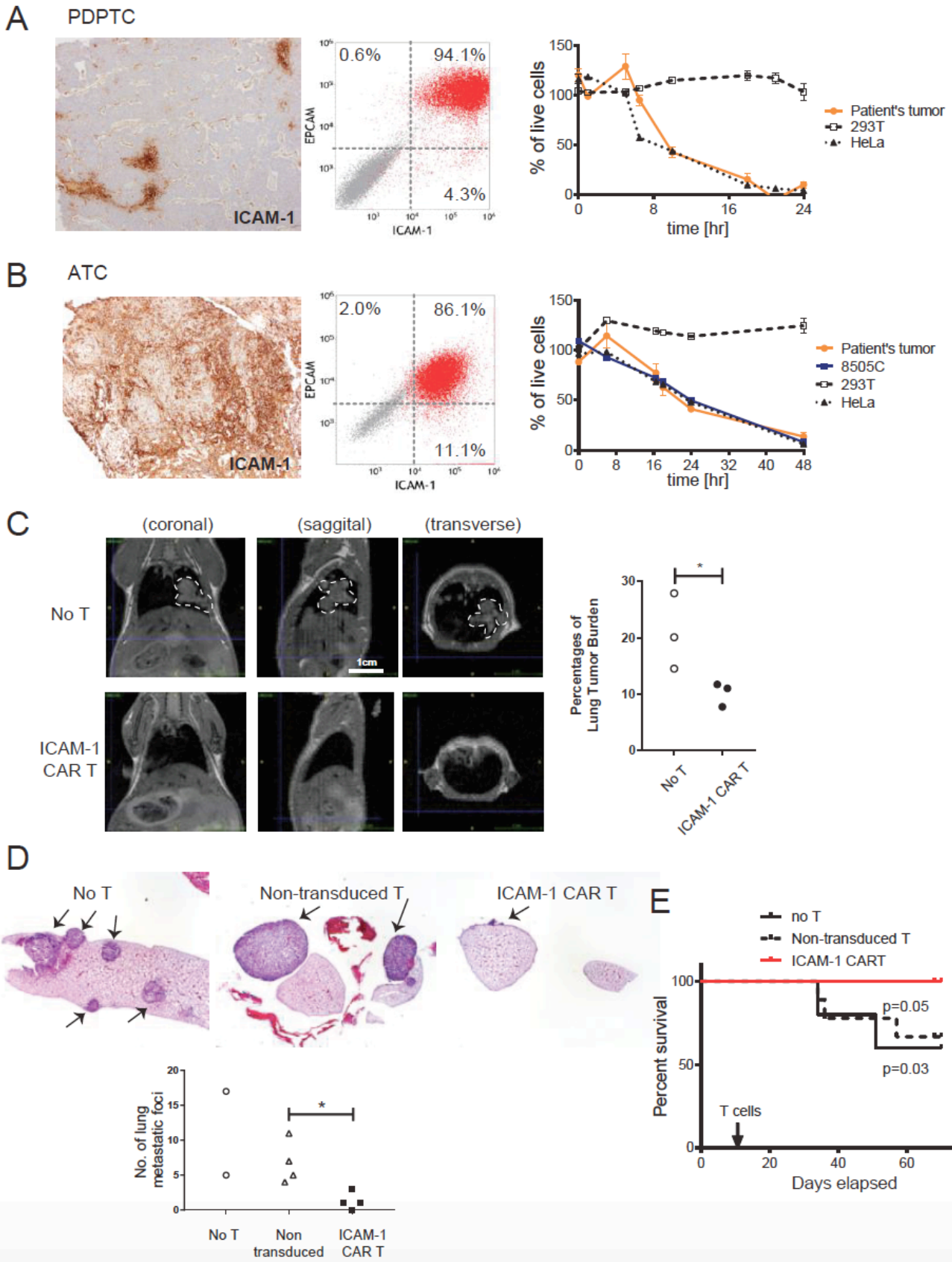
A
PDPTC
ICAM-1
0.6%
94.1%
4.3%
EPCAM
ICAM-1
% of live cells
time [hr]
Patient's tumor
293T
HeLa
B
ATC
ICAM-1
2.0%
86.1%
11.1%
EPCAM
ICAM-1
% of live cells
time [hr]
Patient's tumor
8505C
293T
HeLa
C
(coronal)
(saggital)
(transverse)
No T
ICAM-1 CAR T
1cm
Percentages of Lung Tumor Burden
No T
ICAM-1 CAR T
D
No T
Non-transduced T
ICAM-1 CAR T
No. of lung metastatic foci
No T
Non transduced
ICAM-1 CAR T
E
no T
Non-transduced T
ICAM-1 CART
p=0.05
p=0.03
T cells
Percent survival
Days elapsed

**Figure 2.13 Autologous ICAM-1 CAR T cells are effective in reducing tumor burden in thyroid cancer patient-derived tumor cells *in vitro* and *in vivo*.**

**(A-B)** Tumors from PDPTC (A) and ATC (B) patients are analyzed by ICAM-1-specific IHC (10x magnification) (left) and flow cytometry for EPCAM and ICAM-1 expression (middle). E:T assays using autologous ICAM-1 CAR T cells against primary tumors along with control 293T and HeLa cells are shown on the right. **(C)** Single cell-resuspensions were isolated from subcutaneous xenografts of ATC patient's primary cells (Supplemental Figure 8) were i.v. injected into NSG mice for secondary transplantation. After 11 days, autologous ICAM-1 CAR T and non-transduced T cells were infused i.v. to assess therapeutic efficacy *in vivo*. T1 MRI analysis was carried out in no T cell and ICAM-1 CAR T groups at 67-72 days post-xenograft to estimate tumor burden in the lung. Tumor outline is demarcated with white dotted lines. Quantification of the percentages of lung tumor burden were summarized and compared between no treatment and ICAM-1 CAR T-treatment groups (*, $p<0.05$; n=3 per group) **D.** H&E staining of lung lobes in untreated, non-transduced T, and ICAM-1 CAR T administered animals. Numbers of lung tumor nodules were quantified and analyzed to assess significant differences between non-transduced T and ICAM-1 CAR T-treated animals. (*, $p<0.05$; n=3 for no T and n=4 for T cell groups, one untreated mouse showed diffuse lung metastasis and therefore not quantified) **E.** Survival curves of ATC patient-derived tumor xenografted mice comparing no treatment, treatment with non-transduced T cells, and treatment with ICAM-1 CAR T cells up to 80 days post-xenograft. Kaplan-Meier analysis was

performed to assess statistical difference between different treatment groups (n = 5, 7, 10 for no T, non-transduced T, and ICAM-1 CAR T, respectively).

A

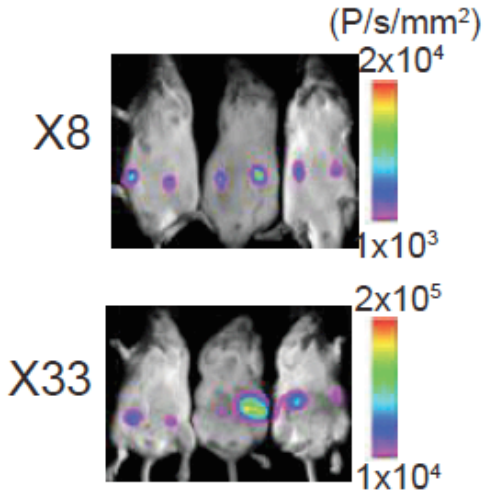
(P/s/mm²)
2x10⁴
X8
1x10³
2x10⁵
X33
1x10⁴

B

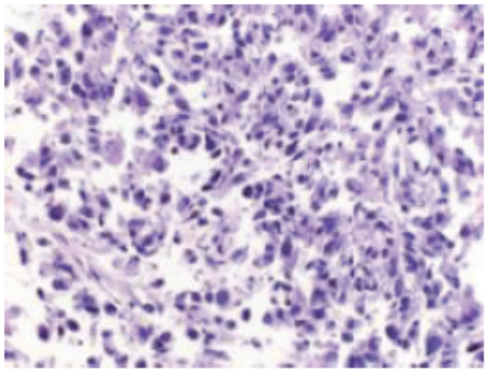
(H&E)

C

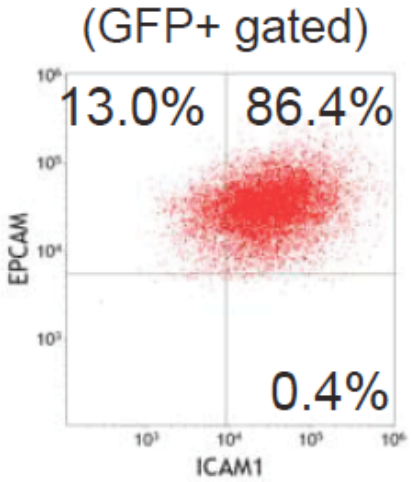
(GFP+ gated)
13.0%
86.4%
0.4%
EPCAM
ICAM1

**Figure 2.14 Establishment of ATC patient-derived xenografts.**

(A) Patient-derived ATC tumors were transduced with GFP and fLuc expressing lentivirus, and subcutaneous bilateral tumor growths in NSG mice were tracked via bioluminescence imaging. (B) H & E stained tumor cells with nuclear morphology characteristic of ATC (10X magnification). (C) GFP+ tumor cells from bulk tumor were analyzed for ICAM-1 and EPCAM1 expression by flow cytometry.

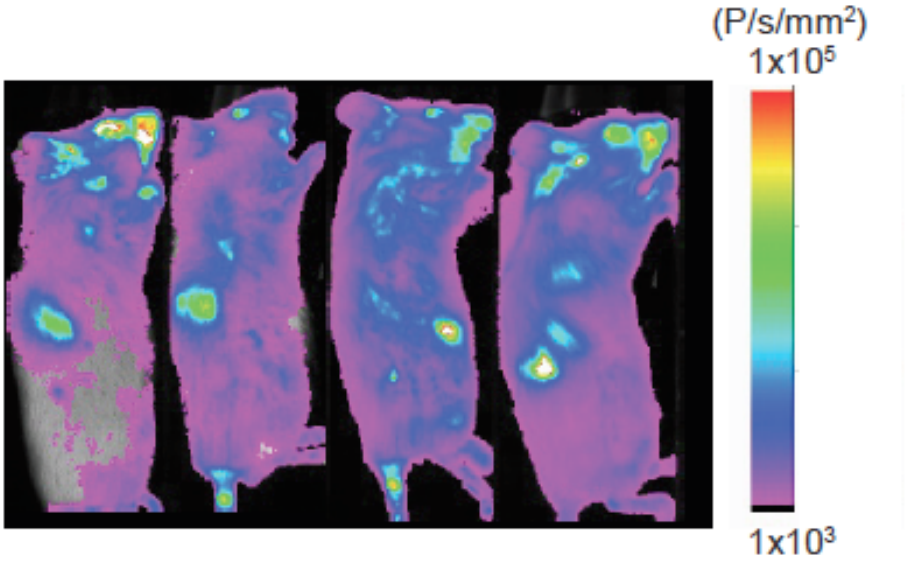


**Figure 2.15 CAR T activity is detectable throughout the body.**

Bioluminescence of rLuc activity is detectable in spleens and other organs in ICAM-1 CAR T-treated xenografts at X31T19.

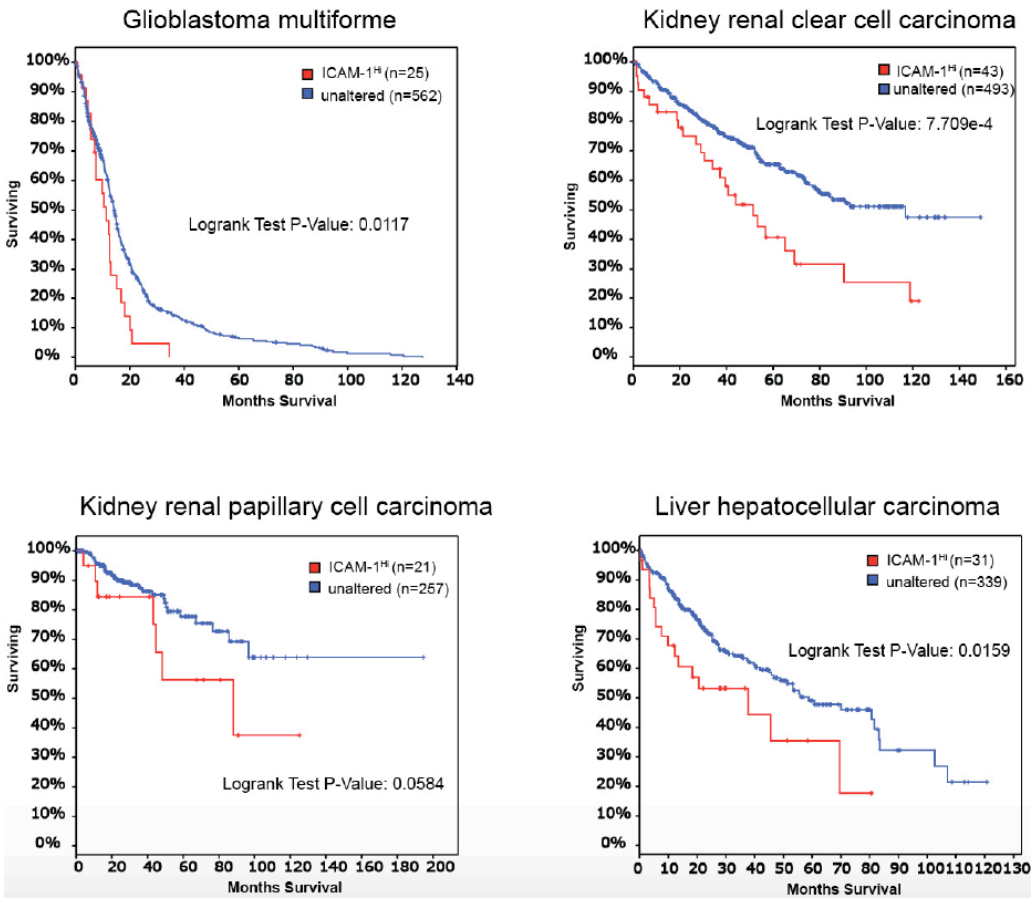


**Figure 2.16 Correlation between ICAM-1 overexpression in TCGA cancer patient tumors and overall survival.**

Kaplan-Meier plots demonstrate significant differences between the overall survival rates of patients with glioblastoma multiforme, kidney renal clear cell carcinoma, kidney renal papillary cell carcinoma, and liver hepatocellular carcinoma with unaltered and ICAM-1-overexpression (Z score>1.5). Clinical information and ICAM-1 expression levels were derived from TCGA datasets [39]. Retrospectively, sample size was estimated to be able to detect differences in survival with 80% power using a two-sided, 0.05 alpha level.

response from healthy donor-derived ICAM-1 CAR cells, which showed faster killing of target cells with high ICAM-1 expression (Figure 2.6E-F).

To more closely examine and predict patient-specific efficacy of ICAM-1 CAR T therapy, we further established ATC patient-derived xenograft models in NSG mice. The patient-derived ATC tumors carried a mutational profile (mutations in NRAS, p53, and PTEN) that differed from that of 8505C, which carries known mutations in $BRAF^{V600E}$ and p53 [40]. ATC patient-derived tumor cells were transduced with the fLuc-F2A-GFP lentivirus obtaining GFP expression of 15%. ATC cells were first injected subcutaneously into bilateral flanks, which, over a period of one month, grew to form uneven tumor masses (Figure 2.14A). Tumors harvested from xenografted mice displayed distinct pleiomorphism, hyperchromatism, increased nuclear to cytoplasmic ratio, and multiple mitoses, which are known features of undifferentiated thyroid cancer cells (Supplemental Fig 8B). At this stage, the percentages of $GFP^+$ cells in the bulk tumor were reduced to approximately 5%, yet $GFP^+$ tumor cells were found to retain the same EPCAM/ICAM-1 profile as the original primary patient cell cultures (Figure 2.14C).

Patient cells derived from subcutaneous tumors (as in Figure 2.14) were expanded in culture for additional 2 passages, and i.v. injected to produce metastatic tumor xenografts in NSG mice. Similar to the 8505C cell line xenografts, patient-derived ATC cells grew predominantly in the lungs (Figure 2.13C & 6D). Because of the difficulty in obtaining tumor cells with sufficiently high GFP and fLuc expression for tracking tumor growth by luminescence, we used MRI to detect the tumors in lungs, and quantified the volume fractions of tumor to the pulmonary cavity in

untreated and ICAM-1 CAR T-treated mice (Figure 2.13C). Lung tumor burden at 67-72 days after xenografts was significantly reduced in mice treated with a single infusion of autologous ICAM-1 CAR T (>1.5 million cells per mouse) compared to untreated (No T) controls. Lung tissues obtained from untreated mice showed tumor growth characteristics that were either diffuse, nodular, or both in the lung parenchyma and pleura (Figure 2.13D). In comparison, the alveolar space was almost tumor free in CAR T-treated lung tissues with small remnant tumors found in pleural and perivascular regions. The number of visible metastatic tumor nodules within the lung lobes of ICAM-1 CAR T-treated mice was significantly reduced compared to non-CAR controls as measured by IHC (Figure 2.13D). Finally, ICAM-1 CAR T treatment led to a significant improvement in the overall survival of ATC xenografted mice compared to non-treated controls that lasted approximately 70-80 days post-treatment (Figure 2.13E). During this period, whole body luminescence imaging confirmed persistence of rLuc-positive CAR T cells prominently in the head and the spleen, and weakly in lungs and other organs (Figure 2.15).

**Discussion**

Encouraged by impressive clinical developments of CAR T therapy for treatments of hematologic malignancies, we sought to develop CAR T therapeutics for advanced thyroid cancers. Here, we demonstrated the therapeutic potential of CAR T cells recognizing ICAM-1 for the treatment of a metastatic, aggressive thyroid cancer such as ATC, which is known to have one of the shortest median survival times among all solid tumors. Remarkably, we also showed that ICAM-1 CAR T cells manufactured

from the peripheral blood of a patient already compromised by ATC led to a significant reduction of tumor burden and led to prolonged overall survival of animals xenografted with autologous ATC tumors. To our knowledge, our approach is the first report utilizing patient-derived CAR T cells for the treatment of patient-derived, autologous solid tumor xenografts. This novel modeling approach can be used to aid the optimization of clinical protocols regarding treatment doses, timing, and administration of additional adjuvants to maximize therapy efficacy and safety.

Our rationale for developing therapeutics targeting ICAM-1 for treatment-refractory thyroid cancer is based upon several observations. ICAM-1 is significantly elevated in ATC and other thyroid cancer subtypes that metastasize to distant organs, thus presenting ICAM-1 as a useful prognostic marker for metastatic, aggressive thyroid cancer subtypes. From the analyses of TCGA PTC genomics in combination with clinical data, the level of ICAM-1 expression was found to correlate with aggressive tumorigenic features. This correlation was also experimentally validated in our study across multiple thyroid cancer cell lines. Moreover, ICAM-1 targeting therapy has potential applications in the treatments of other malignancies, including pancreatic ductal adenocarcinoma [18], breast cancer [17], multiple myeloma [41], and gastric tumors [19], where ICAM-1 surface expression is also significantly elevated compared to normal tissues. Along with thyroid carcinoma, TCGA studies indicated that overall patient survival was shorter when levels of ICAM-1 mRNA were upregulated in glioblastoma multiforme, kidney renal clear cell carcinoma, kidney renal papillary cell carcinoma, and liver hepatocellular carcinoma (Figure 2.16) [39, 42].

To target tumor cells with surface ICAM-1 expression, we adopted a scFv from R6.5 [36], a murine monoclonal antibody against ICAM-1, and fused it with the transmembrane and intracellular signaling components of a third-generation CAR construct incorporating CD28 and 4-1BB co-stimulatory domains [43]. The R6.5 antibody (enlimomab) binds to the junction between the first and second domain of ICAM-1 and prevents interaction with LFA-1 [44]. The R6.5 antibody has a proven safety and tolerability record with benefits for relieving inflammatory activity in patients with rheumatoid arthritis, burn injuries, and receiving transplants [21-24]. Its use for the treatment of stroke cases generated side effects due to a complement reaction attributable to the Fc portion of the mouse IgG2a [45]. The F(ab) of R6.5 has an estimated affinity of 10 nM [29], and the R6.5 scFv in the present ICAM-1 CAR T construct endowed T cells with ICAM-1 specific cytotoxicity that recognizes ICAM-1-overexpressing target tumor cells while sparing normal tissue with basal ICAM-1 expression. One possible concern with using a CAR specific to ICAM-1 is the CAR's competition with LFA-1 and potential inhibition of ensuing downstream signaling from T cell-LFA-1 engagement with ICAM-1 on target cells. This engagement elicits cytoplasmic $Ca^{2+}$ release in target cells and downstream perforin/gramzyme B dependent cytolytic T cell activity, and appears to affect TCR and CAR activities as well [46, 47]. Alternatively, competition between LFA-1 and R6.5 scFv in the CAR for ICAM-1 binding may aid CAR T cells to be selective to target cells overexpressing ICAM-1 and to avoid excessive avidity interactions involving CD3 and other co-stimulatory molecules, which can cause T cells to undergo activation induced exhaustion.

In addition to ICAM-1's function as a tumor antigen, ICAM-1 possesses additional characteristics that can augment the anti-tumor activity of targeted CAR T cells. ICAM-1 is a well-documented inflammatory marker, and chronic inflammation has long been known to shape local and systemic immunity to promote an immunosuppressive tumor microenvironment and aid tumor development [48]. Specifically, tumor-associated fibroblasts and tumor-associated macrophages are known to interact with tumor cells through ICAM-1 and promote cancer growth and metastasis [49, 50]. Selective targeting of ICAM-1 expressing tumor and stroma by ICAM-1 CAR T may therefore yield synergistic anti-tumor activities when treating thyroid cancer.

The marked enhancement of ICAM-1 expression in thyroid cancer cells upon addition of exogenous IFN-γ suggests that its expression in advanced thyroid cancer cells *in vivo* is likely to increase upon antigen recognition and subsequent IFN-γ release by infused ICAM-1 CAR T cells. In comparison, ICAM-1 expression is constitutively low in a variety of tissues, but its expression may be induced via pro-inflammatory cytokines such as IFN-γ, TNF-α, IL-1β in endothelial and some other cell types [15, 36, 51, 52]. Given that the IFN-γ secretion by CAR T cells is a key indicator of their anti-tumor activity [53], concerns will arise over the possibility that paracrine IFN-γ signaling may induce ICAM-1 expression in healthy neighboring cells, thus exposing them to CAR T cell cytotoxicity. Antigen density-dependent T cell activation is a known property of native T cells, where a threshold density of peptide/MHC is necessary for activation of TCR [54]. One strategy to further increase the therapeutic index of CAR T cells is lowering the CAR's antigen affinity to

increase T cell selectivity for targets with highly expressed antigens only and sparing normal cells with weaker expression. This hypothesis was tested and validated preclinically in prior studies using Her2 and EGFR-directed CAR T cells [55, 56]. Decreasing the R6.5 scFv affinity to that of typical TCR-pMHC interactions (1-100 μM) may endow ICAM-1 CAR T cells with a similar ability to discriminate between ATC with high ICAM-1 overexpression and nonmalignant tissue cells with lower ICAM-1 expression. Dynamic ICAM-1 expression across various acute and chronic medical conditions including cytokine release syndrome [53, 57] warrant further investigation as certain comorbidities may amplify ICAM-1 expression resulting in an increased risk of on-target off-tumor toxicity. Optimizing strategies to increase the therapeutic index and to limit off target toxicity will be crucial in bringing ICAM-1 CAR T into a clinical setting.

A number of studies suggest that thyroid cancers can evade immunosurveillance by immune evasion [58] or by developing immunosuppressive mechanisms [59, 60]. Advanced thyroid cancers including ATC are associated with a more diffuse and intense expression of the checkpoint ligand PD-L1 [59, 61]. It is unclear as to whether this augmented expression is reflective of an active immune response at the tumor site or if it is a signature of tumor cells that escaped immune attack [62]. Notably, the IFN-γ signaling pathway plays a critical role in both PD-L1 expression [63] and also in ICAM-1 expression as demonstrated in previous as well as the current study [64]. Blockade of the PD1-PD-L1 signaling axis has led to durable responses in several solid tumor indications, and it will be important to assess whether its combination with ICAM-1 CAR T therapy could bring further benefits to patients with advanced thyroid

cancers. The combination of a BRAF inhibitor with an anti-PD-L1 antibody in an immunocompetent model of ATC demonstrated significant treatment benefits compared to monotherapy suggesting that immune therapy used in combination has the potential to benefit patients with ATC [65].

In conclusion, we report the first demonstration of robust and durable CAR T therapeutic effects in preclinical models of ATC using both cell lines and patient-derived tumors. The substantial surface and diffuse ICAM-1 expression patterns across almost all examined ATC samples demonstrate its potential as a target for CAR T therapies. ATC tumors are characterized by their heterogeneity, complex mutational landscape, and poor expression of molecules that have previously been exploited as molecular and cellular targets [3, 35, 66]. The prolonged survival achieved upon treatment of ATC inoculated mice with ICAM-1 CAR T was particularly notable when compared with previous treatment strategies in preclinical metastatic models using the same ATC cell line [67-69]. The preclinical xenograft model used here is limited by the inability to monitor potential toxicity mediated by ICAM-1 CAR against non-tumor tissue. However, additional modifications with emerging technologies such as inducible CAR expression [70], CAR T cell elimination via suicide gene activation [71], combinatorial antigen targeting [72], and affinity-tuned [55, 56] CAR T are likely to enhance safety while preserving on-target efficacy, thus providing a framework for adaptation of CAR T cells targeting ICAM-1 as a new treatment modality for advanced thyroid cancers and other solid tumors with ICAM-1 overexpression.

REFERENCE


1. Li, Y., et al., *Controlled assembly of dendrimer-like DNA*. Nat Mater, 2004. **3**(1): p. 38-42.
2. Siegel, R.L., K.D. Miller, and A. Jemal, *Cancer Statistics, 2017*. CA Cancer J Clin, 2017. **67**(1): p. 7-30.
3. Xu, B. and R. Ghossein, *Genomic Landscape of poorly Differentiated and Anaplastic Thyroid Carcinoma*. Endocr Pathol, 2016. **27**(3): p. 205-12.
4. Shou, J., et al., *Nuclear factor of activated T cells in cancer development and treatment*. Cancer Lett, 2015. **361**(2): p. 174-84.
5. Smallridge, R.C., et al., *American Thyroid Association guidelines for management of patients with anaplastic thyroid cancer*. Thyroid, 2012. **22**(11): p. 1104-39.
6. Wagle, N., et al., *Response and acquired resistance to everolimus in anaplastic thyroid cancer*. N Engl J Med, 2014. **371**(15): p. 1426-33.
7. Rosove, M.H., P.F. Peddi, and J.A. Glaspy, *BRAF V600E inhibition in anaplastic thyroid cancer*. N Engl J Med, 2013. **368**(7): p. 684-5.
8. Rosenberg, S.A. and N.P. Restifo, *Adoptive cell transfer as personalized immunotherapy for human cancer*. Science, 2015. **348**(6230): p. 62-8.
9. Haworth, K.B., et al., *Going back to class I: MHC and immunotherapies for childhood cancer*. Pediatr Blood Cancer, 2015. **62**(4): p. 571-6.
10. Gross, G., T. Waks, and Z. Eshhar, *Expression of immunoglobulin-T-cell receptor chimeric molecules as functional receptors with antibody-type specificity*. Proc Natl Acad Sci U S A, 1989. **86**(24): p. 10024-8.
11. Maher, J., et al., *Human T-lymphocyte cytotoxicity and proliferation directed by a single chimeric TCRzeta /CD28 receptor*. Nat Biotechnol, 2002. **20**(1): p. 70-5.
12. Milone, M.C., et al., *Chimeric receptors containing CD137 signal transduction domains mediate enhanced survival of T cells and increased antileukemic efficacy in vivo*. Mol Ther, 2009. **17**(8): p. 1453-64.
13. Maude, S.L., et al., *Chimeric antigen receptor T cells for sustained remissions in leukemia*. N Engl J Med, 2014. **371**(16): p. 1507-17.
14. Till, B.G., et al., *CD20-specific adoptive immunotherapy for lymphoma using a chimeric antigen receptor with both CD28 and 4-1BB domains: pilot clinical trial results*. Blood, 2012. **119**(17): p. 3940-50.
15. Pober, J.S., et al., *Overlapping patterns of activation of human endothelial cells by interleukin 1, tumor necrosis factor, and immune interferon*. J Immunol, 1986. **137**(6): p. 1893-6.
16. Schmidmaier, R., et al., *Evidence for cell adhesionmediated drug resistance of multiple myeloma cells in vivo*. Int J Biol Markers, 2006. **21**(4): p. 218-222.
17. Guo, P., et al., *ICAM-1 as a molecular target for triple negative breast cancer*. Proc Natl Acad Sci U S A, 2014. **111**(41): p. 14710-5.

18. Huang, C., et al., *Tumour-derived Interleukin 35 promotes pancreatic ductal adenocarcinoma cell extravasation and metastasis by inducing ICAM1 expression*. Nat Commun, 2017. **8**: p. 14035.
19. Maruo, Y., et al., *ICAM-1 expression and the soluble ICAM-1 level for evaluating the metastatic potential of gastric cancer*. Int J Cancer, 2002. **100**(4): p. 486-90.
20. Kotteas, E.A., et al., *The intercellular cell adhesion molecule-1 (icam-1) in lung cancer: implications for disease progression and prognosis*. Anticancer Res, 2014. **34**(9): p. 4665-72.
21. Kavanaugh, A.F., et al., *A phase I/II open label study of the safety and efficacy of an anti-ICAM-1 (intercellular adhesion molecule-1; CD54) monoclonal antibody in early rheumatoid arthritis*. J Rheumatol, 1996. **23**(8): p. 1338-44.
22. Cosimi, A.B., et al., *In vivo effects of monoclonal antibody to ICAM-1 (CD54) in nonhuman primates with renal allografts*. J Immunol, 1990. **144**(12): p. 4604-12.
23. Mileski, W.J., et al., *Clinical effects of inhibiting leukocyte adhesion with monoclonal antibody to intercellular adhesion molecule-1 (enlimomab) in the treatment of partial-thickness burn injury*. J Trauma, 2003. **54**(5): p. 950-8.
24. Enlimomab Acute Stroke Trial, I., *Use of anti-ICAM-1 therapy in ischemic stroke: results of the Enlimomab Acute Stroke Trial*. Neurology, 2001. **57**(8): p. 1428-34.
25. Hansson, M., et al., *A Phase I Dose-Escalation Study of Antibody BI-505 in Relapsed/Refractory Multiple Myeloma*. Clin Cancer Res, 2015. **21**(12): p. 2730-6.
26. Buitrago, D., et al., *Intercellular adhesion molecule-1 (ICAM-1) is upregulated in aggressive papillary thyroid carcinoma*. Ann Surg Oncol, 2012. **19**(3): p. 973-80.
27. Zhang, K.E., et al., *Intercellular adhesion molecule 1 is a sensitive and diagnostically useful immunohistochemical marker of papillary thyroid cancer (PTC) and of PTC-like nuclear alterations in Hashimoto's thyroiditis*. Oncol Lett, 2016. **11**(3): p. 1722-1730.
28. Vedvyas, Y., et al., *Longitudinal PET imaging demonstrates biphasic CAR T cell responses in survivors*. JCI Insight, 2016. **1**(19): p. e90064.
29. Leelawattanachai, J., et al., *Side-by-Side Comparison of Commonly Used Biomolecules That Differ in Size and Affinity on Tumor Uptake and Internalization*. PLoS One, 2015. **10**(4): p. e0124440.
30. Zhang, L., et al., *An in vivo mouse model of metastatic human thyroid cancer*. Thyroid, 2014. **24**(4): p. 695-704.
31. Cancer Genome Atlas Research, N., *Integrated genomic characterization of papillary thyroid carcinoma*. Cell, 2014. **159**(3): p. 676-90.
32. Pratilas, C.A., et al., *(V600E)BRAF is associated with disabled feedback inhibition of RAF-MEK signaling and elevated transcriptional output of the pathway*. Proc Natl Acad Sci U S A, 2009. **106**(11): p. 4519-24.
33. Namba, H., et al., *Clinical implication of hot spot BRAF mutation, V599E, in papillary thyroid cancers*. J Clin Endocrinol Metab, 2003. **88**(9): p. 4393-7.

34. Pita, J.M., et al., *Cell cycle deregulation and TP53 and RAS mutations are major events in poorly differentiated and undifferentiated thyroid carcinomas*. J Clin Endocrinol Metab, 2014. **99**(3): p. E497-507.
35. Landa, I., et al., *Genomic and transcriptomic hallmarks of poorly differentiated and anaplastic thyroid cancers*. J Clin Invest, 2016. **126**(3): p. 1052-66.
36. Smith, C.W., et al., *Recognition of an endothelial determinant for CD 18-dependent human neutrophil adherence and transendothelial migration*. J Clin Invest, 1988. **82**(5): p. 1746-56.
37. Uhlen, M., et al., *Proteomics. Tissue-based map of the human proteome*. Science, 2015. **347**(6220): p. 1260419.
38. Hayes, S.H. and G.M. Seigel, *Immunoreactivity of ICAM-1 in human tumors, metastases and normal tissues*. Int J Clin Exp Pathol, 2009. **2**(6): p. 553-60.
39. Gao, J., et al., *Integrative analysis of complex cancer genomics and clinical profiles using the cBioPortal*. Sci Signal, 2013. **6**(269): p. pl1.
40. Pilli, T., et al., *Potential utility and limitations of thyroid cancer cell lines as models for studying thyroid cancer*. Thyroid, 2009. **19**(12): p. 1333-42.
41. Veitonmaki, N., et al., *A human ICAM-1 antibody isolated by a function-first approach has potent macrophage-dependent antimyeloma activity in vivo*. Cancer Cell, 2013. **23**(4): p. 502-15.
42. Boeggeman, E.E., B. Ramakrishnan, and P.K. Qasba, *The N-terminal stem region of bovine and human β1,4-galactosyltransferase I increases the in vitro folding efficiency of their catalytic domain from inclusion bodies*. Protein Expression and Purification, 2003. **30**(2): p. 219-229.
43. Carpenito, C., et al., *Control of large, established tumor xenografts with genetically retargeted human T cells containing CD28 and CD137 domains*. Proc Natl Acad Sci U S A, 2009. **106**(9): p. 3360-5.
44. Staunton, D.E., et al., *The arrangement of the immunoglobulin-like domains of ICAM-1 and the binding sites for LFA-1 and rhinovirus*. Cell, 1990. **61**(2): p. 243-54.
45. Vuorte, J., et al., *Anti-ICAM-1 monoclonal antibody R6.5 (Enlimomab) promotes activation of neutrophils in whole blood*. J Immunol, 1999. **162**(4): p. 2353-7.
46. Frick, M., et al., *Distinct patterns of cytolytic T-cell activation by different tumour cells revealed by Ca2+ signalling and granule mobilization*. Immunology, 2017. **150**(2): p. 199-212.
47. Laurin, D., et al., *Upregulation of adhesion molecules on leukemia targets improves the efficacy of cytotoxic T cells transduced with chimeric anti-CD19 receptor*. J Immunother, 2013. **36**(3): p. 181-9.
48. Shalapour, S. and M. Karin, *Immunity, inflammation, and cancer: an eternal fight between good and evil*. J Clin Invest, 2015. **125**(9): p. 3347-55.
49. Schellerer, V.S., et al., *Tumor-associated fibroblasts isolated from colorectal cancer tissues exhibit increased ICAM-1 expression and affinity for monocytes*. Oncol Rep, 2014. **31**(1): p. 255-61.

50. Yin, M., et al., *Tumor-associated macrophages drive spheroid formation during early transcoelomic metastasis of ovarian cancer*. J Clin Invest, 2016. **126**(11): p. 4157-4173.
51. Mickelson, J.K., et al., *Differential expression and release of CD54 induced by cytokines*. Hepatology, 1995. **22**(3): p. 866-75.
52. Lu, Y., et al., *Nitric oxide inhibits hetero-adhesion of cancer cells to endothelial cells: restraining circulating tumor cells from initiating metastatic cascade*. Sci Rep, 2014. **4**: p. 4344.
53. Teachey, D.T., et al., *Identification of Predictive Biomarkers for Cytokine Release Syndrome after Chimeric Antigen Receptor T-cell Therapy for Acute Lymphoblastic Leukemia*. Cancer Discov, 2016. **6**(6): p. 664-79.
54. Kalergis, A.M., et al., *Efficient T cell activation requires an optimal dwell-time of interaction between the TCR and the pMHC complex*. Nat Immunol, 2001. **2**(3): p. 229-34.
55. Liu, X., et al., *Affinity-Tuned ErbB2 or EGFR Chimeric Antigen Receptor T Cells Exhibit an Increased Therapeutic Index against Tumors in Mice*. Cancer Res, 2015. **75**(17): p. 3596-607.
56. Caruso, H.G., et al., *Tuning Sensitivity of CAR to EGFR Density Limits Recognition of Normal Tissue While Maintaining Potent Antitumor Activity*. Cancer Res, 2015. **75**(17): p. 3505-18.
57. Pinsky, M.R., et al., *Serum cytokine levels in human septic shock. Relation to multiple-system organ failure and mortality*. Chest, 1993. **103**(2): p. 565-75.
58. Angell, T.E., et al., *MHC class I loss is a frequent mechanism of immune escape in papillary thyroid cancer that is reversed by interferon and selumetinib treatment in vitro*. Clin Cancer Res, 2014. **20**(23): p. 6034-44.
59. Bastman, J.J., et al., *Tumor-Infiltrating T Cells and the PD-1 Checkpoint Pathway in Advanced Differentiated and Anaplastic Thyroid Cancer*. J Clin Endocrinol Metab, 2016. **101**(7): p. 2863-73.
60. Angell, T.E., et al., *BRAF V600E in papillary thyroid carcinoma is associated with increased programmed death ligand 1 expression and suppressive immune cell infiltration*. Thyroid, 2014. **24**(9): p. 1385-93.
61. Ahn, S., et al., *Comprehensive screening for PD-L1 expression in thyroid cancer*. Endocr Relat Cancer, 2017. **24**(2): p. 97-106.
62. Sharma, P. and J.P. Allison, *The future of immune checkpoint therapy*. Science, 2015. **348**(6230): p. 56-61.
63. Zaretsky, J.M., et al., *Mutations Associated with Acquired Resistance to PD-1 Blockade in Melanoma*. N Engl J Med, 2016. **375**(9): p. 819-29.
64. Chang, Y.J., M.J. Holtzman, and C.C. Chen, *Interferon-gamma-induced epithelial ICAM-1 expression and monocyte adhesion. Involvement of protein kinase C-dependent c-Src tyrosine kinase activation pathway*. J Biol Chem, 2002. **277**(9): p. 7118-26.
65. Brauner, E., et al., *Combining BRAF inhibitor and anti PD-L1 antibody dramatically improves tumor regression and anti tumor immunity in an immunocompetent murine model of anaplastic thyroid cancer*. Oncotarget, 2016. **7**(13): p. 17194-211.

66. Ensinger, C., et al., *Her2/neu expression in poorly-differentiated and anaplastic thyroid carcinomas*. Anticancer Res, 2003. **23**(3B): p. 2349-53.
67. Sadowski, S.M., et al., *Torin2 targets dysregulated pathways in anaplastic thyroid cancer and inhibits tumor growth and metastasis*. Oncotarget, 2015. **6**(20): p. 18038-49.
68. Mehta, A., et al., *Inhibition of Survivin with YM155 Induces Durable Tumor Response in Anaplastic Thyroid Cancer*. Clin Cancer Res, 2015. **21**(18): p. 4123-32.
69. Bauerle, K.T., et al., *Nuclear factor kappaB-dependent regulation of angiogenesis, and metastasis in an in vivo model of thyroid cancer is associated with secreted interleukin-8*. J Clin Endocrinol Metab, 2014. **99**(8): p. E1436-44.
70. Wu, C.Y., et al., *Remote control of therapeutic T cells through a small molecule-gated chimeric receptor*. Science, 2015. **350**(6258): p. aab4077.
71. Di Stasi, A., et al., *Inducible apoptosis as a safety switch for adoptive cell therapy*. N Engl J Med, 2011. **365**(18): p. 1673-83.
72. Kloss, C.C., et al., *Combinatorial antigen recognition with balanced signaling promotes selective tumor eradication by engineered T cells*. Nat Biotechnol, 2013. **31**(1): p. 71-5.

2

# CHAPTER 3

# LONGITUDINAL AND QUANTITATIVE IMAGING OF THE EXPANSION AND CONTRACTION OF TUMOR-TARGETED ADOPTIVELY TRANSFERRED T CELLS


**Summary**

Clinical monitoring of adoptive T cell transfer (ACT) utilizes serial blood analyses to discern T cell activity. While useful, these data are 1-dimensional and lack spatiotemporal information related to treatment efficacy or toxicity. We utilized a human genetic reporter, somatostatin receptor 2 (SSTR2), and PET, to quantitatively and longitudinally visualize whole-body T cell distribution and antitumor dynamics using a clinically approved radiotracer. Initial evaluations determined that SSTR2-expressing T cells were detectable at low densities with high sensitivity and specificity. SSTR2-based PET was applied to ACT of chimeric antigen receptor (CAR) T cells targeting intercellular adhesion molecule-1, which is overexpressed in anaplastic thyroid tumors. Timely CAR T cell infusions resulted in survival of tumor-bearing mice, while later infusions led to uniform death. Real-time PET imaging revealed biphasic T cell expansion and contraction at tumor sites among survivors, with peak tumor burden preceding peak T cell burden by several days. In contrast,


---


This chapter was originally published in JCI Insight (Vedvyas, Y., Shevlin, E., Zaman, M., Min, I.M., Amor-Coarasa, A., Park, S., Park, S., Kwon, K.K., Smith, T., Luo, Y., Kim, D., Kim, Y., Law, B., Ting, R., Babich, J., and Jin, M.M., *JCI Insight*. 2016;1(19):e90064. ) and is reprinted with permission. Vedvyas Y contributed to all aspects of this study. Covering the conception, design and execution of all of the work.

non-survivors displayed unrelenting increases in tumor and T cell burden, indicating that tumor growth was outpacing T cell killing. Thus, longitudinal PET imaging of SSTR2-positive ACT dynamics enables prognostic, spatiotemporal monitoring with unprecedented clarity and detail to facilitate comprehensive therapy evaluation with potential for clinical translation.

**Introduction**

Adoptive T cell transfer (ACT) of cytotoxic T lymphocytes is being studied as a potent treatment strategy for cancers that are refractory to standard chemotherapy and radiation therapy. Clinical advances have been made in patients with metastatic melanoma using autologous tumor-infiltrating lymphocytes (TILs) and in several B cell malignancies using autologous chimeric antigen receptor–modified (CAR-modified) T cells [1]. Methods used to predict or monitor the activity of infused T cells in patients provide useful but limited data related to treatment efficacy. Current practices involve serum pro ling of cytokines associated with T cell activation, direct enumeration of tumor-specific T cell numbers in peripheral circulation, and tumor biopsies [2, 3]. Changes in serum cytokine levels, while useful, likely reflect a broader, systemic immune response, illustrating not only the activation of adoptively transferred T cells, but also their effects on neighboring immune cells and dying tumor cells [4]. Similarly, while the quantification of adoptively transferred cells in circulation provides useful information regarding their proliferation, researchers and clinicians are blind as to whether the dynamism in T cell numbers relates to expansion at the primary tumor site, metastatic foci, or at off-tumor sites [5]. The ability to map the physical distribution and expansion of adoptively transferred T cells throughout

the body in a longitudinal manner could therefore significantly improve real-time monitoring of T cell activity against tumors, potential toxicity from off-tumor-site targeting, and contribute to exploring adjuvant therapies to enhance adoptive T cell efficacy against solid cancers [5–7].

The imaging modalities with the highest potential for whole-body visualization of cell trafficking in humans are magnetic resonance imaging (MRI), single-photon emission computed tomography (SPECT), positron emission tomography (PET)/CT, or PET/MRI techniques for detection of labeled cells and co-registration of anatomical information of the body [8–10]. PET is particularly amenable to clinical use as it enables noninvasive, highly sensitive, repetitive, and quantitative imaging of positron-emitting, target- specific probes. The introduction of microPET for small-animal imaging has similarly made PET amenable to preclinical studies [11]. Ongoing activity of ACT against both on- and off-tumor sites can therefore be monitored in vivo by quantitative, radiotracer-based imaging of T cell distribution and expansion upon interaction with target antigen–expressing cells [2, 10, 12]. However, previous attempts to systemically monitor ACT in patients have yet to be adopted [13]. Passive labeling of T cells with positron-emitting probes ex vivo has been used to monitor the early-stage migration of infused T cells but suffers from potential inaccuracies due to signals from dead or dying cells, probe dilution upon cell division, and a limited ability to track cells over extended periods of time owing to short probe half-life [10]. Alternatively, the stable transduction of T cells with a specific reporter gene allows for extended longitudinal studies using serial infusions of reporter-specific probes. Additionally, as only live cells are capable of continually expressing the reporter gene,

observed signals are limited to these cells only. Current reporter genes used in preclinical and clinical studies are based on both intracellular enzymes, e.g., herpes simplex virus type-1 thymidine kinase (HSV1-tk) and human deoxycytidine kinase [14–16], and surface receptors, e.g., sodium iodide symporter [NIS] [17], prostate-specific membrane antigen (PSMA) [18], and SSTR2 (19]. However, previous imaging studies have failed to demonstrate quantitative monitoring of critical T cell efficacy parameters, namely, whole-body, longitudinal visualization of T cell dynamics spanning initial localization, expansion, and subsequent contraction at primary and/or metastatic tumor sites, and the relationship between these parameters and tumor killing [5, 13, 20–22]. More importantly, imaging studies have yet to fully de ne treatment response parameters or prognostic markers of ACT efficacy and toxicity, and how these affect clinical outcomes in patients.

We have chosen human SSTR2 as a reporter marker in efforts to determine the detection limit of T cells infiltrating solid tumors, and to predict the temporal kinetics of T cell recruitment and expansion, directly related to T cell activity against tumors. SSTR2 belongs to a family of G protein–coupled receptors, with expression restricted to the cerebrum and kidneys, and at low levels in the gastrointestinal tract [23]. It is a potentially ideal reporter marker for monitoring ACT owing to its limited basal expression throughout the body and the availability of clinically approved radiotracers for SSTR2, for example, gallium-68–chelated octreotide analogues ($^{68}$Ga-DOTATOC) for the detection of SSTR2-overexpressing neuroendocrine tumors [19, 24–26]. To determine the detection limit of T cells within a solid tumor mass, we

introduced SSTR2 into Jurkat T cells and titrated these with wild-type Jurkats to produce subcutaneous Jurkat tumor xenografts, each with defined ratios of SSTR2-expressing cells ranging from 0% to 100%. With this model, it became possible to replicate the varying degrees of T cell localization, penetration, and expansion at or within the tumor site. Over the course of tumor growth, PET/CT imaging was performed using $^{68}$Ga-DOTATOC to quantify the detection limit of SSTR2-positive T cells within the tumor and to correlate radiotracer uptake with tumor size and percentages of SSTR2-expressing cells. To further demonstrate the utility of SSTR2 for imaging T cell distribution and expansion in a more physiologically relevant setting, we designed a single lentivirus vector to engineer primary human T cells to express both SSTR2 and a CAR specific to intercellular adhesion molecule-1 (ICAM-1), which is overexpressed in a range of malignant cancers [27–32]. Longitudinal, whole-body imaging of SSTR2-expressing, ICAM-1–specific CAR T cells by PET/CT was then performed in mice with systemic growth of poorly differentiated, radioactive iodine–resistant, anaplastic thyroid tumors [33, 34]. The kinetics of $^{68}$Ga-DOTATOC uptake in survivors demonstrated a biphasic T cell expansion and contraction pattern, the timing of which largely matched tumor burden kinetics except for a consistent lag in T cell contraction after tumor destruction. In contrast, unabated increases in $^{68}$Ga-DOTATOC uptake and tumor burden combined with rapid weight loss were observed in non-survivors, providing evidence that the rate of tumor killing by T cells in these instances is outpaced by that of tumor growth.

**Experimental procedures**

*Mammalian cell culture*.

Parental HeLa (ATCC), HEK 293 (ATCC), and 8505C (DSMZ) cells were transduced with lentivirus encoding Fire y Luciferase-F2A-GFP (Biosettia) followed by fluorescence- activated cell sorting (FACS) to purify GFP-expressing cells. HeLa-$FLuc^{+}GFP^{+}$ and HEK 293-$FLuc^{+}GFP^{+}$ cells were cultured in Advanced Dulbecco's Modified Eagle Medium containing 10% (v/v) FBS, 2 mM L-alanyl-L-glutamine dipeptide (Gibco), and 100 U/ml penicillin-streptomycin (Pen/Strep) (Gibco). 8505C-$FLuc^{+}GFP^{+}$ cells were cultured in RPMI-1640 supplemented with 10% (v/v) FBS, 2 mM L-alanyl- L-glutamine dipeptide, and 100 U/ml Pen/Strep. Human peripheral blood was obtained from healthy volunteer donors by venipuncture. Peripheral blood mononuclear cells (PBMCs) were isolated over Ficoll- Paque PLUS (GE Healthcare) and cultured in Optimizer CTS T-cell Expansion SFM (Thermo Fisher) supplemented with 5% human AB serum (Sigma-Aldrich), 2 mM L-alanyl-L-glutamine dipeptide, 100 U/ ml Pen/Strep and 30 IU/ml human IL-2 (Cell Sciences). Nonadherent cells were removed after 24 hours and magnetically enriched for T cells with Dynabeads CD3/CD28 T cell expander (Thermo Fisher) at a 2:1 bead/T cell ratio. Dynabead-bound T cells were subsequently cultured in IL-2–containing media at a density of $1 \times 10^6$ to $2 \times 10^6$ cells/ml. All cells were incubated at 37°C in a 5% $CO_2$ humidified incubator.

*Construction of ICAM-1 CAR and SSTR2 reporter genes*.

The CAR gene specific to ICAM-1 was derived from the scFv sequence of a murine monoclonal anti–human R6.5 antibody — itself derived from hybridoma (ATCC) [56, 57]. The R6.5-speci c scFv was then fused to the transmembrane and cytoplasmic domains of CD28, CD137, and CD3ζ of an independent third-generation pLenti plasmid (a gift from Carl June at the University of Pennsylvania, Philadelphia, Pennsylvania, USA) [35]. A lentivirus vector (derived from the CAR vector) encoding human SSTR2 (NM_001050) was constructed by synthesizing the SSTR2- coding sequence (IDT) and inserting it into the vector using Xba1 and Sal1 sites.

*Lentivirus production and transduction of T cells*.

Lentivirus particles were produced by transiently transfecting HEK 293 cells using calcium phosphate. Brie y, 10 μg transfer gene, 7.5 μg CMV-dR8.2 (Addgene) and 5 μg pCMV-VSVG (Addgene) were mixed and incubated with 2 M $CaCl_2$ followed by 2× Hanks' balanced salt solution (HBSS). Resulting solutions were added dropwise to 10-cm cell culture dishes seeded with $3.2 \times 10^6$ HEK 293 in 10 ml DMEM 24 hours previously. Transfection media was replaced after 6 hours. Media containing lentivirus was harvested at 48 and 72 hours after transfection, filtered through 0.45-μm filters, and concentrated by ultracentrifugation at 75,000 *g* for 2 hours at 4°C. Lentivirus was then resuspended in serum-containing media at an approximate titer of $10^8$/ml and frozen at –80°C. Human T cells were transduced 24–72 hours after activation with CD3/CD28 Dynabeads either by spinfection at 1,000 *g*

for 1 hour at 32°C or by overnight incubation of lentivirus in the presence of Synperonic F108 (Sigma-Aldrich) [58]. T cells were also transduced a second time, 24 hours after initial transduction. The viral titer was adjusted to obtain a transduction level of approximately 50%. During and following transduction, media containing IL-2 was replaced with media containing human IL-7 (10 ng/ml) and IL-15 (5 ng/ml) (Peprotech), which was found to augment T cell persistence in vivo [59, 60]. Jurkat T cells were transduced by a single incubation with lentivirus overnight in the presence of Synperonic F108.

*Conformation of SSTR2 functionality and measurement of site density*.

SSTR2-transduced Jurkat T cells were incubated with or without 1 μM octreotide (Sigma-Aldrich) for 30 minutes at 37 °C. Subsequent internalization of SSTR2 was measured by flow cytometry analysis of SSTR2 expression. The site density of SSTR2 expression on Jurkats was determined by incubating nontransduced and SSTR2-transduced Jurkat T cells with DOTATOC (8–250 nM) at either 37°C or 4°C for 30 minutes in PBS/0.1% BSA. After incubation, cells were washed 3 times and DOTATOC uptake was measured using a gamma counter (Packard, Cobra II Auto-Gamma). Values obtained were used for Scatchard analysis to estimate affinity and site density.

*Subcutaneous Jurkat T cell xenograft*.

SSTR2-expressing Jurkats were spiked with increasing numbers of nontransduced Jurkats to derive distinct cultures containing defined percentages of

SSTR2 expression ranging from 100%–0%. For each subcutaneous xenograft, $5 \times 10^6$ total cells were resuspended in 100 µl Matrigel Basement Membrane Matrix (Corning) and injected bilaterally into nonobese diabetic (NOD)/ LtSz-*Prkdc*$^{scid}$*Il2rg*$^{tm1Wjl}$/J (NSG) mice (Jackson Laboratory). Measurements of tumor size were made using a digital caliper. Tumor volume was calculated by using the modified ellipsoid formula $0.5 \times (\text{length} \times \text{width}^2)$. Length was measured as the longer dimension. Each dimensional measurement was rounded to the nearest 0.5 mm.

*Labeling of $^{68}$Ga-DOTATOC.*

DOTATOC (1,4,7,10-tetraazacyclododecane-$N^I$,$N^{II}$,$N^{III}$,$N^{IIII}$- tetraacetic acid (D)-Phe$^1$-thy$^3$-octreotide, GMP grade) was obtained as 1 mg lyophilized powder (ABX Pharmaceuticals). The DOTATOC vial content was diluted with 18 MOhm water to 2 ml (0.5 mg/ml solution) and stored at 4°C as a stock solution. $^{68}$Ga was obtained by eluting an ITG $^{68}$Ge/$^{68}$Ga generator (ITM) with 4 ml 0.05 M HCl solution. To the eluted $^{68}Ga^{3+}$, 50 µl of the DOTATOC stock solution (25 µg) was added, followed by 80 µl of a 3N NaOAc solution for buffering. The mixture was immediately placed in a Thermomixer (Eppendorf) at 95°C and incubated for 15 minutes. Following incubation, the mixture was passed through a previously activated C-18 Sep-Pak Lite (Waters) to trap the labeled peptide. The labeling vial was washed with 5 ml 18 MOhm water and the resulting wash was also passed through the C-18 Sep-Pak. Finally, the Sep-Pak was washed with an extra 5 ml of 18 MOhm water to eliminate any remaining free $^{68}$Ga. The trapped $^{68}$Ga-DOTATOC was then slowly

eluted from the C-18 Sep-Pak using 100 µl of ethanol followed by 900 µl of saline solution for injection, providing the final product in a 10% ethanol, isotonic, injectable solution. The purity of the final product was checked by reverse-phase HPLC.

*E:T assay*.

$2 \times 10^5$ HeLa-FLuc$^+$GFP$^+$, 8505c-FLuc$^+$GFP$^+$, or HEK 293-FLuc$^+$GFP$^+$ cells were cocultured with either nontransduced or CAR-expressing T cells (SSTR2-R6.5 or R6.5) at varying E:T ratios as indicated. Cocultures were carried out in T cell media containing 150 µg/ml D-luciferin (Gold Biotechnology) with no cytokine supplementation. Luminescence was measured using a plate reader (TECAN in nite M1000 PRO) with readings in each E:T condition normalized to the nontransduced T cell/target co-culture controls.

*8505C mouse model, measurement of ex vivo organs and whole-body tumor growth*.

8505c-FLuc$^+$GFP$^+$ cells ($1 \times 10^6$) were injected into NSG mice via tail vein. Primary human T cells ($2 \times 10^6$ to $3 \times 10^6$) were injected via tail vein 7–15 days after tumor cell injection. Luminescence imaging of tumor xenografts in live mice was performed using a whole-body optical imager (In-Vivo Extreme 4MP, Bruker). Mice were first anesthetized with 3% isoflurane at 2 l/min $O_2$ and subsequent to this, maintained at 2% isofurane at 2 l/ min $O_2$. Growth or reduction in tumor burden was estimated by integration of luminescence over the lungs or the entire mouse body. Ex vivo fluorescence imaging of mouse liver, lungs, spleen, and resected tumors was

performed using a whole-body optical imager (In-Vivo F Pro, Bruker).

*PET/CT imaging*.

Registered CT images were acquired using a micro-PET/CT scanner (Inveon, Siemens) 1–2 hours after DOTATOC injection. Projection data were acquired in a cone-beam geometry with approximately 1-second steps at 1° angular increments. At least $10 \times 10^6$ coincidence events were acquired for PET per study using a 250- to 750-keV energy window and a 6-nanosecond timing window. A reference was included using a tube containing 100 μl of 10 %ID/$cm^3$ for quantification of DOTATOC uptake in vivo. To compute DOTATOC uptake by Jurkat tumors, the ellipsoidal ROIs (AMIDE software; http://amide.sourceforge.net/index.html) were placed to enclose subcutaneous tumors that closely match overall tumor size and shape. For systemic 8505C tumor models, ellipsoids were drawn separately on the left and right sides of lungs to enclose all 5 lobes of mouse lungs. The %ID/$cm^3$ values, computed relative to the counts in a reference tube, can be approximated to a standard uptake value (SUV) [61] by dividing %ID/$cm^3$ by 4, assuming an injection ef ciency of 100% and 25 g body weight. Visualization and analyses of PET/CT images were performed using AMIDE.

*Flow cytometry*.

Jurkat tumor xenografts or mouse organs (lungs and liver) were harvested from mice following completion of PET/CT imaging. Tissues were diced and flushed through an 80-μm cell strainer to yield single-cell suspensions. Red blood cells were

lysed by incubating the cell suspension with 1× Ammonium-Chloride-Potassium lysing buffer (Thermo Fisher), followed by washing and resuspension in 1× HBSS containing 2% normal goat serum. Prior to staining, cells were blocked with mouse IgG (Sigma-Aldrich, 15381) at 2 μg/ml for 10 minutes. This was followed by live staining with 1 μg/ml propidium iodide (PI, Invitrogen, P3566) in combination with 2 μg/ml murine anti–human CD3-Alexa Fluor 647 (Biolegend, 300322) or 2 μg/ml PE-conjugated murine anti–human SSTR2 (R&D Systems, FAB4224P). Flow cytometry gates were rst determined by live-cell gating (PI negative) and subsequently by staining of respective antibodies. ICAM-1 expression on tumor cell lines was determined using a murine anti–human R6.5 monoclonal antibody (10 μg/ml) derived from hybridoma (ATCC) [57]. R6.5-CAR expression on T cells was detected using FITC-conjugated goat anti–mouse F(ab′)2 secondary antibody (Thermo Fisher, 31543).

*Histology*.

Jurkat tumor xenografts were harvested, fixed in 4% paraformaldehyde in PBS, embedded in paraffin, and were cut to produce 5-μm sections (Microtome, Leica). Paraffin-embedded sections were stained with hematoxylin and eosin (H&E) or hematoxylin only for CD3 immunostaining (performed by HistoWiz, Inc.). After euthanasia, mouse lungs were perfused via the trachea with 4% paraformaldehyde, and each of 5 lobes was separated after fixation and embedded in paraffin. Liver tissue was harvested and processed identically for histology. Histological analysis was performed by an experienced pathologist.

*Statistics*.

One-way ANOVA and unpaired, 2-tailed Student's *t* test were performed using Prism 7 (GraphPad) on data indicated. A *P* value less than 0.05 was considered significant.

*Study approval*.

The protocol for blood draw from healthy volunteers is approved by the Institutional Review Board of Weill Cornell Medicine (permit number: 1302013613). All animal experiments were performed in strict accordance with the recommendations contained within the National Institute of Health's Guide for the Care and Use of Laboratory Animals and animal handling protocols were approved by the Institutional Laboratory Animal Use and Care Committee of Weill Cornell Medicine (permit number: 2012-0063).

**Results**

*Expression and characterization of SSTR2 in Jurkat T cells*.

We constructed a lentivirus vector for expression of SSTR2 by inserting the human SSTR2 gene downstream of the elongation factor-1α promoter [35]. With increasing lentivirus titer, 100% of Jurkat T cells were transduced to express SSTR2 as measured by antibody binding (Figure 3.1A). Consistent with agonist-induced internalization of SSTR2 [36], incubation of T cells with the synthetic SSTR2 agonist

octreotide reduced surface expression of SSTR2, as indicated by reduced antibody binding (Figure 3.1B). Labeling of SSTR2-transduced Jurkat T cells with $^{68}$Ga-DOTATOC (hereafter referred to as DOTATOC) at concentrations ranging from 8 nM to 250 nM followed a first-order Langmuir isotherm equation, giving a dissociation constant (Kd) of 38 nM (Figure 3.1C). In comparison, DOTATOC uptake by nontransduced T cells was approximately 10-fold lower. Similar to the Kd estimated by Langmuir isotherm, Scatchard analysis estimated the Kd of DOTATOC to be 32 nM and the site density of SSTR2 to be approximately $3.2 \times 10^6$ molecules per cell (Figure 3.1D). Actual site density is likely to be lower due to recycling of SSTR2 after internalization of DOTATOC and some level of nonspecific binding. Incubation of cells at 4°C to inhibit SSTR2 recycling resulted in an estimated site density of $1.8 \times 10^6$ molecules per cell; however, the affinity of DOTATOC for SSTR2 was also determined to be substantially lower (Kd = 170 nM) at this temperature (Figure 3.1D).

*PET imaging of DOTATOC uptake in SSTR2$^+$ T cell xenografts*.

To examine the utility of SSTR2 for the detection of sparsely distributed T cells in tumors, we produced subcutaneous Jurkat T cell xenografts in mice with a mixture of SSTR2-transduced (referred to as SSTR2$^+$) and nontransduced (wild-type) cells. These were titrated against each other immediately prior to xenografting to vary the levels of SSTR2- expressing cells within tumors from 0% to approximately 100%. Xenografted Jurkat T cell tumors began to show palpable growth at ~30 days after xenograft and exhibited continuous growth for the next 25 days, reaching

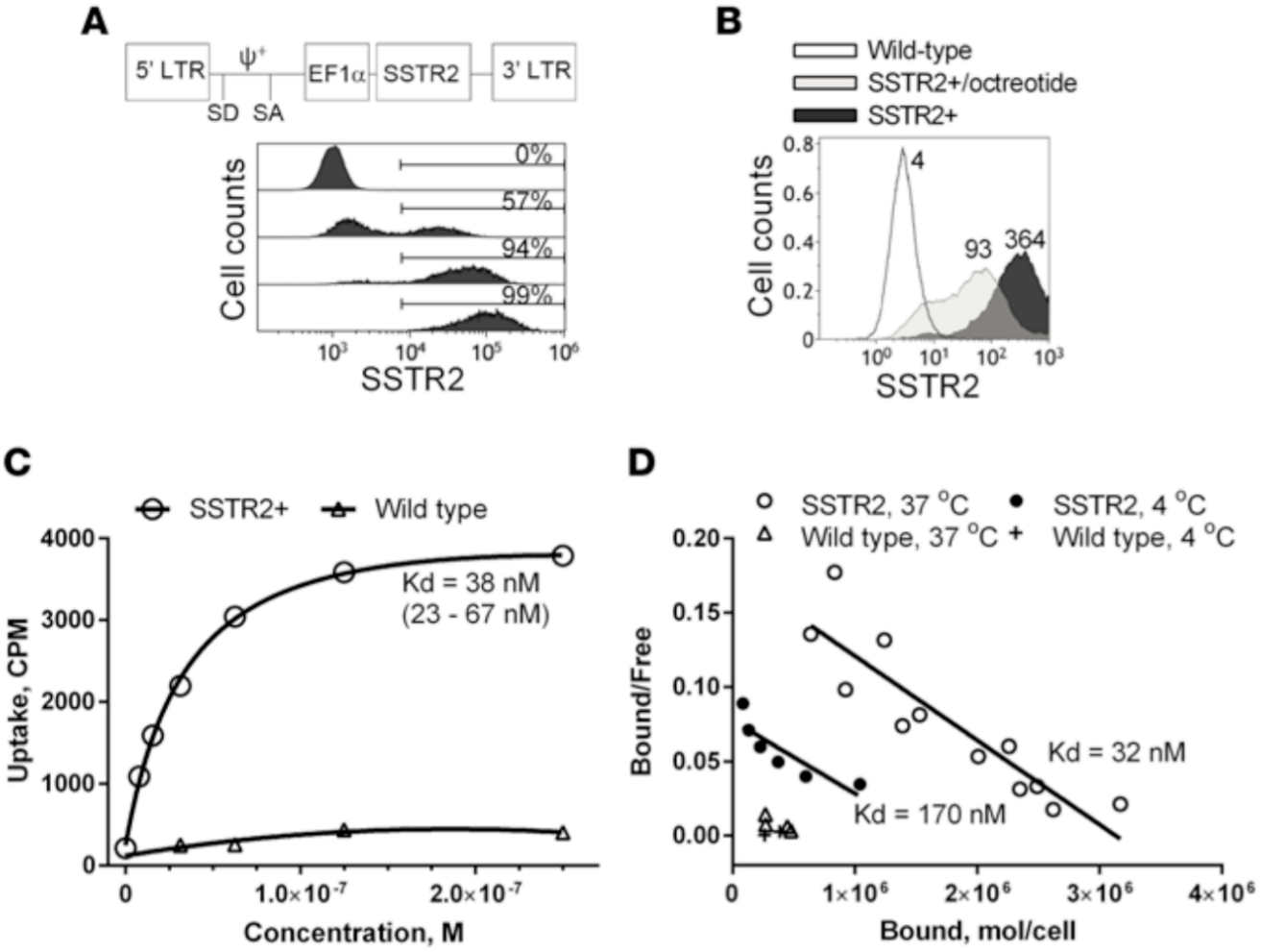
A
5' LTR
ψ+
SD
SA
EF1α
SSTR2
3' LTR
Cell counts
0%
57%
94%
99%
SSTR2
B
Wild-type
SSTR2+/octreotide
SSTR2+
Cell counts
4
93
364
SSTR2
C
SSTR2+
Wild type
Kd = 38 nM
(23 - 67 nM)
Uptake, CPM
Concentration, M
D
SSTR2, 37 °C
SSTR2, 4 °C
Wild type, 37 °C
Wild type, 4 °C
Kd = 32 nM
Kd = 170 nM
Bound/Free
Bound, mol/cell

**Figure 3.1 Expression of human SSTR2 by lentivirus vector in T cells.**

(**A**) A schematic of the lentivirus vector encoding human SSTR2 is shown. LTR, long terminal repeat; SD, splice donor; SA, splice acceptor; EF1α, elongation factor 1α promoter; $\psi^+$, encapsidation signal. Histograms show the level of SSTR2-speci c antibody binding to wild-type Jurkat T cells (0%, top) and Jurkat T cells transduced with increasing virus titers. Percentages of SSTR2- positive cells are indicated. (**B**) Level of SSTR2- specific antibody binding to SSTR2-transduced Jurkat T cells with and without preincubation with 1 μM octreotide (37°C, 30 minutes). The numbers denote mean fluorescence intensity. (**C**) DOTATOC uptake by SSTR2-transduced and wild-type Jurkat T cells versus input DOTATOC concentration is shown. A first-order Langmuir isotherm equation was used to t the data and to nd the equilibrium dissociation constant (Kd). Confidence interval of Kd is shown in parentheses. (**D**) DOTATOC uptake at 37°C and 4°C by SSTR2-transduced and wild-type Jurkat T cells is shown via Scatchard plot. Predicted Kd is shown. Data shown are from 3 independent experiments. CPM, counts per minute.

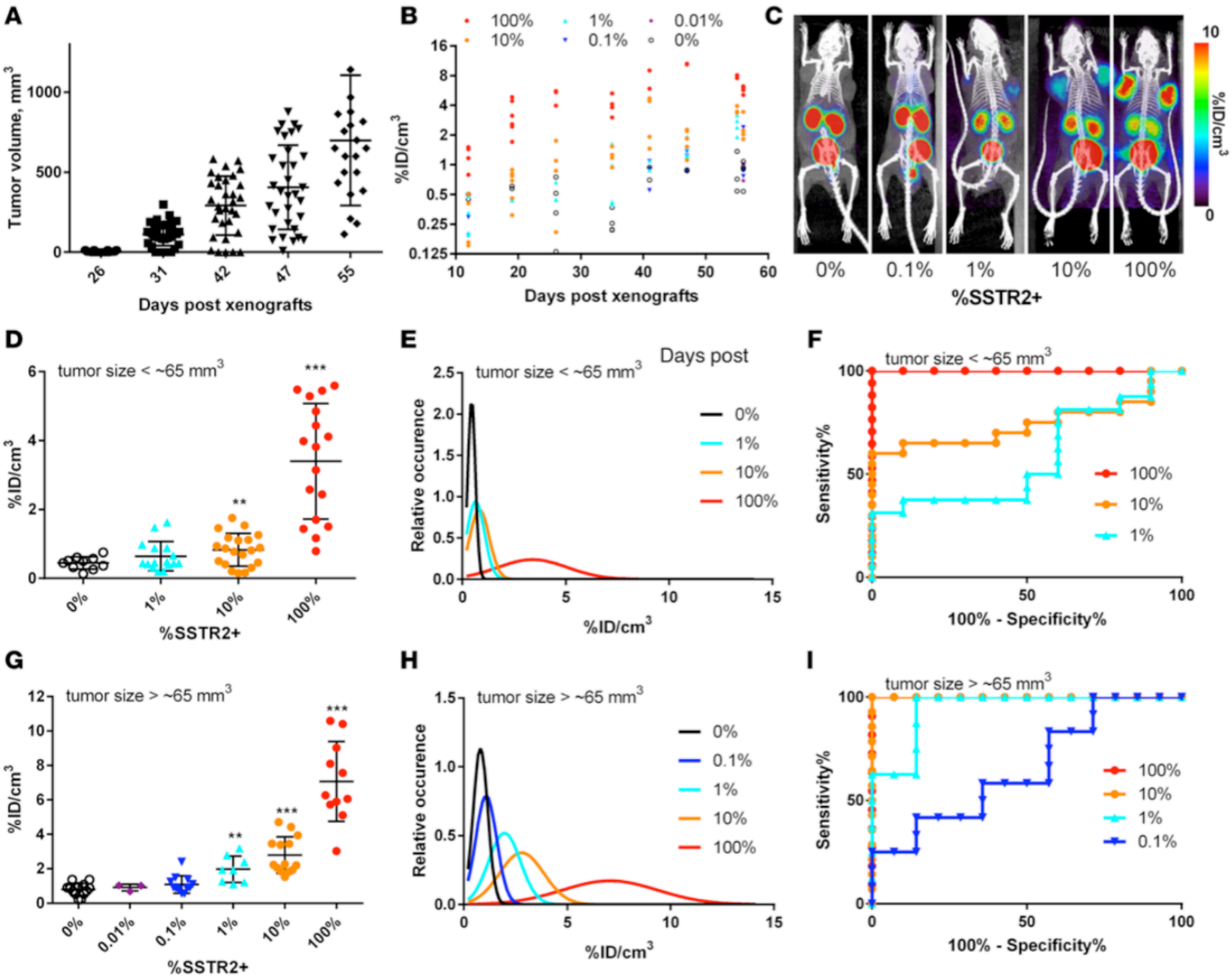
A
Tumor volume, mm3
1000
500
0
26
31
42
47
55
Days post xenografts
B
100%
10%
1%
0.1%
0.01%
0%
%ID/cm3
16
8
4
2
1
0.5
0.25
0.125
10
20
30
40
50
60
Days post xenografts
C
10
%ID/cm3
0
0%
0.1%
1%
10%
100%
%SSTR2+
D
tumor size < ~65 mm3
%ID/cm3
6
4
2
0
***
**
0%
1%
10%
100%
%SSTR2+
E
tumor size < ~65 mm3
Days post
Relative occurence
2.5
2.0
1.5
1.0
0.5
0.0
0%
1%
10%
100%
0
5
10
15
%ID/cm3
F
tumor size < ~65 mm3
Sensitivity%
100
50
0
100%
10%
1%
0
50
100
100% - Specificity%
G
tumor size > ~65 mm3
%ID/cm3
12
10
8
6
4
2
0
***
**
***
0%
0.01%
0.1%
1%
10%
100%
%SSTR2+
H
tumor size > ~65 mm3
Relative occurence
1.5
1.0
0.5
0.0
0%
0.1%
1%
10%
100%
0
5
10
15
%ID/cm3
I
tumor size > ~65 mm3
Sensitivity%
100
50
0
100%
10%
1%
0.1%
0
50
100
100% - Specificity%

**Figure 3.2 Quantitative PET/CT measurement of DOTATOC uptake by Jurkat tumors and statistical analysis.** (**A**) Tumor volume ($mm^3$) plotted against number of days after xenograft. (**B**) Measured DOTATOC uptake is quantified as percentage injection dose per volume (%ID/$cm^3$) for Jurkat tumors (100%–0% $SSTR2^+$) over the course of tumor growth. (**C**) Representative PET/CT images of mice xenografted with Jurkat T cells at 0%, 0.1%, 1%, 10%, and 100% SSTR2 expression. Images are maximum intensity projections (MIPs) of the entire mouse body (~20-mm-thick plane). PET intensity is pseudocolored in the range of 0–10 %ID/$cm^3$. (**D** and **G**) DOTATOC uptake (%ID/$cm^3$) for Jurkat tumors less or greater than 65 $mm^3$, respectively. (**E** and **H**) Simulated Gaussian distribution as a function of the measured mean and standard deviation of DOTATOC uptake for each percentage $SSTR2^+$ tumor when the volume is less or greater than 65 $mm^3$, respectively. (**F** and **I**) Receiver operating characteristic (ROC) curves of percentage sensitivity and specificity are shown for tumors less than 65 $mm^3$ (**D**) and greater than 65 $mm^3$ (**G**). ** $P < 0.01$ vs. 0%, *** $P < 0.001$ vs. 0%, by Student's *t* test.

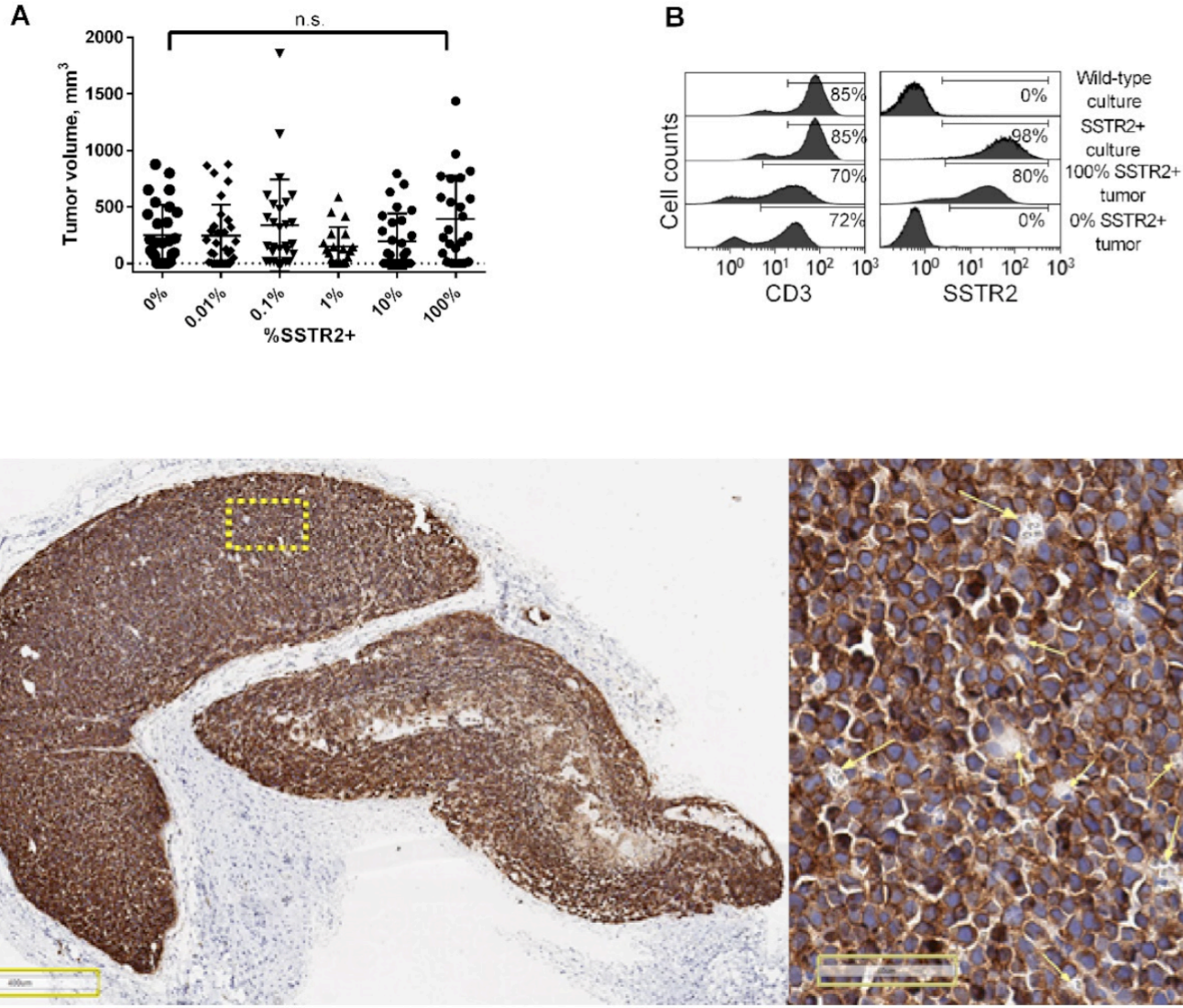
A
n.s.
Tumor volume, mm3
2000
1500
1000
500
0
0%
0.01%
0.1%
1%
10%
100%
%SSTR2+
B
Cell counts
85%
85%
70%
72%
0%
98%
80%
0%
Wild-type culture
SSTR2+ culture
100% SSTR2+ tumor
0% SSTR2+ tumor
CD3
SSTR2
C

**Figure 3.3 Growth *in vivo* of mosaic Jurkat tumors.**

(**A**) Comparison of tumor volume across multiple xenografted Jurkat tumors containing a range of SSTR2+ ratios. No significance (n.s.) by one-way ANOVA was found among SSTR2+ groups. (**B**) CD3- and SSTR2-specific antibody binding to SSTR2+ and wild-type Jurkat T cells in culture and to the same cells harvested from tumors is shown in histograms. Percentages of CD3 and SSTR2 positive cells are indicated. (**C**) Paraffin embedded, hematoxylin stained section of Jurkat tumor was stained with anti-human CD3 antibody to visualize distribution of Jurkat T cells and stroma cells. Shown on the right is a high magnification view of the dotted yellow box in left image. Stroma containing blood vessels are identified by yellow arrows. Scale bar = 400 μm on left image and 60 μm on right.

approximately 0.7 $cm^3$ (Figure 3.2A). Longitudinal measurement of tumor size across different $SSTR2^+$ tumors revealed that the level of SSTR2 expression had no significant effect on the growth of Jurkat T cell tumors (Figure 3.3A; supplemental material available online with this article; doi:10.1172/jci.insight.90064DS1). We tested our ability to detect $SSTR2^+$ T cells within tumors when both their tumor density and absolute numbers ranged from low to high in both respects. Thus, to cover this range, we initiated PET/CT imaging 12 days after xenograft of 0% to 100% $SSTR2^+$ tumors, that is, before we could detect palpable tumor growth, and continued imaging until 56 days after xenograft (Figure 3.2B). The level of DOTATOC uptake by tumors was quantified as percentage injection dose per volume (%ID/$cm^3$) based on the region of interest (ROI) enclosing tumors. The ROIs were defined by tumor-size measurements and anatomical information from CT images. Over the course of tumor growth, DOTATOC uptake was higher in tumors comprising increasing percentages of $SSTR2^+$ cells (Figure 3.2B). PET/CT images showed DOTATOC uptake by tumors and uniformly higher uptake by the kidneys and bladder — consistent with its known biodistribution and renal clearance (Figure 3.2C) [19]. DOTATOC uptake values, as measured by %ID/$cm^3$, agreed with visual assessments of PET/CT images over the course of tumor growth and correlated with increasing $SSTR2^+$ percentages within the tumors (Figure 3.2, B and C, and Figure 3.4). We also noted a minor increase in DOTATOC uptake during growth of 0% $SSTR2^+$ tumors, which we speculate to be caused by the increasing leaky vasculature and stagnant blood pooling within tumors (Figure 3.2B).

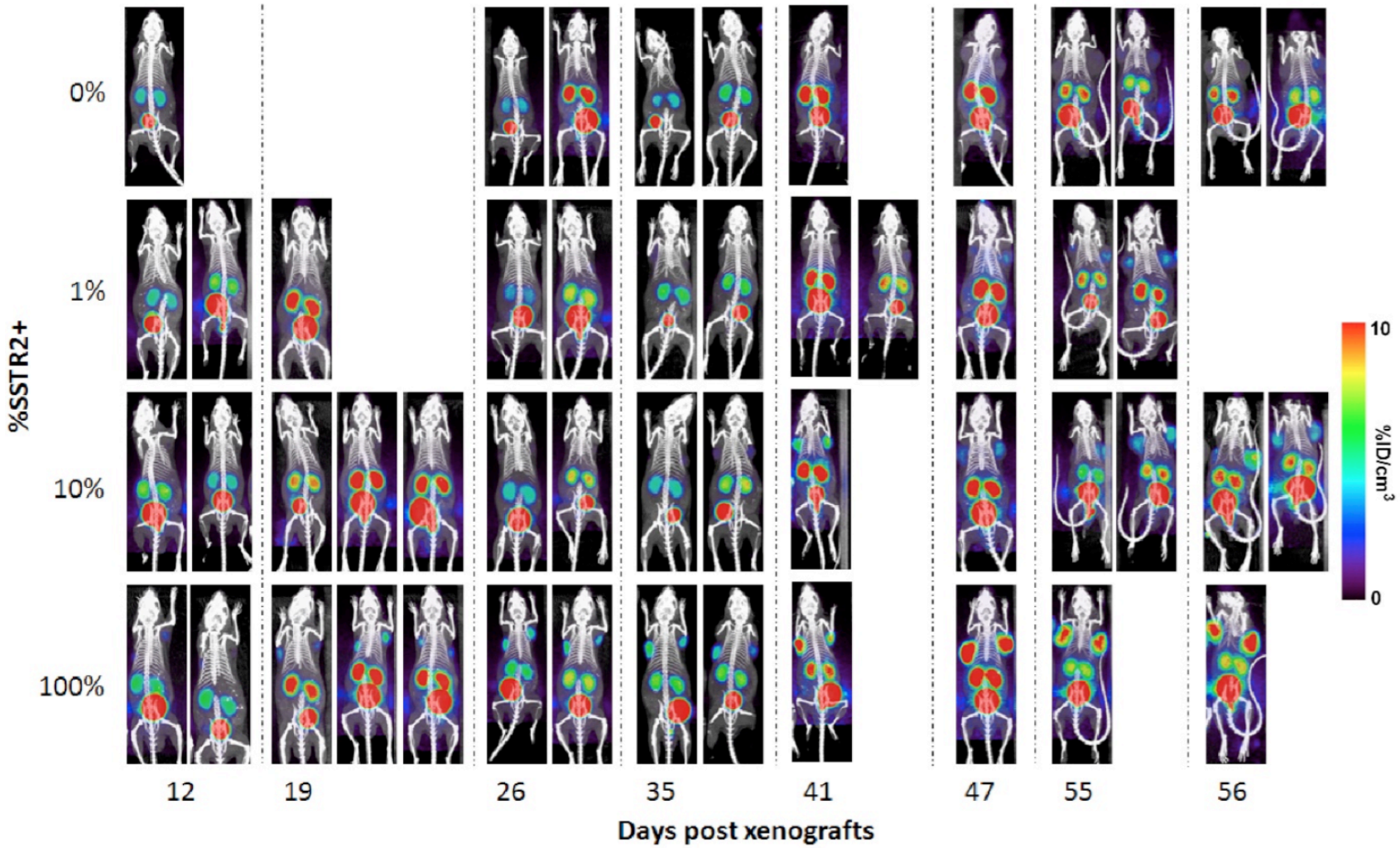


**Figure 3.4 PET/CT images of DOTATOC distribution by Jurkat mosaic tumors.** PET/CT images from NSG mice xenografted with Jurkat T cells containing varying ratios of SSTR2 transduced cells. Mice were injected intravenously with DOTATOC and imaged on average once per week beginning on day 12 post xenograft and continuing until day 56.

*Defining detection limit, specificity, and sensitivity of SSTR2$^+$ T cells*.

We next analyzed DOTATOC uptake values to determine the detection sensitivity and specificity of SSTR2-expressing T cell density within tumors. Regarding small, palpable tumors (below ~65 mm$^3$), DOTATOC uptake was slightly higher in those containing 1% SSTR2$^+$ cells (0.64 ± 0.4 %ID/cm$^3$; $P$ = 0.1 vs. 0% SSTR2$^+$), but was significantly higher in tumors containing SSTR2$^+$ T cell densities of 10% (0.83 ± 0.5 %ID/cm$^3$) and 100% (3.4 ± 1.7 %ID/cm$^3$), compared with uptake within 0% SSTR2$^+$ tumors (0.44 ± 0.2 %ID/cm$^3$) (Figure 3.2D). Assuming a normal distribution of DOTATOC uptake values (Figure 3.2E), a threshold of 0.6 %ID/cm$^3$ was the DOTATOC uptake cutoff in order to obtain 95% specificity (5% false positive rate) for tumors of this size. The detection sensitivity (% true positive rates) for 1%, 10%, and 100% SSTR2$^+$ tumors with the 0.6 %ID/cm$^3$ threshold was calculated to be 54%, 69%, and 95%, respectively. The detection limit for 10% SSTR2$^+$ tumors below ~65 mm$^3$ was considered marginally acceptable with an area under the receiver operating characteristic (ROC) curve (AUC) [37] value of 0.75 (Figure 3.2F). In contrast, DOTATOC uptake for more discernible SSTR2$^+$ tumors (larger than 65 mm$^3$) was significantly higher within 100%, 10%, and 1% SSTR2$^+$ tumors (7.1 ± 2.3, 2.8 ± 1.1, and 2.0 ± 0.77 %ID/cm$^3$, respectively) when compared with background uptake by 0% SSTR2$^+$ tumors (0.8 ± 0.35 %ID/cm$^3$) (Figure 3.2G). Uptake was also detectable, although not significant, even within 0.1% SSTR2$^+$ tumors (1.1 ± 0.51

%ID/cm$^3$, $P = 0.12$). A DOTATOC uptake cutoff of 1.1 %ID/cm$^3$ gave 95% specificity and 87% sensitivity for 1% SSTR2$^+$ tumors within the Jurkat model (Figure 3.2H). With the same threshold, one achieves greater than 95% sensitivity for tumors in which the SSTR2$^+$ T cell density is at or above 10%. The ROC curve of DOTATOC uptake by 1% SSTR2$^+$ tumors gives 0.95 AUC, while 0.1% SSTR2$^+$ tumors gives 0.68 AUC (Figure 3.2I). SSTR2$^+$ T cells in culture were ~100% SSTR2$^+$ by antibody staining (Figure 3.3B). However, later resection of 100% SSTR2$^+$ tumors followed by staining for SSTR2 by flow cytometry revealed that the level of SSTR2 expression was reduced to ~80%, with the 20% reduction reflecting the presence of mouse stromal cells within tumors (Figure 3.3, B and C). The reduction of SSTR2 expression was not caused by the loss of SSTR2 expression during tumor growth, as a similar level of reduction was seen by CD3 staining: 70% CD3$^+$ in cells harvested from tumors, reduced from 80%–85% CD3$^+$ from the same cells in culture.

To express the observed SSTR2$^+$ T cell tumor density as an absolute number per volume, we resected Jurkat tumors and determined the average total cell density to be $5.1 \pm 1.3 \times 10^8$/cm$^3$ ($n = 4$). Accordingly, 1% SSTR2$^+$ tumors (comprising approximately $4 \times 10^8$/cm$^3$ Jurkat T cells and $1 \times 10^8$/cm$^3$ stroma) would contain ~$4 \times 10^6$ SSTR2$^+$ T cells per cm$^3$. Based on the data obtained using the Jurkat model, we proceeded to utilize SSTR2-based PET imaging to estimate and longitudinally monitor the density of reporter- expressing CAR T cells infiltrating solid tumors.

*Efficacy of ICAM-1–specific CAR T cells against thyroid tumor cells*.

Radioiodine-resistant, poorly differentiated thyroid cancers have been found to overexpress ICAM-1 at levels correlating with tumor malignancy and metastatic potential [30]. The anaplastic thyroid cancer cell line 8505C was also found to be ICAM-1 positive (Figure 3.5A), the level of which varied due to culture conditions and growth in vivo. The anti–ICAM-1 CAR is third generation and consists of an ICAM-1–specific single-chain variable fragment (scFv) from the R6.5 antibody [38], the transmembrane and cytoplasmic domains of CD28, followed by CD137 and CD3ζ [35]. A lentiviral vector encoding both SSTR2 and R6.5-CAR was constructed by linking SSTR2 to the R6.5-CAR with a ribosome-skipping porcine teschovirus-1 2A (P2A) sequence [39] (Figure 3.5B). Primary T cells were transduced to express SSTR2 and R6.5-CAR at approximately 50% (Figure 3.5B). Expression levels of both SSTR2 and R6.5-CAR obtained via the single SSTR2-R6.5-CAR (SR) vector were comparable to what could be attained by separate SSTR2 (SS) and R6.5-CAR (RR) vectors at similar virus titers (Figure 3.5, B and C). To test the selectivity of CAR T cell–mediated killing of 8505C cells, we also used the cervical cancer cell line, HeLa, exhibiting high basal levels of ICAM- 1, and the ICAM-1–negative cell line, HEK 293, as positive and negative controls, respectively (Figure 3.5A). All target cells were lentivirally transduced to express GFP and re y luciferase in order to quantitatively monitor cell viability. Incubation of CAR T cells with ICAM-1–positive and –negative cell lines showed that CAR T cell killing of target was strictly dependent upon ICAM-1 expression. After 24 hours, 17% ± 11% of HeLa and 52% ± 15% of 8505C cells were viable at effector to target (E:T) ratios of 2.5:1, with no killing of HEK 293 cells

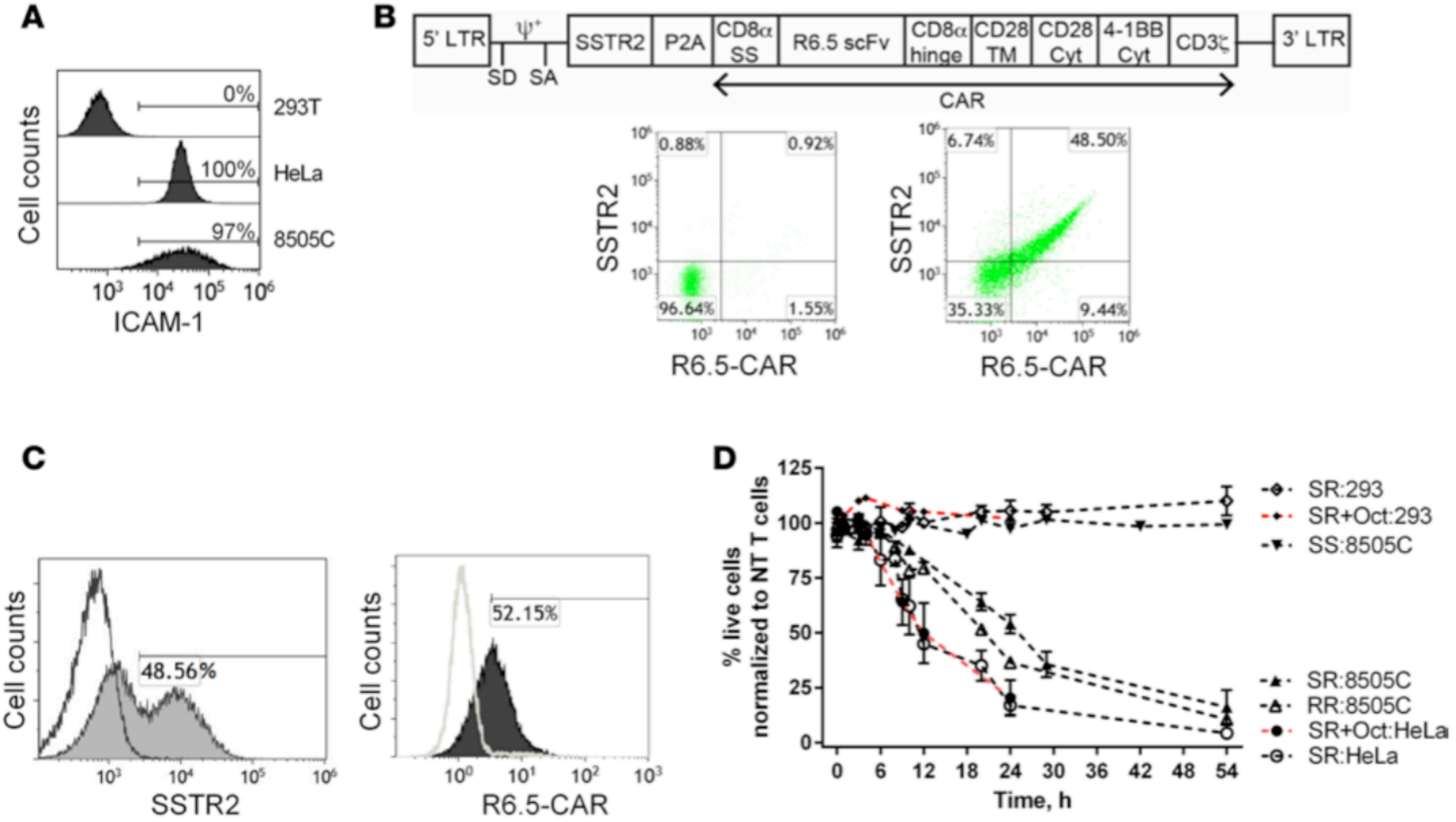
A
Cell counts
0%
293T
100%
HeLa
97%
8505C
ICAM-1
B
5' LTR
ψ+
SD
SA
SSTR2
P2A
CD8α SS
R6.5 scFv
CD8α hinge
CD28 TM
CD28 Cyt
4-1BB Cyt
CD3ζ
3' LTR
CAR
SSTR2
0.88%
0.92%
96.64%
1.55%
R6.5-CAR
6.74%
48.50%
35.33%
9.44%
C
Cell counts
48.56%
SSTR2
52.15%
R6.5-CAR
D
% live cells normalized to NT T cells
Time, h
SR:293
SR+Oct:293
SS:8505C
SR:8505C
RR:8505C
SR+Oct:HeLa
SR:HeLa

**Figure 3.5 CAR T cell efficacy against thyroid tumor cells in vitro and in vivo.** (**A**) Representative histograms showing the level of anti–ICAM-1 antibody binding to ICAM-1–negative HEK 293T, ICAM-1–positive HeLa, and 8505C cells. (**B**) Schematic of the lentivirus vector encoding SSTR2-R6.5-CAR. CD8α SS (signal sequence); TM, transmembrane; Cyt, cytoplasmic domain. Representative dot plots showing anti-SSTR2 and anti-CAR antibody binding to nontransduced (left) and SSTR2-P2A-R6.5-CAR–transduced (right) primary human T cells. (**C**) Primary human T cells were transduced separately with individual vectors encoding either SSTR2 or R6.5-CAR. Representative histograms show anti-SSTR2 antibody binding to either R6.5-CAR– or SSTR2- transduced ( lled) and nontransduced (open) primary T cells. (**D**) E ector/target (E:T) assay measuring lysis of target expressing (HeLa and 8505C) or control (HEK 293) cells by CAR T cells at a 2.5:1 E:T ratio. Percentages of live cells were measured by bioluminescence intensity normalized to the levels of target cells incubated with nontransduced T cells. Octreotide (1 μM) was added to SR T cells as indicated (SR+Oct). *n* = 3–6 from 3 different donor T cells. NT, nontransduced T cells; SS, SSTR2-transduced T cells; RR, R6.5-CAR–transduced T cells; SR, SSTR2-R6.5-CAR–transduced T cells.

observed (106% ± 8%) (Figure 3.5D). Additionally, no killing of 8505C cells (97% ± 2%) was observed upon coincubation with SS T cells. The rate of kill- ing of 8505C cells by RR and SR T cells, and that of HeLa by SR T cells with or without the addition of octreotide (1 μM) was comparable. This confirmed that SSTR2 expression on T cells, as well as binding of its cognate ligand (DOTATOC), does not alter CAR T cell functionality.

*Longitudinal PET imaging of SSTR2$^+$ CAR T cells in vivo*.

In order to test the ability of an SSTR2-based reporter system to acquire in vivo visual mapping of CAR T cell localization and antitumor dynamics, NSG mice were first xenografted by systemic injection of $1 \times 10^6$ 8505C-FLuc$^+$GFP$^+$ cells. Bioluminescence imaging demonstrated that primary 8505C tumors localized to the lungs, with metastases occurring within the liver and at more distant sites (Figure 3.6A), consistent with previously reported observations of 8505C tumor growth characteristics in mice [40]. Using bioluminescence as a measure of tumor burden, it was observed that an initial infusion of $1 \times 10^6$ tumor cells expanded 50- to 100-fold over 21 days (Figure 3.6A). Tumor growth was not hampered by treatment with SS T cells 10–13 days after tumor xenograft (SS1–5, as defined in Figure 3.7), confirming the absence of nonspecific killing by non-CAR T cells in vivo. Prior to conducting DOTATOC imaging of SR T cells, we first examined the circumstances that give rise to nonspecific DOTATOC uptake, which may include leaky tumor vessels within areas of high tumor burden causing blood pooling. First, CT images of mice with no tumors that were infused with SS T cells showed the heart and tumor-free alveolar air

space in the lungs (Figure 3.6B). The level of DOTATOC uptake in these mice (0.7 %ID/cm$^3$) was comparable to those in Jurkat tumors containing 0% SSTR2$^+$ cells (0.6–0.8 %ID/cm$^3$) and is thus indicative of the absence of CAR T cell expansion. In comparison, mice xenografted with 8505C tumors had alveolar air space replaced by the growth of tumor cells (accounting for as much as 22% of total live cells in lungs), which generated increased alveolar tissue density in transverse CT images of these mice (Figure 3.6C). We observed low yet gradually increasing nonspecific DOTATOC uptake in the thoracic cavity of mice with high tumor burden (1.3 ± 0.5 %ID/cm$^3$ for 23 to 27 days after tumor xenograft) that received either no T cells or SS T cells. This was found to be due to subjects' poor health and slower heartbeat, causing a longer circulation time and a delay in DOTATOC clearance. Mice treated with RR T cells (RR1–3, Figure 3.7) were also found to show only background levels of DOTATOC uptake in the lungs (1.0 %ID/cm$^3$) (Figure 3.6D). This was despite the fact that over the course of tumor killing, RR T cells had expanded such that they accounted for 36% of total live cells in lungs.

After confirming the relative absence of lung-specific DOTATOC uptake related to tumor burden itself or SSTR2-negative T cell expansion, we then treated tumor-bearing mice with SR T cells at days 7, 10, 13, and 15 after xenograft. Mice were subjected to longitudinal bioluminescence and concurrent PET/CT imaging to visualize the relationship between tumor burden and the dynamism of infused SR T cells over the course of their localization, tumor engagement, and killing (Figure 3.7, and Figure 3.8, A and E). Progressive delays in T cell infusion after tumor xenograft

were used in order to observe potential differences in CAR T cell dynamics related to differences in tumor burden. Primary tumor burden in the lungs from mice treated with SR T cells 7 and 10 days after xenograft (SR1–4) began noticeably decreasing at approximately 16 days after tumor xenograft with little change in body weight (Figure 3.8, A–C). Increasing tumor burden over time correlated with increasing DOTATOC uptake within the lungs, indicating that infused SR T cells had stably localized to the tumor site where they were actively proliferating in response to engagement with ICAM-1–positive tumor cells (Figure 3.8A). It was also found that peak DOTATOC uptake, and therefore peak CAR T cell expansion, lagged behind peak tumor bioluminescence by approximately 4 days. Peak DOTATOC uptake within the lungs was followed by gradual curtailment and contraction corresponding to diminishing T cell numbers, thus demonstrating a biphasic antitumor CAR T cell response, incorporating classical antigen-mediated T cell expansion followed by T cell contraction upon antigen withdrawal (Supplemental Video 1 and Figure 3.8A). In contrast with the swift tumor elimination, followed by CAR T cell contraction within the lungs of surviving mice, further delay of treatment with SR T cells to 13 to 15 days after tumor xenograft (SR5–9) failed to reduce tumor burden and restore health before euthanasia was invoked (deemed necessary after a 25%–30% loss in body weight) (Figure 3.8, E–G). This was despite increasing lung-specific DOTATOC uptake confirming SR T cell expansion in the lungs of these mice (Supplemental Video 2 and Figure 3.8E). Longitudinal transverse CT images revealed that while tissue density in lungs associated with tumor and CAR T cell burden persisted in nonsurvivors, it was

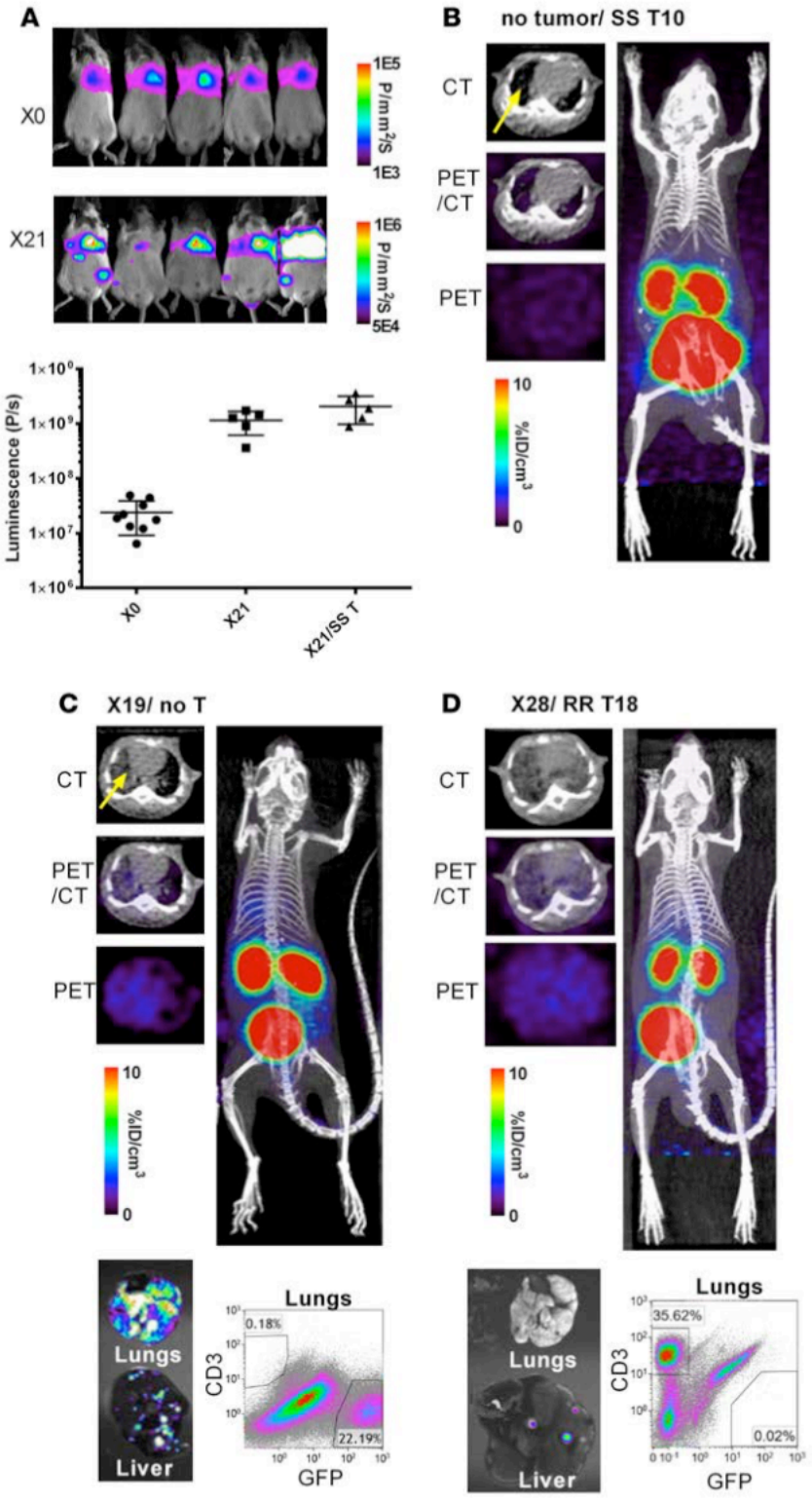
A
X0
X21
1E5
P/mm²/S
1E3
1E6
P/mm²/S
5E4
Luminescence (P/s)
X0
X21
X21/SS T
B
no tumor/ SS T10
CT
PET /CT
PET
10
%ID/cm³
0
C
X19/ no T
CT
PET /CT
PET
10
%ID/cm³
0
Lungs
Liver
Lungs
CD3
GFP
0.18%
22.19%
D
X28/ RR T18
CT
PET /CT
PET
10
%ID/cm³
0
Lungs
Liver
Lungs
CD3
GFP
35.62%
0.02%

**Figure 3.6 Whole-body imaging of tumor growth by luminescence and DOTATOC uptake by PET/CT.** (**A**) Tumor burden from day of intravenous tumor xenograft via tail vein (X0) and 21 days after (X21) was visualized and quanti ed by bioluminescence. (**B**–**D**) Transverse CT-only, PET-only, and PET/ CT superimposed images are shown alongside a coronal view of the entire mouse body. PET images are drawn in indicated ranges. Ex vivo uorescence images of lungs and liver are shown together with ow cytometry analysis of the $CD3^+$ (T cell) and $GFP^+$ (tumor cell) populations of the same lungs are also shown (**C** and **D**). Each PET/CT image is representative of at least 3 independent experiments. SS, SSTR2- transduced T cells; RR, R6.5-CAR–transduced T cells; no T, no T cell treatment.

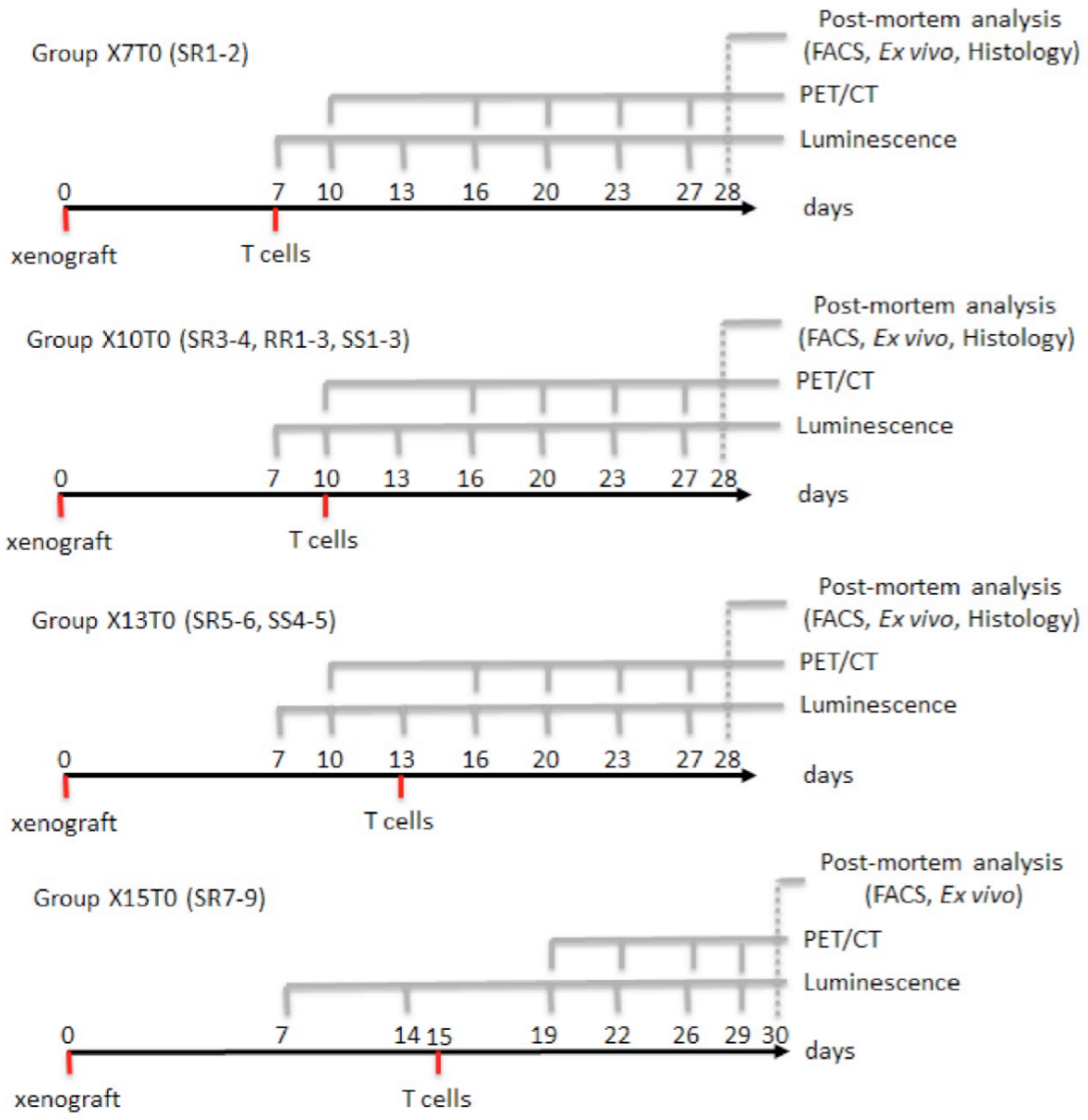


**Figure 3.7 Schematic of the longitudinal CAR T cell imaging experiment.** Mice are divided into four groups according to the day of T cell treatment post tumor xenograft. SR = SSTR2-R6.5-CAR T cells; SS = SSTR2, non-CAR T cells; and RR = non-SSTR2, R6.5- CAR T cells. Days of xenograft, T cell injection, imaging and post-mortem analysis are indicated.

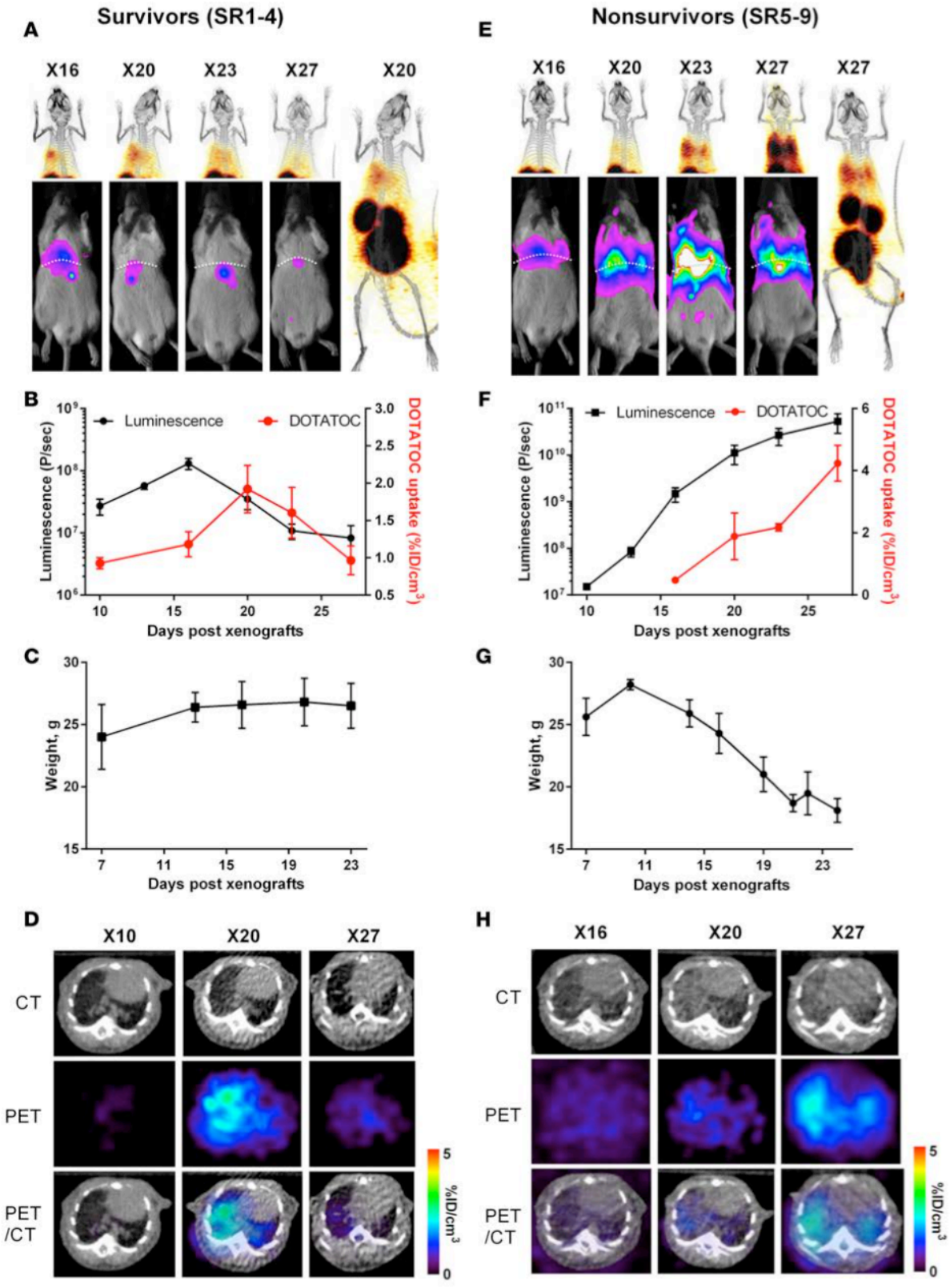
A
Survivors (SR1-4)
X16
X20
X23
X27
X20
E
Nonsurvivors (SR5-9)
X16
X20
X23
X27
X27
B
Luminescence
DOTATOC
Luminescence (P/sec)
DOTATOC uptake (%ID/cm3)
Days post xenografts
F
Luminescence
DOTATOC
Luminescence (P/sec)
DOTATOC uptake (%ID/cm3)
Days post xenografts
C
Weight, g
Days post xenografts
G
Weight, g
Days post xenografts
D
X10
X20
X27
CT
PET
PET /CT
%ID/cm3
H
X16
X20
X27
CT
PET
PET /CT
%ID/cm3

**Figure 3.8 Quantitative PET for detection of CAR T cells and luminescence of tumor burden in survivors vs. nonsurvivors.** Representative longitudinal, PET/CT (coronal view of 20-mm-thick plane, maximum intensity projection [MIP]) and concurrent bioluminescence imaging of survivors ($n$ = 4) (**A**) vs. nonsurvivors ($n$ = 5) (**E**). Diaphragms are traced with dotted lines, drawn to visualize tumor burdens separately in lungs and liver. Trend-line graphs plot region of interest (ROI) values for DOTATOC uptake (percentage injection dose per volume [%ID/$cm^3$]) against bioluminescence values (photons [P]/sec) in the lungs taken from the same mice on the same day. Luminescence images are drawn with the same upper bound ($10^6$ P/$mm^2$/sec) with gradually increasing lower bounds (X16, X20 for $2.5 \times 10^4$ P/$mm^2$/sec and X23, X27 for $5 \times 10^4$ P/$mm^2$/sec) for clarity of delineating tumor burden. Longitudinal PET/ CT images of the upper body cropped at the kidney apex are drawn with a uniform range of DOTATOC concentrations (0.5–5.0 %ID/$cm^3$), while whole-body PET/CT images are drawn in 0.5–5.0 %ID/$cm^3$ for (**A**) and 1–10 %ID/$cm^3$ for (**E**). Quanti cation of luminescence and DOTATOC uptake by the lungs (**B** and **F**) and body weight change (**C** and **G**) is shown for survivors and nonsurvivors. Representative longitudinal, PET/CT (transverse view of 1-mm-thick plane, MIP) views of lungs are shown for survivors (**D**) and nonsurvivors (**H**). PET images are drawn in indicated ranges. X, number of days after tumor xenograft; SR, treated with SSTR2-R6.5-CAR–transduced T cells.

*Confirmation of PET and bioluminescence imaging by ex vivo analysis*.

Assessment of CAR T cell–mediated tumor killing by ex vivo fluorescence imaging of the lungs and liver (performed on day 28 after tumor xenograft) confirmed that tumor elimination had indeed occurred in survivors treated with SR T cells on days 7–10 after tumor xenograft (Figure 3.9A). Flow cytometry analysis of lungs that were determined to have undergone CAR T cell contraction by DOTATOC uptake showed that $CD3^+$ cell levels were reduced to less than 1% of total lung cells (Figure 3.9A). It also confirmed continuing expansion of SR T cells and substantial reduction of tumor burden in nonsurviving mice treated on days 13–15 after tumor xenograft (2.5%), compared with mice that received no T cells (22%) (Figure 3.9B vs. Figure 3.6C). Furthermore, plotting the percentage of human $CD3^+$ cells in the lungs of SR-treated mice against DOTATOC uptake from same, demonstrated that CD3 staining by ow cytometry was largely proportional to DOTATOC signal obtained by PET (Figure 3.9C). The observation that DOTATOC uptake values greater than 3 corresponded to greater than 10% $CD3^+$ T cells was in quantitative agreement with the findings from the Jurkat tumor model (Figure 3.5.2, G and H).

Histological analysis of lung tissues further corroborated the conclusions drawn from whole-body PET/bioluminescence imaging, flow cytometry, and ex vivo organ images. Lung tissues from untreated mice (X23/no T cells) revealed extensive infiltration and growth of tumor cells into the alveoli, bronchioles, pulmonary vessels, and pleural spaces compared with their healthy no-tumor counterparts (Figure 3.9D and Figure 3.10). Lung tissues harvested from survivors (SR1–4) were

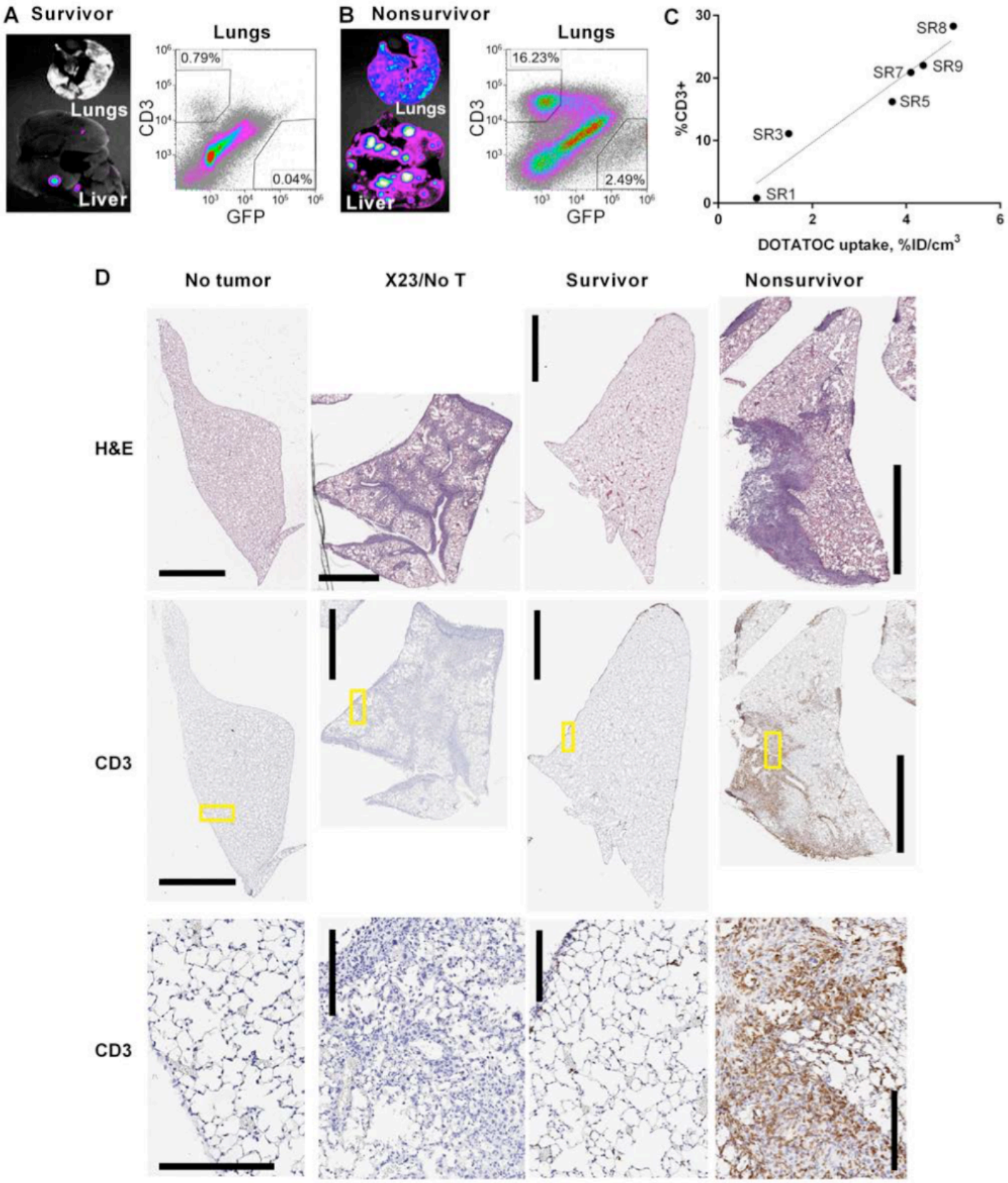
A Survivor
Lungs
Liver
Lungs
CD3
GFP
0.79%
0.04%
B Nonsurvivor
Lungs
Liver
Lungs
CD3
GFP
16.23%
2.49%
C
%CD3+
DOTATOC uptake, %ID/cm3
SR1
SR3
SR5
SR7
SR8
SR9
D
No tumor
X23/No T
Survivor
Nonsurvivor
H&E
CD3
CD3

**Figure 3.9 Ex vivo analysis of CAR T cell and tumor density in lungs.** Ex vivo, $GFP^+$ tumor cell uorescence of representative lungs and liver, and ow cytometry of total, live-gated lung cells from (**A**) survivors ($n = 4$) and (**B**) nonsurvivors ($n = 5$). Organs were harvested, imaged, and analyzed by ow cytometry on day 28 after xenograft (X28). (**C**) DOTATOC uptake (percentage injection dose per volume [%ID/$cm^3$]) by the lungs in SR1–SR9 mice are plotted against the percentages of T cells ($CD3^+$) determined by ow cytometry. (**D**) Representative histological images are shown for para n-embedded H&E-stained sections of 1 entire lung lobe (top), and anti–human CD3 antibody with hematoxylin counterstain (middle). High-magni cation views (yellow boxed regions in middle sections) show tumor cells and CD3-stained T cells (bottom). Tumor cells are identi ed by dark hematoxylin-stained nuclei. Human $CD3^+$ cells are stained brown. Scale bars: 2 mm (top and middle sections) and 200 μm (bottom sections). Lungs were harvested from healthy mice with no tumor, mice 23 days after tumor xenograft and no T cell treatment (X23/no T cell), and X28 for T cell–treated survivors and nonsurvivors.

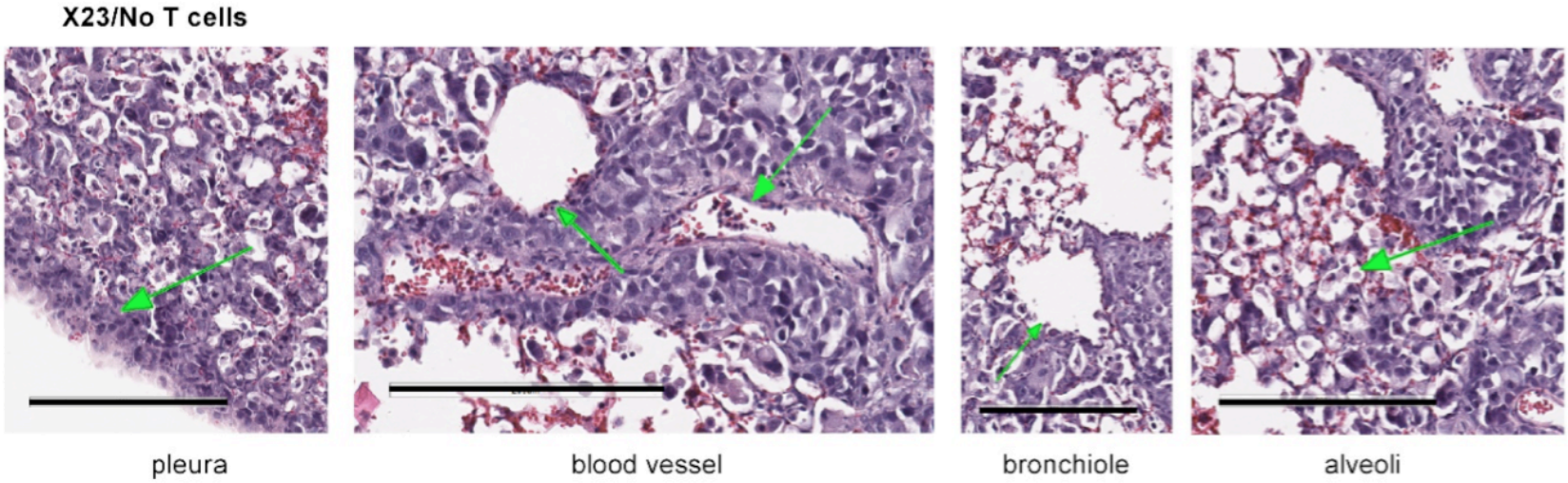




**Figure 3.10 Histology of lungs visualizing tumor growth.** Paraffin embedded H&E stained lung sections of a mouse that did not receive T cell treatment (X23/No T cells; Figure 3.9D) are shown with higher magnification to identify (green arrows) tumor growth in pleural, blood vessels, bronchioles, and alveolar spaces. Tumor cells are identified by diffuse hematoxylin staining, large nuclei with dark nucleoli. Scale bar = 200 μm.

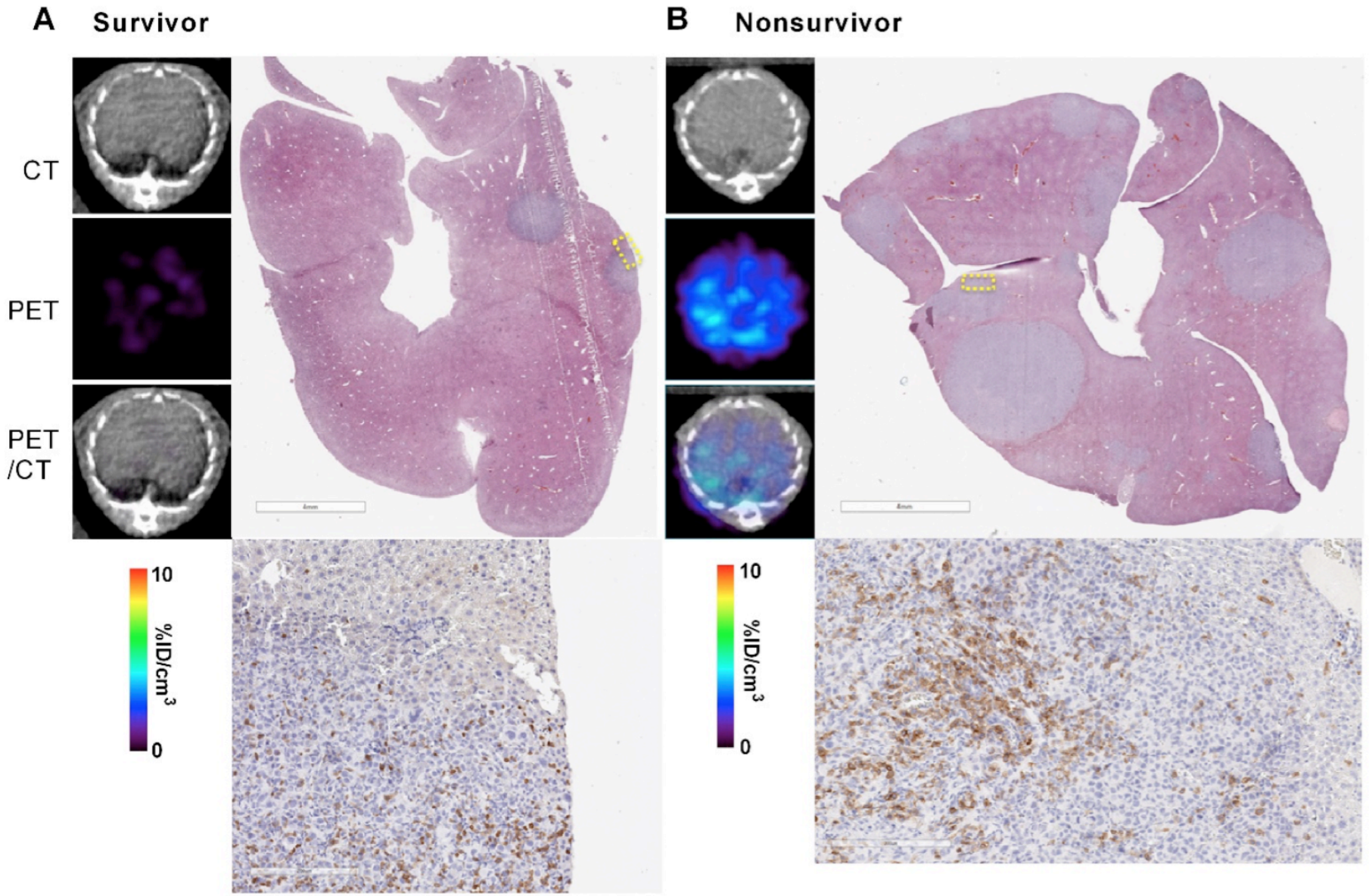
A
Survivor
B
Nonsurvivor
CT
PET
PET
/CT
10
%ID/cm3
0
10
%ID/cm3
0

**Figure 3.11 DOTATOC uptake and histology of the liver.** Transverse CT-only, PET-only and PET/CT images of the liver (1 mm thick slice, maximum intensity projection) of survivor (**A**) vs. nonsurvivor (**B**). Paraffin embedded H&E stained section of the liver from the same mouse, and CD3 stained sections shown at higher magnification underneath (selected area is marked with a dotted box). Scale bar = 4 mm (a&b, top) and 200 μm (a&b, bottom).

mostly devoid of tumor infiltrates and SR T cells, and appeared to have restored normal alveoli structure. Nonsurvivor lung tissues (SR5–9) revealed much higher burden of tumor, yet infiltrating T cells (CD3 staining) were found to colocalize with tumor lesions, confirming ongoing tumor elimination by CAR T cells (Figure 3.9D).

In contrast with the more evenly distributed and synchronized growth of tumors in the lungs, metastatic lesions in the liver were distinctive, isolated, and smaller, measuring only millimeters in size (Figure 3.6, C and D, Figure 3.9, A and B, and Figure 3.11). In most cases, these liver metastases would be of insufficient size to generate CAR T cell expansion to requisite densities for visual detection by DOTATOC/PET — even during efficient CAR T cell responses. However, we were able to detect elevated DOTATOC levels in certain livers with tumor metastases as visualized by luminescence, particularly within nonsurvivors (Figure 3.9B and Figure 3.11B). Such elevated DOTATOC accumulation was scarce in survivors where large tumor lesions in the liver were absent (Figure 3.9A and Figure 3.11A). Infiltration of CAR T cells into metastatic liver lesions irrespective of their size was also confirmed by histology (Figure 3.11). These data therefore confirmed that dynamic DOTATOC uptake by SSTR2-expressing, adoptively transferred T cells can be used to monitor the presence of T cell infiltrates at both primary tumor sites and metastatic lesions.

**Discussion**

Recent clinical studies have strived to find both primary and secondary indicators to enable real-time monitoring of adoptively transferred T cell activity and to predict the likelihood of systemic toxicity [41]. However, as ACT has demonstrated both profound potency and at times, lethal toxicity, there is a clear need for tracking modalities that can provide additional spatiotemporal information to enable both baseline mapping of T cell localization and real-time visualization of multiple sites of T cell expansion. Quantitative PET imaging is increasingly used for diagnostic purposes and to gauge therapy response in a more accurate and objective manner [42]. To our knowledge, this study is the first to utilize PET/CT to conduct high- quality, longitudinal whole-body mapping of ACT localization that illustrates how its dynamics affect the course of treatment and survival outcomes. Furthermore, this was achieved using clinically approved imaging tools to demonstrate critical events such as T cell migration, expansion, peak expansion, and contraction — correlated to tumor burden.

SSTR2 was chosen as a genetic reporter for several reasons. One was to take advantage of the FDA- approved PET radiotracer specific to SSTR2, which is currently in use in clinics to probe for overexpressed SSTR2 in neuroendocrine tumors [43]. SPECT-based imaging is also available using $^{111}$In-DTPAOC (octreoscan) [44]. SSTR2 displays restricted basal expression in tissues and all major organs except in the kidneys and cerebrum, making it ideal for detection of adoptively transferred T cells targeting a multitude of solid tumors. SSTR2 can potentially function as a dual

reporter-suicide gene by conjugation of the therapeutic high-energy radioisotopes $^{177}$lutetium, $^{90}$yttrium, or $^{213}$bismuth to DOTATOC instead of $^{68}$gallium [25, 45], thus enabling elimination of SSTR2-expressing T cells in the case of CAR T cell toxicity. Compared with HSV1-tk, SSTR2 is surface expressed and therefore does not require prior radioligand internalization into the cell. It has previously been shown that SSTR2 facilitates rapid radiotracer uptake, and this combined with swift renal clearance of unbound DOTATOC means that high-quality, clinical- grade images can be obtained 1 hour after DOTATOC injection [46] compared with 2 to 3 hours using HSV1-tk–based systems [13, 47]. DOTATOC also has a short half-life of 68 minutes which, combined with its rapid clearance, delivers a low radiation dose to the patient. The fact that SSTR2 is of human origin should also limit its immunogenicity, which has plagued experiments using nonhuman genetic reporters [48, 49]. Another surface-expressed reporter gene, PSMA, is reportedly superior to more widely tested receptors such as HSV1-tk and NIS for imaging purposes [18]. Therefore, with the myriad of available genetic reporters, choosing the most suitable for imaging adoptively transferred T cells will depend foremost on the tumor being targeted. For example, SSTR2 would be unsuitable for imaging ACT targeting neuroendocrine tumors because of its inherent overexpression in this malignancy. Therefore, it is inevitable that were the adoption of human reporter genes to become widespread, a repertoire of multiple reporters would be required to circumvent potential on-target, off–T cell radiotracer uptake. Interestingly, the synchronous use of distinct genetic reporters may create novel opportunities for near-simultaneous live imaging of multiple infused cell populations [50]. For example, central memory and naive T cells were recently

reported to provide superior antitumor efficacy compared with effector memory cells or clinical products derived from unenriched T cells [51, 52]. However, these studies lack in vivo mechanistic data demonstrating the differences in T cell dynamics behind the observations. Coexpression of CAR or T cell receptor with separate population-specific reporter genes, for example SSTR2 and PSMA, followed by sequential, time-delayed injection of cognate PET radiotracers, could reveal underexplored dynamics of, and interactions between, these populations in both clinical and preclinical studies.

Adoptively transferred T cells have been shown to penetrate and distribute throughout tumor tissue [12]. The utility of any imaging modality capable of monitoring ACT will therefore depend upon a limit- of-detection threshold sensitive enough to enable monitoring of meaningful T cell activity at low tissue densities. Moreover, evaluation of this detection limit in a physiologically relevant model must also account for the sensitivity and specificity of the infused imaging agent for the reporter in question, whose density at the tumor site will vary exponentially as its cognate T cells expand and contract in response to target elimination. Therefore, to approximate the DOTATOC-based detection limit of tumor-infiltrating SSTR2-transduced T cells, we utilized mosaic tumor xenografts of Jurkat T cells with increasing ratios of SSTR2 expression to create a standard by which quantitative PET signals can be related to T cells of known density within tumors. Using the lentivirus developed in this study, the surface expression of SSTR2 in transduced Jurkat T cells was in the range of several million per cell, a level significantly higher than previously published [19] and therefore likely to extend the lower limit of $SSTR2^{+}$ T cell

detection. We observed that with a known threshold of radiotracer uptake, one can detect tumor-infiltrating T cells down to a minimum density of 0.8% or ~$4 \times 10^6$ cells/$cm^3$, with 95% specificity and 87% sensitivity. This compares favorably with a previous report using PET to detect tumor-infiltrating T cells that used flow cytometry– based detection in a separate, equally treated cohort of mice as a reference to purport a tumor-infiltrating T cell detection limit of 0.5% within tumors [53].

To demonstrate the feasibility of SSTR2 reporter–based imaging to predict and monitor tumor-directed T cell activity, we chose ICAM-1–positive anaplastic thyroid cancer cells as a target model and engineered T cells to express both ICAM-1–specific CAR and SSTR2 using a single lentiviral vector. A potential drawback to the use of genetic reporters for imaging receptor-modified ACT is that the T cells in question require the stable expression of 2 separate genes, which can substantially reduce the percentage of cells coexpressing both genes. However, with the use of a self-cleaving P2A sequence [39], we demonstrated that both CAR and reporter genes can be successfully expressed on the same individual cell without compromising the level of expression otherwise achievable using 2 independent vectors.

T cells expressing the SSTR2-R6.5 CAR efficiently and specifically lysed ICAM-1–expressing 8505C and HeLa tumor cell lines within 24 hours, as monitored by bioluminescence, while leaving ICAM-1– negative HEK293 cells largely untouched. Furthermore, efficient killing was also observed at lower E:T ratios, thus demonstrating both specificity and high activity of the SSTR2-R6.5 CAR for ICAM-1– expressing target cells. This targeting efficacy was replicated in vivo, as treatment

of 8505C tumor-bearing mice with SSTR2-R6.5-CAR T cells resulted in a significant reduction in tumor burden across all treated mice compared with those that received T cells expressing SSTR2 only. Tumor lysis occurred 1–2 weeks after treatment, with the time required for CAR T cell–mediated tumor reduction correlating with tumor burden at time of treatment. Expanding SSTR2-R6.5-CAR T cells at the tumor site were visualized via increasing DOTATOC signals. PET imaging of SSTR2-R6.5-CAR T cells was sensitive enough to visualize their perfusion throughout the lungs such that the lung footprint and outline became distinguishable by the presence of T cells alone. This was confirmed by histological analysis of tissue sections, which demonstrated the ubiquitous presence of human $CD3^+$ T cells throughout the lungs of treated mice. Despite the small size (several mm) of metastatic nodules in the liver, localized DOTATOC accumulation was also recorded, which coincided with the emergence, followed by attenuation, of distinct liver tumor nodules as detected by bioluminescence imaging. Extrapolation of the image quality and sensitivity obtained in the current study to similar scenarios in humans would likely enable equal if not better monitoring of ACT tracking to primary, metastatic, and critically, to on-target, off-tumor sites. Visualization of ACT expansion may even draw attention to previously undetected metastatic sites such that sufficiently sensitive reporter imaging of ACT may provide additional theranostic capabilities.

Because of reported dose-limiting toxicity, the number of modified T cells infused to patients is typically in the range of $1 \times 10^6$ to $10 \times 10^6$ T cells/kg [2, 3, 41, 54], and target-mediated expansion and persistence of T cells is therefore a

prerequisite for substantive tumor destruction to occur. Indeed, it has been reported that higher peak expansion of infused T cells correlates with increased rates of disease remission [2, 54]. Tumor-bearing mice in the current study were treated with approximately $1.5 \times 10^6$ SSTR2-CAR$^+$ T cells at days 7–15 after xenograft. Subsequent longitudinal monitoring of both tumor growth and CAR T cell expansion at the tumor site enabled several observations to be made. Timely infusion of CAR T cells resulted in survival of all subjects without weight loss, while later treatments led to uniform death despite evidence of tumor killing by CAR T cells. Survivors exhibited a biphasic pattern of DOTATOC uptake within the lungs, with a similar luminescence pattern observed regarding primary lung tumors. A notable feature of this correlative pattern was that the peak DOTATOC signal, and therefore peak T cell expansion, lagged behind peak tumor burden by several days. This expansion of T cells past the onset of peak tumor burden in survivors may result from enduring cognate antigen–mediated signals, causing continued CAR T cell expansion before eventual exhaustion and contraction occurred [55]. Swift contraction of CAR T cells following peak expansion indicates that target antigen density has fallen to levels no longer capable of sustaining CAR T cell expansion and that tumor elimination was achieved without immediate relapse. The biphasic pattern of DOTATOC uptake in survivors stood in stark contrast to the unrelenting increases in both T cell and tumor burdens in nonsurvivors where tumor growth was evidently surpassing the rate of killing by T cells. It would be interesting to investigate whether a similar pattern is observed in additional tumor models and in clinical studies. Finally, DOTATOC uptake values obtained in the longitudinal study enabled comparisons with uptake

values derived from the SSTR2-titrated Jurkat model. This indicated that peak CAR T cell density in 8505C tumors ranged from below 1% at infusion to ~10% in survivors and to well over 10% in mice with high tumor burden.

In conclusion, we have demonstrated a clinically adaptable, quantitative imaging system capable of specifically detecting adoptively transferred CAR T cells and monitoring their target-specific expansion and contraction at the tumor site with unprecedented detail. A simple method for estimating the density of solid tumor–infiltrating T cells has also been established. We anticipate that the SSTR2 system can be easily adapted to multiple ACT models and can facilitate efforts towards increasing our understanding of the parameters behind the success and failures of ACT with particular regard to monitoring systemic toxicities and the responses to solid tumors.

REFERENCES


1. Rosenberg SA, Restifo NP. Adoptive cell transfer as personalized immunotherapy for human cancer. *Science*. 2015;348(6230):62– 68.
2. Porter DL, Levine BL, Kalos M, Bagg A, June CH. Chimeric antigen receptor-modified T cells in chronic lymphoid leukemia. *N Engl J Med*. 2011;365(8):725–733.
3. Brentjens R, Yeh R, Bernal Y, Riviere I, Sadelain M. Treatment of chronic lymphocytic leukemia with genetically targeted autologous T cells: case report of an unforeseen adverse event in a phase I clinical trial. *Mol Ther*. 2010;18(4):666–668.
4. Teachey DT, et al. Identification of predictive biomarkers for cytokine release syndrome after chimeric antigen receptor T-cell therapy for acute lymphoblastic leukemia. *Cancer Discov*. 2016;6(6):664–679.
5. McCracken MN, Vatakis DN, Dixit D, McLaughlin J, Zack JA, Witte ON. Noninvasive detection of tumor-infiltrating T cells by PET reporter imaging. *J Clin Invest*. 2015;125(5):1815–1826.
6. Pittet MJ, et al. In vivo imaging of T cell delivery to tumors after adoptive transfer therapy. *Proc Natl Acad Sci U S A*. 2007;104(30):12457–12461.
7. de Jong M, Essers J, van Weerden WM. Imaging preclinical tumour models: improving translational power. *Nat Rev Cancer*. 2014;14(7):481–493.
8. Kircher MF, Gambhir SS, Grimm J. Noninvasive cell-tracking methods. *Nat Rev Clin Oncol*. 2011;8(11):677–688.
9. Ahrens ET, Bulte JW. Tracking immune cells in vivo using magnetic resonance imaging. *Nat Rev Immunol*. 2013;13(10):755–763.
10. Liu Z, Li Z. Molecular imaging in tracking tumor-specific cytotoxic T lymphocytes (CTLs). *Theranostics*. 2014;4(10):990–1001.
11. Herschman HR. Micro-PET imaging and small animal models of disease. *Curr Opin Immunol*. 2003;15(4):378–384.
12. Boissonnas A, Fetler L, Zeelenberg IS, Hugues S, Amigorena S. In vivo imaging of cytotoxic T cell infiltration and elimination of a solid tumor. *J Exp Med*. 2007;204(2):345–356.
13. Yaghoubi SS, et al. Noninvasive detection of therapeutic cytolytic T cells with $^{18}$F-FHBG PET in a patient with glioma. *Nat Clin Pract Oncol*. 2009;6(1):53–58.
14. Yaghoubi S, et al. Human pharmacokinetic and dosimetry studies of [(18)F]FHBG: a reporter probe for imaging herpes simplex virus type-1 thymidine kinase reporter gene expression. *J Nucl Med*. 2001;42(8):1225–1234.
15. Peñuelas I, et al. Positron emission tomography imaging of adenoviral-mediated transgene expression in liver cancer patients. *Gastroenterology*. 2005;128(7):1787–1795.
16. Su H, Chang DS, Gambhir SS, Braun J. Monitoring the antitumor response of naive and memory CD8 T cells in RAG1$^{-/-}$ mice by positron-emission

tomography. *J Immunol*. 2006;176(7):4459–4467.
17. Barton KN, et al. Phase I study of noninvasive imaging of adenovirus-mediated gene expression in the human prostate. *Mol Ther*. 2008;16(10):1761–1769.
18. Castanares MA, et al. Evaluation of prostate-specific membrane antigen as an imaging reporter. *J Nucl Med*. 2014;55(5):805–811.
19. Zhang H, et al. Imaging expression of the human somatostatin receptor subtype-2 reporter gene with $^{68}$Ga-DOTATOC. *J Nucl Med*. 2011;52(1):123–131.
20. Moroz MA, et al. Comparative analysis of T cell imaging with human nuclear reporter genes. *J Nucl Med*. 2015;56(7):1055–1060.
21. Griessinger CM, et al. In vivo tracking of Th1 cells by PET reveals quantitative and temporal distribution and specific homing in lymphatic tissue. *J Nucl Med*. 2014;55(2):301–307.
22. Dobrenkov K, et al. Monitoring the efficacy of adoptively transferred prostate cancer-targeted human T lymphocytes with PET and bioluminescence imaging. *J Nucl Med*. 2008;49(7):1162–1170.
23. Yamada Y, Post SR, Wang K, Tager HS, Bell GI, Seino S. Cloning and functional characterization of a family of human and mouse somatostatin receptors expressed in brain, gastrointestinal tract, and kidney. *Proc Natl Acad Sci U S A*. 1992;89(1):251– 255.
24. Garkavij M, et al. $^{177}$Lu-[DOTA0,Tyr3] octreotate therapy in patients with disseminated neuroendocrine tumors: Analysis of dosimetry with impact on future therapeutic strategy. *Cancer*. 2010;116(4 Suppl):1084–1092.
25. Kratochwil C, et al. $^{213}$Bi-DOTATOC receptor-targeted alpha-radionuclide therapy induces remission in neuroendocrine tumours refractory to beta radiation: a first-in-human experience. *Eur J Nucl Med Mol Imaging*. 2014;41(11):2106–2119.
26. Wulfert S, et al. Multimodal imaging for early functional response assessment of (90)Y-/ (177)Lu-DOTATOC peptide receptor targeted radiotherapy with DW-MRI and (68)Ga-DOTATOC-PET/CT. *Mol Imaging Biol*. 2014;16(4):586–594.
27. Koyama S, Ebihara T, Fukao K. Expression of intercellular adhesion molecule 1 (ICAM-1) during the development of invasion and/or metastasis of gastric carcinoma. *J Cancer Res Clin Oncol*. 1992;118(8):609–614.
28. Tempia-Caliera AA, et al. Adhesion molecules in human pancreatic cancer. *J Surg Oncol*. 2002;79(2):93–100.
29. Shimoyama S, Gansauge F, Gansauge S, Widmaier U, Oohara T, Beger HG. Overexpression of intercellular adhesion molecule-1 (ICAM-1) in pancreatic adenocarcinoma in comparison with normal pancreas. *Pancreas*. 1997;14(2):181–186.
30. Buitrago D, et al. Intercellular adhesion molecule-1 (ICAM-1) is upregulated in aggressive papillary thyroid carcinoma. *Ann Surg Oncol*. 2012;19(3):973–980.
31. Guo P, et al. ICAM-1 as a molecular target for triple negative breast cancer..*Proc Natl Acad Sci U S A*. 2014;111(41):14710–14715.
32. Chen X, et al. Inflamed leukocyte-mimetic nanoparticles for molecular imaging of inflammation. *Biomaterials*. 2011;32(30):7651–7661.

33. Rivera M, Ghossein RA, Schoder H, Gomez D, Larson SM, Tuttle RM. Histopathologic characterization of radioactive iodine-refractory fluorodeoxyglucose-positron emission tomography-positive thyroid carcinoma. *Cancer*. 2008;113(1):48-56.
34. Higgins MJ, Forastiere A, Marur S. New directions in the systemic treatment of metastatic thyroid cancer. *Oncology (Williston Park, NY)*. 2009;23(9):768–775.
35. Carpenito C, et al. Control of large, established tumor xenografts with genetically retargeted human T cells containing CD28 and CD137 domains. *Proc Natl Acad Sci USA*. 2009;106(9):3360–3365.
36. Cescato R, et al. Internalization of sst2, sst3, and sst5 receptors: effects of somatostatin agonists and antagonists. *J Nucl Med*. 2006;47(3):502–511.
37. Zou KH, O'Malley AJ, Mauri L. Receiver-operating characteristic analysis for evaluating diagnostic tests and predictive models. *Circulation*. 2007;115(5):654–657.
38. Cosimi AB, et al. In vivo effects of monoclonal antibody to ICAM-1 (CD54) in nonhuman primates with renal allografts. *J Immunol*. 1990;144(12):4604–4612.
39. Kim JH, et al. High cleavage efficiency of a 2A peptide derived from porcine teschovirus-1 in human cell lines, zebrafish and mice. *PLoS One*. 2011;6(4):e18556.
40. Zhang L, Gaskins K, Yu Z, Xiong Y, Merino MJ, Kebebew E. An in vivo mouse model of metastatic human thyroid cancer. *Thyroid*. 2014;24(4):695–704.
41. Turtle CJ, et al. CD19 CAR-T cells of defined $CD4^+$:$CD8^+$ composition in adult B cell ALL patients. *J Clin Invest*. 2016;126(6):2123–2138.
42. Yaghoubi SS, Campbell DO, Radu CG, Czernin J. Positron emission tomography reporter genes and reporter probes: gene and cell therapy applications. *Theranostics*. 2012;2(4):374–391.
43. Kratochwil C, et al. SUV of [$^{68}$Ga]DOTATOC-PET/CT predicts response probability of PRRT in neuroendocrine tumors. *Mol Imaging Biol*. 2015;17(3):313–318.
44. Buchmann I, et al. Comparison of $^{68}$Ga-DOTATOC PET and $^{111}$In-DTPAOC (Octreoscan) SPECT in patients with neuroendocrine tumours. *Eur J Nucl Med Mol Imaging*. 2007;34(10):1617–1626.
45. Forrer F, Uusijärvi H, Storch D, Maecke HR, Mueller-Brand J. Treatment with $^{177}$Lu-DOTATOC of patients with relapse of neuroendocrine tumors after treatment with $^{90}$Y-DOTATOC. *J Nucl Med*. 2005;46(8):1310–1316.
46. Velikyan I, et al. Quantitative and qualitative intrapatient comparison of $^{68}$Ga-DOTATOC and $^{68}$Ga-DOTATATE: net uptake rate for accurate quantification. *J Nucl Med*. 2014;55(2):204–210.
47. Yaghoubi SS, Gambhir SS. PET imaging of herpes simplex virus type 1 thymidine kinase (HSV1-tk) or mutant HSV1-sr39tk reporter gene expression in mice and humans using [$^{18}$F]FHBG. *Nat Protoc*. 2006;1(6):3069–3075.
48. Berger C, Flowers ME, Warren EH, Riddell SR. Analysis of transgene-specific

immune responses that limit the in vivo per- sistence of adoptively transferred HSV-TK-modified donor T cells after allogeneic hematopoietic cell transplantation. *Blood*. 2006;107(6):2294–2302.
49. Riddell SR, et al. T-cell mediated rejection of gene-modified HIV-specific cytotoxic T lymphocytes in HIV-infected patients. *Nat Med*. 1996;2(2):216–223.
50. Doubrovin MM, Doubrovina ES, Zanzonico P, Sadelain M, Larson SM, O'Reilly RJ. In vivo imaging and quantitation of adoptively transferred human antigen-specific T cells transduced to express a human norepinephrine transporter gene. *Cancer Res*. 2007;67(24):11959–11969.
51. Hinrichs CS, et al. Adoptively transferred effector cells derived from naive rather than central memory $CD8^+$ T cells mediate superior antitumor immunity. *Proc Natl Acad Sci USA*. 2009;106(41):17469–17474.
52. Klebanoff CA, et al. Central memory self/tumor-reactive $CD8^+$ T cells confer superior antitumor immunity compared with effector memory T cells. *Proc Natl Acad Sci USA*. 2005;102(27):9571–9576.
53. Vatakis DN, et al. Antitumor activity from antigen-specific CD8 T cells generated in vivo from genetically engineered human hematopoietic stem cells. *Proc Natl Acad Sci USA*. 2011;108(51):E1408–E1416.
54. Grupp SA, et al. Chimeric antigen receptor-modified T cells for acute lymphoid leukemia. *N Engl J Med*. 2013;368(16):1509– 1518.
55. van Stipdonk MJ, Lemmens EE, Schoenberger SP. Naïve CTLs require a single brief period of antigenic stimulation for clonal expansion and differentiation. *Nat Immunol*. 2001;2(5):423–429.
56. Smith CW, et al. Recognition of an endothelial determinant for CD 18-dependent human neutrophil adherence and transendothelial migration. *J Clin Invest*. 1988;82(5):1746–1756.
57. Leelawattanachai J, Kwon KW, Michael P, Ting R, Kim JY, Jin MM. Side-by-side comparison of commonly used biomolecules that differ in size and affinity on tumor uptake and internalization. *PLoS One*. 2015;10(4):e0124440.
58. Höfig I, Atkinson MJ, Mall S, Krackhardt AM, Thirion C, Anastasov N. Poloxamer synperonic F108 improves cellular transduction with lentiviral vectors. *J Gene Med*. 2012;14(8):549–560.
59. Gargett T, Brown MP. Different cytokine and stimulation conditions influence the expansion and immune phenotype of third-generation chimeric antigen receptor T cells specific for tumor antigen GD2. *Cytotherapy*. 2015;17(4):487–495.
60. Xu Y, et al. Closely related T-memory stem cells correlate with in vivo expansion of CAR.CD19-T cells and are preserved by IL-7 and IL-15. *Blood*. 2014;123(24):3750–3759.
61. Kinahan PE, Fletcher JW. Positron emission tomography-computed tomography standardized uptake values in clinical practice and assessing response to therapy. *Semin Ultrasound CT MR*. 2010;31(6):496–505.

# CHAPTER 4

## UTILIZING SSTR2 REPORTER TO STUDY THE DYNAMICS OF AFFINITY TUNING CAR-T THERAPY

**Summary**

Adoptive transfer of high-affinity chimeric antigen receptor (CAR) T cells targeting hematological cancers has yielded impressive clinical results. However, safety concerns regarding target expression on healthy tissue and poor efficacy have hampered application to solid tumors. Here, a panel of affinity-variant CARs were constructed targeting overexpressed ICAM-1, a broad tumor biomarker, using its physiological ligand, LFA-1. Anti-tumor T cell potency *in vitro* was directly proportional to CAR affinity and ICAM-1 density. In a solid tumor mouse model allowing simultaneous monitoring of anti-tumor potency and systemic off-tumor toxicity, micromolar affinity CAR T cells demonstrated superior anti-tumor efficacy and safety compared to their nanomolar counterparts. Longitudinal T cell tracking by PET/CT and concurrent cytokine measurement revealed expansion and contraction kinetics of micromolar affinity CAR T cells and inflammatory cytokines. Therefore, we developed an ICAM-1-specific CAR with broad anti-tumor applicability that utilized a reduced affinity targeting strategy to significantly boost efficacy and safety.

---

This chapter was originally published in Scientific Reports (Park, S., Shevlin, E., Vedvyas, Y., Zaman, M., Park, S., Hsu, Y, Min,IM. And Jin, MM. SciEntific RePoRts | 7: *14366* | DOI:10.1038/s41598-017-14749-3 and is reprinted with permission. Vedvyas Y contributed CAR T vector construction, lentivirus production, Radiotracer sunthesis, PET imaging , Histology and cytokine analysis. This includes experiments and writing related to Figures 4.1, 4.4, 4.5, and 4.6.

## Introduction

CAR molecules are composed of synthetic binding moieties, typically an antibody-derived single chain fragment variable (svFv) or any native antigen-sensing element, fused to intracellular signaling domains composed of the TCR zeta chain and costimulatory molecules such as CD28 and/or 4-1BB[1, 2]. The advantages of CAR mediated targeting include: 1) the provision of activation, proliferation, and survival signals in-cis via a single binding event, compared to the natural, non-integrated TCR and costimulatory signaling; 2) the ability to bypass the downregulation of MHC by tumor cells through MHC-independent antigen recognition; and 3) a reduced activation threshold as well as recognition of tumor cells with low antigen density enabled by the high affinity interaction between CAR and antigen [3, 4]. As such, T cells modified with scFv-based CARs to recognize the pan B-cell antigen CD19 have demonstrated unprecedented remission rates in relapsed and refractory B cell leukemia and lymphomas[5-8]. However, CD19 CAR T cell therapies have also caused profound treatment-related toxicities, such as cytokine release syndrome, encephalopathy, B-cell aplasia, graft versus host disease, and coagulopathy [9]. In comparison, the advancement of CAR T cell therapy in solid tumors has been limited due to the scarcity of tumor antigens that are deemed safe for targeting. Thus far, clinical outcomes in solid malignancies have been poor in comparison to those in hematological settings [10, 11], and methods to improve efficacy are being actively investigated.

The ideal CAR target antigen would be a native, surface-exposed tumor neoantigen that is highly expressed and is undetectable in healthy tissues. However, due to the implicit rarity of such antigens, many commonly targeted solid tumor antigens, such as human epidermal growth factor receptor 2 (ErbB2), epidermal growth factor receptor (EGFR), mucine 1 (MUC1), prostate-specific membrane antigen (PSMA), and diganglioside (GD2)[10], are also expressed by non-tumor tissues, albeit at lower levels. CAR molecules with high affinity to such antigens can lead to collateral targeting of healthy tissues resulting in on-target, off-tumor toxicity, a major limiting factor to the progress of CAR T cell therapy to date. In the case of CD19-specific CAR T cells, elimination of healthy B cells is a manageable morbidity and therefore has not been a critical safety issue. However, recent reports on severe adverse toxicities and fatalities associated with CAR T cells in solid tumor settings[12-14] illustrate the importance of ligand-receptor pair selection and the role of affinity in determining the therapeutic index.

The affinity of a TCR for its cognate pMHC typically ranges between 1-100 μM, thus endowing T cells with tolerance towards cells with subthreshold levels of pMHC expression [15-17]. Similarly, T cells possessing micromolar affinity (1 μM) CARs are capable of lysing cells overexpressing target antigens while sparing those with much lower densities [18]. The affinity and avidity of a CAR for its target antigen also influences cytokine release, the rate of tumor killing, and T cell persistence [3, 18-20]. Studies using engineered TCRs with pMHC affinities significantly above their natural range caused T cells to exhibit rapid exhaustion and poor persistence *in vivo*[21-23]. Together, these studies emphasize the need to

reconsider the criteria used to determine optimal CAR affinities to achieve enhanced therapeutic indices.

In this study, we redirected affinity variant CAR T cells toward intercellular adhesion molecule (ICAM)-1, a molecule that is upregulated in several carcinomas and the associated stroma[24] as well as in inflammatory conditions[25]. Aside from diseased tissues, ICAM-1 is basally expressed in several cell types including endothelial cells, immune cells, and some epithelial cells [25]. The antigen-binding domain of the CAR used in this study is constructed from the native ligand for ICAM-1, the inserted (I) domain of lymphocyte function-associated antigen (LFA)-1, which exhibits a solution affinity of approximately 1 mM[26]. Previously, the I domain was engineered using directed evolution to isolate variants exhibiting affinities to ICAM-1 that span six orders of magnitude ($K_D$ ~1 nM to 1 mM)[27]. As human LFA-1 I domain exhibits the capability of cross reacting with both murine and human ICAM-1 with comparable affinities[28], we were able to preclinically address potency against human tumors overexpressing ICAM-1 and simultaneously monitor potential on-target, off-tumor systemic toxicity against normal mouse tissues expressing murine ICAM-1. We found that I domain CARs exhibiting affinities in the micromolar range (~10 μM) exhibited a significantly higher therapeutic index, while increasing the affinity further (1-100 nM) caused unbiased reactivity against normal cells with basal ICAM-1 expression and led to less efficient tumor regression. Simultaneous expression of a reporter gene, human somatostatin receptor 2 (SSTR2), on affinity variant CAR T cells utilized for longitudinal position emission tomography and

computed tomography (PET/CT) imaging [29] enabled spatiotemporal mapping and further evaluation of adoptively transferred T cells *in vivo*.

## Experimental Procedures

*Cell lines and primary human lymphocytes*

Human dermal microvascular endothelial cells (HMEC-1) were obtained from the Center for Disease Control and were cultured in MCDB 131 medium (Invitrogen) supplemented with 10% (v/v) fetal bovine serum (FBS, Atlanta Biologicals), 10 mM L-alanyl-L-glutamine dipeptide (Gibco), 100 units/ml Penicillin-Streptomycin (Pen-strep), 1 μg/ml hydrocortisome (MP Biomedicals), and 10 ng/ml recombinant human epidermal growth factors (Invitrogen). Mouse brain microvascular endothelial cells (bEnd.3, ATCC) were maintained in Advanced Dulbecco's Modified Eagle Medium (ADMEM, Invitrogen) supplemented with 4 mM L-glutamine, 100 units/ml Pen-strep, and 10% FBS. HeLa cells (ATCC) were cultured in ADMEM containing 10% FBS, 2 mM L-glutamine, and 100 units/ml Pen-strep. 8505C cells (DSMZ) were cultured in RPMI-1640 medium (Invitrogen) containing 10% FBS, 2 mM L-glutamine, and 100 units/ml Pen-strep. HMEC-1, bEnd.3, HeLa, and 8505c cells were transduced with lentivirus encoding Firefly Luciferase-F2A-GFP (Biosettia) and sorted based on fluorescence.

Human peripheral blood was obtained from healthy volunteer donors by venipuncture. Peripheral blood mononuclear cells were isolated using Ficoll-Paque PLUS (GE Healthcare) and cultured in Optimizer CTS T-cell Expansion SFM (Thermo) supplemented with 5% human AB serum (Sigma), 2 mM L-alanyl-L-

glutamine dipeptide, and 30 IU/ml human IL-2 (Cell Sciences) (T cell culture medium). Non-adherent cells were removed after 24h and enriched for T cells with Dynabeads CD3/CD28 T cell expander (Thermo) at a 2:1 bead to T cell ratio. Dynabead-bound T cells were subsequently cultured in IL-2 containing media at a density of 1 x $10^6$ cells/ml. All cells were incubated at 37°C in a 5% $CO_2$ humidified incubator.

*Construction of I domain CAR vector*

Genetic sequences encoding LFA-1 I domains of varying affinities to ICAM-1 were derived from a previous study[27]. I domain variants were fused at the C-terminus directly to the CD8 hinge, CD28 transmembrane domain, and the intracellular portions of the 3$^{rd}$ generation CAR architecture incorporating the cytoplasmic domains of CD28, CD137, and CD3ζ. The complete CAR inserts were then subcloned into a pLenti backbone [29]. A reporter gene for CAR T cell imaging, SSTR2, was linked to I domain at the N-terminus using a 'ribosome skipping' porcine teschovirus-1 2A (P2A) sequence to ensure comparable production of CAR and SSTR2 from the same mRNA.

*Lentivirus production and transduction of T cells*

Lentivirus was produced by transiently transfecting HEK 293T cells using calcium phosphate. Briefly, 10 µg of transfer gene, 7.5 µg of pCMV-dR8.2 (Addgene) and 5 µg of pCMV-VSVG (Addgene) were mixed and incubated with 2 M $CaCl_2$ followed by 2x HBSS. Resulting solutions were added dropwise to 10 $cm^2$ cell culture

dishes seeded with 3.2 x $10^6$ HEK 293T cells in 10 ml DMEM 24h previously. Transfection media was replaced after 6 h. Media containing lentivirus was harvested at 48 and 72 h post transfection, filtered through 0.45 μm filters, and concentrated by ultracentrifugation at 75,000x g for 2 h at 4 °C. Lentivirus was then resuspended in serum containing media and frozen at -80 °C. Human T cells were transduced 24 – 72 h post activation with anti-CD3/CD28 Dynabeads either by spinfection (1,000 g for 1 h at 32 °C) or by overnight incubation with lentivirus. T cells were transduced once more 24 h after the first transduction. During and following transductions, media containing IL-2 was replaced with media containing human IL-7 (10 ng/ml) and IL-15 (5 ng/ml) (Peprotech). Jurkat T cells were transduced by a single overnight incubation with lentivirus.

*In vitro target cell killing assay*

2 x $10^5$ target cells (HMEC-1, bEnd.3, HeLa, and 8505c) stably transduced to express GFP and firefly luciferase were co-cultured with either non-transduced or I domain CAR T cells at varying effector to target ratios (E:T). In certain conditions, the ICAM-1 gene was disrupted in 8505C cells using CRISPR/Cas9 (Santa Cruz, #sc-400098; denoted as 8505C/-ICAM-1) or, alternatively, 8505C cells were exposed to 1 μg/ml lipopolysaccharide (LPS; *Escherichia coli* O26:B6, Sigma) for 12 h to induce overexpression of ICAM-1 (denoted as 8505C/LPS). Co-cultures were carried out in T cell culture medium containing 150 μg/ml D-Luciferin (Gold Biotechnology) and no cytokine supplementation. Luminescence was measured using a plate reader (TECAN

infinite M1000 PRO) with readings in each E:T condition normalized to the non-transduced T cell:target co-culture controls.

*8505C mouse model, whole-body tumor imaging, and serum cytokine analysis*

7.5 x $10^5$ 8505C cells were injected into NSG mice via tail vein. 1-3 x $10^6$ T cells were injected via tail vein 8-10 days after tumor cell injection. Injection timing was chosen based on prior studies with R6.5 CAR T cells which demonstrated tumor elimination using similar CAR dosages at up to 10-days post xenograft[29]. Luminescence imaging of tumor xenografts in live mice was performed using a whole body optical imager (In-Vivo Extreme, Bruker). Mice were anesthetized with 2% isoflurane in 2 L/min $O_2$. Tumor burden was quantified through integration of luminescence over chest cavity and the entire mouse body. For serum cytokine analysis, 50-100 μl of blood was collected via tail-vein into Eppendorf tubes on ice. Plasma was immediately isolated after removing cell pellet by centrifugation at 2,000 g for 10 min at 4 °C, and stored at -80 °C. Human cytokines (GM-CSF, IL-2, IL-6, IFN-γ, TNF-α, CXCL10) were measured in duplicate using Bio-Plex MAGPIX (Bio Rad) according to the manufacturer's instructions.

*Ex vivo cellular analysis*

Tumor xenografts were resected from mice at appropriate time points. Resected tumors were diced and flushed through 80 μm cell strainers to yield single cell suspensions. Red blood cells were lysed by incubation with 1x RBC lysis buffer (eBiosciences). Remaining cells were washed, re-suspended in 1x HBSS containing

2% normal goat serum, and blocked with mouse IgG at 2 μg/ml for 10 min. This was followed by staining with 1 μg/ml Propidium Iodide (Invitrogen) in combination with 2 μg/ml mouse anti-human CD3-Alexa Fluor 647 (Biolegend) or 2 μg/ml rabbit anti-c-myc-Alexa Fluor 647 (Biolegend). Resulting cells were acquired on a Gallios flow cytometer (Beckman Coulter). Initial flow cytometry gates were determined based on live cell gating (Propidium Iodide negative).

*ICAM-1 and CAR expression quantification*

ICAM-1 expression on various cell lines was determined using a mouse anti-human R6.5 monoclonal antibody (10 μg/ml) obtained from hybridoma (ATCC). I domain CAR expression on T cells was detected using 2 μg/ml rabbit anti-c-myc-Alexa Fluor 647 (Biolegend). I domain Jurkat T cell variants were incubated with 10 μg/ml recombinant human ICAM-1 fused to human Fcγ (R&D Systems). Cells were then washed and resuspended in 1 μg/ml rabbit anti-human PE (Santa Cruz Biotechnology) prior to flow cytometry analysis.

*In vitro measurement of IFN-γ*

Target cells were washed and suspended at $1 \times 10^6$ cells/ml in T cell culture medium without cytokines. 100 μl of each target cell was added in triplicate to a 96-well round bottom plate (Corning). T cells resuspended at $5 \times 10^6$ cells/ml in T cell culture medium were combined with target cells in appropriate wells. Plates were incubated at 37°C for 24 – 48 h. After incubation, supernatants were collected for ELISA to detect IFN-γ (Biolegend).

*CD25 and CD69 staining*

Jurkat cells modified with I domain CARs were co-cultured with target cells at an effector to target ratio of 1:1 ($1 \times 10^5$ effectors: $1 \times 10^5$ targets) in a 96-well plate. The plate was incubated at 37 °C for 6 h. After incubation, cells were washed prior to labelling with 2 μg/ml anti-human CD25-allophycocyanin (APC; Biolegend) for 30 min on ice. After incubation, samples were washed and analyzed by flow cytometry. As an alternative to ICAM-1 expressing cells, we also used microbeads coated with known amounts of ICAM-1. 1 x $10^6$ sulfate latex microbeads (8 mm, ThermoFisher Scientific) were resuspended in 100 mL of PBS containing indicated amounts of human or murine recombinant ICAM-1-Fcγ (R&D Systems) conjugated with Cy5.5 (Sulfo-Cyanine5.5 NHS ester, Lumiprobe) overnight at room temperature with gentle mixing. Protein-labeled particles were pelleted and resuspended in fresh PBS containing 0.1 M glycine pH 7.4 for 1 h, while supernatant was used to measure bead adsorption efficiency by fluorescence (TECAN infinite M1000 PRO). After saturation of bead surface with glycine, beads were pelleted and resuspended in PBS containing 5 mM $MgCl_2$. Jurkat cells modified with each I domain CAR variant were incubated with ICAM-1-bound latex beads at 1:3 (cell:bead) ratio overnight at 37°C. Cells were then collected, labeled with 2 μg/ml anti-human CD69-APC (Biolegend) for analysis by flow cytometry.

*V-bottom adhesion assay*

V-bottom 96-well plates (Corning) were coated with either murine or human ICAM-1-Fcγ (10 μg/ml in PBS, pH 7.4) or 2% BSA at 4°C overnight. The plates were then blocked with 2% BSA for 1h at 37°C. I domain CAR T clones were first stained with CellTracker Orange according to manufacturer's protocol and then added to ICAM-1-coated wells in 50 μl of PBS containing 5 mM $MgCl_2$ and 1% BSA. Plates were immediately centrifuged at 200 *g* for 15 min at room temperature. Nonadherent cells that accumulated at the bottom of the V-bottom plates were quantified by a fluorescence plate reader (TECAN infinite M1000 PRO). Cell binding to ICAM-1 was calculated from the fluorescence intensity values of experimental measurements ($F_{CAR}$ and $F_{NT}$) and normalized to the fluorescence from the wells coated with BSA alone ($F_{BSA}$): 100 x (($F_{BSA}$-$F_{CAR}$)/$F_{BSA}$)/(($F_{BSA}$-$F_{NT}$)/$F_{BSA}$).

*Labeling of $^{18}$F-NOTA-octreotide (NOTAOCT)*

NOTAOCT (1,4,7-Triazacyclononane-1,4,7-triacetic acid-octreotide[30], GMP grade) was obtained as a 1 mg lyophilized powder (cat #9762, ABX Pharmaceuticals). The NOTAOCT vial content was diluted with 18 MW water to 200 μl (5 mg/ml solution) and stored at 4 ºC as a stock solution. For chelation of NOTA with Fluorine-18[31], 5 μl of NOTAOCT was added to 10 μl of 0.1 M sodium acetate, pH 4, 6 μl of 2 mM AlCl3, and 100 μl containing ~30 mCi $^{18}$F. The solution was immediately placed in a Thermomixer (Eppendorf) at 100 ºC and incubated for 15 minutes followed by cooling to room temperature and dilution in 15 ml $ddH_2O$. A Sep-Pak light C18 column was regenerated in 3 ml 100% ethanol and washed twice in 5 ml

dd$H_2O$ with an observed flow rate of 10 drops per minute. NOTAOCT was then loaded to the Sep-Pak column, which was later washed in 15 ml 18 MW water to eliminate any remaining free $^{18}F$. Trapped NOTAOCT was eluted from the column using 300 μl of ethanol and diluted to 1.5 ml with PBS for injection, providing the final product in ~15% ethanol isotonic, injectable solution. The eluent was passed through 0.2 μm filter. The purity of the final product was checked by reverse phase HPLC.

*PET/CT imaging*

Registered CT images were acquired using a micro-PET/CT scanner (Inveon, Siemens) at 1-2 h post NOTAOCT injection. Projection data was acquired in a cone-beam geometry with approximately 1 s steps at 1 degree angular increments. At least 10 million coincidence events were acquired for PET per study using a 250 to 750 keV energy window and a 6 ns timing window. A reference tube containing 100 μl of a 10 %ID/$cm^3$ equivalent dose for quantification of NOTATOC uptake *in vivo*. To compute NOTAOCT uptake within mouse lungs, ellipsoids were drawn separately on the left and right sides of lungs to enclose the majority of their footprint. The %ID/$cm^3$ values, computed relative to the counts obtained in the reference tube, were approximated to a standard uptake value (SUV [32]) by dividing %ID/$cm^3$ by four, assuming injection efficiency of 100% and 25 g of body weight. Visualization and analyses of PET/CT images were performed using AMIDE software (http://amide.sourceforge.net).

*Histology*

After euthanasia, mouse lungs were perfused via trachea with 4% paraformaldehyde, and each of five lobes were separated post fixation and embedded in paraffin. Tissues were cut to produce 5 μm sections (Microtome, Leica). Paraffin embedded sections were stained with hematoxylin and eosin (H&E) or hematoxylin only for CD3 and GFP immunostaining (performed by HistoWiz, Inc.). Histological analysis was performed by an experienced pathologist.

*Statistical analysis*

One-way ANOVA, Dunnett's multiple comparisons test, and unpaired Student's t-test were performed using Prism (GraphPad) on data indicated.

*Study Approval*

The protocol for blood draw from healthy volunteers was approved by the Institutional Review Board of Weill Cornell Medicine (Permit Number: 1302013613). All animal experiments were performed in strict accordance with the recommendations contained within the National Institute of Health's Guide for the Care and Use of Laboratory Animals. Animal handling protocols were approved by the Institutional Laboratory Animal Use and Care Committee of Weill Cornell Medicine (Permit Number: 2012-0063).

**Results.**

*ICAM-1 specific CAR T cells with $10^6$-fold, step-wise variation in affinity.*

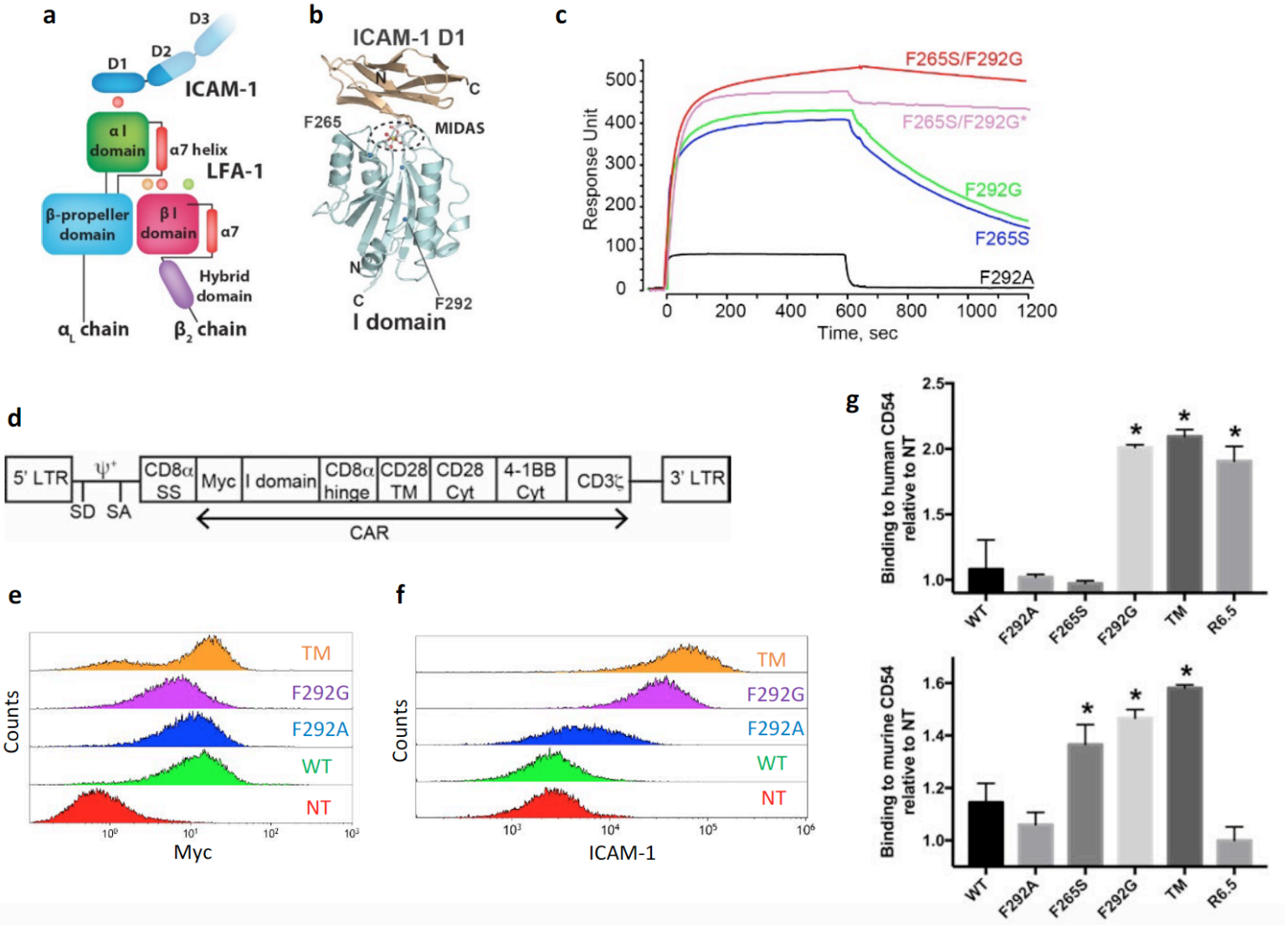
a
D3
D2
D1
ICAM-1
α I domain
α7 helix
LFA-1
β-propeller domain
β I domain
α7
Hybrid domain
α_L chain
β_2 chain
b
ICAM-1 D1
N
C
F265
MIDAS
N
C
F292
I domain
c
F265S/F292G
F265S/F292G*
F292G
F265S
F292A
Response Unit
Time, sec
d
5' LTR
Ψ+
SD
SA
CD8α SS
Myc
I domain
CD8α hinge
CD28 TM
CD28 Cyt
4-1BB Cyt
CD3ζ
3' LTR
CAR
e
TM
F292G
F292A
WT
NT
Counts
Myc
f
TM
F292G
F292A
WT
NT
Counts
ICAM-1
g
Binding to human CD54 relative to NT
WT
F292A
F265S
F292G
TM
R6.5
Binding to murine CD54 relative to NT
WT
F292A
F265S
F292G
TM
R6.5

**Figure 4.1 Construction of ICAM-1 specific CARs with step-wise, $10^6$-fold variations in affinity. (a)** Schematic of LFA-1 in complex with ICAM-1. α and β chains, and modular domains of LFA-1 integrin are labeled. Metal ions necessary for LFA-1 and ICAM-1 interaction are shown in circles. **(b)** Structural model of LFA-1 I domain and the N-terminal domain of ICAM-1 (D1) are drawn in ribbon diagram. N and C-termini, and mutational hot spots are indicated. **(c)** SPR sensogram of I domain variants binding to immobilized human ICAM-1, except F265S/F292G*, which was flowed over murine ICAM-1 (adapted from Fig 2 of Jin et. al.[33], and Fig 1 of Wong et. al[34]). **(d)** A schematic of the lentivirus vector encoding I domain CAR. LTR = long terminal repeat; SD = splice donor; SA = splice acceptor; $\psi^+$ = packaging signal; SS = signal sequence; TM = transmembrane; Cyt = cytosolic domain. **(e)** Anti-Myc antibody binding to Jurkat T cells transduced with Myc-tagged CARs (TM, F292G, F292A, and WT I domain). NT = non-transduced. **(f)** Recombinant ICAM-1-Fc binding to CARs expressed in HEK 293T cells. **(g)** V-bottom adhesion assay measuring relative binding affinities between I domain CARs expressed in Jurkat T cells and soluble human (top) and murine (bottom) ICAM-1 (CD54) coated surfaces. n=3; $p < 0.01$ for * vs. NT by Dunnett's multiple comparisons test.

CAR constructs specific to ICAM-1 were built using the I domain derived from LFA-1 (Figure 4.1a,b). Various activating point mutations in the I domain have previously been isolated, which were localized outside of the binding interface that includes a region known as the metal-ion dependent adhesion site (MIDAS) (Figure 4.1b). The step-wise elevation of affinity to ICAM-1 is proposed to be induced by lowering the energy barrier of the transition from inactive (closed) to active (open) conformations. For example, substitution of Phe-292 located in the C-terminal α7-helix with Ala (F292A) and Gly (F292G) led to affinities ($K_D$) of ~20 μM and 0.1 μM, respectively (Table 1). The combination of F292G with another comparably activating mutation in Phe-265 (F265S/F292G) led to an affinity of 6 nM, approximately 200,000-fold higher than the wild-type (WT) I domain ($K_D$ = 1.5 mM) (Figure 4.1c). To lock the C-terminal α7-helix of F265S/F292G in the open position (Figure 4.1a), Gly-311 was replaced with Cys (G311C) in the F265S/F292G mutant (F265S/F292G/G311C, dubbed triple mutant or TM) to form a disulfide bond with the naturally unpaired Cys-125 (Table 1). Therefore, the monovalent affinities of individual I domain variants for ICAM-1 span approximately six orders of magnitude ($K_D$ ~1 nM to 1 mM), as measured by surface plasmon resonance (SPR) or estimated by flow cytometry (Figure 4.1c; Table 1). Human I domain binds murine ICAM-1 with comparable affinity to human ICAM-1 (2 nM vs. 6 nM respectively; Figure 4.1c). Cross-reactivity with its murine homologue enables examination of on-target, off-tumor toxicity of I domain CAR T cells concurrently with on-target, on-tumor efficacy in preclinical mouse models with human tumor xenografts. In comparison, the R6.5 scFv (derived from the

**Table 1. Measured affinity of LFA-1 I domain to ICAM-1**

| Name | Sequence | Affinity |
|---|---|---|
| Wild-type (WT) | G128-G311 | 1.5 mM* |
| F292A | G128-G311 | 20 μM* |
| F292G | G128-G311 | 119 nM* |
| F265S | G128-G311 | 145 nM* |
| F265S/F292G (DM) | G128-G311 | 6 nM* |
| F265S/F292G/G311C (TM) | E124-S313 | ~1 nM* |
| R6.5 | scFv | 10 nM** |

*SPR measurements; **Estimated from titrated R6.5 antibody binding to HeLa cells[35].

mouse hybridoma clone, R6.5[36]) has a Kd of 10 nM for human ICAM-1 (Table 1) but does not cross-react with murine ICAM-1.

To test whether the mutant I domain affinities correlate with CAR affinities, HEK 293T and Jurkat T cells were transduced with lentivirus encoding 3$^{rd}$ generation CARs containing TM, F292G, F292A, or WT I domain, and assayed for ICAM-1 binding. A myc tag was appended to the N-terminus of each I domain variant to aid measurement of CAR expression (Figure 4.1d,e). To avoid background ICAM-1 binding to endogenous LFA-1 in Jurkat T cells, CAR affinity for ICAM-1 was estimated using the I domain CAR-transduced HEK 293T cells. The level of recombinant human ICAM-1 binding to I domain CAR-expressing HEK 293T cells correlated with solution affinity measurements, with TM exhibiting the strongest binding, followed by F292G and F292A, and no detectable binding to WT compared to non-transduced (NT) T cells (Figure 4.1f). Differential CAR affinities for ICAM-1 and cross-reactivity with murine ICAM-1 were also examined by measuring cell adhesion to V-bottom plates coated with recombinant human or murine ICAM-1 (Figure 4.1g). Jurkat cells transduced with TM and F292G CARs demonstrated a higher level of binding to both human and murine ICAM-1 compared to non-transduced cells. However, despite increased binding of recombinant ICAM-1 to F292A CAR-expressing HEK 293T cells compared to their WT I domain-expressing counterparts (Figure 4.1f), F292A CAR-Jurkat cells lacked any additional binding to plate-bound ICAM-1 compared to NT or WT I domain-expressing cells (Figure 4.1g). In the case of F265S I domain, which demonstrated soluble ICAM-1-binding comparable to F292G (145 vs. 119 nM, Table 1), F265S CAR T cells failed to

demonstrate any additional binding to plate-bound human ICAM-1 while elevated binding was more apparent to murine ICAM-1. As anticipated, T cells transduced to express R6.5 CAR, which is specific to human ICAM-1 only, exhibited elevated binding to human but not to murine ICAM-1 (Figure 4.1g).

*Influence of CAR affinity and target antigen density on CAR T cell activation in vitro.*

Jurkat T cells expressing I domain CARs were used to examine the extent to which CAR T cell activation was influenced by CAR affinity and ICAM-1 antigen density in target cells. Jurkat T cells were incubated with various target cell lines with different ICAM-1 expression levels (Figure 4.2a). ICAM-1 surface densities of target cell lines were estimated by first assaying the levels of anti-ICAM-1 antibody binding to them and comparing these signals to those obtained using latex beads pre-coated with known amounts of the same antibody (Figure 4.2a; top panel). The panel of target cells include: HMEC-1 and bEnd.3, representing, respectively, healthy human and mouse cells with physiological levels of ICAM-1 ($\sim 10^4$ molecules per cell); anaplastic thyroid carcinoma (8505C) expressing an intermediate level ($\sim 10^5$ per cell); and cervical cancer (HeLa) cell lines expressing a high level of ICAM-1 ($\sim 10^6$ per cell). For additional comparisons, we included 8505C with CRISPR/Cas9-mediated ICAM-1 gene inactivation (8505C/-ICAM-1) and 8505C treated with LPS to upregulate ICAM-1 expression (8505C/LPS). Activation of CAR T cells upon interaction with target cells was examined by measuring CD25 (IL-2 receptor $\alpha$) and CD69 expression (Figure 4.2b,c). Elevated levels of CD25 were observed in WT I domain CAR T cells following incubation with LPS-stimulated 8505C but not with other cell lines

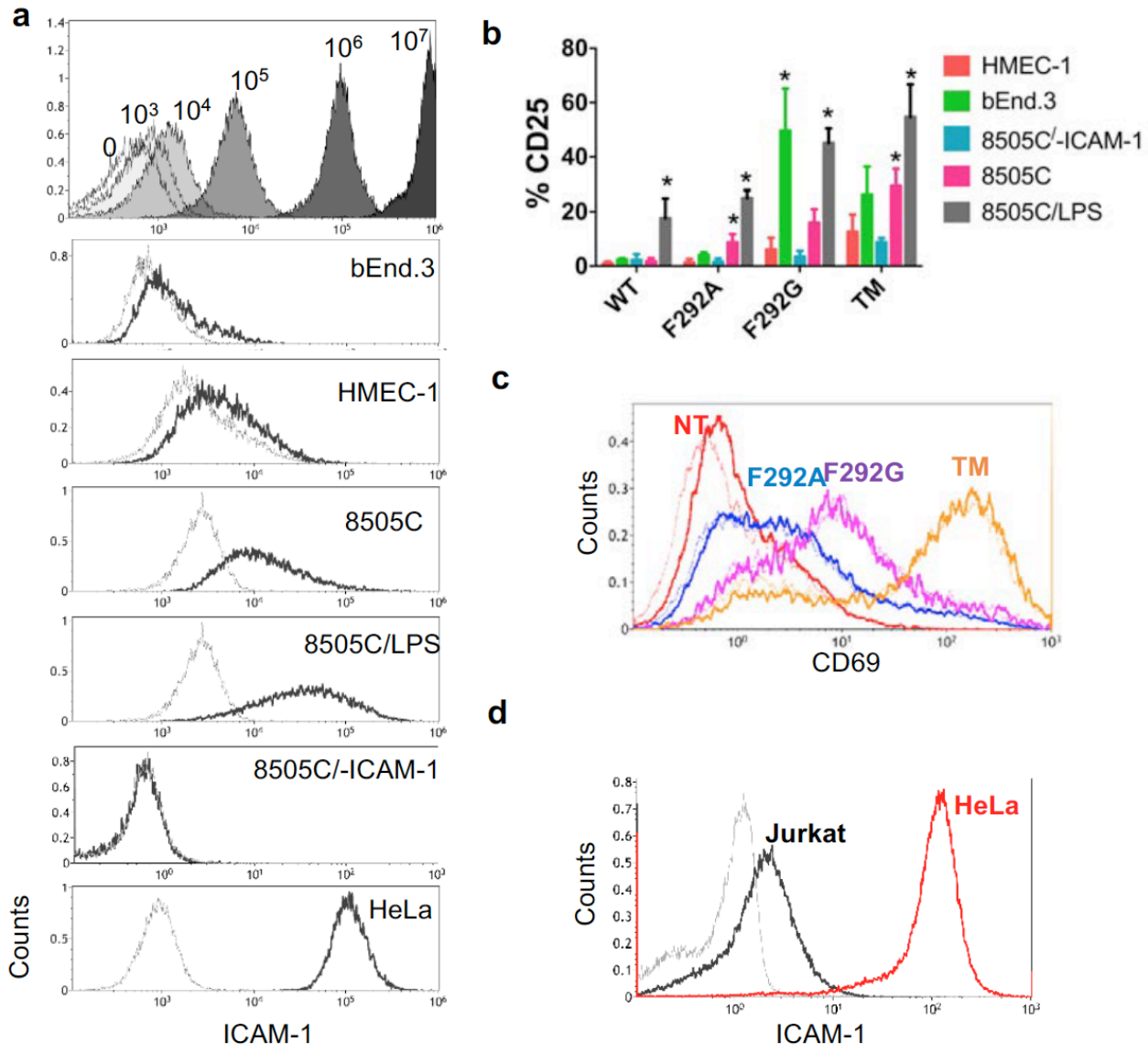
a
0
10^3
10^4
10^5
10^6
10^7
bEnd.3
HMEC-1
8505C
8505C/LPS
8505C/-ICAM-1
HeLa
Counts
ICAM-1
b
% CD25
HMEC-1
bEnd.3
8505C-/-ICAM-1
8505C
8505C/LPS
WT
F292A
F292G
TM
c
NT
F292A
F292G
TM
Counts
CD69
d
Jurkat
HeLa
Counts
ICAM-1

**Figure 4.2 Affinity and antigen-density dependent activation of Jurkat CAR T cells *in vitro*. (a)** Top, histograms depicting 8 μm latex beads coupled with known amounts of R6.5 antibody conjugated with cy5.5 ($10^3$-$10^7$ antibodies per bead). The level of shift after incubation with R6.5 (black) from non-labeled (grey) was used to estimate ICAM-1 density in each indicated target cell line. 8505C/-ICAM-1; 8505C cells with ICAM-1 gene inactivation by CRISPR/Cas9. 8505C/LPS, 8505C cells were incubated with LPS to induce overexpression of ICAM-1. **(b)** CD25 expression in Jurkat CAR T cells (WT, F292A, F292G, and TM) after co-incubation with different target cell lines for 24 h (n = 3-4). $p < 0.01$ for * vs. 8505C/-ICAM-1 by Dunnett's multiple comparisons test. **(c)** Induction of CD69 after incubation with latex beads coated with $10^6$ recombinant human ICAM-1-Fc molecules. Histograms correspond to CD69 expression in Jurkat cells without (thin, dotted line) and with (think) bead incubation. **(d)** ICAM-1 expression in Jurkat T cells compared to HeLa cells. Grey and black histograms correspond to unlabeled cells and R6.5 antibody-labeled cells, respectively.

expressing lower levels of ICAM-1 (Figure 4.2b). In contrast, increased CD25 expression was seen when high affinity TM CAR T cells were incubated with high ICAM-1 expressing cells as well as with HMEC-1 and bEnd.3 cells expressing basal levels of ICAM-1. A low-level of CD25 expression was detected on TM CAR T cells following incubation with target cells lacking ICAM-1 expression (8505C/-ICAM-1), likely due to homotypic cellular contacts mediated by molecular interactions between TM CAR and basal expression of ICAM-1 on Jurkat cells (~$10^4$ molecules/cell; Figure 4.2e). T cells expressing F292G behaved similar to TM, except that CD25 expression was close to background levels following co-incubation with 8505C/-ICAM-1. The micromolar affinity F292A T cells demonstrated selective activation displaying elevated CD25 expression only upon incubation with 8505C and 8505C/LPS cells (Figure 4.2b). This indicates that a threshold target antigen density of $>10^5$ ICAM-1 molecules per cell was required for F292A CAR T cell activation. In contrast to the ICAM-1 density-dependent activation of CD25, increased CD69 expression was observed even in the absence of target cells, with expression levels aligning closely with CAR affinity to ICAM-1, which was not further enhanced by incubation with ICAM-1 coated latex beads (Figure 4.2c). Compared to CD25, CD69 induction appeared to require a lower level threshold of antigen density for activation, which was provided by homotypic interaction between CAR T cells.

*Influence of CAR affinity and target antigen density on CAR T cell cytotoxicity in vitro.*

After validating affinity and antigen-dependent activation of CAR-modified Jurkat T cells, we sought to examine the influence of CAR affinity and antigen density on primary T cell activation and cytotoxicity *in vitro*. Primary T cells were transduced with TM, F292A, F292G, and WT I domain CARs, and added to various target cells to determine their cytotoxic efficacy *in vitro*. Overall, there was a positive correlation between the rate of target cell lysis and ICAM-1 expression (HeLa > 8505C/LPS > 8505C > HMEC-1 > bEND.3) across all I domain variant CAR T cells (Figure 4.3a). The rate of killing was also faster when T cells expressed CARs possessing higher affinity for ICAM-1 (TM > F292G > F292A > WT). To quantitatively compare the efficacy of killing by affinity variant CAR T cells, a variable slope sigmoidal curve (%live = $100/[1+10^{(t-\tau\_50\%)* \text{Slope}}]$) was used to find the best fit values describing the time required to achieve 50% killing (τ_50%) and the Hill slope (Figure 4.3b). The time to 50% target killing was longer with either lower affinity CAR T cells or lower antigen density for the same CAR T cells. The Hill slope, corresponding to the rate of target killing by CAR T cells, was higher with increases in affinity (lower Kd) for the same target cells. The Hill slope was also greater with increases in antigen density for the same CAR T cells. CAR T cell killing of target cells was specific as evidenced by the lack of observed killing of ICAM-1 negative 8505C cells by all of I domain variant CARs except TM. Low yet gradual killing of 8505C/-ICAM-1 by TM T cells was likely due to cytotoxic activation caused by homotypic cellular contacts mediated by TM interaction with ICAM-1 in T cells. ICAM-1 expression in primary T cells can be induced after T cell activation such as by incubation with CD3/CD28 beads (~$10^5$ molecules/cell; Figure 4.3c). In comparison, WT CAR T cells possessing millimolar

affinity (Kd = 1.5 mM) could specifically lyse HeLa cells only, indicating a threshold antigen density of approximately $10^6$ molecules per cell for ~1 mM Kd CAR T cells. Importantly, F292A and WT I domain CAR T cells (Kd > 10 μM) were unreactive to human and murine healthy control cells, HMEC-1 and b.END3 (~$10^4$ per cell; Figure 4.3a). Likewise, IFN-γ release by CAR T cells aligned closely with the rate of target cell death, where increasing levels were found in co-cultures containing higher affinity CAR T cells and/or higher levels of target antigen expression (Figure 4.3d). One exception to target antigen density-dependent IFN-γ release was TM and F292G, which showed significant amounts of IFN-γ release (>1 ng/ml) in the absence of target molecules (8505C/-ICAM-1). This is again likely due to the homotypic interactions between T cells, which is also supported by the observation of the difficulty with expanding TM CAR T cells, particularly when the level of CAR expression was high. Release of IFN-γ by micromolar affinity CAR T cells (F292A) was in proportion to the ICAM-1 density in target cells, demonstrated by a lack of release upon incubation with 8505C/-ICAM-1, and progressively increasing with incubation with HMEC-1, 8505C, 8505C/LPS, and HeLa in this order (Figure 4.3d). Consistent with WT I domain's cytotoxicity toward HeLa cells, IFN-γ release upon incubation with HeLa was comparable to the levels secreted by other higher affinity CAR T cells.

*In vivo efficacy of affinity-tuned I domain CAR T cells.*

We examined how affinity-dependent CAR T cell cytotoxicity patterns *in vitro* would translate to tumor xenograft models *in vivo*. In solid tumors, CAR T cell

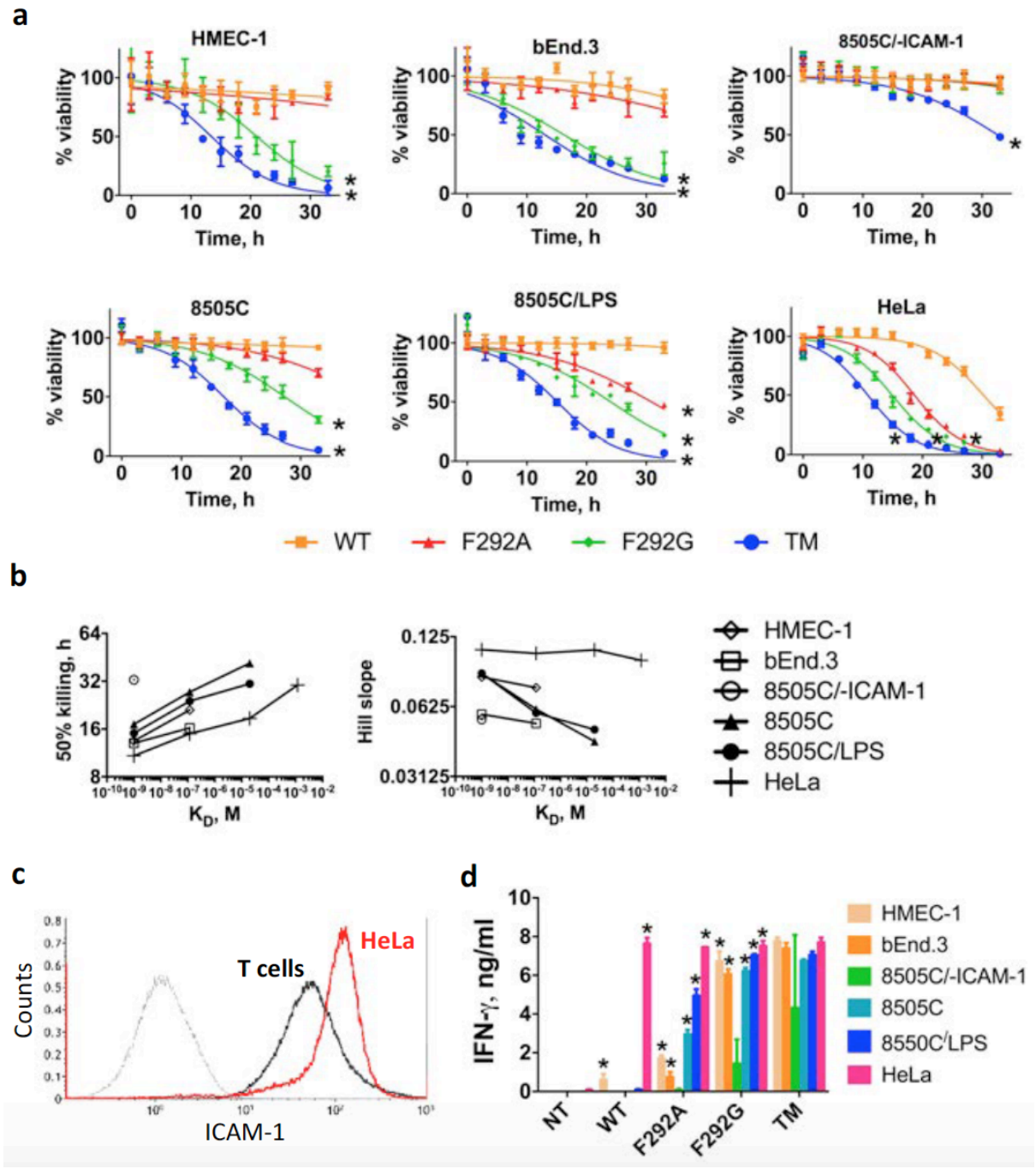
a
HMEC-1
bEnd.3
8505C/-ICAM-1
8505C
8505C/LPS
HeLa
% viability
Time, h
WT
F292A
F292G
TM
b
50% killing, h
Hill slope
K_D, M
HMEC-1
bEnd.3
8505C/-ICAM-1
8505C
8505C/LPS
HeLa
c
Counts
T cells
HeLa
ICAM-1
d
IFN-γ, ng/ml
NT
WT
F292A
F292G
TM
HMEC-1
bEnd.3
8505C/-ICAM-1
8505C
8550C/LPS
HeLa

**Figure 4.3 Affinity and antigen-density dependent activation of primary CAR T cells *in vitro*. (a)** Effector to target (E:T) assay for measuring target killing by primary T cells transduced with different I domain CARs. Each target was separately incubated with TM, F292G, F292A or WT CAR T cells at 5:1 E:T ratio. Percent viability was normalized to luminescence from target cells incubated with NT T cells (n=3, ± = standard deviation (SD)). A variable slope sigmoidal curve equation was used to fit data. $p < 0.01$ for * vs. NT by Dunnett's multiple comparisons test. **(b)** The best fit values of 50% killing and Hill slope of the sigmoidal equation were plotted against the affinities of I domain CARs. The best fit values with r-square values higher than 0.85 were plotted. **(c)** ICAM-1 expression in primary T cells in comparison to HeLa cells. Grey and black histograms correspond to unlabeled cells and R6.5 antibody-labeled cells, respectively. **(d)** IFN-γ release was measured by ELISA for each CAR T variant after co-incubation with different target cells for 24 h (n=3). $p < 0.01$ for * vs. 8505C/-ICAM-1 by Dunnett's multiple comparisons test.

efficacy is influenced by their ability to traffic to tumor sites, penetrate, serially lyse tumor cells, and undergo expansion and contraction in accordance with tumor burden. Here, mice were xenografted by systemic *i.v.* injections of $0.75x10^6$ 8505C-$FLuc^+GFP^+$ cells followed by treatment with ~$1\text{-}3x10^6$ I domain CAR T cells (WT, F292A, F265S, F292G, and TM), SSTR2-R6.5 CAR[29], NT T cells, and no T cells at 8-10 days post-xenograft (5-20% CAR expression). Tumor burden was evaluated by whole-body luminescence imaging of firefly luciferase activity. Primary tumors localized to the lungs and liver with distant metastatic foci evident throughout the body (Figure 4.4a). Cohorts receiving either no T cells or NT T cells succumbed to tumor burden within 3-4 weeks of tumor inoculation. Mice treated with TM CAR T cells displayed rapid initial reductions in tumor burden; however, at approximately 7 days post T cell injection, mice began to show symptoms of systemic toxicity indicated by lethargy and weight loss, resulting in death by day 15 post treatment (Figure 4.4a,b). F292G CAR T cells were capable of tumor elimination with inconsistent toxicity development, which appeared to be partially dependent on tumor burden at the time of CAR T cell treatment. For example, either delayed infusions of F292G CAR T cells (day 10) or higher tumor burden at the time of treatment led to more frequent deaths. T cells expressing F265S CARs (Table 1), eliminated tumors without observable toxicity. This suggests that an I domain CAR affinity of ~100 nM Kd defines an approximate threshold affinity above which treatment leads to reduced discrimination between high and low antigen densities and an increased likelihood of on-target off-tumor toxicity. Consistent with limited or lack of killing of 8505C by WT CAR T cells *in vitro*, tumor progression *in vivo* was unimpeded by the treatment,

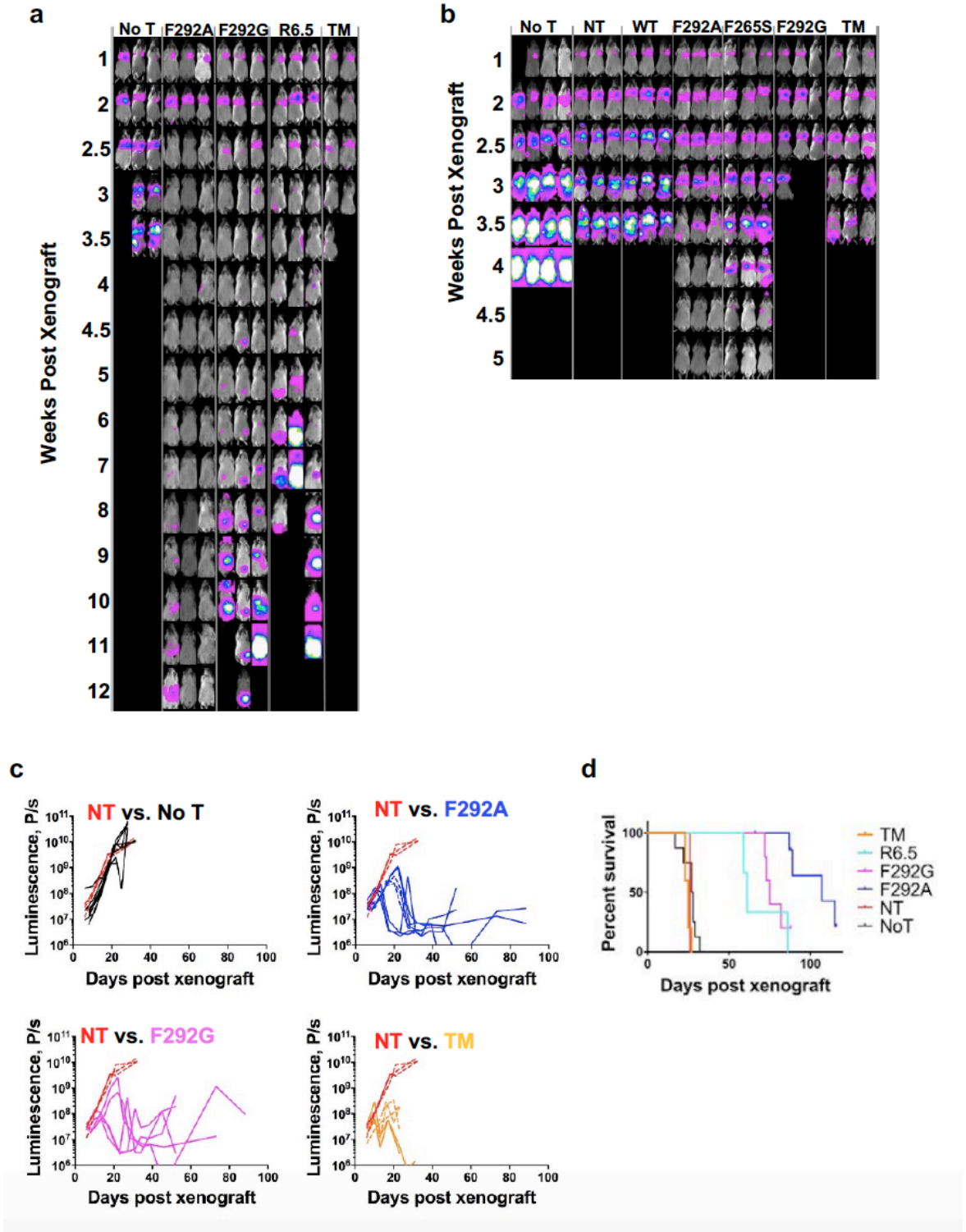
a
No T
F292A
F292G
R6.5
TM
Weeks Post Xenograft
1
2
2.5
3
3.5
4
4.5
5
6
7
8
9
10
11
12
b
No T
NT
WT
F292A
F265S
F292G
TM
Weeks Post Xenograft
1
2
2.5
3
3.5
4
4.5
5
c
NT vs. No T
NT vs. F292A
NT vs. F292G
NT vs. TM
Luminescence, P/s
Days post xenograft
d
Percent survival
Days post xenograft
TM
R6.5
F292G
F292A
NT
NoT

**Figure 4.4 Micromolar affinity CAR T cells provide superior tumor eradication, suppression of tumor relapse, and survival benefit. (a)** Whole-body luminescence imaging was used to estimate tumor burden in mice infused with different CAR T cell variants 8 days post-tumor implantation. No T = mice received no T cells. **(b)** Mice were treated with CAR T cells 10 days post tumor implantation. NT = non-transduced T cells. **(c)** Luminescence measurements of mice treated with different CAR T cells. Individual lines indicate luminescence values from each mouse. P values of two-tailed student's t-test versus NT (n = 3) are not-significant for No T (n = 8), $p<0.001$ for F292A (n = 8) and F292G (n = 5), and $p<0.05$ for TM (n = 5). **(d)** Survival curves of mice receiving different treatments. Log-rank (Mantel-Cox) test P values versus NT are not-significant for No T and TM, and $p = 0.008$ for F292G, $p = 0.025$ for R6.5, and $p = 0.0016$ for F292A.

similar to NT T cells (Figure 4.4b). In contrast, F292A CAR T cells, which exhibited a much slower *in vitro* rate of 8505C killing compared to its higher affinity counterparts, achieved rapid reductions in tumor burden with no apparent toxicity irrespective of treatment timing (Figure 4.4a-c). Moreover, F292A CAR T *in vivo* efficacy was superior to the scFv-based R6.5 CAR despite >1,000-fold lower affinity to ICAM-1 (10 nM vs. 20 μM), as evidenced by a faster rate of tumor clearance and durable suppression of tumor relapse (Figure 4.4a). Overall, the anti-tumor efficacy of I domain CAR T cells led to statistically significant increases in cohort survival compared with no T or NT T cell treated mice (Figure 4.4d). However, CAR T cell-treated mice even with no to little tumor burden began to show signs of toxicity (e.g., weight loss, loss of fur) that eventually led to frequent death ~10 weeks after T cell injections. This was suspected to be related to graft-versus-host disease[37] and not on-target, off-tumor toxicity as similar toxicities were observed in mice treated with R6.5 CAR T cells that exclusively target human ICAM-1.

*Cellular analysis of CAR T cell efficacy and toxicity.*

Cellular analysis of tumor and T cells by flow cytometry revealed the cause for systemic toxicity induced by high affinity CAR T cells, such as TM. Similar to the previously observed biphasic expansion and contraction response of human ICAM-1-specific, R6.5 CAR T cells[29], TM CAR T cells also exhibited gradual expansion concurrent with reductions in tumor burden. However, in contrast to R6.5 CAR, TM CAR continued to expand even after tumor elimination, eventually accounting for ~50% of live cells in the lungs at the time of death or sacrifice (Figure 4.5a). This

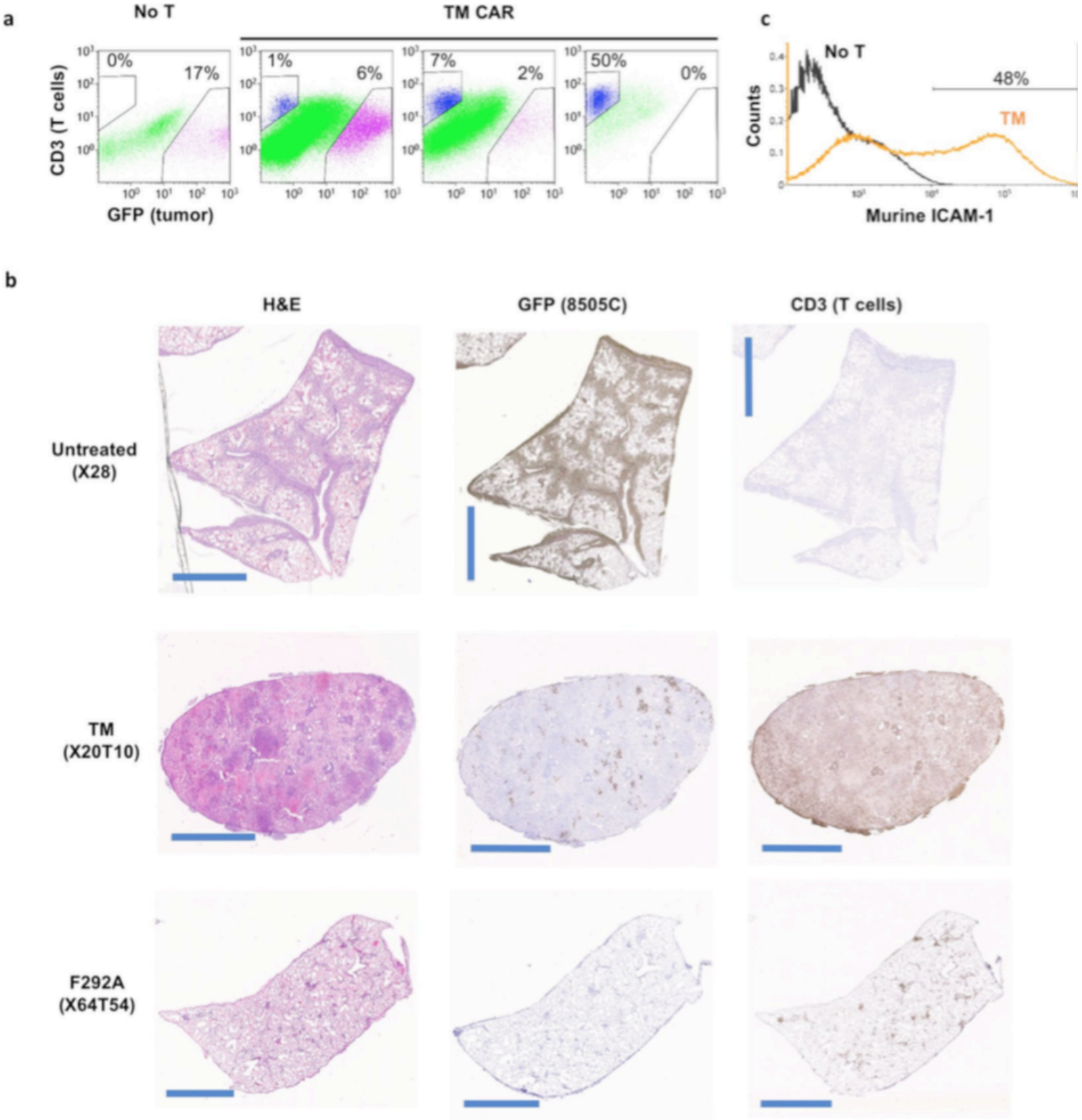
a
No T
TM CAR
CD3 (T cells)
GFP (tumor)
0%
17%
1%
6%
7%
2%
50%
0%
c
No T
TM
48%
Counts
Murine ICAM-1
b
H&E
GFP (8505C)
CD3 (T cells)
Untreated
(X28)
TM
(X20T10)
F292A
(X64T54)

**Figure 4.5 Analysis of systemic toxicity by flow cytometry and histology. (a)** Flow cytometry analysis of cells harvested from the lungs of non treated (No T) or treated (TM CAR) mice. GFP and CD3 were used as markers of 8505C tumor and T cells, respectively. Mice treated with TM CAR T cells were sacrificed at different time points to represent the association between tumor burden and TM CAR T cells. **(b)** Lung tissues harvested from untreated mice and mice treated with TM and F292A CAR T cells were processed for H&E, GFP and CD3 staining. The scale bar in each image is 2 mm. Tissue sacrifice time points are indicated on the left. For example, X20T10 represents 20 days post tumor xenograft and 10 days post T cell infusion. **(c)** Murine ICAM-1 expression in lung cells harvested from tumor-bearing mice after treatment with TM CAR T cells.

expansion of TM CAR T cells in the absence of or with very low tumor burden was also confirmed by histology (Figure 4.5b). Compared to the heavy tumor burden in lungs of untreated mice, the lungs from mice treated with TM CAR T cells exhibited sparsely distributed tumor cells while demonstrating heavy infiltration with CD3 positive T cells. In comparison, the lungs of mice treated with F292A CAR T cells were almost entirely tumor-free with only sparsely distributed T cells present, indicative of the T cell contraction observed previously with R6.5 CAR T cells after tumor elimination in the same model[29]. The near uniform systemic toxicity observed in mice treated with TM CAR T cells appeared to depend on the initial presence of tumor as there was no apparent systemic toxicity observed in non-tumor bearing mice that received TM CAR T cells (4/4 mice surviving more than 2 months after T cell infusion). We speculate that TM and at times, F292G CAR T cells reacted with murine ICAM-1 that was upregulated in response to exposure to inflammatory cytokines secreted by CAR T cells or lysed tumor cells during interaction with human ICAM-1-expressing tumors. Indeed, similar to the induction of ICAM-1 in the lungs by LPS in our previous study [38], ~50% of live lung cells from TM CAR T-treated mice stained positive for murine ICAM-1, compared to much lower expression and percentage of ICAM-1 stained cells from non-tumor bearing or tumor-xenografted mice without T cell treatment (Figure 4.6 a&b in Kang et al.,[38]; Figure 4.5c).

*Real-time imaging of CAR T cell kinetics, efficacy, toxicity, and correlation with cytokine profiles.*

To spatiotemporally monitor T cell distribution in real-time by PET/CT, we introduced an imaging reporter gene, SSTR2 into the I domain CAR vector using a ribosome skipping P2A sequence to ensure equal expression of CAR and the reporter on the surface of T cells (Figure 4.6a). Expression of SSTR2 enables binding and intracellular accumulation of an infused, positron-emitting, SSTR2-specfic radiotracer, $^{18}$F-NOTA-Octreotide[30]. Emitted signals can then be detected with high resolution with no tissue penetration issues by a micro PET scanner. Expression of SSTR2 and Myc tagged I domain was confirmed by antibody staining, although higher level of binding was found with SSTR2 antibody (Figure 4.6b). Mice were xenografted with 8505C tumors as before, and were treated with NT, F292A, or F292G CAR T cells. Whole-body luminescence imaging was performed to estimate tumor burden while PET/CT imaging was performed on the same day to track CAR T cell distribution (Figure 4.6c). At each time point, blood was collected to measure human cytokines for correlation with T cell dynamics. PET/CT images in mice displayed expected background levels in gall bladder, kidneys and bladder caused by radiotracer excretion (Figure 4.6c; far-right). In the NT treated control cohort, a small but gradual increase in non-specific tracer uptake was observed, which was due to increasing tumor burden and the associated increase in blood pooling (Figure 4.6c,d). In contrast, specific tracer uptake was observed in mice treated with SSTR2-F292A CAR T cells, demonstrating the expansion and contraction phases in the lungs, with peak CAR T cell signal occurring approximately 4 days following peak tumor burden and gradually decreasing to background levels (Figure 4.6c,d). This biphasic T cell expansion and contraction phenomenon was reminiscent of our previous study using SSTR2-R6.5

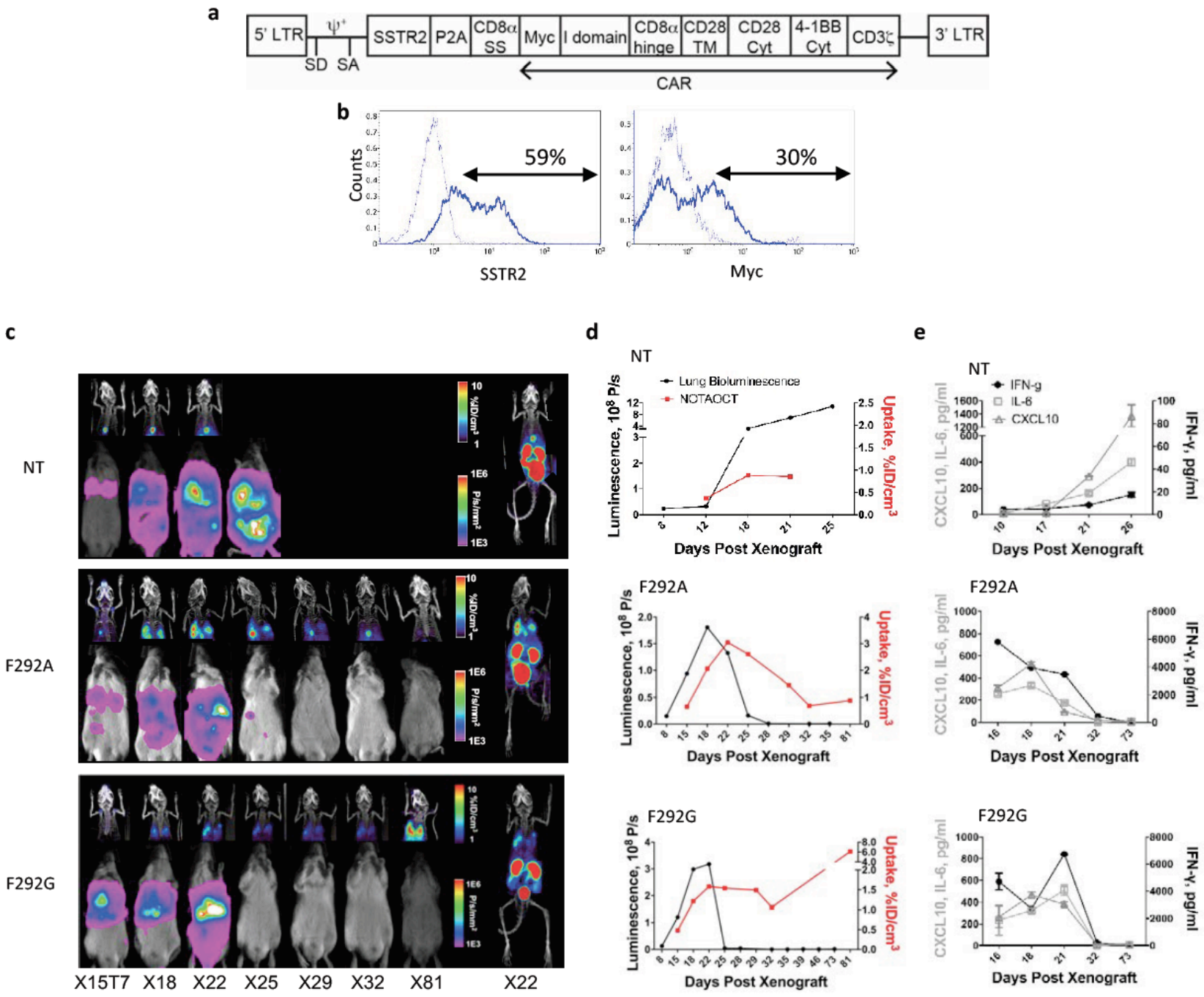
a
5' LTR
ψ+
SD
SA
SSTR2
P2A
CD8α SS
Myc
I domain
CD8α hinge
CD28 TM
CD28 Cyt
4-1BB Cyt
CD3ζ
3' LTR
CAR
b
Counts
59%
30%
SSTR2
Myc
c
NT
F292A
F292G
X15T7
X18
X22
X25
X29
X32
X81
X22
d
NT
Lung Bioluminescence
NOTA0CT
Luminescence, 10^8 P/s
Uptake, %ID/cm3
Days Post Xenograft
F292A
F292G
e
NT
IFN-g
IL-6
CXCL10
CXCL10, IL-6, pg/ml
IFN-γ, pg/ml
Days Post Xenograft
F292A
F292G

**Figure 4.6 Longitudinal, concurrent measurements of tumor burden, T cell distribution, and cytokine release. (a)** Schematic of SSTR2-I domain vector. **(b)** Flow cytometry measurements of SSTR2 reporter gene and Myc-tag expression representing CAR on the surface of primary human T cells. Thin and thick histograms represent T cells with and without antibody labeling, respectively. **(c)** Longitudinal measurements of NOTAOCT uptake by PET/CT (top half of each panel), and tumor burden by whole body luminescence imaging (bottom half of each panel). Images are representative of four mice in each cohort. Whole body PET/CT images, taken on the day of maximum tracer uptake, are shown on the far right. Imaging time points are indicated below the bottom panel. For example, X15T7 represents 15 days post tumor xenograft and 7 days post T cell infusion. **(d)** Quantification of luminescence and tracer uptake in the lungs of mice treated as indicated. **(e)** Cytokine levels measured from blood drawn at various time points from the same mice in ‘c’ and ‘d’ are plotted (mean ± SD, duplicate measurements).

CAR T cells in the same mouse tumor model[29]. Cytokine analysis of serum obtained from treated mice demonstrated a surge in IFN-γ, IL-6, and CXCL10 concentrations prior to peak T cell expansion, which also returned to background levels post tumor elimination and following contraction of T cell density in the lungs to background levels (Figure 4.6e). F292G CAR T-treated mice showed similar yet lower T cell expansion in the lungs, with a peak T cell density being nearly concurrent with the maximum tumor burden. The serum cytokine profile was similar to that observed in F292A CAR T-treated mice. Again, in some instances treatment with F292G CAR T led to host mortality, likely due to on-target, off-tumor toxicity. This was clearly evidenced by a gradual increase in F292G CAR T cell presence in lungs and other organs, as detected by PET/CT imaging, leading to a tracer uptake of ~6% ID/cm$^3$ even after tumor clearance. Based on our previous study, we estimate that this level of uptake corresponds to a T cell density in lungs that is significantly above 10% (which gave ~3 ID/cm$^3$ in 10% SSTR2 positive Jurkat mosaic tumors). The level of tracer uptake, far higher than T cell peak from interaction with tumor, was reminiscent of the case with TM CAR T cells, where T cells accounted for >50% of total cells in lungs post tumor eradication (Figure 4.5a).

**Discussion**

The paucity of native, surface-expressed, and tumor-specific antigens presents a significant hurdle to developing CAR T cell therapy against solid cancers[39, 40]. Conventional CARs are constructed using a single-chain antibody format, and are selectively engineered to possess sub- to low nanomolar affinities for target antigens.

However, increased CAR T cell sensitivity may be an advantage only when targeting true tumor antigens or those with the highest levels of restriction[17, 39]. Otherwise, increased sensitivity comes at the price of reduced selectivity with lysis of target-expressing cells in a manner largely insensitive to antigen density[18]. By functionally investigating CAR affinities spanning step-wise across a $10^6$-fold range, concurrently with target cells with varying levels of antigen expression, we systematically examined the influence of CAR affinity and antigen density on T cell efficacy *in vitro* and *in vivo*. T cell activation status *in vitro*, as measured by CD25, cytokine release, and cytotoxicity, was to a remarkable degree dependent on affinity and target antigen density, resulting in more potent T cell activation and target killing with increases in CAR affinity and antigen density. The activation threshold of nanomolar affinity CAR T cells (TM, F292G) was less dependent on antigen density compared to the micromolar affinity CAR T cells (F292A), reacting to antigen density as low as $10^4$ molecules/cell. In contrast, F292A CAR T cells rapidly lost the ability to lyse cells expressing target antigens below $10^5$ molecules/cell. Millimolar affinity CAR T cells (WT) were largely unreactive to target cells with low to moderate levels of antigen, requiring a threshold antigen density of $10^6$ molecules/cell for detectable activation, cytokine release, and target lysis to occur. The quantitative harmony between CAR affinity and anti-tumor potency *in vitro* was discordant with quantitative *in vivo* observations whereby micromolar affinity CAR T cells were superior to higher affinity CAR T cells as measured by the rate of expansion at the tumor site, the rate of tumor eradication, frequency of tumor relapse, and levels of on-target, off-tumor toxicity.

The ability of I domain CAR T cells to cross-react with murine ICAM-1 allowed for a rigorous and simultaneous assessment of CAR T cell efficacy against human tumor cells and on-target, off-tumor toxicity against murine ICAM-1 on healthy tissues. Onset of toxicity appeared to be dependent on CAR affinity and tumor-burden, as demonstrated by the uniform fatalities in mice treated with the highest affinity (TM) CAR T cells, the increased rate of toxicity observed in F292G CAR-treated mice with larger tumor burden, and the absence of detectable toxicity after treatment with micromolar affinity F292A CAR T cells. The relationship between tumor-burden and CAR-mediated toxicity is likely a consequence of ICAM-1 biology. ICAM-1 is an inducible adhesion molecule that is sensitive to inflammatory stimuli and the tumor-related inflammatory milieu[41-44]. We suspect that cytokine-induced ICAM-1 overexpression is a reason for the onset of toxicity mediated by the high affinity CAR T cells, demonstrated by the lack of apparent toxicity following TM CAR T treatment in non-tumor bearing animals. This observation suggests that either ICAM-1 density is below the threshold antigen density for TM ($10^4$ molecules/cell) or the cells expressing ICAM-1 above this threshold are not exposed to TM CAR T cells. Leukocyte adhesion and diapedesis requires LFA-1 to be in an activated, open configuration along with concurrent upregulation of ICAM-1 on endothelial cells[45]. This augments the hypothesis that ICAM-1 upregulation on healthy tissues is also necessary for activation of even nanomolar affinity I domain CAR T cells. Rapid expansion of CAR T cells in response to growing tumor burden may drive local concentrations of inflammatory cytokines to breach the antigen threshold to cause both F292G and TM CAR T cells to become fatal to the host despite the approximately

100-fold difference in affinity. Despite induction of similar peripheral concentrations of inflammatory cytokines (IFN-γ, IL-6, and CXCL10) in mice treated with F292G or F292A CAR T cells, local or systemic toxicity by F292A CAR T was not observed. Given the estimated threshold antigen density requirement of ~$10^5$/cell for F292A mediated-cytotoxicity to occur, we speculated that inflammation-induced murine ICAM-1 may still be below this threshold. Systemic toxicity and fatality were also absent in animals treated with F265S CAR T cells. The F265S CAR demonstrated weaker binding to plate-bound ICAM-1 *in vitro* compared to F292G CAR despite their comparable solution affinity to ICAM-1.

To investigate the mechanics of affinity-variant CARs *in vivo*, we employed longitudinal and concurrent measurements of cytokine release, T cell distribution, and tumor killing. In our model, high concentrations of IFN-γ, IL-6, and CXCL10 were measured as early as 7 days post-infusion of T cells, indicating that infused T cells were engaging their target and proliferating. In agreement with our previous study using R6.5 CAR T cells targeting human ICAM-1 only[29], there was a time delay between peak tumor burden and peak I domain CAR T cell expansion as measured by PET/CT. The swift reduction in tumor burden and CAR T cell numbers at the tumor site, along with the resolution of inflammation as measured by cytokines, is indicative of therapeutic efficacy in a manner similar to classical infection scenarios[46, 47]. This biphasic response is absent in situations where CAR T cells fail to properly control tumor growth[29]. The onset of cytokine release detected prior to observable T cell expansion by PET/CT using the SSTR2 radiotracer suggests that any improvement on imaging sensitivity (currently 1% $SSTR2^+$ T cell density within

tumors) can shorten this imaging latency period and aid in determining if heightened T cell activity is at on- or off-target sites. Peak serum IL-2 levels were determined to be relatively low (<50 pg/ml) in comparison to IFN-γ, IL-6, and CXCL10 levels. As severe cytokine release syndrome was determined as the cause of death in some patients enrolled in CD19-targeting CAR T cell trials, our cytokine kinetics data suggests that blood analysis immediately after T cell infusion will be critical to estimate T cell activity. Once a cytokine surge is observed, patients receiving tumor-targeted T cells expressing SSTR2 can be subjected to PET/CT to examine the T cell distribution profile and determine whether they are expanding at the tumor site, indicating T cell killing of tumor, or, if they are expanding away from the tumor, indicating the onset of off-tumor toxicities. In our study, the continued expansion of the nanomolar affinity F292G CAR T cells despite elimination of tumors was likely caused by activation of CAR T cells by inflammation-induced ICAM-1. Such instances of off-tumor T cell expansion in patients could be easily diagnosed and localized by imaging techniques such as PET/CT, which we anticipate will be increasingly utilized in future adoptive T cell trials to provide detailed trafficking information and thus aid general therapy development including dosing protocols and intervention strategies to avoid harmful or even fatal toxicities by administered cells[48, 49].

The functional goal when creating affinity tuned CAR T cells in prior studies has been to minimize off-tumor toxicity against basally expressed antigens in normal tissues[18, 50]. However, we believe that CARs possessing affinities in the micromolar range may be superior to those in the nanomolar range for additional

reasons. Engagement of target antigen by nanomolar affinity CAR T cells (e.g., TM, F292G, and R6.5 CAR) likely results in an unnaturally slow off rate, deviating from transient and dynamic nature of interactions natively found between TCRs and pMHCs[51]. High affinity and avidity interactions by CAR can reduce T cells' propensity for serial killing, potentially causing exhaustion or increased susceptibility to activation-induced cell death[52]. The fact that the majority of CARs developed to-date rely upon nanomolar-affinity scFvs raises the possibility that these CAR T cells may not have achieved their maximum potential therapeutic index. This speculation also draws on prior observations on the influence of high affinity TCR and pMHC interactions on T cell fate [15, 16, 21, 23, 53]. Future CAR engineering strategies should evaluate a broader affinity range to examine the influence on T cell behavior and functionality *in vivo* more rigorously. This particularly applies to CARs targeting solid tumor antigens, which are likely to require evolved strategies to counter the more challenging environment.

In summary, our study demonstrates that CAR T cells with target-affinities mimicking that of native TCR for pMHC can eschew targeting of healthy tissue with basal antigen expression while simultaneously exhibiting increased potency and long-term efficacy against tumor tissue with high target expression. The micromolar affinity F292A CAR enabled T cells to neglect tissues expressing less than $10^5$ molecules/cell, a threshold which anaplastic thyroid tumors surpass yet healthy tissues that we examined do not. Various protein engineering approaches including directed evolution, alanine substitution within antibody complementary determining regions, or humanization of mouse antibodies[27, 50, 54, 55] to isolate lower affinity variants can

be used to modulate the affinity of scFv-based CARs or TCRs. Systematic studies examining the influence of scFv-based CAR (e.g., CD19 CAR) affinity on CAR T cell efficacy and toxicity will be necessary to further examine the hypothesis that T cells expressing traditional nanomolar affinity CARs are operating sub-optimally and may be more prone to exhaustion and excessive cytokine release, ultimately facilitating off-tumor toxicity or

REFERENCE


1. Maher, J., et al., *Human T-lymphocyte cytotoxicity and proliferation directed by a single chimeric TCRzeta /CD28 receptor*. Nat Biotechnol, 2002. **20**(1): p. 70-5.
2. Gross, G., T. Waks, and Z. Eshhar, *Expression of immunoglobulin-T-cell receptor chimeric molecules as functional receptors with antibody-type specificity*. Proc Natl Acad Sci U S A, 1989. **86**(24): p. 10024-8.
3. Hudecek, M., et al., *Receptor affinity and extracellular domain modifications affect tumor recognition by ROR1-specific chimeric antigen receptor T cells*. Clin Cancer Res, 2013. **19**(12): p. 3153-64.
4. Watanabe, K., et al., *Target antigen density governs the efficacy of anti-CD20-CD28-CD3 zeta chimeric antigen receptor-modified effector CD8+ T cells*. J Immunol, 2015. **194**(3): p. 911-20.
5. Kochenderfer, J.N., et al., *Eradication of B-lineage cells and regression of lymphoma in a patient treated with autologous T cells genetically engineered to recognize CD19*. Blood, 2010. **116**(20): p. 4099-102.
6. Porter, D.L., et al., *Chimeric antigen receptor-modified T cells in chronic lymphoid leukemia*. New England Journal of Medicine, 2011. **365**(8): p. 725--733.
7. Grupp, S.A., et al., *Chimeric antigen receptor-modified T cells for acute lymphoid leukemia*. N Engl J Med, 2013. **368**(16): p. 1509-18.
8. Brentjens, R.J., et al., *CD19-targeted T cells rapidly induce molecular remissions in adults with chemotherapy-refractory acute lymphoblastic leukemia*. Sci Transl Med, 2013. **5**(177): p. 177ra38.
9. Brudno, J.N. and J.N. Kochenderfer, *Toxicities of chimeric antigen receptor T cells: recognition and management*. Blood, 2016. **127**(26): p. 3321-30.
10. Cheever, M.A., et al., *The prioritization of cancer antigens: a national cancer institute pilot project for the acceleration of translational research*. Clin Cancer Res, 2009. **15**(17): p. 5323-37.
11. Kakarla, S. and S. Gottschalk, *CAR T cells for solid tumors: armed and ready to go?* Cancer J, 2014. **20**(2): p. 151-5.
12. Lamers, C.H., et al., *Treatment of metastatic renal cell carcinoma with autologous T-lymphocytes genetically retargeted against carbonic anhydrase IX: first clinical experience*. J Clin Oncol, 2006. **24**(13): p. e20-2.
13. Parkhurst, M.R., et al., *T cells targeting carcinoembryonic antigen can mediate regression of metastatic colorectal cancer but induce severe transient colitis*. Mol Ther, 2011. **19**(3): p. 620-6.
14. Morgan, R.A., et al., *Case report of a serious adverse event following the administration of T cells transduced with a chimeric antigen receptor recognizing ERBB2*. Mol Ther, 2010. **18**(4): p. 843-51.
15. Tian, S., et al., *CD8+ T cell activation is governed by TCR-peptide/MHC affinity, not dissociation rate*. J Immunol, 2007. **179**(5): p. 2952-60.

16. Hebeisen, M., et al., *Identifying Individual T Cell Receptors of Optimal Avidity for Tumor Antigens*. Front Immunol, 2015. **6**: p. 582.
17. Zhong, S., et al., *T-cell receptor affinity and avidity defines antitumor response and autoimmunity in T-cell immunotherapy*. Proc Natl Acad Sci U S A, 2013. **110**(17): p. 6973-8.
18. Liu, X., et al., *Affinity-Tuned ErbB2 or EGFR Chimeric Antigen Receptor T Cells Exhibit an Increased Therapeutic Index against Tumors in Mice*. Cancer Res, 2015. **75**(17): p. 3596-607.
19. Caruso, H.G., et al., *Tuning Sensitivity of CAR to EGFR Density Limits Recognition of Normal Tissue While Maintaining Potent Antitumor Activity*. Cancer Res, 2015. **75**(17): p. 3505--3518.
20. Arcangeli, S., et al., *Balance of Anti-CD123 Chimeric Antigen Receptor Binding Affinity and Density for the Targeting of Acute Myeloid Leukemia*. Mol Ther, 2017.
21. Chmielewski, M., et al., *T cell activation by antibody-like immunoreceptors: increase in affinity of the single-chain fragment domain above threshold does not increase T cell activation against antigen-positive target cells but decreases selectivity*. J Immunol, 2004. **173**(12): p. 7647-53.
22. Schmid, D.A., et al., *Evidence for a TCR affinity threshold delimiting maximal CD8 T cell function*. J Immunol, 2010. **184**(9): p. 4936-46.
23. Corse, E., et al., *Attenuated T cell responses to a high-potency ligand in vivo*. PLoS Biol, 2010. **8**(9).
24. Park, S., et al., *Tumor suppression via paclitaxel-loaded drug carriers that target inflammation marker upregulated in tumor vasculature and macrophages*. Biomaterials, 2013. **34**(2): p. 598--605.
25. Dustin, M.L., et al., *Induction by IL 1 and interferon-gamma: tissue distribution, biochemistry, and function of a natural adherence molecule (ICAM-1)*. J Immunol, 1986. **137**(1): p. 245-54.
26. Shimaoka, M., et al., *Reversibly locking a protein fold in an active conformation with a disulfide bond: integrin alphaL I domains with high affinity and antagonist activity in vivo*. Proc Natl Acad Sci U S A, 2001. **98**(11): p. 6009-14.
27. Jin, M., et al., *Directed evolution to probe protein allostery and integrin I domains of 200,000-fold higher affinity*. Proc Natl Acad Sci U S A, 2006. **103**(15): p. 5758--5763.
28. Wong, R., et al., *Visualizing and Quantifying Acute Inflammation Using ICAM-1 Specific Nanoparticles and MRI Quantitative Susceptibility Mapping*. Ann Biomed Eng, 2011. **40**(6): p. 1328--1338.
29. Vedvyas, Y., et al., *Longitudinal PET imaging demonstrates biphasic CAR T cell responses in survivors*. JCI Insight, 2016. **1**(19): p. e90064.
30. Laverman, P., et al., *A novel facile method of labeling octreotide with (18)F-fluorine*. J Nucl Med, 2010. **51**(3): p. 454-61.
31. McBride, W.J., et al., *A novel method of 18F radiolabeling for PET*. J Nucl Med, 2009. **50**(6): p. 991-8.

32. Kinahan, P.E. and J.W. Fletcher, *Positron emission tomography-computed tomography standardized uptake values in clinical practice and assessing response to therapy*. Semin Ultrasound CT MR, 2010. **31**(6): p. 496-505.
33. Jin, M., et al., *Directed evolution to probe protein allostery and integrin I domains of 200,000-fold higher affinity*. Proc Natl Acad Sci U S A, 2006. **103**(15): p. 5758-63.
34. Wong, R., et al., *Visualizing and quantifying acute inflammation using ICAM-1 specific nanoparticles and MRI quantitative susceptibility mapping*. Ann Biomed Eng, 2012. **40**(6): p. 1328-38.
35. Leelawattanachai, J., et al., *Side-by-Side Comparison of Commonly Used Biomolecules That Differ in Size and Affinity on Tumor Uptake and Internalization*. PLoS One, 2015. **10**(4): p. e0124440.
36. Leelawattanachai, J., et al., *Side-by-Side Comparison of Commonly Used Biomolecules That Differ in Size and Affinity on Tumor Uptake and Internalization*. PLoS One, 2015. **10**(4): p. e0124440.
37. Poirot, L., et al., *Multiplex Genome-Edited T-cell Manufacturing Platform for "Off-the-Shelf" Adoptive T-cell Immunotherapies*. Cancer Res, 2015. **75**(18): p. 3853-64.
38. Kang, S., et al., *Virus-mimetic polyplex particles for systemic and inflammation-specific targeted delivery of large genetic contents*. Gene Ther, 2013. **20**(11): p. 1042-52.
39. Hinrichs, C.S. and N.P. Restifo, *Reassessing target antigens for adoptive T-cell therapy*. Nat Biotechnol, 2013. **31**(11): p. 999-1008.
40. Newick, K., et al., *CAR T Cell Therapy for Solid Tumors*. Annu Rev Med, 2017. **68**: p. 139-152.
41. Ledebur, H.C. and T.P. Parks, *Transcriptional regulation of the intercellular adhesion molecule-1 gene by inflammatory cytokines in human endothelial cells. Essential roles of a variant NF-kappa B site and p65 homodimers*. J Biol Chem, 1995. **270**(2): p. 933-43.
42. Usami, Y., et al., *Intercellular adhesion molecule-1 (ICAM-1) expression correlates with oral cancer progression and induces macrophage/cancer cell adhesion*. Int J Cancer, 2013. **133**(3): p. 568-78.
43. Roland, C.L., et al., *ICAM-1 expression determines malignant potential of cancer*. Surgery, 2007. **141**(6): p. 705-7.
44. Guo, P., et al., *ICAM-1 as a molecular target for triple negative breast cancer*. Proc Natl Acad Sci U S A, 2014. **111**(41): p. 14710-5.
45. Carman, C.V. and T.A. Springer, *Integrin avidity regulation: are changes in affinity and conformation underemphasized?* Curr Opin Cell Biol, 2003. **15**(5): p. 547-56.
46. Boissonnas, A., et al., *In vivo imaging of cytotoxic T cell infiltration and elimination of a solid tumor*. J Exp Med, 2007. **204**(2): p. 345-56.
47. Porter, B.B. and J.T. Harty, *The onset of CD8+-T-cell contraction is influenced by the peak of Listeria monocytogenes infection and antigen display*. Infect Immun, 2006. **74**(3): p. 1528-36.

48. Keu, K.V., et al., *Reporter gene imaging of targeted T cell immunotherapy in recurrent glioma*. Sci Transl Med, 2017. **9**(373).
49. Yaghoubi, S.S., et al., *Noninvasive detection of therapeutic cytolytic T cells with 18F-FHBG PET in a patient with glioma*. Nat Clin Pract Oncol, 2009. **6**(1): p. 53-8.
50. Drent, E., et al., *A Rational Strategy for Reducing On-Target Off-Tumor Effects of CD38-Chimeric Antigen Receptors by Affinity Optimization*. Mol Ther, 2017.
51. Kalergis, A.M., et al., *Efficient T cell activation requires an optimal dwell-time of interaction between the TCR and the pMHC complex*. Nat Immunol, 2001. **2**(3): p. 229-34.
52. Valitutti, S., *The Serial Engagement Model 17 Years After: From TCR Triggering to Immunotherapy*. Front Immunol, 2012. **3**: p. 272.
53. McMahan, R.H., et al., *Relating TCR-peptide-MHC affinity to immunogenicity for the design of tumor vaccines*. J Clin Invest, 2006. **116**(9): p. 2543-51.
54. Robbins, P.F., et al., *Single and dual amino acid substitutions in TCR CDRs can enhance antigen-specific T cell functions*. J Immunol, 2008. **180**(9): p. 6116-31.
55. Co, M.S., et al., *Humanized antibodies for antiviral therapy*. Proc Natl Acad Sci U S A, 1991. **88**(7): p. 2869-73.

# CHAPTER 5

# TAKING ADVANTAGE OF SSTR2 BIOLOGY FOR SPATIOTEMPORAL CONTROL OF CAR T CELLS AND UTILIZING THIS REPORTER WITH OTHER CAR T THERAPYS AND THERAPY COMBINATIONS

**Summary**

So far we have been successful in our ability to target ICAM1 positive tumors and utilizing SSTR2 as a PET reporter to track CAR T cell bio-distribution and dynamics. Here, we share data that opens the possibility of utilizing SSTR2 beyond a simple PET reporter. Here, we also share additional preliminary data imaging SSTR2 in combination with other ACT's, such as CD19 targeting CAR T.

## Using SSTR2 to control CAR T cell activation

SSTR2 expression in T cells is absent or very low, while high levels of expression have been found in some neuroendocrine tumors [1, 2]. In terms of SSTR2 expression on the surface of tumors (specifically neuroendocrine and pituitary tumors), the signaling mediated via SSTR2 imparts anti-proliferative action through phosphotyrosine phosphatases which modulate MAPK and PI3K/Akt pathways [3]. SSTR2 is a G-protein coupled receptor with 7-transmemberane domains, and is categorized as Gα-GPCR. SSTR2 belongs specifically to Gαi, as its induction inhibits adenylyl cyclase and cAMP production [4]. SSTR2 has also been shown to activate phospholipase C [5]. All of these signaling cascades in tumor cells seem to induce anti-proliferative qualities to the cells. However in the context of T cell biology, it has long been understood that it is absolutely essential for the depletion/inhibition of cAMP in order for TCR mediated T cell activation to occur[2, 6-8]. Therefore, it was logical to perceive that inducing SSTR2 signaling cascade would lead to the depletion of cAMP and encourage/simulate TCR

mediated T cell activation. These same signaling cascades, when applied to T cell biology, not only can activate T cells but could possibly also induce chemotaxis.

To answer this possibility, we tested these signaling cascades in human primary T cells with and without SSTR2 transduction. First, we confirmed the signaling cascade in primary T cells follows the same molecular events as those described in tumors cells in the past: Ca2+ induction via phospholipase C, induction of phosphoAKT via MAPK and PI3K/Akt pathways, and even cAMP inhibition. All of these molecular events were confirmed via the use of Lanreotide (SSTR2 agonist) only on SSTR2-transduced T cells, with no effect on non-transduced T cells. We looked at and confirmed activation markers, such as CD69, being induced via SSTR2+Lanreotide incubation. In addition, we also verified the induction of activation/proliferative cytokine (IL2) secretion, upon Lanreotide incubation. This gave us the indication that SSTR2 induced activation to some degree mimics TCR mediated T cell activation.

***Experimental procedure***

CD69 activation check.

To measure intracellular calcium release, the CMyc-F292A-CAR-P2A-SSTR2 (mAS) transduced and NT Primary T cells were left un-treated or treated with 1μM Lanreotide or 1μM Ionomycin for 2hours. These cells were then labeled with 2 μg/ml anti-human CD69-APC (Biolegend) for analysis by flow cytometry (Gallios cytometer, Beckman Coulter).

Ca2+ signaling check.

To measure intracellular calcium release, the CMyc-F292A-CAR-P2A-SSTR2 (mAS) transduced and NT Primary T cells were stained with 2 μg/mL Fluo-4 AM (Molecular Probes) at 37 °C for 30 min followed by incubation in fresh media for an additional 10 min. To test Ca2+ excitement via Flow cytometry (Gallios cytometer, Beckman Coulter),

cells were gated for Live cells using CalceinBlue-AM. Cells were read without stimulation. After significant events were captured, the reading was paused and Lanreotide was spiked-in at the final concentration at 1μM. After significant events were captured, the reading was paused and Ionomycin was spiked-in at the final concentration at 1μM, before the final event was captured. For measurements on a microscope (EVOS, Thermo Fisher), the same Fluo-4 AM labeled cells were plated on an 8-chamber slide (NUNC, Inc) and protected from light. A time lapse image is initiated and within 10-15 seconds 1μM final Lanreotide was spiked-in, and about 60-80 seconds later 1μM final Ionomycin was spiked-in. Collected time-lapse images were analyzed using ImageJ mean intensity quantification.

cAMP and IL2 ELISA.

To measure the cAMP level, human primary T-Cells were first incubated with 10μM forskolin (Invitrogen) at 37 °C for 30 min and then stimulated by incubating with 1μM SDF1alpha or 1 μM Lanreotide for 5 min. The cells were washed with PBS and immediately lysed in cell lysis buffer. cAMP level in the lysates was determined using a cAMP Elisa Kit (cAMP complete ELISA Kit, Enzo Life Science, Inc.). To test IL2 secretion, SSTR2 transduced and Non-Transduced T cells were incubated in media with and without 1μM Lanreotide. After 24Hr incubation, the media was collected and the level of IL2 secretion was quantified using ELISA (Biolegend, USA).

Phosphor-AKT Western Blot.

Non-Transduced human primary T cells and T cells transduced to express SSTR2 were treated at different concentrations of Lanreotide. Alternatively, these same cells were either treated with 1μM SDF1alpha or 1μM Lanreotide, and sampled over a time course (10min, 30min, 1hr, 3hr, 6hr). Total cell lysates were prepared and Western blot analysis

was performed using rabbit polyclonal antibodies specific for phospho-Akt (Ser473) and GAPDH (Cell Signaling).

SSTR2 + CD3 cell expansion test.

To test the possibility of using Lanreotide as a means of T cell activation as well as maintenance of proliferation and differentiation, human primary T cells transduced with CMyc-F292A-CAR-P2A-SSTR2 (mAS) were washed and re-suspended in cytokine free media. These cells were plated at 0.5x $10^6$ cell/ml and separated into 5 conditions (no addition, IL2 at 30UI/ml, CD3 conjugated DynaBeads, 1μM Lanreotide, and CD3 conjugated DynaBeads + 1μM Lanreotide.) 1/10 of the culture was tested for viability via Calcein-AM Flow Cytometry, 4 days post incubation.

***Results: SSTR2 mediated activation of CAR T cells is achievable with FDA approved drugs***

We see clear signs of SSTR2 transduced Primary T cells being activated, while being incubated with FDA approved SSTR2 agonist (Lanreotide). CD69 is an early inducible cell surface glycoprotein acquired during lymphoid activation and is involved in lymphocyte proliferation. We see clear signs that CD69 is unregulated when incubated with Lanreotide only with SSTR2 transduced primary T cells (Figure 5.1A), presumably due to inhibition of cAMP production (Figure 5.2 B). There is basal level of activation of the CAR T transduced T cells, as naive t cells have minor expression of ICAM-1.This CAR T is against ICAM-1, imparting minor level of basal activation. At the same time the same level of CD69 up-regulation is seen in both non-transduced and SSTR2-transduced Primary T cells when incubated with Ionomycin, an experiment control to verify the function in both cell types.

We also verified that SSTR2-transduced cells mediate Ca2+ release. Using Fluo-4 AM to label intracellular Ca2+, florescence imaging and flowcytometry showed an

increase in calcium signaling in the transduced cells upon Lanreotide addition (Figure 5.1 B&D). Calcium ion increase leads to NFAT activation, required for T cell activation, IL-2 production and T cell survival[9].

The Akt/protein kinase B plays a central role in T-cell proliferation, function, and survival. pAKT expression in activated human T cells increased proliferation and cytokine production, a likely result of their sustained expression of nuclear factor-κB (NF-κB), and provided resistance to apoptosis by up regulating anti-apoptotic molecules. Here we see that even at a very low concentration of Lanreotide (10nM) we are able to induce phosphoAKT in SSTR2-transduced Primary T cells (Figure 5.1C). We evaluated the duration of this induction, which lasts between 3-6 hours when incubated with 1μM Lanreotide in SSTR2-Transduced cell, with no signs of induction in non-transduced cells (Figure 5.2A). We then verified the secretion of IL2 by these cells when incubated with Lanreotide (Figure 5.2 B), an indication that SSTR2 induced activation to some degree mimics TCR mediated T cell activation induction of activation/proliferative cytokine (IL2) secretion. To this point we can keep SSTR2-Transduced cells alive without replenishing additional proliferative cytokines (Figure 5.2D).

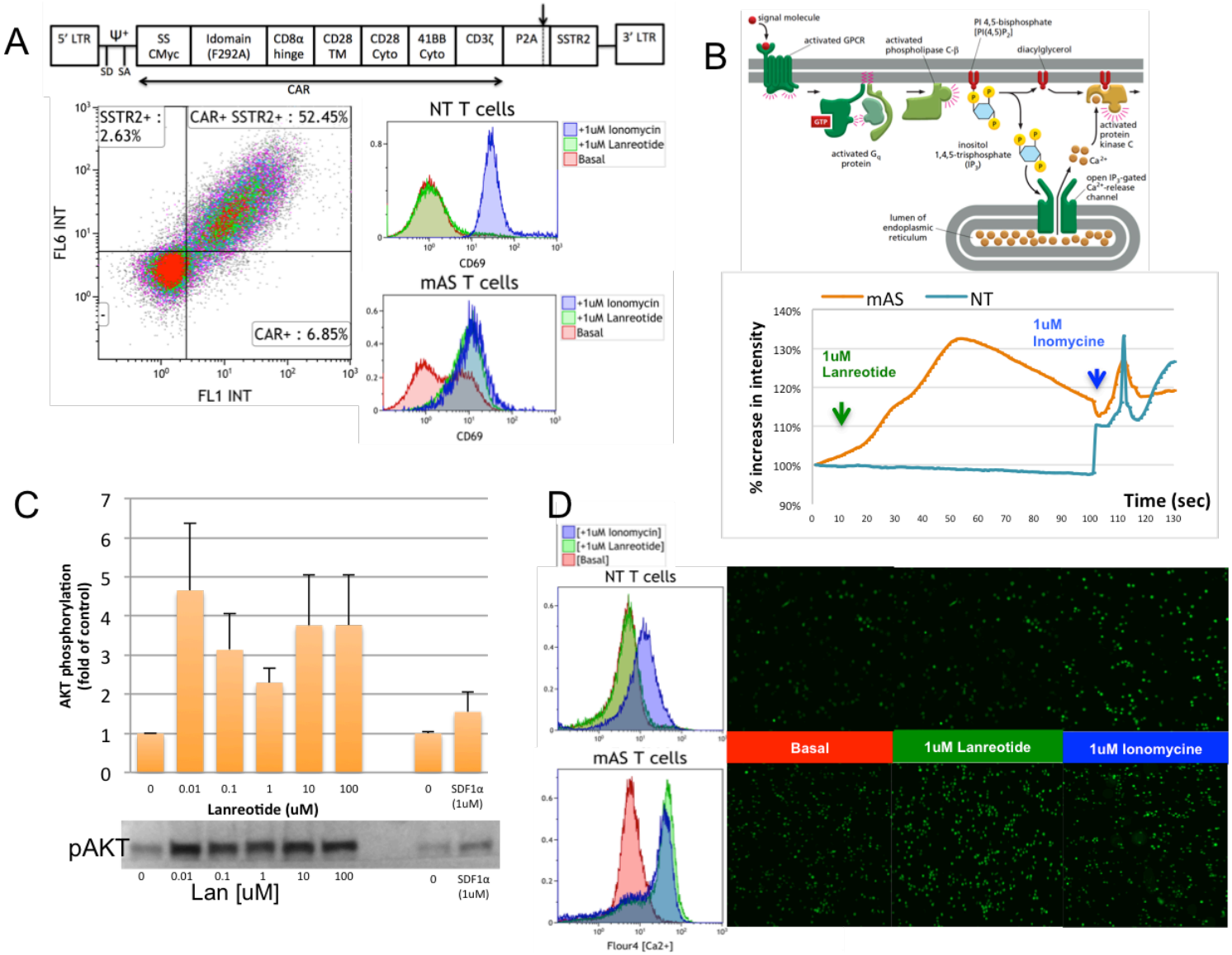
A
5′ LTR
Ψ+
SD SA
SS CMyc
Idomain (F292A)
CD8α hinge
CD28 TM
CD28 Cyto
41BB Cyto
CD3ζ
P2A
SSTR2
3′ LTR
CAR
SSTR2+ : 2.63%
CAR+ SSTR2+ : 52.45%
CAR+ : 6.85%
FL6 INT
FL1 INT
NT T cells
mAS T cells
+1uM Ionomycin
+1uM Lanreotide
Basal
CD69
B
signal molecule
activated GPCR
activated phospholipase C-β
PI 4,5-bisphosphate [PI(4,5)P2]
diacylglycerol
activated protein kinase C
activated Gq protein
inositol 1,4,5-trisphosphate (IP3)
Ca2+
open IP3-gated Ca2+-release channel
lumen of endoplasmic reticulum
mAS
NT
1uM Lanreotide
1uM Inomycine
% increase in intensity
Time (sec)
C
AKT phosphorylation (fold of control)
Lanreotide (uM)
SDF1α (1uM)
pAKT
Lan [uM]
D
[+1uM Ionomycin]
[+1uM Lanreotide]
[Basal]
NT T cells
mAS T cells
Flour4 [Ca2+]
Basal
1uM Lanreotide
1uM Ionomycine

**Figure 5.1 Verifying SSTR2 can be used to activate Primary T cells.**

A. Illustrated on top: Schematic of lentiviral construct used to transduce Primary T cells. Left panel: dot-blot of flowcytometry check for expression of both CMyc-Fused ICAM1-CAR (anti-CMyc-FITC), and SSTR2(Anti-SSTR2-APC), cells were gated for live cell population only via CalceinBlue AM(FL9). Center panel: non-transduced , Right panel CMyc-F292A-CAR-P2A-SSTR2 (mAS) -Transduced Human Primary T cells untreated or incubated 1μM Lanreotide or 1μM Ionomycin at 37 °C for 2 hr and stained for CD69 expression
B. Top: Graphic Illustration of SSTR2 associated Ga signaling cascade, belongs to Gai, inhibiting adenyl cyclase and cAMP production. [10]
C. Bottom: Analyzed using ImageJ mean intensity quantification. Fluo-4 AM labeled cells imaged over time. After imaging initiated, within 10-15 seconds 1μM final Lanreotide is spiked-in, and about 60-80 seconds later 1μM final Ionomycin is spiked-in. Graph illustrates change in Flour-4 fluorescence intensity over the time coarse, measuring intracellular calcium release. Orange line is SSTR2-transduced cells, Blue line are non-transduced cells.
D. Western Blot for phospho-Akt (Ser473). CMyc-F292A-CAR-P2A-SSTR2 (mAS) transduced un-treated or treated at different concentrations of Lanreotide (0.01μM to 100μM) or SDF1a (1μM). Bar graph showing average fold increase in blot, normalized to untreated cells.
E. Flow cytometry to measure intracellular calcium release, the CMyc-F292A-CAR-P2A-SSTR2 (mAS) transduced and NT Primary T cells were stained with Fluo-4 AM Cells were read without stimulation (Red), 1μM Lanreotide (Green), 1μM Ionomycin (Blue), Right imaging panel are representative images from Figure 5.1 B.

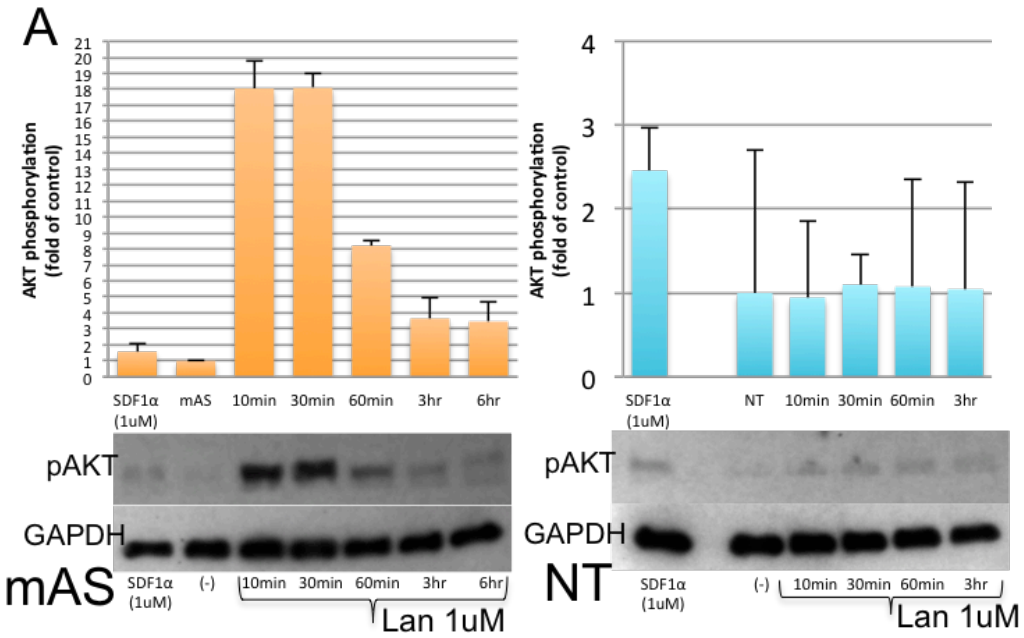
A
AKT phosphorylation (fold of control)
SDF1α (1uM)
mAS
10min
30min
60min
3hr
6hr
NT
pAKT
GAPDH
(-)
Lan 1uM

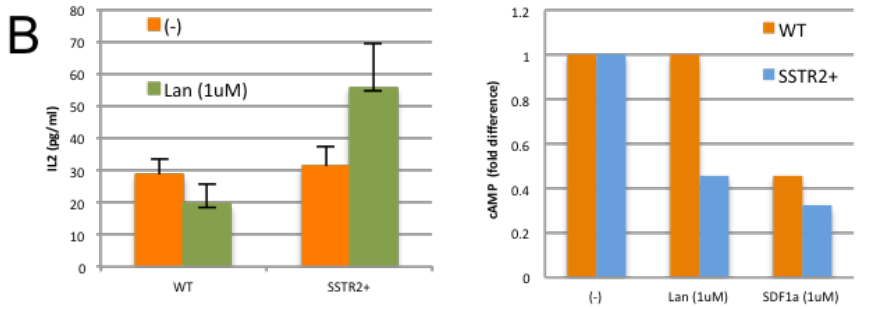
B
(-)
Lan (1uM)
IL2 (pg/ml)
WT
SSTR2+
cAMP (fold difference)
SDF1a (1uM)

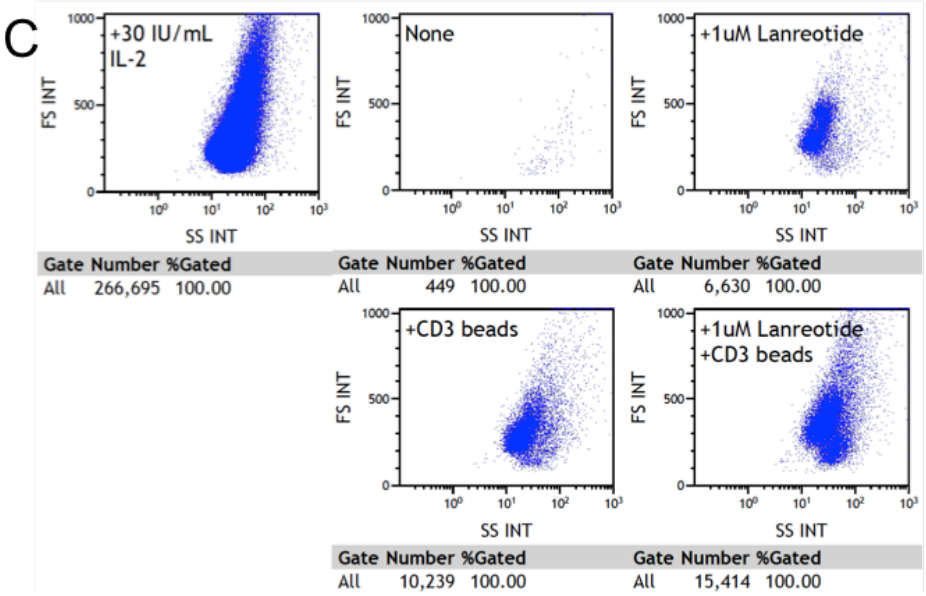
C
+30 IU/mL IL-2
None
+1uM Lanreotide
+CD3 beads
+1uM Lanreotide +CD3 beads
FS INT
SS INT
Gate Number %Gated
All 266,695 100.00
All 449 100.00
All 6,630 100.00
All 10,239 100.00
All 15,414 100.00

**Figure 5.2 Verifying SSTR2 signaling cascades in Primary T cells**

A. Western Blot for phospho-Akt (Ser473). CMyc-F292A-CAR-P2A-SSTR2 (mAS) transduced (right) vs. non-transduced T cells. Un-treated or treated with 1μM Lanreotide (over a time coarse 10min, 30min, 1hr, 3hr, 6Hr) or SDF1a (1μM). Bar graph showing average fold increase in blot, normalized to untreated cells.
B. ELISA quantitation of IL2 secretion from Primary T cells. CMyc-F292A-CAR-P2A-SSTR2 (mAS) transduced (right) vs. non-transduced T cells (left), when incubated with or without Lanreotide (1μM) for 24Hr .
C. ELISA of cAMP induction/depletion from Primary T cells. CMyc-F292A-CAR-P2A-SSTR2 (mAS) transduced (orange) vs. non-transduced T cells.(blue). All cells pretreated with Forskolin for 30min, then washed, and either treated with Lanreotide (1μM) or SDF1alpha (1μM) for 10min before cell lysis. Graph illustrates fold decrease of cAMP.
D. Flow cytometry to see the amount of CMyc-F292A-CAR-P2A-SSTR2 (mAS) transduced Primary T cells. Dot-blot of FS/SS, after gating for Live cells via CalceinAM.

**Adapting SSTR2 mediated imaging on Other CAR T therapies (CD19-CAR)**

CD19-specific CAR T cell immunotherapy has shown significant antitumor activity in the treatment of high-risk relapsed and refractory leukemia and lymphoma, and has revolutionized the treatment landscape for patients with advanced lymphoid malignancies. However, manipulating the immune system is also associated with unique and potentially life-threatening toxicities. Two of these therapies (Kymriah™ and Yescarta™) were recently approved by the FDA[11]. Kymriah™ (tisagenlecleucel) is for the treatment of pediatric patients and young adults with refractory or relapse (R/R) B cell precursor acute lymphoblastic leukemia (ALL). Yescarta™ (axicabtagene ciloleucel) is for the treatment of adult patients with R/R large B cell lymphoma. They are both genetically modified autologous T cells expressing a CD19-specific CAR, lysing CD19-positive targets (normal and malignant B lineage cells). A noted difference is shown in the vectors used for Kymriah™ (lentiviral vector) and Yescarta™ (ϒ-retroviral vector). Their dramatic efficacy in the short term has been highlighted by many media reports. By contrast, their glaring safety gaps behind the miracles remain much less addressed. To help answer these concerns and keep a watchful eye on these cells *in-vivo*, we did a preliminary study to evaluate SSTR2 as a PET-reporter to image CD19 CAR. Though this study has not mimicked what others have published, it does show that SSTR2 as a PET reporter monitor CD19-CAR *in-vivo*.

***Experimental procedure***

Construction of SSTR2-CD19 CAR vector.

Genetic sequences encoding single chain fragment variable (scfv) against anti-CD19 (mAb clone FMC63) were derived from a previous study[12, 13]. CD19-scfv were fused at the C-terminus directly to the CD8 hinge, CD28 trans-membrane domain, and the intracellular portions of the 3$^{rd}$ generation CAR architecture incorporating the

cytoplasmic domains of CD28, CD137, and CD3ζ. In addition a CMyc tag was fused to the N-terminus of the CD19-scfv, to enable cell surface expression verification. The complete CAR insert was then subcloned into a pLenti backbone. A reporter gene for CAR T cell imaging, SSTR2, was linked to CD19-CAR at the N-terminus using a 'ribosome skipping' porcine teschovirus-1 2 A (P2A) sequence to ensure comparable production of CAR and SSTR2 from the same mRNA.

Lentivirus production and transduction of T cells.

Lentivirus was produced by transiently transfecting HEK 293 T cells using calcium phosphate. Briefly, 10 μg of transfer gene, 7.5 μg of pCMV-dR8.2 (Addgene) and 5 μg of pCMV-VSVG (Addgene) were mixed and incubated with 2 M $CaCl_2$ followed by 2x HBSS. Resulting solutions were added drop-wise to 10 $cm^2$ cell culture dishes seeded with $3.2 \times 10^6$ HEK 293 T cells in 10 ml DMEM 24hr previously. Transfection media was replaced after 6 h. Media containing lentivirus was harvested at 48 and 72 h post transfection, Filtered through 0.45 μm filters, and concentrated by ultracentrifugation at 75,000x g for 2 h at 4 °C. Lentivirus was then re-suspended in serum containing media and frozen at −80 °C. Human T cells were transduced 24–72 h post activation with anti-CD3/CD28 Dynabeads either by spinfection (1,000 g for 1 h at 32 °C) or by overnight incubation with lentivirus. T cells were transduced once more 24 hr after the transduction. During and following transductions, media containing IL-2 was replaced with media containing human IL-7 (10 ng/ml) and IL-15 (5 ng/ml) (Peprotech).

Burkitt Lymphoma mouse model, whole-body tumor imaging.

All animal studies were approved by Weill Cornell Medicine's Institutional Animal Care and Use Committee. 8 to 10-week old female and male NOD-scidIL2Rg$^{null}$ (NSG) mice (Jackson Laboratory) were used for xenograft experiments with Raji cells. GFP and fLuc-expressing Raji ($0.75x10^6$cells per mouse) were intravenously injected to establish the

xenograft. Longitudinal measurements of Raji tumor burdens were taken using a whole-body optical imager (In-Vivo Xtreme 4MP, Bruker) 15 minutes after intra-peritoneal injection of 100 mL of 150 mg/mL D-luciferin (GoldBio). Total tumor burden was measured by generating full body region of interests (ROI) and integrating total flux of luminescence using Bruker Analysis software. GFP-expressing livers, spleen, heart, and lungs were extracted from mice and imaged with a whole-body optical imager (In-vivo F-Pro, Bruker). Mice were then treated with $5x10^6$ CAR T+ cells, or matched dose of Non-transduced (NT) T cell control. T cells were injected via Tail-vein 7 days post Tumor injection. To image the CAR T distribution PET/ CT is performed targeting SSTR2 PET reporter.

Labeling of $^{18}$F-NOTA-octreotide (NOTAOCT).

NOTAOCT (1,4,7-Triazacyclononane-1,4,7-triacetic acid-octreotide, GMP grade) was obtained as a 1 mg lyophilized powder (cat #9762, ABX Pharmaceuticals). NOTAOCT vial content was diluted with 18 MOHM-cm water to 200 µl (5 mg/ml solution) and stored at 4 °C as a stock solution. For chelation of NOTA with Fluorine-18, 5 µl of NOTAOCT was added to 10 µl of 0.1 M sodium acetate, pH 4, 6 µl of 2 mM AlCl3, and 100 µl containing ~30 mCi$^{18}$F. The solution was immediately placed in a thermomixer (Eppendorf ) at 100 °C and incubated for 15 minutes followed by cooling to room temperature and dilution in 15 ml dd$H_2O$. A Sep-Pak light C18 column was regenerated in 3 ml 100% ethanol and washed twice in 5 ml dd$H_2O$ with an observed flow rate of 10 drops per minute. NOTAOCT was then loaded to the Sep-Pak column, which was later washed in 15 ml 18 MW water to eliminate any remaining free$^{18}$F. Trapped NOTAOCT was eluted from the column using 300 µl of ethanol and diluted to 1.5 ml with PBS for injection, providing the final product in ~15% ethanol isotonic, injectable solution. The eluent was passed through 0.2 µm filter purity of the final product was checked by reverse phase HPLC.

PET/CT imaging.

Registered CT images were acquired using a micro-PET/CT scanner (Inveon, Siemens) at 1–2 h post NOTAOCT injection. Projection data was acquired in a cone-beam geometry with approximately 1 sec steps at 1 degree angular increments. At least 10 million coincidence events were acquired for PET per study using a 250 to 750 keV energy window and a 6 ns timing window. References tube containing 100 µl of a 10%ID/$cm^3$ equivalent dose for quantification of NOTATOC uptake *in-vivo*. To compute NOTAOCT uptake within mouse lungs, ellipsoids were drawn separately on the left and right sides of lungs to enclose the majority of their footprint. e %ID/$cm^3$ values, computed relative to the counts obtained in the reference tube, were approximated to a standard uptake value (SUV) by dividing %ID/$cm^3$ by four, assuming injection efficiency of 100% and 25 g of body weight. Visualization and analyses of PET/CT images were performed using AMIDE software (http:// amide.sourceforge.net).

Histology.

After euthanasia, mouse tissue was harvested and fixed with 4% paraformaldehyde. Post fixation and embedded in paraffin. Tissues were cut to produce 5 µm sections (Microtome, Leica). Sections were stained with hematoxylin and eosin (H&E) or hematoxylin only for CD3 immunostaining (performed by HistoWiz, Inc.).

Study Approval.

The protocol for blood draw along with acquisition of informed consent from healthy volunteers was approved by the Institutional Review Board (IRB) of Weill Cornell Medicine (Permit Number: 1302013613). Studies involving human blood were carried out in strict accordance with Weill Cornell's IRB guidelines and regulation. All animal experiments were performed in strict accordance with the recommendations contained

within the National Institute of Health's Guide for the Care and Use of Laboratory Animals. Animal handling protocols were approved by the Institutional Laboratory Animal Use and Care Committee of Weill Cornell Medicine (Permit Number: 2012–0063).

***Results: Real-time imaging of CD19-CAR T cell kinetics, efficacy, and toxicity.***

To spatiotemporally monitor T cell distribution in real-time by PET/CT, we introduced an imaging reporter gene, SSTR2, into CD19 CAR (3$^{rd}$ generation) vector using a ribosome skipping P2A sequence to ensure equal expression of CAR and the reporter on the surface of T cells (Figure 5.3A). Expression of SSTR2 enables binding and intracellular accumulation of an infused, positron-emitting, SSTR2-specfic radiotracer, $^{18}$F-NOTA-Octreotide (NOTAOCT) Emitted signals can then be detected with high resolution without limits on tissue penetration by a micro PET scanner. Expression of SSTR2 and CMyc-tagged I domain was confirmed by antibody staining (Figure 5.3A), although a higher level of binding was found with the SSTR2 antibody, likely due to lower background noise. Mice were xenografted with Raji tumors that were transduced with GFP-Firefly Luciferase. As before, the mice were then treated with NT, or CD19-CAR T cells 7 days post tumor xenograft. Whole-body luminescence imaging (Figure 5.3B) was performed to estimate tumor burden while PET/CT imaging was performed on the same day to track CAR T cell distribution (Figure 5.4C). PET/CT images in mice displayed expected background uptake levels of NOTAOCT in gallbladder, kidneys, and bladder caused by radiotracer excretion (Figure 5.3 C)[14]. In the NT treated control cohort, a small but gradual increase in non-specific tracer uptake was observed, which was due to increasing tumor bur- den and the associated increase in blood pooling (Figure 5.3 C). In contrast, specific tracer uptake was observed in mice treated with SSTR2-CD19-CAR T cells, demonstrating the expansion wherever the Raji tumor cells seem to be present via luminescence (Figure 5.3B) head, lungs, liver and

spine. Radiotracer shows some background uptake by the liver, resulting in bright signals in the gall bladder, which clears through gut. It is also cleared through kidneys and bladder. While there is no biphasic expansion and contraction observed like our previous study[13].

It is clear that the early attempts of this study did not follow the scenario that others have published [15-18]. It requires optimization in carrying out the ideal dose for both tumor and T cell. Furthermore it is important to evaluate multiple generations of this construct, in-order for us to properly evaluate this therapy. However, it is clear that the SSTR2-PET in conjunction with this CAR T would work. As it is obvious the co-localization was clear in PET/CT (Figure 5.3C) and even evident in histology (Figure 5.3D). Xenograft shows growth in the brain (subarachnoid, ventricles), spine, lymph nodes, liver, and bones. Tumor-specific localization and expansion of SSTR2-CD19CAR T-Cells are confirmed by PET/CT using a radiotracer 18F-NOTA-Octreotide, CAR T cell expansion in seen in the head, lungs, liver, and spine. Video recording show great impact with this therapy. These Raji cells seems to travel the subarachnoid and ventricles spaces surrounding the nervous system, produced great toxicity, where mice were showing severe hind limb paralysis. After a few days of CD19-CAR, these paralytic incidences vanished in the CAR treated mice. Additionally, we clearly see via histology the localization of T cell, along with Raji cells logged in between the cerebrum and cerebellum in mice were the T cell expansion was not fast enough to completely clear the Raji tumors (Figure 5.3D). A broader study for evaluating multiple generations of CD19-CAR is currently underway. In addition to analyzing if there are any dynamics of expansion and contraction, when it comes to non-solid tumors.

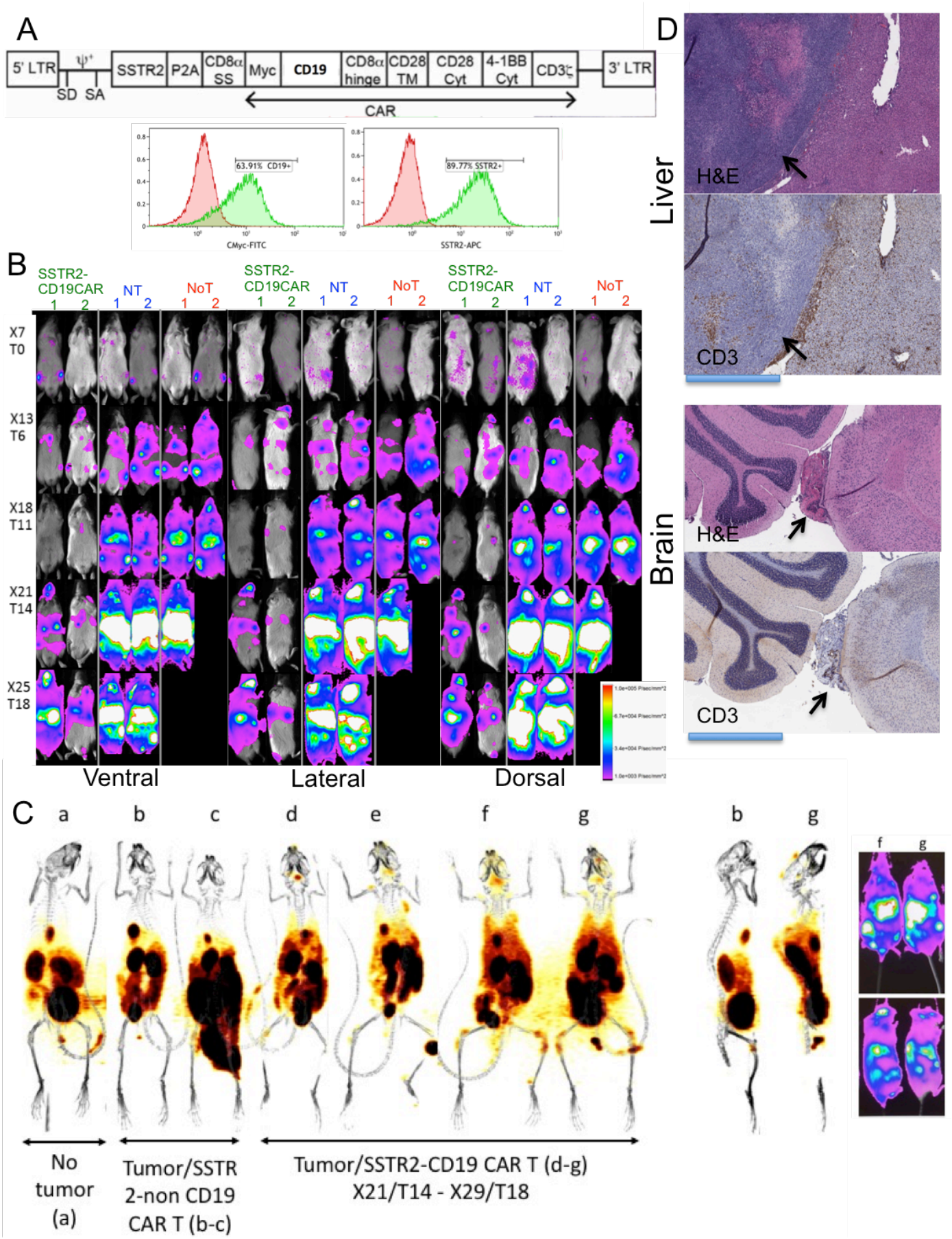
A
5' LTR
ψ+
SD SA
SSTR2
P2A
CD8α SS
Myc
CD19
CD8α hinge
CD28 TM
CD28 Cyt
4-1BB Cyt
CD3ζ
3' LTR
CAR
63.91% CD19+
CMyc-FITC
89.77% SSTR2+
SSTR2-APC
B
SSTR2-CD19CAR
NT
NoT
X7 T0
X13 T6
X18 T11
X21 T14
X25 T18
Ventral
Lateral
Dorsal
D
Liver
H&E
CD3
Brain
H&E
CD3
C
a
b
c
d
e
f
g
No tumor (a)
Tumor/SSTR 2-non CD19 CAR T (b-c)
Tumor/SSTR2-CD19 CAR T (d-g) X21/T14 - X29/T18

**Figure 5.3 Longitudinal, concurrent measurements of tumor burden, T cell distribution for CD19-CAR**

A. Schematic of the lentivirus vector encoding SSTR2-CD19CAR. LTR = long terminal repeat; SD = splice donor; SA = splice acceptor; ψ+ = packaging signal; SS = signal sequence; TM = transmembrane; Cyt = cytosolic domain. Anti-Myc antibody binding and Anti-SSTR2 binding to T cells transduced with SSTR2-CD19CAR=green histogram. Red histogram= non-transduced T cells.
B. Whole-body luminescence imaging was used to estimate tumor burden in mice infused with T cells 7 days post-tumor implantation. NT = non-transduced T cells. No T = mice received no T cells. X# indicating days of Xenografts, T# indicating days of CAR T/NT cell administration.
C. Raji (Burkitt's lymphoma) xenografts shows growth in the brain (subarachnoid, ventricles), spine, lymph nodes, liver, and bones. Tumor-specific localization and expansion of SSTR2-CD19 CAR T Cells are confirmed by PET/CT using a radiotracer 18F-NOTA-Octreotide, CAR T cell expansion in seen in the head(d-g), lungs (f-g), liver (d-g), and spine (g). Radiotracer shows some background uptake by the liver, resulting in bright signals in the gall bladder, which clears through the gut. It is also cleared through kidneys and bladder. Right panel, matching luminescence images of mouse (f) and (g); Ventral image on top, Lateral Right on bottom.
D. Liver and Brain tissues harvested from mice treated with SSTR2-CD19 CAR T cells. Sections were processed for H&E and CD3 staining. scale bar in each image is 1 mm. Arrow indicates tumor

REFERENCES


1. Talme T., e.a., *Somatostatin receptor (SSTR) expression and function in normal and leukaemic T-cells. Evidence for selective effects on adhesion to extracellular matrix components via SSTR2 and/or 3*. Clinical Experimental Immunology, 2001. **125**: p. 71-79.
2. Lichtenstein, C.S.H.a.L.M., *The Role of Cyclic AMP in the Cytolytic Activity of Lymphocytes*. The Journal of Immunology, 1971. **107**(2): p. 610-612.
3. Cakir, M., D. Dworakowska, and A. Grossman, *Somatostatin receptor biology in neuroendocrine and pituitary tumours: part 1--molecular pathways*. J Cell Mol Med, 2010. **14**(11): p. 2570-84.
4. Tomura H., e.a., *Transfected human somatostatin receptor type 2, SSTR2, not only inhibits adenylate cyclase but also stimulates phospholipase C and Ca2+ mobilization*. Biochemical and Biophysical Research Communications, 1994. **200**(2): p. 986-992.
5. E., T.J., *Somatostatin (SSTR2) receptors mediate phospholipase C-independent Ca2+ mobilization in rat AR42J*. Biochemical and Biophysical Research Communications, 1995. **214**(1): p. 91-95.
6. Taskén, V.L.W.a.K., *Molecular Mechanisms for cAMP-Mediated Immunoregulation in T cells - Role of Anchored Protein Kinase A Signaling Units*. Frontiers in Immunology, 2016. **7**: p. 222.
7. Kammer, G.W., *The adenylate cyclase-cAMP-protein kinase A pathway and regulation of the immune response*. Immunology Today, 1988. **9**: p. 222-229.
8. Bjmn S. SkHlhegg, B.F.L., Stein 0.Dskeland, Vida Hransson, Tor Lea, and Tore Jahnsen, *Cyclic AMP-dependent protein kinase type I mediates the inhibitory effects of 3',5'-cyclic adenosine monophosphate on cell replication in human T lymphocytes*. The Journal of Biological Chemistry, 1992. **267**(22): p. 15707-15714.
9. Fracchia, K.M., C.Y. Pai, and C.M. Walsh, *Modulation of T Cell Metabolism and Function through Calcium Signaling*. Front Immunol, 2013. **4**: p. 324.
10. Bruce Alberts, A.J., Julian Lewis, Martin Raff, Keith Roberts, and Peter Walter., *Molecular Biology of the Cell, 5th edition*. 2008.
11. Zheng, P.P., J.M. Kros, and J. Li, *Approved CAR T cell therapies: ice bucket challenges on glaring safety risks and long-term impacts*. Drug Discov Today, 2018.
12. Davila, M.L., et al., *Efficacy and toxicity management of 19-28z CAR T cell therapy in B cell acute lymphoblastic leukemia*. Sci Transl Med, 2014. **6**(224): p. 224ra25.
13. Vedvyas, Y., et al., *Longitudinal PET imaging demonstrates biphasic CAR T cell responses in survivors*. JCI Insight, 2016. **1**(19): p. e90064.
14. Park, S., et al., *Micromolar affinity CAR T cells to ICAM-1 achieves rapid tumor elimination while avoiding systemic toxicity*. Sci Rep, 2017. **7**(1): p. 14366.
15. Brentjens, R., et al., *Treatment of chronic lymphocytic leukemia with genetically targeted autologous T cells: case report of an unforeseen adverse event in a phase I clinical trial*. Mol Ther, 2010. **18**(4): p. 666-8.

16. Kofler, D.M., et al., *CD28 costimulation Impairs the efficacy of a redirected t-cell antitumor attack in the presence of regulatory t cells which can be overcome by preventing Lck activation*. Mol Ther, 2011. **19**(4): p. 760-7.
17. Hawkins, R.E., et al., *Development of adoptive cell therapy for cancer: a clinical perspective*. Hum Gene Ther, 2010. **21**(6): p. 665-72.
18. Lee, D.W., et al., *The future is now: chimeric antigen receptors as new targeted therapies for childhood cancer*. Clin Cancer Res, 2012. **18**(10): p. 2780-90.

# CHAPTER 6

## CONCLUSION AND FUTURE DIRECTION

***Conclusion:***

So far, we have achieved a few goals within the field of Adoptive Cell Therapy (ACT):

- We successfully developed an intercellular adhesion molecule-1 (ICAM-1) targeting CAR T for the treatment of aggressive thyroid cancer in a solid tumor model. This CAR mediated profound tumor killing that resulted in long-term remission and significantly improved the survival outcome compared to that of untreated mice. Additionally, similar results were shown even with patient derived tumors.
- We adapted Somatostatin receptor 2 (SSTR2), as a T cell PET reporter, used with ATC to quantitatively and longitudinally visualize the whole-body T cell distribution and antitumor dynamics by using a clinically approved radiotracer for PET imaging. T cells were detectable at low densities with high sensitivity and specificity.
- We adapting SSTR2-based PET to ICAM-1- Targeting CAR-T cells to show the treatment dynamics *in-vivo* with anaplastic thyroid tumors. This method hinted whether or not the CAR T is actually taking effect *in-vivo* by showing a real-time PET imaging to reveal biphasic T cell expansion and contraction at tumor sites.
- Chapter 4 illustrated how utilizing the same PET reporter helped to establish safety criteria for CAR T. In fact, it also evaluates the ideal affinity of the antigen recognition moiety to use when developing a CAR T therapy, which can significantly boost efficacy and safety.

***Using SSTR2-PET, along with additional ACTs***

One of the most obvious goals of this work would be to apply the use of SSTR2 as a PET reporter to any and all adoptive cell therapies that are currently in use. So far, we have been using ICAM-1 targeting CAR as our launching pad, but recently we have also evaluated CD19-CAR. However, since I made lentiviral constructs for various CAR T models, such as Her2, Mesothelin, and J591(PSMA targeting). I would like to see if this reporter would work in a TCR or even a TIL model. It would be of interest to see if the spatial localization dynamics of these therapies are any different from that of CAR T therapies. Ideally, this would provide some insight into the expansion kinetics of these TILs *in-vivo* and help push this broad therapy for more successful outcomes.

***Utilizing SSTR2 as a "kill-Switch" in-vivo***

One of the most useful tools we need for CAR T therapy is to eradicate the therapeutic in-case there are adverse effects. There are suicide genes currently under evaluation for this purpose, but their path to FDA approval is uncertain. Interestingly enough, the FDA recently approved Lutathera® (lutetium-177 ($^{177}$Lu)-Dotatate) for the treatment of gastro-enteropancreatic neuroendocrine tumors (GEP-NETs), and pancreatic neuroendocrine tumors (PNETs), that express Somatstatin receptors.[1] $^{177}$Lu is a low-energy $\beta^-$-emitter (0.497 $MeV_{max}$) with a relatively short tissue penetration range[2]**.** These physical properties suggest $^{177}$Lu to be an appropriate choice for treating small tumor lesions and micrometastases while limiting normal tissue damage. Since this is already FDA approved, it would be reasonable to try infusing this drug for CAR T cells eradication/killed in-vivo. Also, we can try yo look for a kamikaze effect, where the killing/targeting of CAR T cells leads to the killing of the surrounding tumor, due to CAR T localization.

***Utilizing SSTR2 beyond a PET tracer in-vivo***

We saw clear signs of SSTR2-transduced Primary T cell activation, when it is under incubation with FDA-approved SSTR2 agonist (Lanreotide). This activation could be NFAT-mediated, via calcium ion increase, leading to IL-2 production and T cell survival[3]. Since we see such clear signs of pAKT expression upon Lanreotide incubation, the activation might just be nuclear factor-κB (NF-κB) mediated. After deciphering the exact activation pathway that this signaling mediates, I would like to apply this *in-vivo*, to see if a first generation CAR in combination with SSTR2 activation would mimic the expansion/functional/proliferative dynamics of a 3$^{rd}$ generation.

In addition, I want to explore fusing co-stimulatory domains of CAR directly on to SSTR2, to observe if the functions of these domains can be split between the CAR and SSTR2, where the full cytotoxic function of the CAR-T would only be achieved with presence of Lanreotide. This concept, which is very similar to "Tandem-CAR", would add a layer of safety to the therapy.

***SSTR2 as a molecular switch***

We have clearly seen that SSTR2 activation can lead to the secretion of IL2 and induce CD69. Discovering if this activation is NFAT mediated will allow me to easily generate a cell therapy to induce the secretion of molecules. Using SSTR2 as a molecular switch, would all utilizing CRISPR/Cas9 to introduce molecules of interest to be transcribed downstream from IL2 or CD69. Utilizing a ribosome-skipping (P2A) motif can result in transcribing other cytokines along with IL2 or CD69.

# REFERENCES

1. *DA Approves Lutathera for GEP NET Therapy*. Journal of Nuclear Medicine, 2018. **59**(9N).
2. Rasaneh, S., et al., *177Lu labeling of Herceptin and preclinical validation as a new radiopharmaceutical for radioimmunotherapy of breast cancer*. Nucl Med Biol, 2010. **37**(8): p. 949-55.
3. Fracchia, K.M., C.Y. Pai, and C.M. Walsh, *Modulation of T Cell Metabolism and Function through Calcium Signaling*. Front Immunol, 2013. **4**: p. 324.